Laser-Induced Phosphor Thermometry - Feasibility and Precision in Combustion Applications

Lindén, Johannes

2012

Laser-Induced Phosphor Thermometry

Feasibility and precision in combustion applications

LUND
UNIVERSITY

Johannes Lindén

Lund Report on Combustion Physics, LRCP-154
ISBN 978-91-7473-361-7
ISSN 1102-8718
ISRN LUTFD2/TFCP-154-SE

Printed in Sweden by Media-Tryck, Lund University
Lund 2012

Till Magda och Elvy

Contents

Abstract

Temperature is one of the most fundamental parameters to be measured in many research disciplines. In combustion science, a thorough knowledge of temperature is essential for improving and optimizing combustion processes. Increasingly strict environmental legislation, greater demands for energy, and efforts to reduce dependence upon fossil fuels are forcing the combustion industry to obtain more adequate knowledge of combustion processes generally.

Laser Induced Phosphorescence (LIP) can serve as a tool for measuring temperature. It utilizes the temperature-dependent properties of the phosphorescence emitted by inorganic luminescent materials referred to as thermographic phosphors, after these have been illuminated by laser radiation. Either point- or two-dimensional measurements are usually performed by the use of either the temporal or the spectral temperature-dependent properties involved. The technique has many advantages. When used wisely it can be close to non-intrusive, offers remote sensing capabilities, and allows a high degree of temporal resolution, accuracy and precision to be obtained.

The phosphor is usually applied to a surface either as a point or covering some area. The phosphorescence is detected using either a point light detector, such as a photomultiplier tube (PMT), or an image detector, such as a CCD camera. By seeding phosphor particles in free flow it is also possible to perform temperature measurements in gaseous media.

In the present thesis, temperature measurements using laser-induced phosphorescence will be described and certain limitations of it will be addressed. Since the phosphor is applied to a surface as a very thin layer, the measurements performed are often considered non-intrusive. However, in situations in which the temperature changes very rapidly, such as in a combustion engine, and large temperature gradients are present for short periods of time, a relevant question to ask is whether the temperature of the phosphor agrees with the temperature it is intended to measure. One can also ask whether the phosphor layer acts as an insulator, making the measurements indeed intrusive. These are questions investigated in the thesis. At the same time, the technique is quite susceptible to small systematic errors if measurements of high precision and accuracy are to be performed. The technique also requires highly stable detectors in order for correct temperature values to be obtained. In the thesis, the characteristics of different detectors, both for point- and for 2D measurement, are investigated in terms of non-linear features and saturation effects.

Also the precision of the technique, and how this is related to the spatial resolution achieved, are investigated. In addition, the suitability of the technique for measurements in gaseous media is investigated in terms of the laser heating of the phosphor particles and the relaxation time required for thermal equilibrium to be achieved.

Populärvetenskaplig sammanfattning

80 % av den globala energi som används härrör från fossila bränslen. Ytterligare 10 % baseras på förbränning av någon form av förnyelsebart bränsle. Således är 90 % av vår energianvändning beroende av någon typ av förbränning, oavsett det rör sig om förbränning av olja, kol, gas eller biomassa. I en tid då priset på olja ständigt slår nya rekord, lagstiftningen kring miljöutsläpp blir alltmer strikt samtidigt som efterfrågan på energi bara växer, är det av största intresse att öka kunskapen om förbränning i alla dess former. Detta för att effektivisera och optimera de förbränningsprocesser som redan finns, men också för att hitta nya och bättre sätt att genomföra förbränning.

För att öka kunskaperna om förbränning behöver man mäta. Förbränningsprocesser är dock mycket komplicerade på så sätt att de involverar många olika kemiska ämnen och reaktionen. De är också vanligtvis mycket snabba, t.ex. sker det, i en vanlig bilmotorcylinder, 1000 explosionsliknande förbränningsprocesser per sekund, var och en inte längre än några millisekunder.

Med hjälp av laserbaserad förbränningsdiagnostik kan man mäta många olika parametrar under mycket korta tidsförlopp. De lasrar som används är pulsade, vilket innebär att de ungefär 10 gånger per sekund skjuter extremt korta laserpulser (omkring 10 nanosekunder, dvs. 10 miljarddels sekund). Under den korta tidsperioden kan en förbränningsprocess i princip betraktas som ”stillastående”. Laserljuset belyser de molekyler man vill studera, antingen format som en stråle eller som ett ark, och det ljuset som molekylen sprider detekteras med någon form av detektor. Med hjälp av specialbyggda motorer, delvis byggda av glas, är det möjlig att nå in med laserljuset och att detektera det ljus som sänds ut (s.k. optiskt access). På så sätt kan man mäta många olika parametrar så som temperatur, tryck, flödeshastigeter samt ämneskoncentrationer, i punkter eller tvådimensionella tvärsnitt av förbränningsrummet. De ämnen vars koncentration man kan mäta är bland annat bränsle, olika förbränningsradikaler och sot. Man kan även visualisera flamfronter och studera fenomen så som blandning och bränsleförångning.

En stor fördel med laserbaserade förbränningsdiagnostik är att man kan mäta i stort sett *beröringsfritt* (eng. non-intrusive); att molekyler belyses med laserljus påverkar inte kemin i förbränningsprocessen. På så vis kan man mäta realistiskt i annars besvärliga och svåråtkomliga miljöer som inuti motorer, gasturbiner och förbränningsugnar.

Naturligtvis finns det även nackdelar men tekniken. Den utrustning som används är vanligtvis relativt dyr och kräver ofta specialiserad personal och den

optiska accessen medför ofta att man inte kan köra motorn under realistiska förhållanden.

En av de viktigaste parametrarna att mäta i förbränningssammanhang är temperatur. En mer exakt kunskap om temperaturen är väsentlig för att förstå, förbättra och optimera flera förbränningsprocesser. Bl.a. är de största förlusterna i en bilmotor är de i form av värmeförluster till cylindervägar och avgaser, en gasturbins livslängd avgörs huvudsakligen av livslängden hos de komponenter som utsätts för högst temperatur, etc.

I denna avhandling beskrivs en metod som kallas för laserinducerad fosforescens (eng. Laser-Induced Phosphorescence, LIP) som används för att mäta temperatur, vanligtvis på ytor, antingen i en punkt eller över en del av ytan. Tekniken är på intet sätt ny, utan har varit ämne för utvecklig ungefär sedan 80-talet. Dock finns det utrymme för förbättringar. I avhandlingen redogörs för sådant som är viktigt att tänka på för att mätningar med hög precision och noggrannhet ska vara möjliga.

Temperaturmätning med hjälp av laserinducerad fosforescens går ut på att detektera det ljus som så kallade *fosforer* ger ifrån sig, efter att de har blivit belysta med en mycket kort och intensiv laserpuls. Detta ljus kallas för *fosforescens*. Denna fosforescens lyser under en mycket kort tid (bråkdelar av en sekund) efter det att den har blivit belyst med laser, och *hur* länge beror på hur varm den är. Genom att mäta hur snabbt fosforescensen avklingar kan man alltså mäta dess temperatur, på avstånd och extremt snabbt. Också fosforescensens *våglängd* (ljuset färg) beror på temperaturen. Genom att jämföra intensiteten olika våglängder emellan kan man också få reda på temperaturen.

Med hjälp av laserinducerad fosforescens kan man alltså mäta temperatur nästan helt beröringsfritt, och under extremt korta tidsperioder. Dessutom kan man mäta på avstånd (eng. remote), utan att fysiskt behöva placera en termometer där. Tekniken lämpar sig därför till att mäta i sammanhang där temperaturen ändras mycket snabbt och där det är svårt att komma åt med fysiska termometrar, som t.ex. i motorer, gasturbiner eller förbränningsugnar.

Arbetet som presenteras i avhandlingen redogör för precisionen av tekniken samt berör möjligheten att använda den för att mäta temperatur i friflöden, där fria fosforpartiklar följer med gasflöden. Begränsningar beträffande tjockleken på det fosforlager man applicerar på en yta undersöks. Även de vanligaste detektorerna för punkt- och avbildningsmätningar undersöks, med avseende på icke-linjäritet och mättnadseffekter.

List of papers

I. M.J. Prins, J. Lindén, Z.S. Li, R.J.M. Bastiaans, J.A. van Oijen, M. Aldén and L.P.H. de Goey, *Visualization of Biomass Pyrolysis and Temperature Imaging in a Heated-Grid Reactor* Energy & Fuels, **23**(2): p. 993-1006, 2009.

II. J. Lindén, N. Takada, B. Johansson, M. Richter and M. Aldén, *Investigation of potential laser-induced heating effects when using thermographic phosphors for gas-phase thermometry* Applied Physics B-Lasers and Optics, **96**(2-3): p. 237-240, 2009.

III. C. Knappe, P. Andersson, M. Algotsson, M. Richter, J. Lindén, M. Aldén, M. Tunér and B. Johansson, *Laser-Induced Phosphorescence and the Impact of Phosphor Coating Thickness on Crank-Angle Resolved Cylinder Wall Temperatures* SAE Technical Paper 2011-01-1292, 2011.

IV. B. Li, J. Lindén, Z.S. Li, A.A. Konnov, M. Aldén and L.P.H. de Goey, *Accurate measurements of laminar burning velocity using the Heat Flux method and thermographic phosphor technique* Proceedings of the Combustion Institute, **33**(1): p. 939-946, 2011.

V. C. Knappe, J. Lindén, F. Abou Nada, M. Richter and M. Aldén, *Investigation and compensation of the nonlinear response in photomultiplier tubes for quantitative single-shot measurements* Rev. Sci. Instrum., **83**(3): p. 034901, 2012.

VI. J. Lindén, C. Knappe, M. Richter and M. Aldén, *Limitations of ICCD detectors and optimized 2D phosphor thermometry* Meas. Sci. Technol., **23**: p. 035201, 2012.

VII. J. Lindén, C. Knappe, M. Richter and M. Aldén, *Precision in 2D temperature measurements using thermographic phosphor BAM* Meas. Sci. Technol., **23**: p. 085205, 2012.

VIII. C. Knappe, F. Abou Nada, J. Lindén, M. Richter and M. Aldén, *Response Regime Studies on Standard Detectors for Decay Time Determination in Phosphor Thermometry* proceeding to ITS9, Temperature: Its Measurement and Control in Science and Industry, vol. VIII, eds. C. Meyer et al., AIP, Melville NY, 2013.

Related papers

i. G. Särner, U. Göransson, J. Lindén, M. Richter and M. Aldén, *Using oxygen-quenched pressure-sensitive paint for oxygen concentration measurements in low-temperature combustion environments* Meas. Sci. Technol., **19**(8): p. 085307, 2008.

1 Introduction

"The most exciting phrase to hear in science,
the one that heralds new discoveries, is not
'Eureka!' but rather, 'hmm... that's funny...'"

- Isaac Asimov

From 1973 to 2010, global energy consumption doubled, from 70 000 to 140 000 TWh [1]. It is predicted that in 2030 it will be nearly 200 000 TWh [2]. Today, 80 % of this energy originates from fossil fuels, such as coal, oil and gas. Together with biofuels and waste, these energy resources constitute over 90 % of the global energy supply. All of these energy forms are transformed to useful work and to heat by combustion.

Despite the development of newer techniques, fossil fuels and combustion will remain essential for energy production in the foreseeable future. However, fossil fuel resources are limited and combustion of almost any kind is harmful to the environment. Studies of production in the giant oil fields shows that "peak oil", i.e. the point in time when the maximum rate of petroleum extraction has been reached, will occur sometime between 2008 and 2018 [3]. Combustion of fossil fuels has contributed to the increase of carbon dioxide (CO_2) in the earth's atmosphere from 280 ppm before the start of the industrial era to 379 ppm in 2005 [4]. CO_2 is one of the major contributors to the greenhouse effect, causing global warming and thus the rising of sea levels. In addition, combustion produces pollutants such as carbon monoxide (CO), sulphur oxides (SOx), nitrogen oxides (NOx) and particles, most of which are toxic to living organisms, pollutants that cause acidification, breakdown of the ozone layer, and production of smog, as well as contributing to the greenhouse effect. More strict legislation regarding emissions of these kinds has forced industries to strive for obtaining more clean and environmentally friendly forms of combustion.

As the demand for fossil fuels increases, concurrent with a diminishing supply and probably still more strict legislation, higher combustion efficiency in any context is of central interest. Although alternative technologies for heating, transportation and electricity production are being developed, it is of increasing importance that existing knowledge of combustion is improved in order to minimize pollution, climate change and economic costs.

Overall, a combustion process is usually very complex, and is in practice never quite complete. The study of combustion processes involves different disciplines, such as chemistry, physics, mathematics, mechanical engineering and computing. In order to develop higher fuel efficiency in combustion engines, such as in reciprocal engines or gas turbines, different kinds of diagnostic tools are needed. Measuring various properties of the combustion process, so as to gain a better understanding of them, can enable practical measures to be taken that can improve the efficiency of combustion processes generally.

Laser-based diagnostic techniques have proven to be a highly effective tool for studying combustion processes in both qualitative and quantitative terms. Laser-based diagnostics enable information regarding different essential properties of such processes to be obtained, such as those of pressure, temperature, flow velocity and various species concentrations [5]. They also make it possible to visualize and study in detail such phenomena as fuel vaporization and mixing preparation, which are directly related to pollutant formation and engine performance. Laser-based diagnostics can be performed non-intrusively, that is without disturbing the physical and chemical processes being studied. Thanks to the very short pulse length of pulsed lasers (typically around 10 ns) measurements of very high temporal resolution can be performed. It allows remote sensing, which is beneficial in hostile environments, and it is also able to provide results from 0D to 3D or even time-resolved 3D.

Of course there are some limitations. In order to use lasers in this context, optical access is needed, which may require special designs involving optical components. This may limit the conditions under which such processes can be studied, as higher loads cannot be tolerated due to the risk of the optics employed being damaged, or as particular fuels may be required in order to keep the optics free of soot. In addition, both lasers and the advanced detectors needed are often very expensive, and require high levels of skill to be operated. Nevertheless, laser diagnostics represents a highly important tool in combustion research.

Temperature is one of the most measured physical quantities and plays a significant role in many scientific and technical applications, and in a wide variety of disciplines, not the least in combustion sciences. A precise knowledge of the temperatures involved is essential for gaining an adequate understanding of many combustion processes and for improving and optimizing them. For example, NOx are formed in combustion processes at high temperatures. The greatest loss of energy in a combustion engine is that of heat to the walls of the combustion chamber and to the exhaust gases. The lifetime of a gas turbine is determined by the durability of those components that are exposed to extreme temperatures. In most combustion situations more accurate and precise knowledge of the temperatures involved would contribute to reducing emissions and increasing efficiency.

In the present thesis, temperature measurements performed using a laser-based technique termed laser-induced phosphorescence will be described and certain limitations of it will be addressed. The technique utilizes the afterglow that follows

the laser excitation of so-called *phosphors*. The work conducted within the framework of the thesis involves investigation of the precision of this technique, its suitability for measurements in gaseous media, and its limitations in terms of the intrusiveness of the thickness of the phosphor layer that needs to be applied to the surfaces to be measured. Limitations of the most common detectors for both point- and 2D measurements are investigated, regarding non-linear features and saturation effects. Following the text of the thesis itself, which ends with a summary and outlook section, the thesis ends with a brief summary of the published papers, and with the papers themselves.

2 Temperature Measurements

"A guy who uses one thermometer knows the temperature. A guy who uses two is not sure."

2.1 History

Thermometry, or the measuring of temperature, has a long history, and has been documented already in antiquity by the Greek Philo of Byzantium (3rd Century BC) [6]. The *Philo thermometer* consists of a hollow sphere from which a tube is connected and submerged in water. As the sphere was placed in the sun and the air inside expanded from the heat, Philo observed bubbles of air being released from the end of the tube. Inversely, when the sphere was put in the shade, water rose in the tube as the air contracted.

Many early scientists of the Renaissance, including Galileo Galilei, Ferdinando II de' Medici and Christiaan Huygens, constructed devices that remind one of thermometers. However, the thermometer itself was not a single invention. Rather, it was a development involving a large number of persons. Many attempts to define temperature quantitatively were made through history. In 1727 Daniel Gabriel Fahrenheit (1686-1736) defined the Fahrenheit scale, and in 1742 Anders Celsius (1701-1744) defined the Celsius scale. In 1848 William Thomson (Lord Kelvin) (1824-1907) realized the existence of an absolute zero temperature, and calculated this to be -273°C, which he defined as zero on his scale, the Kelvin scale. Today, Kelvin is the SI-unit for temperature and is defined in terms of the interval between the absolute zero and triple point of pure water, 273.16 K (0.01°C), 1 K being the fraction 1/273.16 of that temperature.

Today, temperature can be measured in a variety of different ways, including mechanically, electrically or radiatively. In 1821 Thomas Johann Seebeck (1770-1831) invented the thermocouple and in 1871 Sir William Siemens (1823-1883) described the resistance thermometer. Everyday simple thermometers are based on a liquid contained in glass, or of bimetals, that register the expansion of matter mechanically. Digital thermometers contain a resistance temperature detector (RTD) or a thermistor. The thermocouple is the electrical thermometer most widely used in industry, because of its wide range of temperature that can be measured, its low cost and its robustness. The mechanical and electrical thermometers have in common that

they need to be in thermal equilibrium with the surroundings in order to give a correct temperature value. Note that a thermometer does not measure any other temperature than its very own. This means that there is a delay in achieving a correct reading value if the temperature of the medium to be measured changes rapidly. Furthermore, because of the fact that the thermometer needs to be in equilibrium with the surroundings, meaning that the thermometer *affects* what is to be measured by changing its temperature, the readout values are always to some extent false and misleading. The temperature of the medium to be measured would thus have been slightly different, if it had not been for the thermometer. This is what is referred to as an *intrusive* measurement.

In contrast, by measuring temperature radiatively, it is measured *non-intrusively*. This is the advantage of for example IR thermometry, which measures the Planck radiation. By using lasers, the temperature can be measured in a number of ways, non-intrusively. Laser-induced phosphor thermometry is a radiative, virtually non-intrusive technique. It has several advantages compared to other techniques, the greatest being that it is fast and remote.

2.2 Thermocouples

A thermocouple consists basically of the junction of two dissimilar metal wires. Seebeck noted that a small difference in voltage appears when a wire is heated at one end, a phenomenon known as the thermoelectric effect or the *Seebeck effect*. By connecting two wires made of slightly different alloys, a net current will flow through the circuit when their junctions are maintained at different temperatures. Due to the predictable and repeatable relationship between temperature and voltage, measuring the voltage provides a correct measurement of temperature.

Thermocouples come in a variety of different types, depending on the metals and alloys used. Different types have different sensitivity and temperature ranges (up to 2300 °C). For example, the two wires of the type K thermocouple are made of chromel (90 % nickel and 10 % chromium) and alumel (95 % nickel and 5 % aluminum), respectively. Such a thermocouple has a temperature range of -40 to 1200 °C and a sensitivity of ±1.5 °C. The response time of a thermocouple depends both on its size and on the material of which it is made, and also on the circumstances under which it is being used (on solids, in fluids, turbulent fluids, etc.). Generally, thermocouples that are smaller have a shorter response time. A typical response time is one of around 0.1 seconds.

As already mentioned, thermocouples are widely used in industry, due to their robustness, low cost and ease of handling. However, they are intrusive and, because of the need of physical contact with the object being measured, they are difficult to install on moving parts, such as rotating turbine blades. Another drawback is the

response time, which limits the use of thermocouples under conditions in which there are rapid temperature changes. In addition, at high temperatures the radiation losses from a thermocouple become a significant source of error, one which needs to be corrected for. Also, the output signal is very weak, which can make thermocouples sensitive to electromagnetic interference from the surrounding environment.

2.3 Infrared thermometry

All matter at a temperature above absolute zero emits thermal radiation, or Planck radiation. When the temperature of an object reaches about 600 °C such radiation becomes visible to the human eye as a dark glow red in color. As the temperature increases the color gradually turns first yellow, then white and finally bluish white, of continuously increasing brightness. Emissions of this type, also referred to as black body radiation, are described by Planck's law

$$\mathrm{E} = \frac{2\pi c^2 h}{\lambda^5 \left(e^{\frac{hc}{\lambda k_B T}} - 1 \right)} \tag{2.1}$$

where c is the speed of light, h Planck's constant, λ the wavelength of the radiation, k_B Boltzmann's constant and T the temperature [7]. Figure 2.1 shows the spectral distribution of the Planck radiation at several different temperatures as emitted by a perfect black body, that is, by an ideal object that absorbs all the radiation incident on it and therefore also is a perfect emitter.

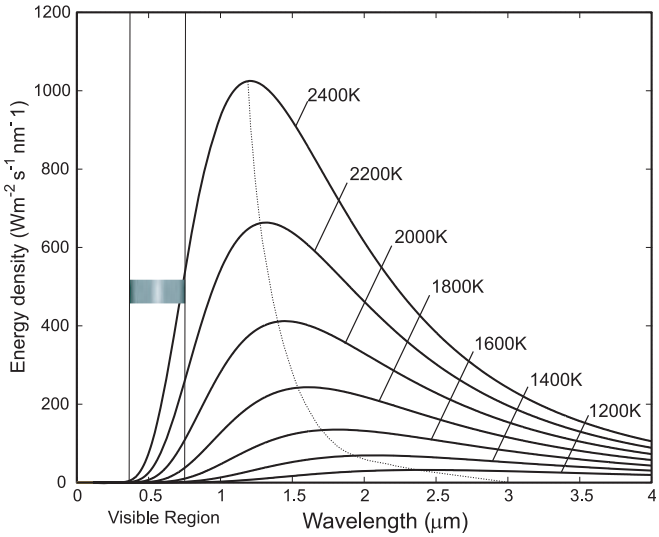

Figure 2.1 *Spectral radiation of a perfect black body*

By measuring the spectral distribution of the radiation of a hot object, one can determine its temperature unsing Planck's law. This is the principle of infrared thermometry, or IR thermometry.

Due to the temperature dependence of the spectral profile, the temperature can be measured by recording the thermal radiation spectrum, without interfering with the object. This is normally done by either detecting a continuous part of the spectrum, the intensity distribution of which is converted to temperature, or by detecting the intensity at two different parts of the spectrum and calculating the ratio of the two, which is then converted to temperature.

IR thermometry is a well-established and commercially available technique. The detector systems differ in complexity and are often very handy and practical to use. Under ideal conditions it is possible to obtain an accuracy of within a few degrees and a resolution of about 0.1 °C [7]. The advantages of IR thermometry include the following:

- no upper temperature limit since the radiation increases with temperature
- fast response; no thermal equilibrium needs to be established
- non-intrusive
- remote; no physical contact being needed
- insensitive to electromagnetic interference from the surroundings [8]

The greatest drawback of IR thermometry is that perfect black bodies do not exist, that is the emissivity, *e*, of a surface is never 100 %. It is varying and depends upon the nature of the surface, as well as wavelength and temperature. Even if the

emissivity of a surface is known, it is complicated to compensate for if it varies during a measurement. Also, IR thermometry is difficult to use in combustion applications, due to interference from luminous flames, reflected radiation, or absorption of the infrared radiation by molecules such as CO_2 and H_2O. The infrared emission may also be very weak, thus requiring a long exposure time, resulting in a low temporal resolution. Some thermometry systems also require liquid nitrogen cooling of the detector array.

2.4 Phosphor thermometry

Phosphor thermometry is based on the temperature-dependent properties of phosphors. A phosphor is a luminescent material, often a ceramic, that contains a small amount of rare earth elements. It is these rare earth elements, doped into the crystal structure of the ceramic, that are responsible for the luminescent properties of a phosphor. This luminescence is expressed as the emission of light after an excitation of some sort, such as UV or near UV light, tentatively from a laser. This emission of light, referred to as *phosphorescence* or *fluorescence*, can show a temperature dependence in a number of ways, which will be dealt with in section 3.3. Phosphors that exhibit these properties are referred to as *thermographic* phosphors. Utilizing these temperature-dependent properties makes it possible to measure temperatures very precisely and accurately, during a very short period of time in environments in which it would not be possible to measure using any other method.

Phosphors are produced in large amounts today. Physically, they are a white or slightly colored fine powder, typically having particle sizes of 1-10 μm. Their major applications are for use as wavelength converters in fluorescent lamps and LEDs, as light sources in CRT screens, X-ray screens and scintillators and as luminescent paint for various marking purposes. Their temperature dependence is thus not a property of primary interest. Nevertheless, phosphor thermometry is considered a well-established technique, subjected to an extensive development during the last decades. Today there are phosphors available for a wide range of temperatures, from cryogenic up to 1700 °C [9, 10], providing resolutions up to 0.1 °C and an accuracy of a few degrees.

3 Thermographic Phosphors

3.1 History and Terminology

The term phosphor has been used ever since the Middle Ages to refer to materials that glow in the dark after exposure to light. The word originates from the ancient Greek name for the planet Venus, Phosphorus, meaning light bearer [11]. In 1603, a cobbler and amateur alchemist, Vincenzo Cascariolo of Bologna, found a heavy crystalline glossy stone at the foot of a volcano [12]. Cascariolo found that, after he had fired the stone in an oven, it emitted a red light in the dark after exposure to sunlight. This stone was named the "Bolognian stone", and based on today's knowledge it appears to have been impure barite ($BaSO_4$). More stones of this sort were later found at various locations in Europe and were commonly termed phosphors. The light emitted from the stones was called phosphorescence, meaning the property of emitting light after excitation radiation ceased. However, the discovery of this phenomenon goes father back in time than the findings of the Bolognian stone. For example, in the 10th Century the Japanese prepared phosphorescent paint from seashells [13].

The word fluorescence, also referring to the emission of light from a substance after being exposed to radiation, referring originally to the light emitted by the mineral fluorite (CaF_2), was suggested by Sir George Gabriel Stokes in 1852 [14].

The difference between phosphorescence and fluorescence was actively discussed during the first half of the last decade, but the two words are still often used interchangeably, depending on context and tradition. The terms were long distinguished only by the duration of the emitted radiation: fluorescence being considered to be emission that disappears immediately when the excitation light ceases, whereas phosphorescence persists after the end of excitation, that is, an after-glow detectable by the human eye. This definition, however, is insufficient since long-lived fluorescence and short-lived phosphorescence are comparable, and also because the duration of the emissions may change with temperature. Hence, emissions considered at room temperature to be phosphorescence could at higher temperatures be considered to be fluorescence. The length of the emission to distinguish the two is not clearly defined: some saying the boundary should be at 10^{-3} s, others at 10^{-8}, 10^{-7} or even at 10^{-2} s. Nevertheless, such a way of defining the two terms is used by some people working in the field today.

One definition, used primarily for organic materials, is based on the quantum mechanical description of the transition: fluorescence originating from a singlet-to-singlet transition, phosphorescence originating instead from a triplet-to-singlet transition.

The term luminescence, which is a general term for light emitted by bodies excited by means other than heat, includes both fluorescence and phosphorescence. Some research groups prefer this term because of the ambiguity of the terms fluorescence and phosphorescence.

In the present work the term phosphorescence will henceforth denote the emission from phosphors, subsequent to excitation.

Today the term phosphor refers to a "solid luminescent material" or a "powder synthesized for purpose of practical application" [13]. They have a variety of applications, both within technology and in daily life: fluorescent lights, LEDs, CRT screens, plasma displays, exit and traffic signs, highlighter pens, outdoor worker jackets, stamps on bills, on credit cards and on driver's licenses, toys that glow in the dark, etc. All of these have in common that they emit light while, and for some time after, being exposed to UV, near UV-light or some other kinds of radiation.

3.2 Fundamentals of Phosphors

Phosphors are usually a fine, white or slightly colored, powder. They often consist of two components: a ceramic, inorganic microcrystalline host material and a dopant or activator from which the light is emitted. Examples of host material are yttrium aluminum garnet (YAG), yttrium oxides (e.g. Y_2O_3), oxysulfides (e.g. La_2O_2S), and aluminum oxide (Al_2O_3). The dopant is often a rare earth ion and the concentration is usually a few percent. Rare earth elements are a group of seventeen elements in the periodic table, including scandium, yttrium and the fifteen lanthanides. Especially the trivalent ions of the lanthanides, ranging from Ce^{3+} (atomic number 58) to Yb^{3+} (atomic number 70), possess luminescent properties in feasible wavelength regions and serve as dopants in most phosphors used for temperature applications. The electronic configuration of these ions is characterized by an incomplete 4f shell of electrons, shielded from the surrounding crystal lattice by the outer, less energetic 5s and 5p shells. Because of this, the 4f electronic energy levels are not affected much by the surrounding crystal field, so the ion can thus be considered as a free ion, giving it the phosphorescence property. However, it is interaction with the host material that enables the thermal response of the phosphorescence to occur [13, 15].

The luminescence process originates from electrons in the rare earth ion being excited to higher energy levels and subsequently returning to the ground state. The excitation may occur in several ways: exposure to electromagnetic radiation (UV, gamma or visible), particle beams (electrons, ions, neutrons), electric current or heat,

etc. Once excited to a higher energy level, the ion may return to the ground state either directly (by emitting a photon with a wavelength corresponding to the energy difference between the two states), or by any intermediate, non-radiative relaxation, such as vibrational relaxation, phonon (vibration quanta) exchange with the host lattice, or some other complex energy transfer mechanisms [7]. Usually the relaxation occurs through a combination of many different processes, both radiative and non-radiative. The radiation emitted is in that case of longer wavelength than that of the absorbed excitation radiation. This is referred to as Stokes shift, which occurs in most luminescent materials. The different de-excitation processes mentioned above are associated with different decay rates. Since transitions between 4f orbitals are spin-forbidden, the time scale of the process of de-excitation is rather large (10^{-3}-100 s), and therefore emissions will continue after excitation has ceased. This is the feature that enables the detectable after-glow, termed phosphorescence, to occur.

Due to the long-lived excitation states of the 4f orbitals, multiple excitation between the metastable electronic states is possible. This allows multiple absorption of one wavelength, with subsequent emission of a shorter wavelength, to take place. This is thus referred to as anti-Stokes shift. The process in question is referred to as upconversion and is a non-linear optical process that trivalent rare-earth doped phosphors also show. This mechanism also enables temperature measurements to be carried out [16, 17].

3.3 Temperature Properties

Due to the interaction between the rare earth ions and the host lattice, phosphors possess temperature sensitivity features. A condition for temperature dependence is described by the Boltzmann distribution of the ion populations at different energy levels. Figure 3.1 presents a simplified configurational coordinate diagram of the ground state and of an excited electronic state of a rare earth ion. The horizontal lines represent different vibrational energy levels in each of the electronic states. After excitation from the lowest vibrational level in the ground state to an upper vibrational level in the excited state, the ion relaxes to the ground vibrational level of the excited state by means of a non-radiative process such as phonon emission. Radiative transition to a higher vibrational level in the ground state may then occur, from which the lowest vibrational level is reached through further phonon emission. At temperatures above 0 K, ions are distributed over different vibrational levels within a particular electronic state, in accordance with the Boltzmann's factor:

$$n_2 = n_1 \, exp\left(-\frac{\Delta E}{k_B T}\right) \tag{3.1}$$

where n_2 and n_1 are the ion population of the upper and the lower vibrational level, respectively, ΔE the energy difference between the two levels, k_B Boltzmann's constant and T the temperature [18]. Thus, at sufficiently high temperatures, ions in the excited state can populate higher vibrational levels, from which they may transfer to the ground state through an intersection point of the two energy potentials, allowing non-radiative relaxation of the ion to occur. The intensity of the luminescence detected then decreases. This is referred to as thermal quenching of the emission, observed in certain phosphors. Another consequence of elevated temperatures is the broadening of some emission lines, since the population is spread over a number of vibrational levels.

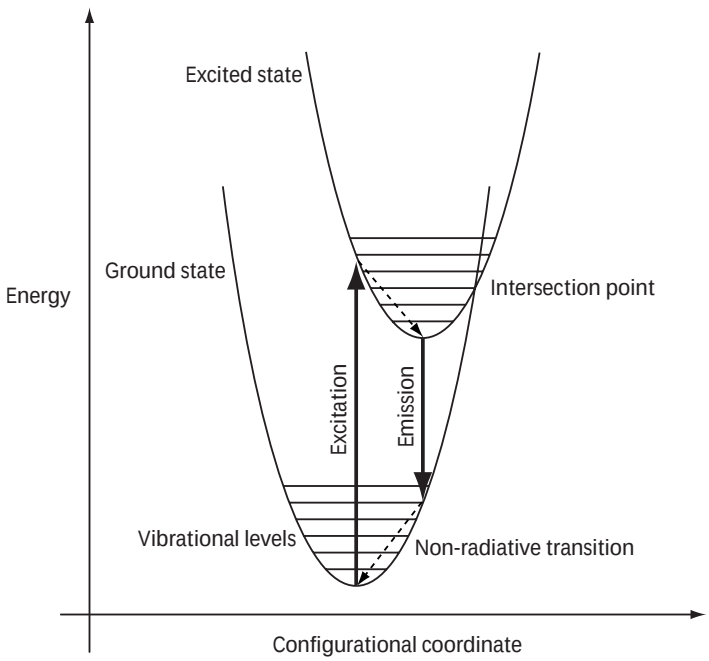

Figure 3.1 *A configuration coordinate diagram*

There is an additional quenching model for Eu^{3+} and Yb^{3+}, one proposed by Fonger and Struck [19] used to describe the thermal quenching of oxysulfides. Figure 3.2 presents a configuration coordinate diagram of the 4*f* levels of Eu^{3+} in a host material, La_2O_2S. The outer crystal field of the host gives rise to another energy potential termed a *charge transfer state* (CTS). The energy of this CTS is very much dependent upon the host material. For Eu^{3+} and Yb^{3+} it is low enough for the state to interact with the 4*f*-levels, as can be seen in the figure. At low temperatures the population of the ^5D_j states is too low for any interaction with the CTS to take place. At higher temperatures, however, electrons may reach the point of intersection between the ^5D_j states and the CTS, a transition then becoming likely. When this occurs, the energy

from the CTS is transferred non-radiatively to lower ^5D_j states, $^5D_0$ in particular, from which transitions to the ground state ^7F_j occur radiatively. Due to these different quenching processes, the decay rate κ increases, since

$$\kappa = A_{1,2} + W_{1,2} \tag{3.2}$$

where $A_{1,2}$ is a constant spontaneous radiative emission component and $W_{1,2}$ is a temperature dependent non-radiative component. Since the lifetime, τ, of the decay is the reciprocal of the decay rate, this results in a decrease in lifetime with an increase in temperature.

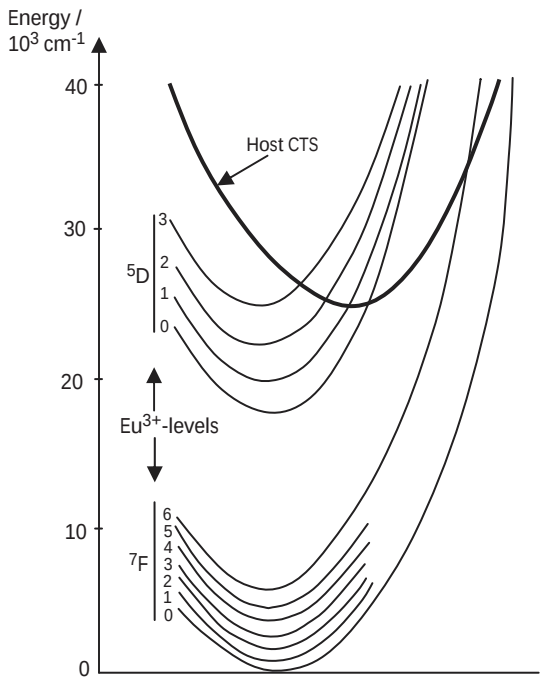

Figure 3.2 *Charge Transfer State [19]*

Many phosphors show this temperature dependence of the lifetime. After excitation ceases, the intensity of the phosphorescence decays exponentially, in the simplest case single exponentially in accordance with

$$I = I_0 e^{-\frac{t}{\tau}} \tag{3.3}$$

where I_0 is the initial emission intensity, t time and τ the lifetime constant of the phosphor. Thus, τ is the time required for the intensity of the phosphorescence to

decrease to $1/e$ of I_0. Whereas most phosphors have a phosphorescence lifetime τ of micro- or milliseconds, phosphor lifetimes both of picoseconds and of several hundred milliseconds do exist. Figure 3.3 presents an example of how the lifetime of the phosphorescence from cadmium tungstate ($CdWO_4$) decreases with an increase in temperature.

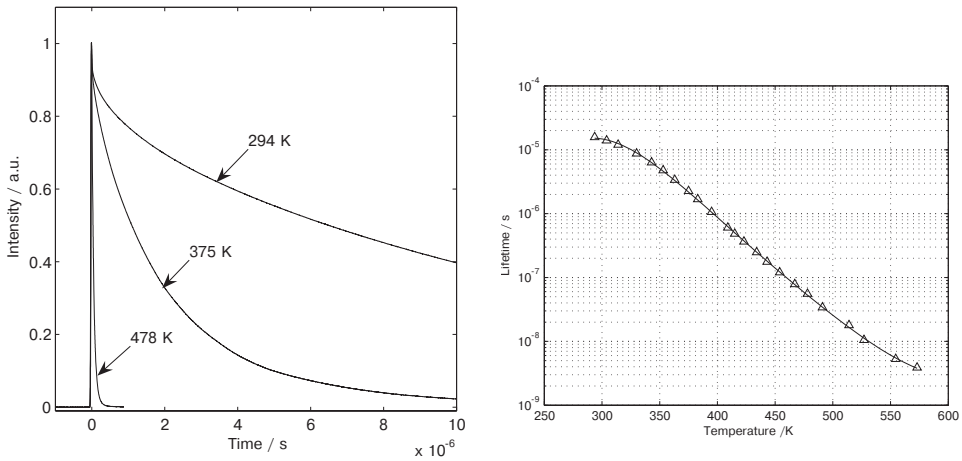

Figure 3.3 *Normalized phosphorescence intensity signals from $CdWO_4$ at three different temperatures (left) and a lifetime-to-temperature calibration chart (right) [20]*

So far, only one excited state has been considered. When two excited states are involved, an additional temperature effect becomes observable. Assuming the population of the states fulfills the Boltzmann law and that the intensity of the emissions is proportional to the population, the ratio of the intensities of the two spectral lines will be temperature dependent, in accordance with the expression

$$R(T) = \frac{I_E}{I_G} = exp\left(-\frac{\Delta E}{k_B T}\right) \tag{3.4}$$

where R is the ratio of the two emission intensities I_E and I_G associated with the respective emission lines, and ΔE the energy difference between the two excited states. Such is the case for dysprosium-activated ytterbium aluminum garnet, or YAG:Dy. Figure 3.4 shows how the relationship between the intensities of two spectral lines emitted from this phosphor changes with temperature.

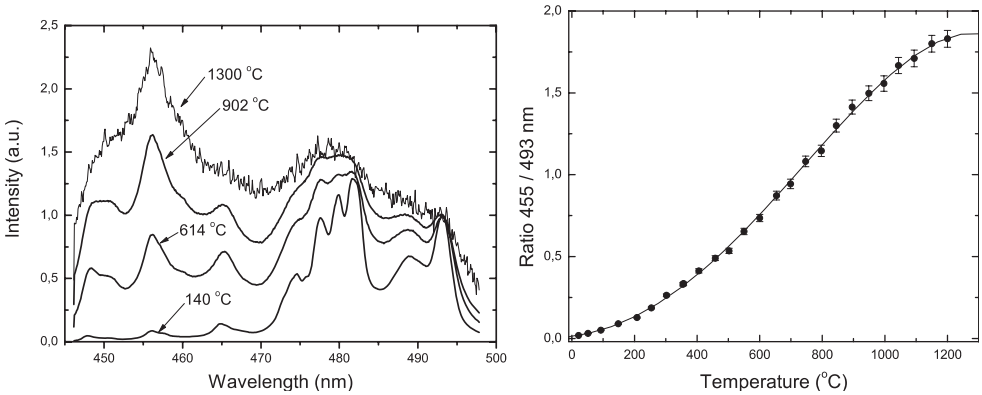

Figure 3.4 *YAG:Dy spectra at different temperatures (left) and the increase in ratio of 455 to 493 mn emission intensity with an increase in temperature (right) [21]*

In addition, the spectral profile of the phosphorescence may be either blue- or red-shifted with increasing temperature. Figure 3.5 shows blue-shift behavior in the emission from europium-activated barium magnesium aluminate ($BaMg_2Al_{16}O_{27}$:Eu), or BAM.

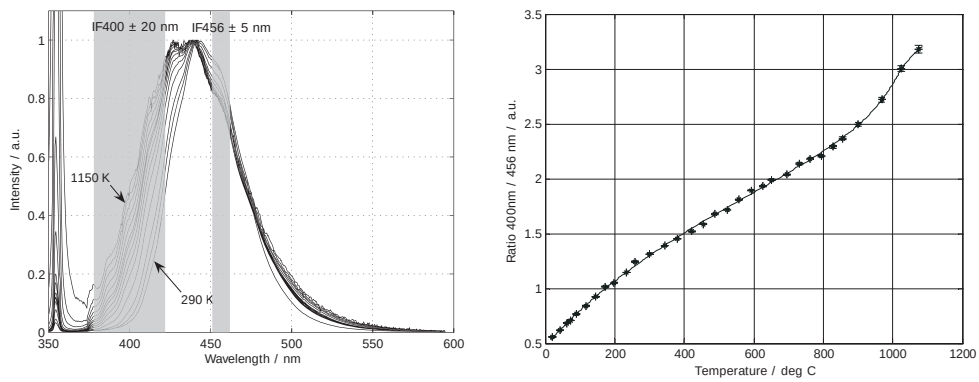

Figure 3.5 *BAM spectra at different temperatures (left) and at increasing ratios of 400 to 456 nm emission intensities with an increase in temperature (right) [20]*

The idea of making use of the temperature-dependent properties of thermographic phosphors was suggested by Neubert as early as 1937 [22]. The temperature dependence of the luminescence of phosphors became a subject of investigation with the introduction of the fluorescent lamp in 1938 [7], since degradation of the luminescence output with an increase in temperature could be a drawback in lamp applications. One of the first temperature measurement applications described

utilizing phosphors was the work of Bradley in 1952 [23]. Despite the early realization that phosphors could be used for thermometry, commercial phosphor thermometry products first became available around the 1980s [24, 25]. The invention of the laser in the 1960s accelerated developments in the area and significant advances in phosphor thermometry were made possible by the introduction of short-pulsed UV lasers in the 1980s. During the 1990s several applications to gas turbines were published [26-29], and thermographic phosphors were integrated in Thermal Barrier Coatings (TBC) to produce so-called smart TBCs, providing both thermal insulation and temperature instrumentation [30].

Thermographic phosphors offer both point measurements and 2D temperature mapping. There are many phosphors available for a wide range of temperatures, from cryogenic to over 1700 °C [9, 10]. Figure 3.6 presents an overview of several different phosphors and their spectral and temporal temperature sensitivity properties, as investigated by Gustaf Särner [20].

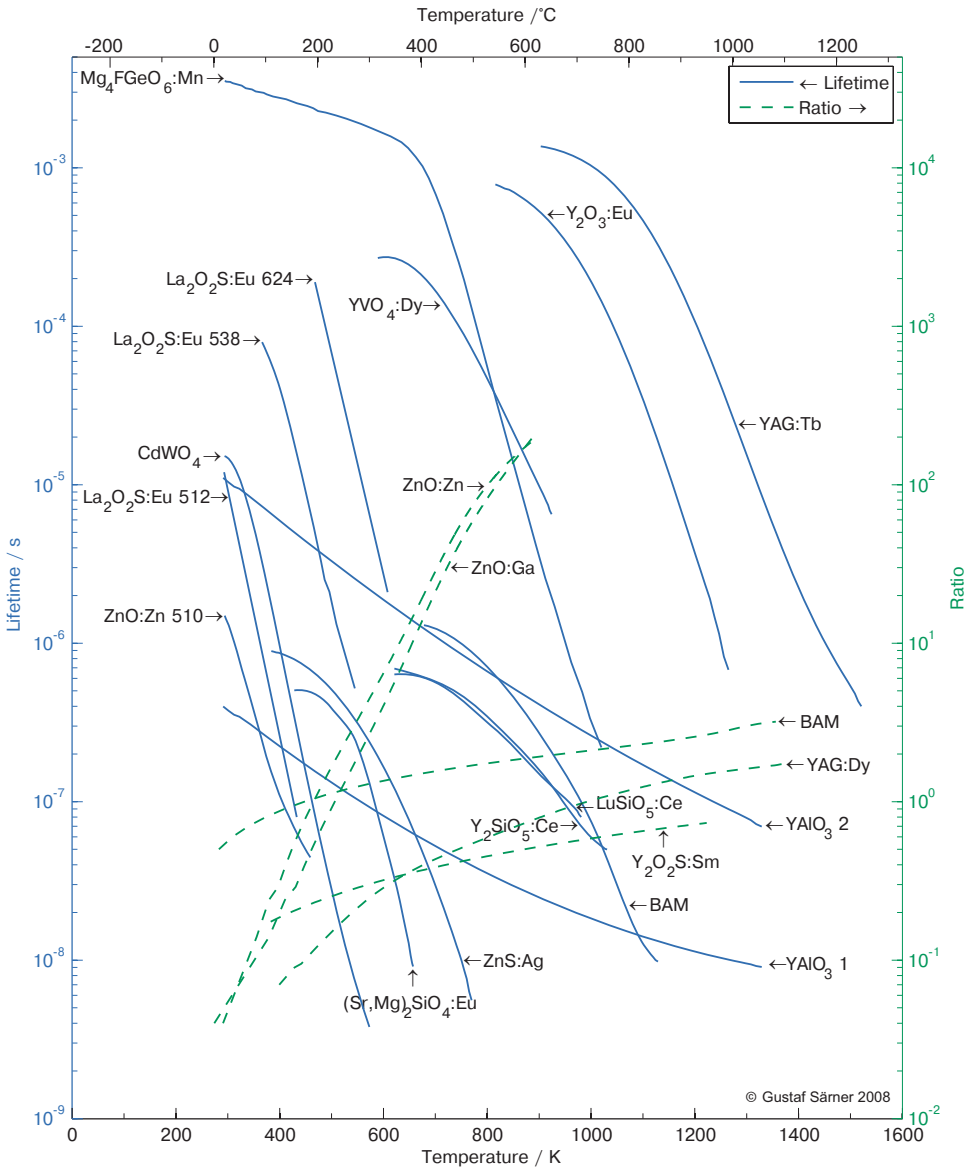

Figure 3.6 *Temperature sensitivities of different phosphors. Lifetime calibrations are shown by the solid lines and can be read on the y-axis to the left, whereas ratio calibrations are shown by the dashed lines and can be read on the y-axis at the right. Adopted from [20].*

4 Laser-Induced Phosphor Thermometry

4.1 Laser diagnostics

Ever since its invention in 1960, the laser has been used increasingly in applications in different areas, such as in medicine, chemistry and physics, for example. In combustion diagnostics the laser has become a standard tool for several areas of investigation, enabling non-intrusive measurements of a variety of different parameters to be carried out. Pulsed lasers, having pulses nanoseconds in length, allow measurements of high temporal resolution to be performed, which can provide detailed insight into complex and turbulent situations. Use of transparent parts in special engines (optical engines) also makes it possible to study many processes in a quasi-realistic environment. Both qualitative and quantitative measurements, for example, on flame propagation, unburnt fuel, soot or different radical species such as OH and CO are likewise possible. Such measurements can be 0D to 3D, and also in time-resolved 3D, using high-repetition-rate laser systems (>10 kHz) and high-speed cameras.

Temperature can be measured in various ways by use of laser-based tools, depending upon the conditions. Established Laser-Induced Fluorescence (LIF) techniques use toluene [31-33], acetone [34], NO [35, 36], OH [37, 38], Indium, Gallium and Thallium [39-41] as fluorescent tracers. These techniques generally provide temperature information in two dimensions, as a laser sheet is used to generate a cross section of the investigated media. Coherent anti-Stokes Raman Scattering (CARS) [42], Raman and Rayleigh spectroscopy [43, 44] are other well established laser-based techniques for temperature measurements. CARS provides very precise point measurements, since it is the volume of crossing laser beams that is being investigated. Raman is usually performed at a particular point or along a line. Rayleigh spectroscopy, just as LIF, is capable of performing 2D thermometry.

The technique of using thermographic phosphors is well established, both for point and for 2D measurements on surfaces. As mentioned in the previous chapter, phosphor thermometry has been performed on different components in gas turbines [26-29, 45, 46]. It has also been used in internal combustion engines [47-49], in hypersonic wind tunnels [50], on droplets and sprays [51, 52], and on burning materials [53]. Attempts have been made to perform measurements in gaseous media

by seeding phosphor particles into gaseous flow [54], and investigations concerning laser heating of seeded phosphor particles are presented in section 5.1 of the thesis. A feasibility study of phosphor particles seeded in a high-pressure combustion cell was also conducted recently by van Lipzig at Eindhoven University of Technology [55].

Thermometry using thermographic phosphors is usually performed in one of two ways. Either the spectral properties are used to provide information concerning the temperature distribution on a surface, or the temporal properties are used to measure the temperature of a very small area, or point, on a surface. The two approaches are described in the following sections. However, both the spectral and the temporal properties allow point or 2D measurements to be made. For example, surface-temperature measurements using temporal properties have been done by Omrane et al. using a framing camera [52, 53], and by Kissel et al. using a high-speed CMOS camera system [56]. In addition, paper IV describe point measurements performed utilizing the spectral properties of the thermographic phosphor ZnO:Zn.

4.2 Point measurements

In performing point temperature measurements, the lifetime temperature dependence of the phosphor is often made use of. A small area of phosphor is applied at some point on the surface to be investigated. The point is then illuminated by a laser of pertinent wavelength and the phosphorescence is recorded by a detector able to temporally resolve the signal, such as a Photomultiplier Tube (PMT), see figure 4.1. For further details on PMTs, see section 4.4.1.

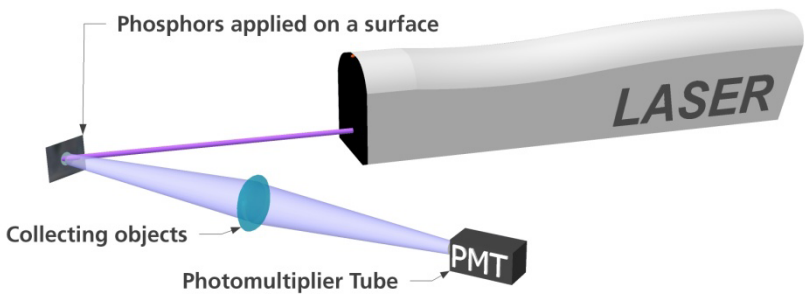

Figure 4.1 *The basic setup for a point temperature measurement using a PMT to measure the phosphorescence emission decay*

With the detector connected to an oscilloscope, the decay of the phosphorescence emission can be recorded. A fitting procedure is then used to determine the value of the lifetime decay constant τ. As mentioned above, the emission from most phosphors decays in a largely single-exponential manner. In cases in which the emission decay is multi-exponential, single-exponential equations can still be employed, since it is not the agreement of the recorded decay with the fitted decay curve that is essential, but rather the reproducibility of the fitting routine, meaning the same value of τ always being obtained from data recorded at the same temperature. However, the reproducibility in such cases is usually reduced, hence affecting the precision negatively.

There are different approaches to determining the lifetime decay constant τ from the data obtained in a point measurement. Figure 4.2 illustrates Ashworth's Rapid Lifetime Determination (RLD) method [57].

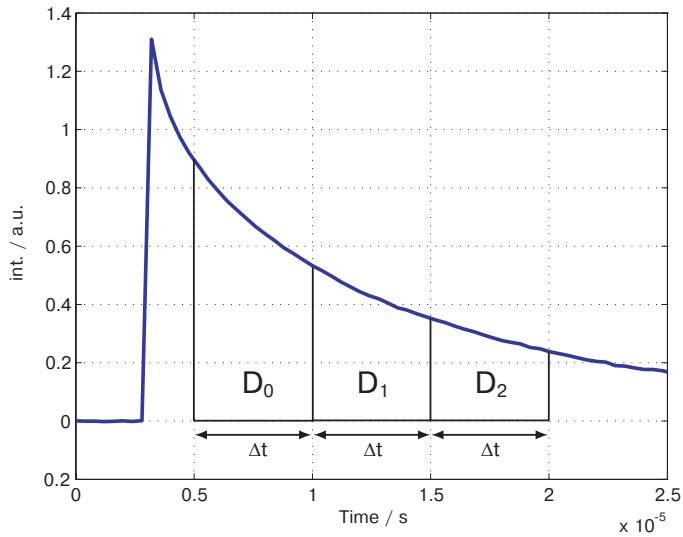

Figure 4.2 *Lifetime evaluation using Ashworth's Rapid Lifetime Determination (RLD) method*

The curve is divided into three parts of equal length, and the sum for each individual part, D_0, D_1 and D_2, is determined. The lifetime can then be approximated by use of the following equations:

$$Y = (D_2 - D_1)/(D_1 - D_0) \tag{4.1}$$

$$\tau = \frac{-\Delta t}{\ln Y} \tag{4.2}$$

Unfortunately, the evaluated lifetime as obtained by use of this method is not reproducible enough for the temperature measurements to be accurate and reliable. However, since the method is very simple and very fast, it is relatively easy to implement in modern oscilloscopes, enabling real-time lifetime evaluations to be made, which in many cases can be very convenient. A more accurate value for the lifetime can subsequently be obtained by use of more sophisticated and time consuming software routines such as that of least square fitting (Levenberg-Marquardt), in which the lifetime evaluated by use of the RLD method can serve as an initial estimation.

The evaluated lifetime depends very much on the size and position of the fitting range used on the recorded decay signal, especially if the decay is multi-exponential. In order to best achieve a non-ambiguous lifetime result, the starting and the end point of the fitting range needs to be defined by the lifetime τ itself. Thus, an iterative algorithm is preferable, one that determines t_1 and t_2 in such a manner that

$$t_1 = t_0 + c_1 \cdot \tau \tag{4.3}$$

becomes the starting point of the fitting range and

$$t_2 = t_0 + c_2 \cdot \tau \tag{4.4}$$

becomes the end point and where c_1 and c_2 are predefined constants. Further details on the iterative algorithm can be found in ref. [58].

The lifetime can also be evaluated by use of an amplitude-modulated light source using the so-called phase-shift method [18, 20, 59]. A laser diode fed by a modulated power supply can be used to excite the phosphor. The intensity of the phosphorescence is thus modulated as well, yet because of the delay in the excited state, a phase-shift between the exciting light and the phosphorescence is introduced. The lifetime can then be determined from the size of this phase-shift, assuming the period time of the modulation is comparable in relative size to the lifetime.

4.3 Two-dimensional surface measurements

In many situations it is desirable to obtain information concerning the temperature distribution over a surface in order to study gradients in more detail. In these cases, the spectral temperature-dependent properties of phosphors are often employed. Use of either two cameras, or of one camera equipped with an image-doubling device (a stereoscope), enables two different wavelengths of the phosphorescence to be detected through use of optical interference filters. Figure 4.3 illustrates a basic setup for

surface temperature measurements by the use of two ICCD cameras. For further details on ICCD cameras, see section 4.4.2.

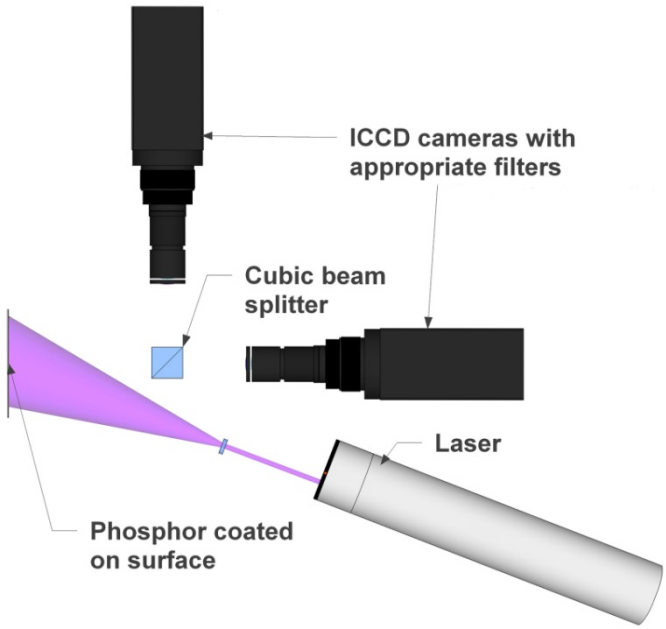

Figure 4.3 *A basic setup for surface measurements using two ICCD cameras and a cubic beam splitter*

As was noted in section 3.3, the spectral profile of the phosphorescence may change with the temperature in several ways. By the use of pertinent interference filters, the relative intensity of different parts of the spectra come to exhibit temperature dependence (see figures 3.4 and 3.5). The surface of interest is photographed through each of the two different filters. Dividing the two images by each other, pixel by pixel, allows a ratio map of the surface to be obtained. This ratio is then translated into temperature by use of a pre-defined ratio-temperature relationship, constructed from calibration measurements obtained under controlled temperature conditions.

The first to employ this intensity-ratio technique for temperature measurements were Goss et al. [60] in 1989, using YAG:Dy, resulting in uncertainties ranging from ±9 to ±50 K, or of about 3 %. However, the measurements were performed not in 2D, but in 1D. One of the first 2D temperature measurements making use of the intensity ratio technique was carried out by Bizzak et al. [61] in 1994, using europium-doped lanthanum oxysulfides ($La_2O_2S:Eu^{+3}$) on a surface area of 11 × 11 pixels or 1.6 mm^2.

Figure 4.3 shows a cubic beam splitter being used to separate the phosphorescence recorded by the two cameras. A cubic beam splitter is preferable to a semi-transparent mirror, due to the risk otherwise of artifacts caused by internal

reflections in the mirror substrate. If a stereoscope is employed, caution should be taken in order to avoid unwanted reflections caused by the internal optics and the interference filters. Figure 4.4 shows a schematic view of the stereoscope. One should be aware of the fact that the interference filters could distort the image, due to their internal design, causing changes both in the focus and in the position of the image on the camera chip. Since the magnitude of this effect differs from filter to filter, it may be impossible to achieve complete focus for both images simultaneously. This effect is usually very small, but if high spatial resolution is required and a stereoscope is the only alternative, the interference filters need to be of high quality.

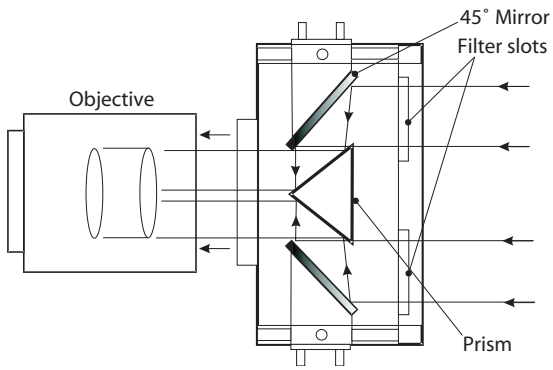

Figure 4.4 *A schematic view of a stereoscope that enables simultaneous imaging of two spectrally separated images of the same object to be obtained using a single camera*

Prior to division, the two images need to be corrected for background and for variations in pixel-to-pixel sensitivity. The background correction involves the recorded images being background subtracted by a background image recorded when the exciting laser is blocked or turned off. Unwanted signals caused by other illuminating sources are thereby eliminated and partly also dark current from the camera. The pixel-to-pixel variations are compensated for using a so-called flat field image. The flat field image consists ideally of a completely uniform surface light source, and is best achieved by using an integrating sphere, with its aperture placed in the image plane of the camera. By dividing the background-subtracted raw images by the flat field image, variations caused not only by pixel-to-pixel variations on the CCD-chip are compensated for, but also variations caused by any optical component of the system, such as camera lenses and various filters.

In order to superimpose the two images and generate an intensity ratio image, the images need to be warped and aligned to ensure that corresponding pixels on the two images represent the same point in the image plane. This is the image registration process, and is enabled by the recording of a reference grid image containing a reference pattern of points and symbols. This pattern is placed and recorded at the same position as the surface of interest. The grid image is then used to construct an

image transformation using software tools (MATLAB), applied later to the final measurement images in order to obtain a proper pixel by pixel overlap.

The resulting ratio image *R* can thus be described as

$$R = \frac{I_1 - BG_1}{FF_1} \Big/ \frac{I_2 - BG_2}{FF_2} \tag{4.5}$$

where *I* is the initial raw image, *BG* the background image and *FF* the flat field image. The subscript indicates which camera, i.e. which spectral part, the images represent. In equation (4.5) either the numerator with the subscript 1 or the denominator with the subscript 2 has been subjected to image transformation, in order to spatially fit the two images.

Both the flat field image and the reference grid image need to be recorded with the interference filters kept on the camera. The reasons for this are that the camera sensitivity shows wavelength dependence, and also, as mentioned above, that the interference filters may introduce image distortion.

Before the flat field image is employed, it is background corrected, and it can also be normalized by dividing it by its maximum value, using the formula

$$FF = \frac{FF_{raw} - BG_{raw}}{\mu} \tag{4.6}$$

where μ is the maximum value for FF_{raw} - BG_{raw}. Although normalization of the flat field image is not necessary, it keeps the resulting count values close to the original ones, which can be convenient. The resulting ratio image *R* is then translated into a temperature map, using a predefined relationship between the ratio and the temperature.

YAG:Dy (see p. 17) is one of the most commonly used thermographic phosphors for two-dimensional surface temperature measurements using the two-color ratio technique [26, 46, 60]. Also, manganese-activated magnesium fluorogermanate, Mg_4FGeO_4:Mn, has been used [51, 62]. Särner et al. have reported the potential of europium-activated barium magnesium aluminate ($BaMg_2Al_{16}O_{27}$:Eu), or BAM, and zinc oxide activated by zinc or gallium (ZnO:Zn or ZnO:Ga, respectively) for two-color phosphor thermometry on surfaces [63]. BAM is the phosphor used in the investigation presented in paper VII, in which the precision in temperature when performing two-color phosphor thermometry on surfaces is investigated.

4.4 Detectors

4.4.1 Point detectors

As mentioned in section 4.2, lifetime measurements require the use of detectors capable of resolving a signal temporally. The detector most commonly employed for lifetime-based phosphor thermometry is the Photomultiplier Tube (PMT). This is a highly sensitive detector used for detecting weak light and transforming it into electronic signals. The spectral sensitivity range extends from 200 to 900 nm, depending on the materials of which the photocathode is made. Two major types of PMTs are available on the market: the dynode chain PMT and the Microchannel Plate (MCP) PMT. Figure 4.5 presents a schematic view of the dynode chain PMT.

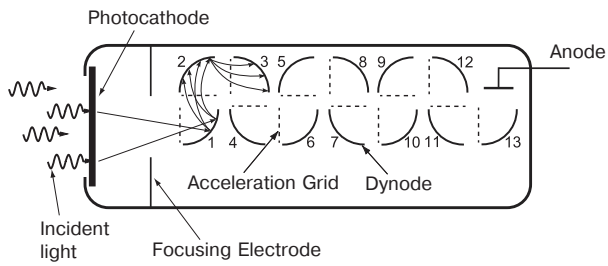

Figure 4.5 *A schematic view of a Photomultiplier Tube involving a chain of dynodes*

When incident photons hit the photocathode, photoelectrons are generated, these being accelerated and focused, by use of a focusing electrode, onto the first dynode, where they are multiplied by means of secondary electron emission. These electrons, in turn, are multiplied by a chain of dynodes, creating an exponential increase in the number of electrons, which are finally collected by the anode. The amplification of the signal is by a factor of 10^6 to 10^7. The dynode chain PMT is quite rapid, having a rise time of a few nanoseconds.

The MCP-PMT has a microchannel plate instead of a dynode chain. The MCP consists of a plate having a large number of parallel capillaries (channels). The inner wall of the channels generates secondary electrons when struck by the initial electrons from the photocathode, which are accelerated by an applied voltage across the both ends of the MCP. As in the dynode chain, the number of electrons increases exponentially before they reach the anode, and are read out as an electric current. MCP-PMTs have a much shorter response time than the dynode PMT, on the picosecond scale, but are also much more expensive.

The signal from a PMT is analog and is translated to digital data by most modern oscilloscopes. However, the current output from the PMT needs to be converted to a voltage before it is read out [64, 65]. This can be done, for example, by

an external signal processing circuit, such as a current-to-voltage amplifier (transimpedance amplifier), before it is fed into the oscilloscope. Caution should be taken if the PMT, when connected directly to the oscilloscope, is terminated by a 50 Ω resistance, since this risks saturating the PMT, leading to non-linear readouts. Alternatively, a higher termination resistance could be employed, although this has the drawback of loss in bandwidth, i.e. in temporal resolution.

In order to guarantee linearity, i.e. a linear response between incoming and output signals, any saturation should be avoided. Paper VIII presents a survey of different detectors for lifetime measurements and describes a procedure for determining the linear region for such a detector. The survey involves four different types of detectors, including two kinds of PMTs, and one MCP-PMT and one Avalanche Photodiode (APD). One of the PMTs can optionally be run in a time-gated mode, giving it the ability to quickly be turned on and off, enabling temporal filtering of unwanted light signals to be performed. In the investigation carried out, it was concluded that the outcome of evaluated exponential decay obtained is strongly biased by light intensity, electrical gain and detector type. This emphasizes the importance of the linearity of the detector employed, a matter taken up further in section 5.3.1.

4.4.2 2D detectors

In contrast to point detectors, which resolve the signal temporally, 2D detectors resolve the signal spatially, integrating the incoming signal over the time of exposure.

Several different detectors for imaging purposes are available today. Common to most of them is the charge-coupled device, or the CCD-chip, that represents the signal-registering circuit, or the sensor, of the detector. This consists of an array of semiconductors, typically some microns in size, that converts the incoming photons into electrons. During a given exposure time, these electrons are collected in each semiconductor. When the exposure ceases, the electrons are read out via shifting of the charges through the array to the analog-to-digital (A/D) converter, which counts the electrons and converts them into a digital signal. The signals from each individual semiconductor are then represented as picture elements, or pixels, to form a picture.

A CMOS (Complementary Metal-Oxide Semiconductor) is one version of the CCD. The basic principle involved is the same as for the CCD, but with the major difference that each and every one of the sensor elements in the array operates as an independent circuit, involving active buffering and amplification. This enables the CMOS to operate at a very high frame rate as compared with the CCD, a rate of up to hundreds of kHz, since it is not limited by a readout process via charge shifting. The major drawback, however, is that since every sensor element also consists of an A/D converter, this produces a significantly higher readout-noise level than would

occur otherwise. The CMOS also suffers from non-linear tendencies, which need to be compensated for in quantitative applications.

The CCD and the CMOS have replaced light-sensitive film in modern cameras. In scientific applications they are often complemented by use of an intensifying device, referred to as an image intensifier. In the CCD case, this is termed an ICCD. The basic principles applying to an image intensifier are shown in figure 4.6.

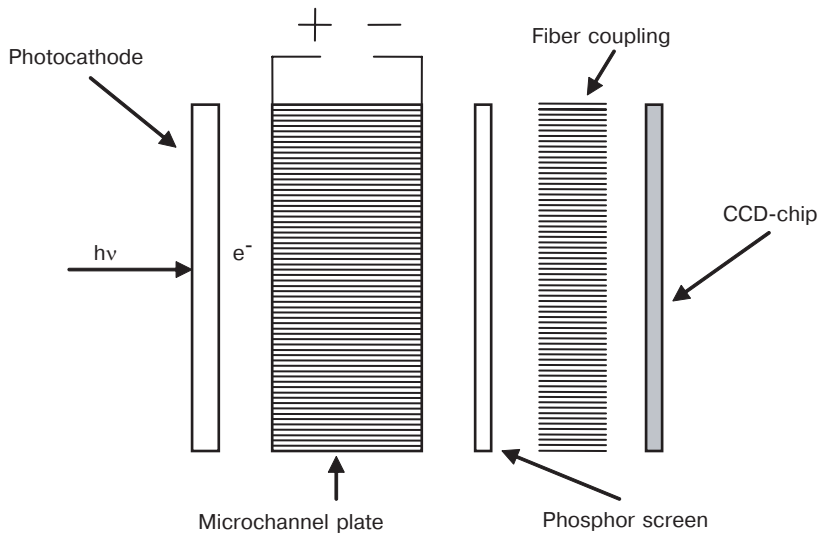

Figure 4.6 *Principles applying to an image intensified CCD (ICCD) camera having fiber coupling*

The functional steps carried out by the intensifier are as follows: The incoming photons are converted into photoelectrons by a photocathode, which are then accelerated by an electrical field toward a microchannel plate (MCP). This in turn multiplies the electrons, which are then converted back into photons by a phosphor screen. Finally, the resulting photons are directed at the CCD chip by either an optical fiber bundle or a lens system, and are read out as a digital image.

The addition of an image intensifier brings certain benefits. One of these is to increase the brightness of weak signals. However, in laser diagnostics applications, the primary benefit is that of time gating. By pulsing the control voltage to either the photocathode or the MCP, the image intensifier can serve as a very fast electronic shutter, making the time gating of short-lived signals possible, which otherwise would have been lost in interfering background such as Planck radiation and chemiluminescence. In addition, the photocathode can be made sensitive to UV radiation. The image intensifier can then frequency shift an incoming UV signal, to which the CCD itself is not sensitive, into the visible range, in which the CCD has a high degree of sensitivity. Together these features make ICCD cameras very useful for pulsed laser applications, where short laser pulses, in the order of 10 ns in duration,

are used for the visualization of various substances, by detecting either the scattered laser light itself or a signal emitted from the substance, induced by the laser light.

The CCD can also be complemented with an electron multiplier, making it into an EMCCD. In contrast to the ICCD, the EMCCD intensifies the signal after it leaves the CCD. When the electrons have been collected in the sensor array, they are read out via a readout register. Before reaching the A/D converter, they pass through a gain register, where the electrons are multiplied in accordance with a gain setting. As a consequence, the readout noise becomes more or less negligible. On the other hand, because of the lack of an electrical shutter mechanism such as that contained in the ICCD, the EMCCD is unsuitable in applications in which background signals need to be discriminated by use of fast time gating.

Back-illuminated CCDs are suitable, as the EMCCD is as well, for the detection of weak signals, since their quantum efficiency is substantially higher (~90 %) than that of traditional front-illuminated CCDs (~50 %).

A CCD sensor, when used alone, functions in a very linear way. When it is combined with use of an image intensifier, however, non-linearities may be introduced. These non-linear features may be very subtle, and would in most applications not be noticed. Nevertheless, due to the two-color ratio method being very susceptible to small deviations, very delicate non-linear features can result in significant readout errors when quantitative measurements are performed. This is caused mainly by the nature of the image intensifiers, a matter that will be addressed in section 5.3.2.

5 Results

This chapter summarizes the results obtained within the framework of the thesis. It is divided into four parts, each referring to some of the papers. The first part, which concerns Paper II, deals with the seeding of phosphor particles in gaseous flows, particular attention being directed at the heating of particles by laser radiation and the "stickiness" of such particles. The second part deals with an engine measurement in which the influence of the thickness of the applied phosphor coating on the temperature measurement results is investigated. This refers to the work reported in paper III. The third part considers matters connected with the non-linear features of detectors used in phosphor thermometry, specifically of PMTs and of ICCD cameras. This work is presented in two subparts, dealing with point detectors (papers V and VIII) and 2D detectors (paper VI), respectively. The fourth and last part, based on the work presented in paper VII, deals with the precision of 2D measurements conducted with use of the two-color technique, examining in part how it relates to spatial resolution.

5.1 Free-flow measurements

Various attempts to use thermographic phosphors for temperature measurements in gaseous flows and fluids have been reported in the literature. For instance, Omrane et al. have described simultaneous 2D gas temperature and flow velocity measurements performed using the thermographic phosphor manganese-activated magnesium fluorogermanate Mg_4FGeO_6:Mn [54]. The flow was determined there on the basis of Particle Image Velocimetry (PIV), using the phosphor particles as PIV-seeding. Omrane has also measured temperatures in free-falling and levitating droplets as well as in sprays [51, 52]. Also Brübach et al. measured temperature in sprays [66].

The following sections address various matters important to take account of in connection with temperature measurements based on use of thermographic phosphors in fluids.

5.1.1 Potential heating by laser

In fluid experiments, the exciting laser beam is preferably formed into a laser sheet in order to obtain spatial resolution in the depth dimension. When this is done, the laser fluence (laser energy per unit area [J/cm^2]) increases dramatically, compared with the fluence of a divergent laser beam often used when the phosphor is applied to a surface. Due to the relatively diluted particle flow present when phosphors are seeded in a fluid, compared with their being applied to a surface, it can be necessary to increase the fluence even more in order to obtain a sufficient phosphorescence signal. The fluence is in the end limited by the optical components involved in the experiment, which can be damaged by fluences of levels higher than 1-2 J/cm^2. When high laser fluence levels are reached, an obvious and still highly relevant question is whether the laser itself is heating the particles. For example, laser-induced incandescence (LII), a standard technique for soot diagnostics where soot particles are heated in order to measure the number density and the particle sizes of the soot, is based on the laser heating of particles. If such heating of the phosphor particles should likewise occur, this would make measurements in gaseous media virtually impossible.

Paper II reports on an investigation of the potential heating of phosphor particles when these are employed in gaseous flow measurements. An air flow at room temperature seeded with the thermographic phosphor BAM was illuminated by laser radiation, the phosphorescence signal being recorded by a spectrometer over a range of different laser fluences. Figure 5.1 shows the experimental setup.

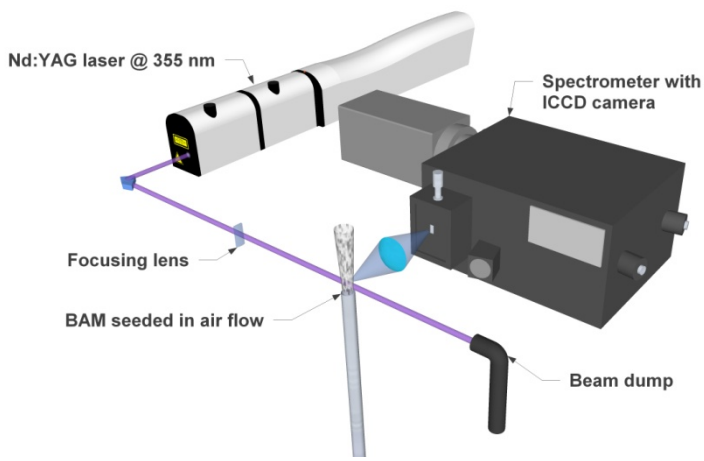

Figure 5.1 *The setup for the fluence dependence experiment*

A 10 Hz pulsed Nd:YAG laser operating at its third harmonic, producing 355 nm radiation, was used as excitation source. The beam was focused, and crossed the phosphor-seeded flow at the focal point. The subsequent phosphorescence emission was collected and dispersed by a spectrometer (Acton SpectraPro-150) and the spectrum was recorded by an ICCD camera (Princeton Instruments).

The fluence of the laser beam at the focal point was 1.5 J/cm^2 at the most. Figure 5.2 shows the phosphorescence emission spectra recorded at three different laser fluences. As can be seen, the spectra overlap completely, indicating that, despite the high laser power, heating effects do not occur, since heating of the particles would result in a blue-shift of the spectrum.

The reason for the phosphor particles not being heated by the laser radiation in this case, as compared with that of Laser Induced Incandescence (LII), probably lies in the differences in the absorption cross-sections of the different particles.

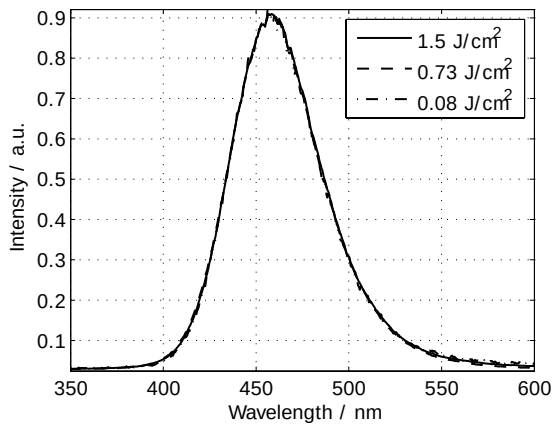

Figure 5.2 *Emission spectra from BAM at three different laser fluences*

In a practical measurement situation, it is seldom the spectrum that is recorded, as described above. Instead, the phosphorescence is photographed through two different adequate interference filters. The similarity of the three spectra shown in figure 5.2 would result, however, in temperature readings being virtually identical as well.

5.1.2 Obstructing optical access

A criterion for LIP temperature measurements, as for most laser based diagnostics techniques, is that of optical access. If the measurements are performed in enclosed spaces, such as in a combustion chamber of an internal combustion engine, optical components are necessary in order for the exciting laser radiation to enter, and for the phosphorescence signals to be collected. Such components are often made of quartz in

order to be transparent for exciting and detecting UV radiation. Using thermographic phosphors as a fine powder seeded into a gaseous flow, however, might hinder optical access through particles sticking to the glass window surfaces. One way to reduce this would be to use coated phosphor particles. Since one of the major applications of phosphors is their use as the luminescent material in fluorescent lamps, where a composition consisting of different phosphor powders is applied to the inside surface of the lamp glass tube, it is preferable for the particles to easily become stuck to the surface. However, the manufacturer (Phosphor Technology, UK) was able to provide two types of "anti-stick" coatings for BAM, namely SiO_2 and Al_2O_3. Such coatings are of nanometer-scale thickness and have only a negligible effect on the structure and size of the particles. Experiments were performed showing that these coatings had no effect on the spectral or temporal properties of the phosphorescence emission. From experience, BAM particles coated with SiO_2 seemed to stick the least. A plausible hypothesis regarding the reason for the decrease in "stickiness" occurring is that the coating changes the van der Waal-forces on the surface of the particles. It was checked whether the coating had any visual effect of the surface topology of the particles. No visual differences between the coated and the uncoated particles could be detected. Figure 5.3 shows examples of four SEM (Scanning Electron Microscope) images of phosphor particles, using a magnification of 10 000.

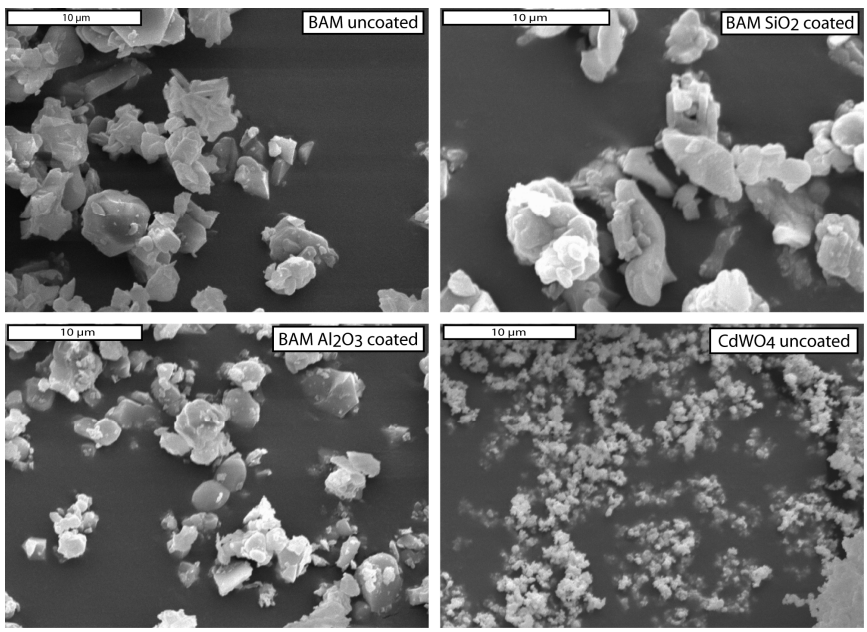

Figure 5.3 *SEM images of four different phosphor samples with magnification of 10 000*

In order to seed particles into gaseous flows a fluidized bed could be used. From the fluidized bed the seeded air is led through hoses or tubes to the area of investigation.

Note that a flow of air containing ceramic particles of micron size can create static electricity, in the case of certain hose materials. From experience, it appeared that use hoses made of polytetrafluoroethylene (Teflon) was not to be recommended. Not only does this tend to charge the hoses and the equipment connected to them, with the accompanying risk of discharges harmful to electrical equipment and also unpleasant for experimenters, but it can also cause additional obstruction of the optical access, since the particles stick to surfaces due to the presence of the electric charge.

5.1.3 Relaxation time for achieving local thermal equilibrium

Another criterion for using seeded particles in fluids to measure the temperature is that the particles establish local thermal equilibrium with the surrounding fluid. Especially in the case of measurements in gaseous flows is this of significant concern. The particles need to adapt to the temperature of the surrounding gas and to do so on a time scale comparable to the temporal variations in temperature. The length of this time scale can be calculated theoretically. Assuming the internal temperature distribution in the phosphor particle to be homogenous, this relaxation time can be estimated by solving the heat convection equation [67]

$$hA(T_\infty - T) = c_p \rho_p V \frac{dT}{dt} \tag{5.1}$$

where h is the convection heat transfer coefficient, A the surface area of the particle, T_∞ the gaseous temperature, T the particle temperature, c_p the specific heat of the particle material, ρ_p the density of the particle, and V the particle volume. For initial conditions such that T_0 is the initial particle temperature and that $t = 0$, the solution is that

$$\frac{(T-T_0)}{(T_\infty - T_0)} = 1 - e^{-\frac{t}{\tau}} \tag{5.2}$$

where τ is the time constant, described as

$$\tau = \frac{\rho_p c_p V}{hA}. \tag{5.3}$$

The time required for the phosphor particles to establish local thermal equilibrium in a gaseous flow of rapidly varying temperature depends very much on the current conditions, such as the difference between the particle temperature and that of the surrounding gas, the particle size, the particle substance, the turbulence, and in particular such air properties as those of density, heat capacity, viscosity, and thermal

conductivity, which are all temperature-dependent. The heat transfer coefficient h can be calculated using the following relationship [68]:

$$\mathrm{Nu} = \frac{hd}{k} = 2 + 0.6 \cdot \mathrm{Pr}^{1/3} \cdot \mathrm{Re}^{1/2} \tag{5.4}$$

where Nu is the Nusselt number, d the particle diameter, k the thermal conductivity of the gas, Pr the Prandtl number, and Re the Reynolds number. For a particle initially at room temperature, this would result in a relaxation time of 170 µs being needed for the particle to reach 90 % of a surrounding air temperature of 700 K. However, since this model is based on spherical particles, which have the smallest possible surface area to volume ratio, the relaxation time for real phosphor particles is thought to be shorter. Also, the assumption that the particles have an even internal temperature distribution is simplified. In practice, a significant part of the phosphorescence emission probably originates from the particle surface, where the temperature more closely corresponds to that of the surrounding gas temperature.

5.2 Thickness of coating

As was mentioned earlier, Laser-Induced Phosphorescence thermometry is considered to be a non-intrusive remote technique. However, whether this is the case depends on the conditions present. It is common practice, when the phosphor is applied to the surface of interest, to apply what is considered to be a "thin" layer. Ideally, the measured temperature reflects the temperature of the coated surface. This is true provided that thermal equilibrium has been established, which requires sufficient elapsed time. In most applications, this need not be regarded as an issue. However, if the temperature changes very rapidly, or if the temperature gradient from the surface to the surrounding gas is very strong, equilibrium may not have time to be established. Under such conditions, LIP thermometry should be regarded as "semi-intrusive". Note too that ceramics, which serves as the host material for most thermographic phosphors, is used for thermal barrier coatings (TBC) in gas turbines, for example [26, 69]. Although the TBC coatings are significantly thicker than those found in LIP thermometry, it is relevant to ask whether the thermal insulating properties of the ceramic host material affect the measured temperatures. In any case, it is preferable to use as thin a layer as possible, as long as it can provide sufficient phosphorescence.

Paper III presents a survey of the impact of the thickness of the phosphor coating on crank-angle-resolved temperature measurements conducted on a reciprocal engine cylinder wall. Figure 5.4 shows the setup used in the experiment.

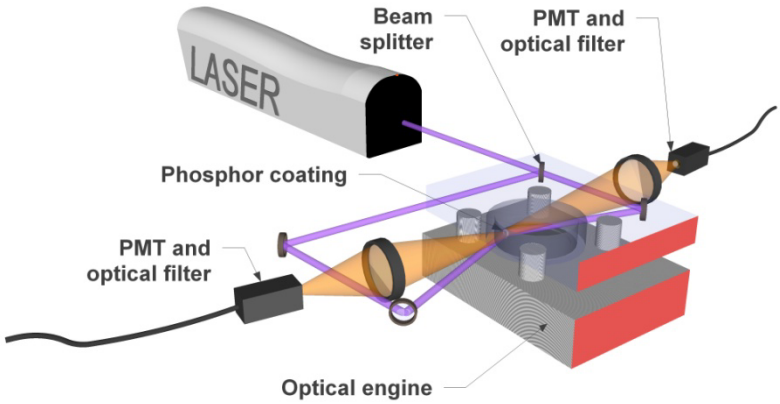

Figure 5.4 *The experimental setup used for two-face phosphor temperature determination in an optical engine*

The thermographic phosphor La_2O_2S:Eu was coated on the inside of the quartz liner extension of a Toyota engine. The phosphor was excited by laser radiation of 355 nm from two directions, from the bottom and from the top of the coating. Accordingly, the temperature could be measured simultaneously from the coating side facing the in-cylinder gas and the side facing the quartz liner. This revealed differences found to depend on the thickness of the phosphor coating. In the experiment, two coating thicknesses were compared: 32 and 59 µm. It was found that the temperature difference between the "gas-side" and the "wall-side" of the phosphor coating increased for thicker coatings and for higher temperature gradients over time. The measurements were conducted as the engine was operating in HCCI mode as well as when it was motored. During the HCCI operation the gradient over the 59 µm layer was 50 K at the most and for the 32 µm layer it was 25 K. During the motored case the gradient was 10 K and 5 K, respectively, for the two different layers.

In most applications, access to the phosphor is only possible from the gas-side, since the engine walls are usually non-transparent to laser radiation. Accordingly, as the results of paper III suggest, caution is called for in applying the technique to measurements in environments in which strong temperature gradients, both spatial and temporal, are present. In engine experiments conducted in similar temperature regimes, the phosphor coating should be kept as thin as possible and well below a thickness of 30 µm if it is important that systematic errors in the order of 30 K be avoided.

For thin phosphor coatings, temperature readings from the gas-side and the wall-side should converge. The layer cannot be made infinitely thin, however, since that would reduce the signal-to-noise ratio and also the durability of the coating. In the experiments reported on in paper III the coating was produced by an airbrush spray pen from which the phosphor was dispersed in a water-based binder (HPC

from ZYP Coatings, Inc.). Using methods other than those involving spraying, one can apply very thin phosphor coatings in the range of 0.1 to 0.5 μm, for example, using such methods as RF magnetron sputtering or Electrostatic Assisted Combustion Chemical Vapor Deposition (EACVD) [26, 70].

5.3 Non-linear features

Any quantitative measurement relies on there being a linear response between incoming and output signals in the detectors that are employed. For optical detectors, such as PMTs and CCD cameras, this corresponds to a linear relationship between the incoming photons and the output number of counts. The linearity is one of the major advantages of the CCD camera. However, equipped with an image intensifier non-linear features may be introduced, depending on usage. Since, as described in section 4.4, an image intensifier and a PMT are very similar in their manner of operation, a PMT can suffer from having non-linear features for the same reasons that an image intensifier can. This is of major importance in connection with temperature measurements involving use of thermographic phosphors, since the LIP thermometry technique is susceptible to the occurrence of small incorrect readouts when very high levels of precision and accuracy are called for.

Papers V and VIII describe investigations of different point detectors, such as PMTs, for the time-resolved measurement of light, and how a non-linear response there can be avoided or compensated for.

Paper VI reports on an investigation of the non-linear response of an ICCD camera, the negative impact that such response can have on the precision of thermometry carried out and how such effect can be avoided. As described in the papers, both for point and for image detectors, these non-linearity features can be associated with saturation effects.

5.3.1 Point detectors

In section 1.1.1 the PMT detector is described. Paper VIII presents an investigation of four different potential detectors for lifetime measurements, including two kinds of PMTs (one of which can be optionally run in a time-gated mode), as well as one MCP-PMT and one Avalanche Photodiode (APD). The linear response regimes of the detectors when used for phosphor thermometry were investigated. The phosphorescence decay from cadmium tungstate ($CdWO_4$) was recorded at fixed temperatures, the detector gain and the excitation laser intensity being varied. The phosphorescence decay time for cadmium tungstate extends from 10 μs at room temperature to less than 10 ns at 550 K. The conclusion of the survey was that the

outcome of the evaluated exponential decay obtained is strongly biased by light intensity, electrical gain and detector type.

Figure 5.5 (left) shows the non-linear response from the ungated PMT (Hamamatsu type H6780-04) when detecting the phosphorescence decay from $CdWO_4$ at a temperature of 373 K. The evaluated decay time is displayed in color as a function of gain and photon impingement. The PMT signal was recorded by a 350 MHz digital oscilloscope using a 50 Ω termination. As can be seen, this tends to result in false evaluation values for the recorded decays, caused by a saturation phenomenon in the PMT. For an ideal detector, all of the matrix elements in figure 5.5 (left) would show identical values. The systematic errors obtained involve false readouts of temperature, the errors being several tens of Kelvins in size.

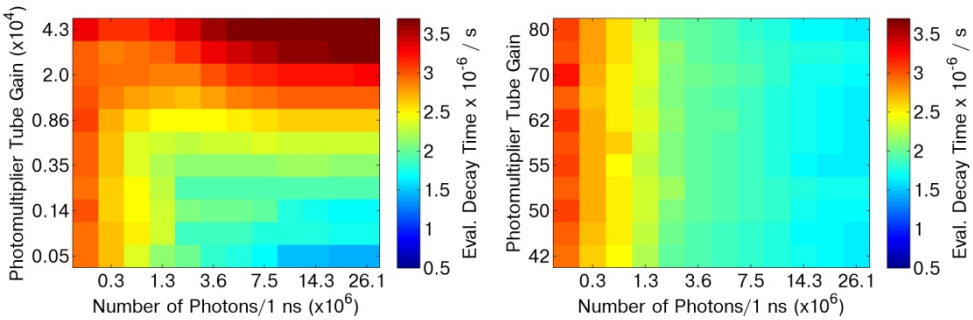

Figure 5.5 *The response surface of an ungated PMT, unamplified (left) and amplified (right) in measuring the phosphorescence decay time from $CdWO_4$ at 373 K*

The false readouts are caused by saturation in the dynode chain of the PMT. At high gain levels, a space charge builds up at the anode and the last few dynode stages. This space charge shields the approaching electrons electrically, driving the dynode chain into a region of saturation [71]. This results in a decay waveform somewhat truncated, which, when evaluated, results in a slightly longer lifetime, and thus appears as a lower temperature.

This gain dependence can be avoided by using an external current-to-voltage amplifier. This results in reasonable signal levels being found at much lower gain settings, but unfortunately also in a reduction in temporal resolution. The lesser gain bias leads to the detector being kept out of the region of saturation, as can be seen in figure 5.5 (right). However, the bandwidth limits the retrieval of shorter decays, i.e. the highest temperatures that $CdWO_4$ responds to.

The time-gated PMT (Hamamatsu type H11526-20-NF) has a significantly higher sensitivity around the emission wavelength of $CdWO_4$ (i.e. around 450 nm), a lesser gain range thus being required. At such a gain setting, saturation can be avoided, since the gain voltage remains below the critical level for the device. Figure 5.6 shows the response surface for the gateable PMT, indicating there to be no

saturation limit for the regions of high intensity, making it more adequate for phosphor thermometry than the ungateable PMT investigated.

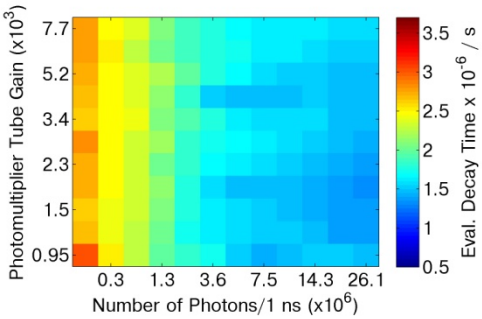

Figure 5.6 *The response surface of a gateable PMT in measuring the phosphorescence decay time from $CdWO_4$ at 373 K*

As can be seen in figure 5.6, however, the evaluated decay time appears to be dependent upon the intensity, indicating there to be a slight increase in the decay time as the number of photons decreases to below $4 \cdot 10^6$ photons/ns. The fact that this behavior can be observed for the ungateable PMT in figure 5.5 as well suggests the phosphor to be a possible cause of this. Similar finding have been reported by Brübach et al. [72], showing the phosphorescence decay time of another phosphor, Mg_4FGeO_6:Mn, to increase when the levels of laser excitation energy decreases.

The results displayed in figure 5.6 were obtained without the gate function of the PMT being employed. Since the saturation region was not reached during the experiments, the time-gate results show very little variation as compared with the ungated ones. Nevertheless, the ability to cut off strong peaks of fluorescence or scattered laser light under some circumstances would increase the signal-to-noise ratio without the detector becoming saturated.

Figure 5.7 (left) illustrates the response of the MCP-PMT detector when detecting the phosphorescence decay from $CdWO_4$ at a temperature of 373 K. As can be seen, the MCP-PMT appears to have a fairly linear response in the upper right corner of the response surface, where the levels of intensity and gain are high.

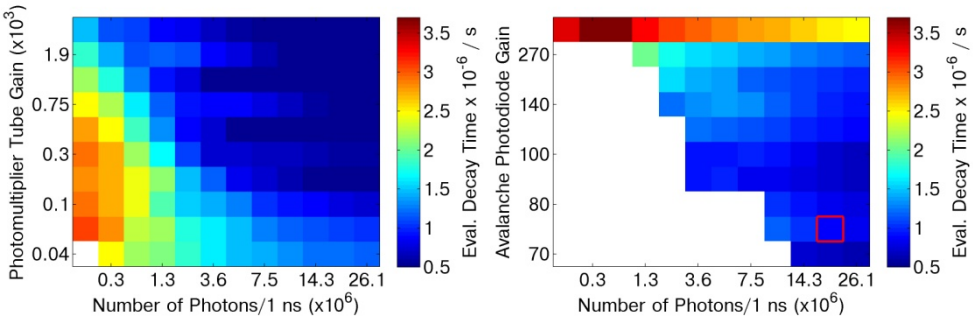

Figure 5.7 *The response surface of MCP-PMT (left) and of APD (right) in measuring the phosphorescence decay time from $CdWO_4$ at 373 K*

Figure 5.7 (right) shows the response surface of the APD (Hamamatsu Si-SPD S5343). As can be seen, a significant amount of data for the low light intensities has been rejected by the S/N-criteria during evaluation. The weak signal appears to be mainly due to losses in the optical fiber coupling of the APD. Also, the gain range for the APD is more moderate than that of the other detectors. Apart from that, the evaluated decay time appears to be stable for a major part of the workspace displayed, except for the row involving the highest gain. This feature appears to be consistent for all measurements using the APD, indicating the global gain limit of the APD.

Figure 5.8 shows the calibration points for each of the four detectors, regarding the five temperatures that were investigated. The value for the decay time selected was that for the element having the second lowest gain and the second strongest light exposure (indicated by the red square in figure 5.7 (right)), since this represents a fairly linear part of the working space for each of the detectors.

The loss in bandwidth for the amplified PMT, and thus the inability of measuring short decay times, results in a reduction in temperature sensitivity. This explains the longer decay times obtained at higher temperatures.

For the MCP-PMT, the point for the lowest temperature is missing. This is due to the limited maximum gate length of 10 µs for the MCP-PMT. Thus, for the MCP-PMT, the decay time at room temperature was too long for a reliable value to be obtained.

The APD was found to exhibit the maximum range of decay time sensitivities of the detectors investigated. The point for the case of the highest temperature is missing, however, due to the low signal output.

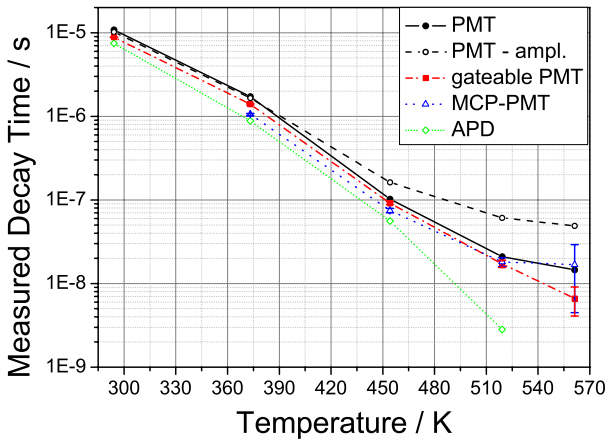

Figure 5.8 *The temperature calibration points for each of the detectors from a fixed response-matrix element. The error bars indicates one standard deviation from the mean value.*

The gateable PMT showed the best performance of all the detectors that were investigated, providing a large linear workspace combined with a broad range of decay time sensitivities. Although time gating was not used in the investigation described above, that function is believed to improve linearity and S/N-ratio for phosphors that exhibit strong fluorescence peaks together with the phosphorescence decay.

5.3.2 2D detectors

As already mentioned, the non-linear features of the ICCD camera are due mainly to the image intensifier. It has been shown that ICCDs suffer from spatially non-uniform image gain factors and non-linear response functions [73, 74]. The non-linearity is due mainly to the onset of saturation within the MCP when the camera is being subjected to high light intensities in combination with gain settings that are too high. This falloff in response, or gain saturation, has to do with the recovery process of the MCP. It is caused by the inability of the MCP to produce a sufficient number of secondary electrons from the original photoelectron [75, 76].

In addition, bleaching of the photocathode, especially when intense long-lived radiation is being collected, can contribute to saturation. The phosphor screen can also be subject to saturation, resulting in a non-linear output, due to a falloff response at higher intensities. Other saturations can occur following the intensifying process, i.e. in the CCD-chip (filled-up charge wells causing blooming) and in the A/D converter. Saturations of such types are usually easy to avoid, however, since it is rather obvious when they occur. In contrast, in most practical situations it is usually

far from obvious when gain saturation in the MCP occurs. Although saturation effects within the intensifier are usually not a major issue when qualitative measurements are carried out, quantitative measurements, in particular with use of the two-color ratio technique, are very easily affected by small non-linear effects.

Paper VI reports on an investigation of non-linearity due to saturation of the MCP and how systematic errors caused by it can be avoided. In the work presented in the paper, the phosphorescence of BAM was detected at room temperature, at different intensifier gains and at different levels of excitation-laser illumination, this creating a response surface for demonstrating the useful workspace that the combination of irradiance and camera gain provides. The detector employed was a Princeton Instruments PI-MAX2 ICCD camera. There was shown to be a possibility of saturating the camera, and in so doing introducing nonlinearity, even though other components of the camera were not saturated. Thus, in performing quantitative measurements here, there was an upper limit of counts that should not be exceeded. The investigation was carried out for a particular setup, a specific camera and a particular phosphor, and should be repeated for other constellations of these three elements in order to confirm that a given experiment generates reliable results.

Figure 5.9 shows the setup for the experiment where the response surface and the characteristics of the ICCD camera are specified. The laser employed was a 10 Hz pulsed Nd:YAG operating at its third harmonic, producing a wavelength of 355 nm with an energy of ~0.5 mJ/pulse. The laser beam was directed and expanded so as to illuminate a glass plate surface coated with BAM. A filter wheel provided with appropriate filters was placed on the camera side of the plate.

As can be seen, only one camera was used here. If one assumes stability over time, it follows that if the filters in front of the camera are switched, the two images obtained, recorded through the two separate filters, would be identical, with the exception of the wavelength detected. Thus, the pixel-to-pixel variations on the CCD chip would cancel out through division of the two images by each other. Accordingly, with use of this single-camera setup, there is no need for any image registration and transformation.

As was mentioned in section 4.3, some interference filters, because of their internal design, may introduce distortion effects that result in displacement of the focal plane and translation of the image. Since the two filters differed in this respect, an effect of this sort would prevent a straightforward superposition of the two images in the experiment carried out. However, the filters being located close to the coated surface resulted in these effects being kept to a minimum. The position of the filter wheel is thus the reason for the phosphor being illuminated from the back.

In order to investigate the linearity of the camera, different areas of the BAM-coated surface were illuminated by different laser fluences. This was achieved by using a filter stack, consisting of five identical neutral-density filters, successively overlapping each other partwise. This approach allowed six different areas of the BAM-coated surface to be illuminated, each with a different laser fluence: one

without any laser attenuation, and five with gradually increasing optical densities. The transmission of the five gradually increasing optical densities was measured as being 9 %, 14 %, 22 %, 39 % and 67 %, respectively.

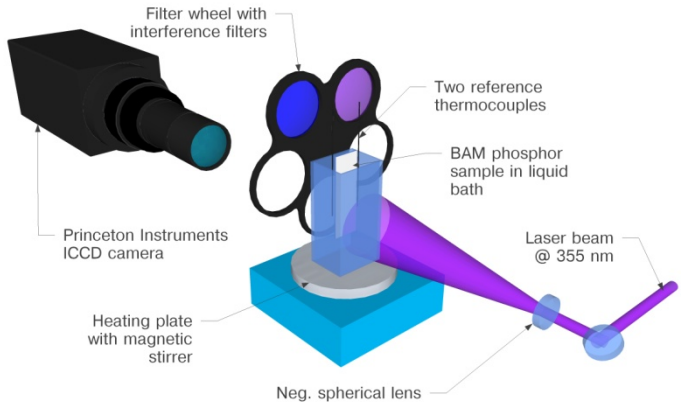

Figure 5.9 *The experimental setup for creating the response surface for the ICCD camera employed*

Figure 5.10 provides an example of two phosphorescence images (a and b) and the resulting ratio image (c) for a particular gain setting of the image intensifier (150 of 255). At this gain setting, the different areas, despite their being illuminated by different laser fluences, give the same ratio in each case, as can be seen in (c), and would thus provide the same temperature, as would be expected. Also, it can be seen that within a single area of a specific laser fluence the evaluated ratio becomes homogeneous, despite the inhomogeneity of the laser profile in the two original phosphorescence images.

For each area, the mean value and the standard deviation of the ratio was determined. This was done for 26 different gain settings, spanning the range of 0-250 in increments of 10. With there being six different areas of differing illumination intensity, this results in 156 different gain and laser fluence combinations that were investigated. Prior to the experiment, the laser energy was adjusted so that, in the measurement involving a gain of 250, the maximum number of counts in the area having the highest intensity was just below the saturation level of the 16 bit A/D converter, i.e. 65 535 counts.

Figure 5.11 displays the mean values obtained, in counts, for all of the 156 different gain and fluence combinations for the two filters employed (left: the 456 nm interference filter, henceforth referred to as IF456, and right: the 400 nm interference filter, henceforth referred to as IF400). Note that the count intensity scale is logarithmic. The maximum mean value for the area illuminated by the highest level of laser fluence and amplified by the highest gain, shown in the upper-right corner in the IF456 chart, is 45 000 counts, or ~$10^{4.6}$.

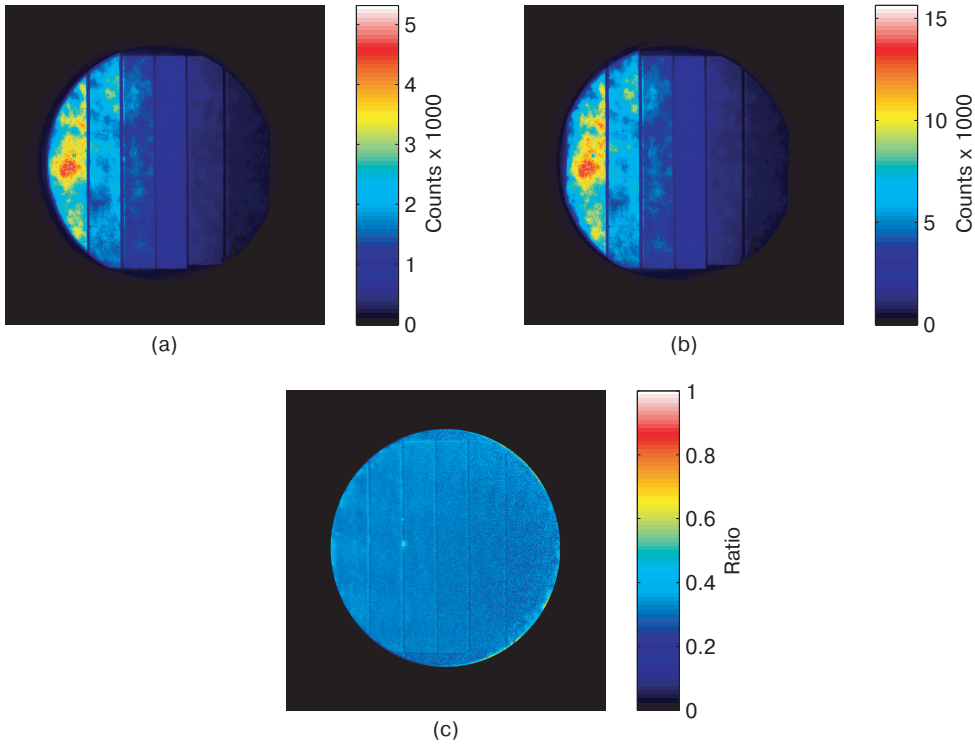

Figure 5.10 *Examples of two phosphorescence images obtained through two different interference filters ((a) 400 ± 20 nm, (b) 456 ± 5 nm) which when divided generate a ratio image (c).*

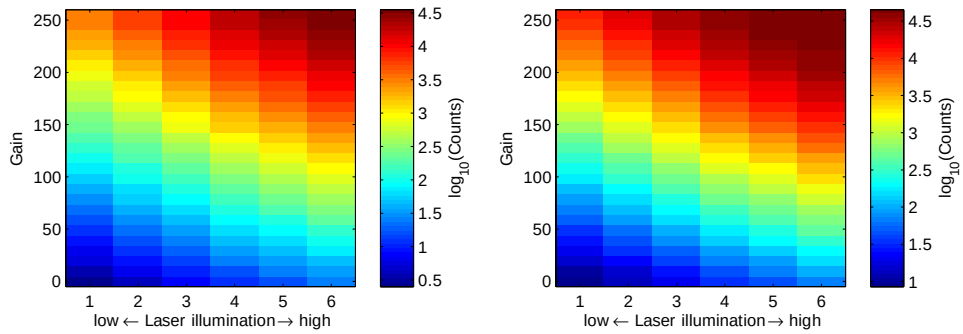

Figure 5.11 *The mean signals in counts for the signals obtained through the IF456 filter (left) and the IF400 filter (right). Note that the count intensity scale is logarithmic.*

Each of the 156 count values for the IF400 image set is divided by the value of the corresponding gain and laser illumination from the IF456 image set. This results in a ratio chart containing 156 ratio values. Figure 5.12 displays these ratio values,

although they are translated into temperature here, using a ratio-to-temperature relationship based on reference measurements obtained at temperatures ranging from room temperature to 500 K.

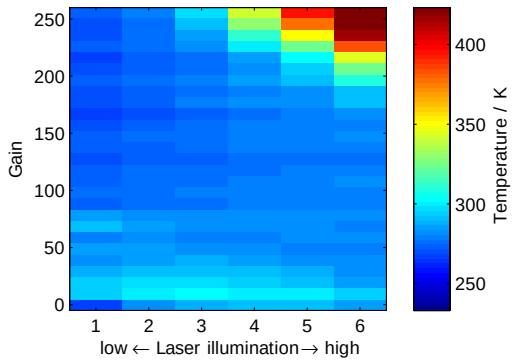

Figure 5.12 *Evaluated temperature values for each of the different gains and laser illuminations*

As can be seen in figure 5.12, the evaluated temperature values are rather constant within the major part of the chart, with the exception of the upper-right corner. Despite the measurements being carried out at constant room temperature, it can be clearly seen that the evaluated temperatures provide misleading results, as the values obtained are too high for the higher levels of laser illumination and intensifier gain. As can be seen in the figure, this results in a false readout of the absolute temperature, there being a deviation of almost 200 K from the true value.

In terms of precision, highly interesting results are shown in figure 5.13. It presents the spatial standard deviation, i.e. the pixel-to-pixel standard deviation, within each combined gain and laser illumination area, translated into corresponding standard deviation in temperature. For BAM, the relationship between the temperature and the ratio is nearly linear within the temperature range considered, with a dT/dR relation being equal to 0.0026 K^{-1}, where T is the temperature and R the ratio. To illustrate this, a standard deviation of 0.009 in ratio corresponds to a standard deviation of the temperature of $0.009/0.0026\ K^{-1} = 3.5$ K.

The diagonally shaped area in figure 5.13, marked off by the two dashed lines, could be identified as a proper working space for high-precision measurements. Within this area, the camera exhibits a linear response, independent of MCP gain and laser illumination. Below the lower of the two dashed lines, the standard deviation is high because of the S/N level being too low there. The signal is still strong enough to provide reasonable values for the absolute temperature, however, as can be seen in figure 5.12, but the noise contribution is too high for the pixel-to-pixel precision to be sufficiently high.

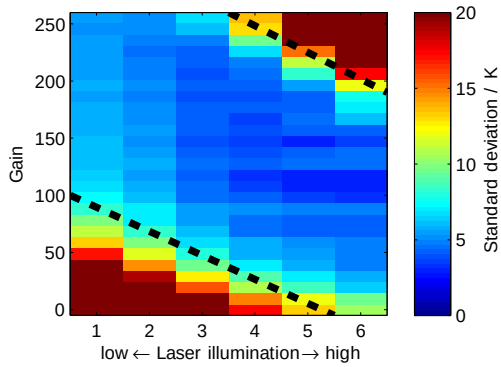

Figure 5.13 *Spatial standard deviations as evaluated for selected areas differing in gain and in laser illumination, translated into standard deviations in temperature*

The increase in standard deviation above the upper dashed line indicates a more critical limitation of the camera. The number of counts at which this limit is reached can be determined through considering figure 5.14, which shows the spatial standard deviation of the count values in each area for each gain and laser illumination combination through the IF456 and IF400, respectively. On the basis of the chart at the left in figure 5.11 then, showing the mean signal in counts obtained through the IF456 filter, it can be determined that this limit corresponds to a count value of 26 000 ($10^{4.42}$). It can be clearly seen in figure 5.14 (left) that signal suppression occurs under these conditions, i.e. that the nonlinear regime has been entered. The standard deviation reaches a maximum value at a gain of 190 and then decreases when the gain becomes higher, indicating that an upper limit of the count values has been reached and that gain saturation occurs for gains and illuminations higher than this.

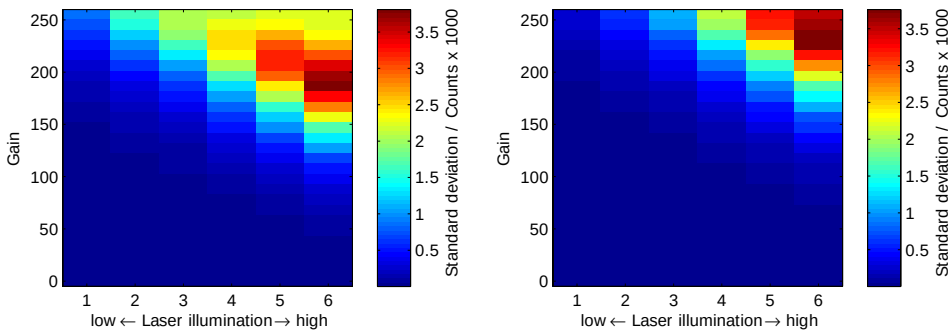

Figure 5.14 *The spatial pixel-to-pixel standard deviation in counts for the signals obtained through the IF456 filter (left) and the IF400 filter (right) for each of the different gains and laser illuminations*

It is to be noted that this level of saturation occurs already at count levels as low as 26 000 counts, less than half of the maximum count level of 65 535. The same effect can be seen for the detected signals passing through the IF400 filter. In figure 5.14 (right) it can be seen that the standard deviation reaches a maximum value in the column for the highest laser illumination, at a gain of 230. On the basis of the chart at the right in figure 5.11, it can be determined that this corresponds to a count value of about 29 000 ($10^{4.47}$).

Figure 5.13 displays a region identified as a useful workspace for the camera and the phosphor involved. The upper-dashed line indicates where the limit for the gain vs. illumination trade-off lies. In the chart at the left in figure 5.11, the position of the upper dashed line would correspond in figure 5.13 to a count-value range of 25 000-30 000 counts ($10^{4.4}$-$10^{4.5}$). Count levels higher than this should be avoided. The fact that there is a range of gain levels between 100 and 190 (see figure 5.13) in which the absolute evaluated temperature and the precision are both rather constant, regardless of the laser illumination, shows that saturation occurs after the photocathode. Thus, neither the strength of the light source itself, nor the photocathode is responsible for the saturation that occurs.

It can be concluded from the work just summarized that there is an upper limit of counts below which the ICCD cameras should be used in order to obtain reliable results. This limit can be shown to be in the 25 000-30 000 count range within the nominal range of up to 65 535 counts allowed by the 16-bit A/D converter. Thus, this limit is less than half of the maximum value, making the occurrence of saturation far from obvious. This value was found to be valid for all of the gain levels considered here.

Note that the experiments were performed using a particular ICCD camera and a particular thermographic phosphor. Accordingly, an investigation such as the one presented here should be carried out prior to any experiment involving quantitative measurements obtained by the use of a two-color ratio method.

The work just reported on was concerned with precision, but a similar study of how the accuracy obtained could be affected by long- and short-term drifts of the cameras employed would be of interest as well. Investigations similar to the one just reported on, but using different types both of ICCD cameras and of thermographic phosphors (the latter differing in terms of emission wavelengths and of lifetimes from those employed here) and involving different temperatures would be of clear interest too.

5.4 Precision

In the precious section, the non-linear features of the ICCD detector were investigated with respect to precision. Within the useful workspace involved, the

precision in temperature ranges from ±1 to ±10 K. This number generally depends upon the type of phosphor employed, the absolute temperature and the other conditions present (detector system, distances, S/N ratio, etc.). Once it has been confirmed that the equipment is being used properly and that the detector is operating in its linear regime, a relevant question is then what levels of precision is achievable.

Estimation of the accuracy and of the precision of temperature measurements can be carried out in different ways, at the same time as the definitions of the two are quite non-ambiguous. The accuracy of a measurement is the degree to which the measured temperature value obtained deviates from the true temperature. In the case of phosphor thermometry, this is ideally determined by the accuracy of the thermocouple used during calibration. A type K thermocouple has an accuracy of ±1.5 K at room temperature. The precision, on the other hand, is the degree to which repeated measurements under unchanged conditions yield the same results each time, i.e. the repeatability or the reproducibility of the measurements. For a specific measurement, the accuracy and precision can both be high or both be low, or the one could be high and the other low, for example. Measurements of high precision but low accuracy could still be useful, if the aim were to measure the temperature difference between several measurement points, and the absolute temperature values are of secondary interest, as in the case taken up in paper IV.

This section will consider in particular an investigation regarding the precision of temperature measurements, one which is described in greater detail in paper VII. The aim of the study was to determine what the highest level of precision is that can be obtained using the thermographic phosphors BAM for two-dimensional surface temperature measurements. The results provide guidance on what precision is to be expected from surface temperature measurements using the two-color ratio technique in combination with thermographic phosphors, and they also confirm the importance of using highly stable and linear ICCD detectors. The precision of the temperature measurements was examined in relation to the spatial resolution. These two quantities involve a trade-off in this case, since it is the *spatial* precision of the temperature measurements obtained that is investigated here. The spatial precision was determined by calculating, on a pixel-by-pixel basis within a given image, the standard deviation of the evaluated temperature. In contrast, the *temporal* precision is the standard deviation of measurements carried out in sequence over a period of time, such as frame-to-frame or shot-to-shot.

Figure 5.15 shows the experimental setup employed, involving two nominally identical PI-MAX2 ICCD cameras. A cubic beam splitter makes it possible for the cameras to observe the target from virtually identical positions. A 10 Hz pulsed Nd:YAG laser, working at its third harmonic, producing laser emission at 355 nm, is used to excite the phosphor. Because of the high fluorescence yield of BAM (80 to 95 %) [77-79], the laser power required is very low, <1 mJ. Taking account of the

expansion of the laser beam, enhanced by the use of a negative lens, the fluence that illuminated the measured surface was calculated to be about 5 μJ/cm^2.

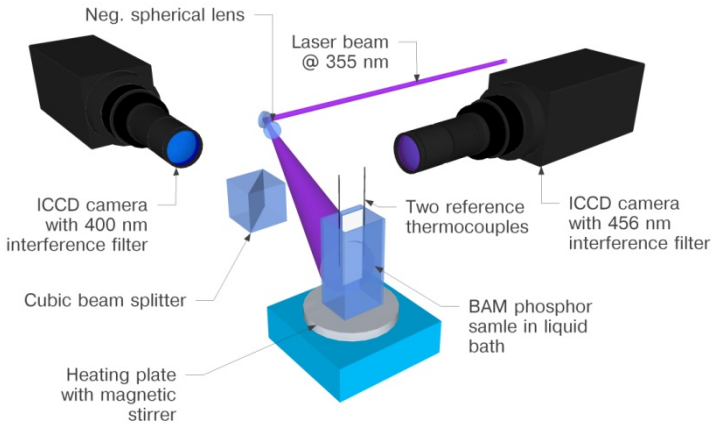

Figure 5.15 *The experimental setup used for the precision estimation measurements*

Since the aim of this study was to investigate the measurement precision of the 2D phosphor thermometry technique, it was important to establish a reference surface having an even temperature distribution. For this purpose a thin glass plate (1 mm thick) was coated with the phosphorescent material and was then joined together with another glass plate to form a hermetically sealed cell in which the layer of phosphor was located between the two glass plates. This cell was then submerged in a liquid bath. The liquid, having a high level of heat capacity, dispersed the heat and served as a buffer against rapid changes in temperature. At lower temperatures, between 273 and 373 K, water served as the dispersing fluid. To extend the temperature range, complementary measurements with glycerol, which has a boiling point of 563 K, were performed. The liquid bath was placed on an electrical heating plate equipped with a magnetic stirrer. Due to the limited capacity of the heater, the maximum temperature that could be reached was 470 K. The temperature in the bath was measured by use of two K-type thermocouples, which provides an accuracy of ±1.5 K within the temperature range observed. During measurements, the temperatures of the two thermocouples were logged and, due to the magnetic stirrer, the standard deviation of the temperature remained below 0.2 K throughout the measurements.

The cameras were triggered by the laser and the exposure time was set to 5 μs. Phosphorescence images of the coated surface were recorded at different temperatures within the range of 279 to 470 K. After stabilization at the desired liquid temperature, ten images through each filter and ten background images were recorded. The images were software-averaged before being processed. The readout noise was not considered to be a problem since the phosphorescence signal was

strong. After background subtraction, flat field correction and image registration transformation, the images taken using the different filters were dealt with as described in section 4.3, generating a ratio image, *R*. The mean value and the spatial standard deviation of the values within the ratio image were evaluated within an area of about 1000 × 850 pixels, corresponding to an object area of about 2.8 × 2.4 cm.

Prior to division, the individual images provided by each camera were smoothed by software Gaussian filtering using MATLAB. This made the precision of overlap of the two images less critical, so that the precision of the ratio was increased, although at the expense of a decrease in spatial resolution.

In addition to the measurements, an image of a resolution test target was recorded, so as to be able to measure the spatial resolution. Repeating the software filtering on the image of the resolution test target enabled a measure of the spatial resolution of the smoothed spectral ratio images to be obtained. This procedure was repeated with use of software Gaussian filtering of different strengths, enabling the relationship between precision and spatial resolution to be computed.

Figure 5.16 shows an example of the results of the measurements, done in water at 331 K. Figures 5.16(a) and (b) show the phosphorescence observed through the IF400 and the IF456 filter, respectively. Figure 5.16(c) displays the resulting ratio image. As can be seen, despite the inhomogeneity of the phosphorescence intensity, evident in figures 5.16(a) and (b), the ratio image obtained was highly homogenous. This illustrates the inherent advantage of the two-color ratio approach, as it does not require an absolutely homogeneous laser excitation profile, a phosphor coating or a linear relationship between laser excitation level and intensity of the phosphorescence.

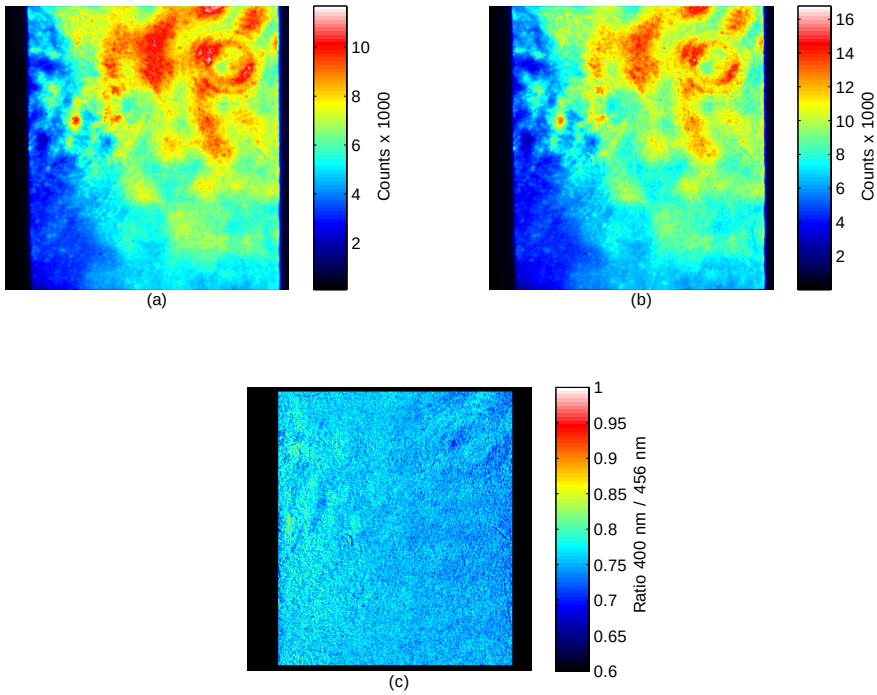

Figure 5.16 *Examples of measurement images obtained at 331 K, showing the phosphorescence at 400 nm (a) and at 456 nm (b), and the resulting ratio image (c). The phosphorescence images represent the average of 10 images each.*

Ratio images similar to those in figure 5.16(c) were generated at 12 different temperatures ranging from 280 to 471 K. For each ratio image, the mean value and the spatial standard deviation of the ratios within the area selected (comprising about 850 000 pixels) were evaluated. Figure 5.17 shows the resulting relationship between the temperature and the ratio, with the error bars indicating the spatial standard deviations of the ratios.

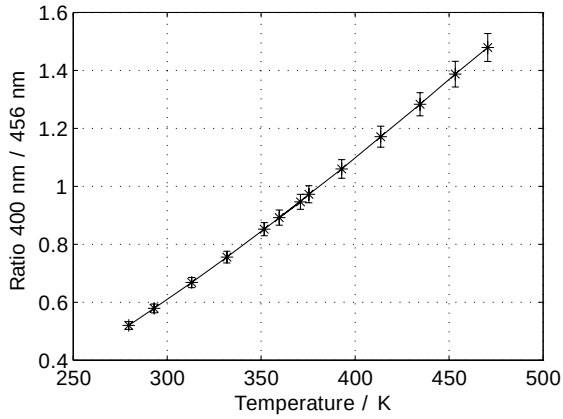

Figure 5.17 *Relationship between the phosphorescence ratio and the temperature*

As can be seen, the relationship is close to linear. The slope of a fitted line gives the temperature sensitivity of the phosphor. The values in figure 5.17 give that the slope, and thus the sensitivity, of BAM is 0.005 K^{-1}, in this experiment. The spatial standard deviation of the ratios within the area selected is ±0.015, at room temperature, indicating the precision to be ±3 K, or 1 %.

As can be seen in figure 5.17, the size of the error bars increases with temperature. Figure 5.18 shows this increase in spatial standard deviation, or degradation in precision that occurs, as the temperature increases, here from 280 to 471 K.

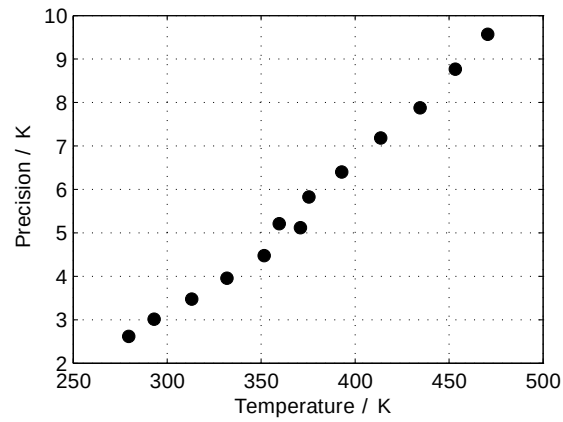

Figure 5.18 *Evaluated precision versus temperature*

The precision at the lowest temperature level is ±2.6 K, or 0.9 %, and at the highest temperature (471 K) is ±9.6 K, or 2 %.

As can be seen, there is a discontinuity between the measurements at 360 and 370 K. This corresponds to the overlap of the measurements carried out in water (280 to 370 K) with those carried out in glycerol (360 to 470 K). The reason for the discontinuity is a drift over time in one of the ICCD cameras. It becomes clear between 360 and 370 K, due to a 3 hour delay between the continuous water and glycerol measurement sequences. During this break the local sensitivity of one of the cameras drifted, causing a gradient offset across the chip, this resulting in a reduction in precision. This instability in the cameras is hardly noticeable in other applications, and indicates how easily affected this two-color ratio method is by small variations in linearity or in detector drift.

The degree of precision shown in figure 5.18 increases if the original phosphorescence images are subjected to spatial smoothing, using a software Gaussian filtering, since this reduces the standard deviation that shot noise gives rise to. A spatial smoothing as such simulates in a way a lower spatial resolution, and also indicates how a pixel binning would increase the S/N ratio. An image of a resolution test target (see figure 5.19) was subjected to the same treatment in order to quantify this reduction in resolution.

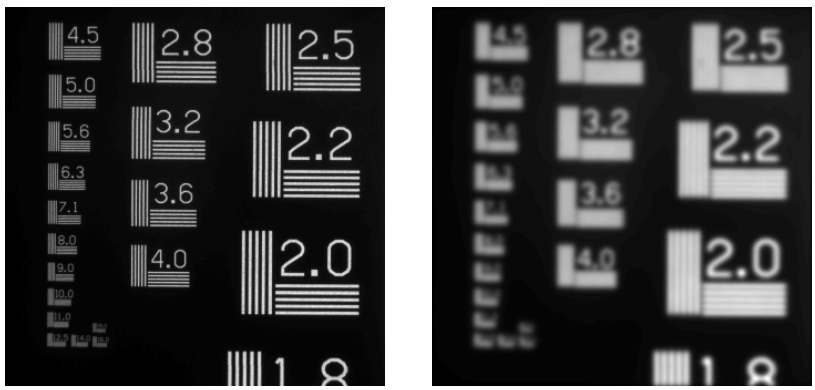

Figure 5.19 *An image of a resolution test target prior to software filtering (left) with a spatial resolution of 11 lines/mm, and after software filtering (right) when the target has been subjected to a spatial smoothing through use of a software Gaussian filter, resulting in a spatial resolution of 2.2 lines/mm.*

Prior to division, the phosphorescence images were processed by software Gaussian filters of differing strengths, smoothing out the resulting ratio image. With increasing strength of the filter, the spatial resolution decreases, whereas the precision increases. This is illustrated in figure 5.20, which shows the relationship between the gain in precision and the loss in resolution for three measurements done at different temperatures.

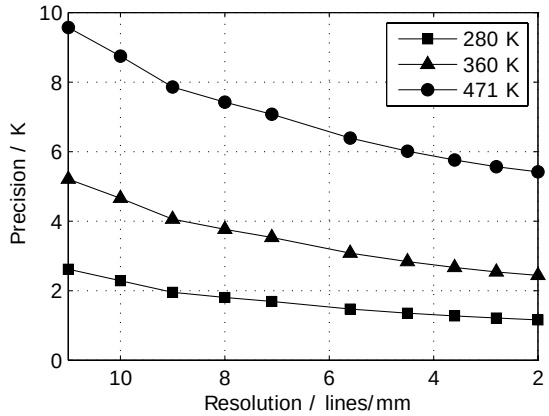

Figure 5.20 *The increase in precision with decreasing resolution shown for three measurements at different temperatures*

For the lowest temperature, the precision increased to ±1.2 K, or 0.4 %, as the resolution was decreased to 2 lines/mm. For the highest temperature, the precision is increased to ±5.4 K, or 1.2 %. Accordingly, the precision varies from 0.4 to 2 %, depending upon the absolute temperature and the resolution. This emphasizes the potential for precision in 2D phosphor thermometry, since the temperature sensitivity of BAM by no means is remarkable, the ratio spanning a factor of three in the temperature range investigated. Särner et al. have shown, for example, that the ratio of ZnO:Zn encompasses more than one order of magnitude in the same temperature interval as investigated here [63].

The experiment just reported on was also performed using a single camera, together with a filter wheel. That experiment was not performed using a single shot, since the aim was to investigate the effect of shot-to-shot variations in laser power, of flat field corrections and of the image registration process on the precision obtained. The results for the two setups were similar, but the precision improved slightly when two cameras were employed. The uncertainties introduced by the shot-to-shot variations in the laser were found to be greater than the uncertainties introduced by the proper use of an image registration procedure. It is thus preferable, as far as precision is concerned, to obtain the data using a single shot.

6 Summary & Outlook

The aim of the thesis was to introduce and describe certain basic principles that apply to thermographic phosphors and examine how these are employed in thermometry using Laser-Induced Phosphorescence. The thesis has been concerned in particular with matter of the precision and the reproducibility of the technique, employed both in point measurements andin two-dimensional surface measurements. A basic conclusion of the work is that, despite the phosphor thermometry technique being well established, caution should be taken with respect to its precision and reproducibility, the thickness of the phosphor layers, the free phosphor particles seeded in gaseous flows and the manner in which the detectors are employed.

Most of the work presented in the thesis has concerned the feasibility of the technique, in particular matters of its precision and of the detectors employed. However, there are many other matters as well that need to be considered, in order to be able to reproduce measurements with a high degree of precision and accuracy.

It is important that the degree of reproducibility on a long-term basis be investigated. Investigations of reproducibility, especially regarding 2D measurements, concerned with how the evaluated absolute temperature can be affected by long- and short-term drifts of the cameras, should be carried out, particularly with respect to the effects of the image intensifier. Also investigations similar to that described in paper VI, but with use of different types of ICCD cameras, different types of thermographic phosphors (differing both in emission wavelengths and in lifetimes) and at different temperatures, would be of clear interest.

Paper III reports on an investigation concerning the thickness of the phosphor layer applied. In the experiment in question, the phosphor was applied using an airbrush pen (Rich AB 300) containing a solution of the phosphor, a water-based binder (HPC) and ethanol. This approach was used for most of the experiments presented in the thesis. Obviously, the phosphor coatings need to have a good thermal contact with the substrate material. In high-temperature applications, however, use of a binder can lead to cracks and eventually to the phosphor layer flaking off. There are alternative methods for applying phosphors for use in high-temperature measurements, methods that avoid the limitations introduced by a binder and by mechanical stress. Chemical Vapor Deposition (CVD) [80], Electrostatic Assisted Combustion Chemical Vapor Deposition (EACVD) [26] and Sol-gel deposition [81, 82] are methods of this sort that avoid use of a binder and result in good thermal stability and provide good thermal and mechanical contact

with the substrate. CVD requires a relatively complex and expensive setup, whereas Sol-gel deposition is rather simple, involving use of a dip-coating technique. Although both these methods require rather small samples and are not easily scaled up for large or permanent components, they should be investigated with respect to precision and reproducibility in temperature measurements, using different types of substrates and at elevated temperatures.

Regarding free flow measurements, tests should be conducted in a liquid prior to a gas, in order to determine the limits of particle density when performing temperature measurements in gaseous flows.

Although phosphors occur in many different applications, their temperature properties are not always known. Alternative phosphors should be investigated regarding their temperature dependence, in order to extend the range of phosphors available. Blue-emitting phosphors are preferable, since emissions having longer wavelengths risk being interfered with by possible Planck radiation. A short emission lifetime is also desirable, since this increases the suppression of such background noise as that of chemiluminescence and also enables measurements of high temporal resolution to be performed.

The use of upconversion excitation of thermographic phosphors is an area of interest for combustion science. Employing IR or NIR laser excitation together with subsequent emission in the visible range has a potential for eliminating the excitation of interfering fluorescent substances that occurs in large amounts in genuine petroleum liquids. Measurements of temperatures in gaseous flows using upconversion thermographic phosphors has been demonstrated [16] and that technique should be developed further. With use of upconversion thermographic phosphors, not only the selection of the phosphors available increases, but also the possibilities are increased of finding phosphors with emissions of shorter wavelengths and lifetimes.

Acknowledgements

My years at the Division of Combustion Physics have indeed been some of the best years of my life. It is difficult for me to imagine a better workplace. I am very grateful to so many people for making this the period in which I have developed the most ever, both personally and professionally.

First of all, I would like to thank my supervisor *Mattias Richter* for his professional guidance and mentorship over the years. I have really appreciated our relationship, spiced with a great deal of humor and sarcasm, but never at the expense of the serious matters.

I am also very grateful to my co-supervisor, who is also the Division Head, Professor *Marcus Aldén*, for giving me the opportunity and the confidence to be a part of the team of our Division.

I am indescribable grateful to all my former and current colleagues, all of whom have made it a pleasure to work at the Division. You are far too many to name all of you personally, but I still do want to point out some of you.

I would like to thank *Jonathan Johnsson* for being such a good friend to me and to my family and a colleague in many disciplines, always available for technical support regarding any matter and for untiring Google searching of any kind.

Thanks also to *Elias Kristensson* for being a great friend to both me and my family, for inspiration, interesting discussions and unforgettable moments of humor.

I am also grateful to *Johan Sjöholm*, whom I have been sharing the office with for the last six years. Thanks for all our interesting and inspiring discussions, your endless support and all our moments of laughter. It has been a great pleasure.

Thank you, *Henrik Bladh*, for taking my advice and not leaving the Division when you finished your PhD in 2007. I will miss our nerdy, endless discussions about small red cottages, public service radio and science.

I would also like to thank *Christoph Knappe*, whom I have been working with a lot. Thanks for all our laughter, interesting discussions and for coping with my "German" humor.

Thanks also to Professor *Per-Erik Bengtsson* for your support in many areas, your kindness and for all the philosophical discussions we have had.

I would also like to thank my former colleague *Gustaf Särner*, whose position I had the honor to succeed. Thanks for your inspiration, our good memories and delightful collaboration in the laboratory.

Thanks also to *Rutger Lorensson* for always finding solutions to technical problems of any kind, and for always being willing to help. It has always been interesting to chat with you and to partake of your vast fund of knowledge. It has been a pleasure getting stuck at your doorstep, chatting for never less than 30 minutes.

Among my other colleague I would like to thank in particular *Andreas Lantz*, *Andreas Ehn*, *Johan Zetterberg*, *Rikard Wellander*, *Fahed Abou Nada*, *Ronald Whiddon* and *Billy Kaldvee*.

During the years I have been here there has been an administrative staff, all of whom really deserve special thanks. These are *Cecilia Bille*, *Anneli Nilsson-Ahlm*, *Minna Ramkull*, *Nina Mårtensson*, *Sara Holmgren* and *Eva Persson*. Thanks for making the Division work.

Thanks also to *Centre of Competence Combustion Processes* (*KCFP*) for the financial support.

I would like to thank my family: my dad *Ola*, my mom *Birgitta* and my sisters *Evelina*, *Teresa* and *Matilda* for your endless encouragement and for always showing undoubting faith in my undertakings. I am also vary thankful to my parents-in-law, *Kenneth* and *Gertrud*, and sisters-in-law, *Kristi* and *Lotta*, without whom it would have been impossible combining parenting, thesis writing *and* having a delightful wife, all at the same time.

Last but not least I would like to thank my wife *Magdalena*, who has encouraged and supported me throughout all of my studies, especially during my time at the Division. Your engagement and genuine interest in my work have often led to fruitful discussions over the evening dinner table where I believe most people couldn't care less about their partner's work-troubles.

References

1. International Energy Agency (IEA), *Key World Energy Statistics 2011*, 2011.
2. International Energy Agency (IEA), *World Energy Outlook 2009*, 2009.
3. F. Robelius, *Giant Oil Fields - The Highway to Oil : Giant Oil Fields and their Importance for Future Oil Production*, Doctoral Thesis, Uppsala University, 2007.
4. IPCC, *Climate Change 2007 - The Physical Science Basis: Summary for Policymakers. Contribution of Working Group I to the Fourth Assessment Report of the Intergovernmental Panel on Climate Change*, 2007.
5. A.C. Eckbreth, *Laser diagnostics for combustion temperature and species*, 2nd ed, Amsterdam, Gordon & Breach, 1996.
6. T.D. McGee, *Principles and Methods of Temperature Measurement*, Wiley, 1988.
7. S.W. Allison and G.T. Gillies, *Remote thermometry with thermographic phosphors: Instrumentation and applications*. Review of Scientific Instruments, **68**(7): p. 2615-2650, 1997.
8. C. Kerr and P. Ivey, *An overview of the measurement errors associated with gas turbine aeroengine pyrometer systems*. Measurement Science & Technology, **13**(6): p. 873-881, 2002.
9. M.R. Cates, S.W. Allison, S.L. Jaiswal and D.L. Beshears, *YAG:Dy and YAG:Tm Fluorescence To 1700 C*, ISA - 49th International Instrumentation Symposium, 2003.
10. M.R. Cates, D.L. Beshears, S.W. Allison and G.M. Simmons, *Phosphor thermometry at cryogenic temperatures*. Review of Scientific Instruments, **68**(6): p. 2412-2417, 1997.
11. B. Valeur and M.N. Berberan-Santos, *A Brief History of Fluorescence and Phosphorescence before the Emergence of Quantum Theory*. Journal of Chemical Education, **88**(6): p. 731-738, 2011.
12. E.N. Harvey, *A history of luminescence from the earliest times until 1900*, Philadelphia, American Philosophical Society, 1957.
13. S. Shionoya, H. Yamamoto and W.M. Yen, *Phosphor handbook*, 2nd ed, CRC Press, 2007.
14. G.G. Stokes, *On the change of refrangibility of light*. Philosophical Transactions of the Royal Society of London, **142**, 1852.
15. A.L. Heyes, S. Seefeldt and J.P. Feist, *Two-colour phosphor thermometry for surface temperature measurement*. Optics and Laser Technology, **38**(4-6): p. 257-265, 2006.

16. D.A. Rothamer and J. Jordan, *Planar imaging thermometry in gaseous flows using upconversion excitation of thermographic phosphors*. Applied Physics B-Lasers and Optics, **106**(2): p. 435-444, 2012.
17. F. Auzel, *Upconversion and anti-stokes processes with f and d ions in solids*. Chemical Reviews, **104**(1): p. 139-173, 2004.
18. S. Svanberg, *Atomic and Molecular Spectroscopy: Basic Aspects and Practical Applications*, 4th ed, Springer, 2004.
19. W.H. Fonger and C.W. Struck, *Eu^{+3} ^5D Resonance Quenching to Charge-Transfer States in Y_2O_2S,La_2O_2S, and LaOCl*. Journal of Chemical Physics, **52**(12): p. 6364-6372, 1970.
20. G. Särner, *Laser-Induced Emission Techniques for Concentration and Temperature Probing in Combustion*, Doctoral Thesis, Lund University, 2008.
21. A. Omrane, *Thermometry using laser-induced emission from thermographic phosphors: development and applications in combustion*, Doctoral Thesis, Lund University, 2005.
22. Neubert, *Device for indicating the temperature distribution of hot bodies,* US Patent No. 2,071,471, 1937
23. L.C. Bradley, *A Temperature-Sensitive Phosphor Used to Measure Surface Temperatures in Aerodynamics*. Review of Scientific Instruments, **24**(3): p. 219-220, 1953.
24. K. Wickersheim and M. Sun, *Phosphors and Fiber Optics Remove Doubt from Difficult Temperature-Measurements*. Research and Development, **27**(11): p. 114-119, 1985.
25. K.A. Wickersheim and R.B. Alves, *Recent Advances in Optical-Temperature Measurement*. Industrial Research and Development, **21**(12): p. 82-89, 1979.
26. J.P. Feist, A.L. Heyes, K.L. Choy and B. Su, *Phosphor thermometry for high temperature gas turbine applications*, 18th International Congress on Instrumentation in Aerospace simulation facilities (ICIASF'99), Toulouse France, 1999.
27. J.P. Feist, A.L. Heyes and S. Seefeldt, *Oxygen quenching of phosphorescence from thermographic phosphors*. Measurement Science and Technology, **14**(5): p. N17-N20, 2003.
28. B.W. Noel, H.M. Borella, W. Lewis, W.D. Turley, D.L. Beshears, G.J. Capps, M.R. Cates, J.D. Muhs and K.W. Tobin, *Evaluating Thermographic Phosphors in an Operating Turbine-Engine*. Journal of Engineering for Gas Turbines and Power-Transactions of the ASME, **113**(2): p. 242-245, 1991.
29. K.W. Tobin, S.W. Allison, M.R. Cates, G.J. Capps, D.L. Beshears, M. Cyr and B.W. Noel, *High-Temperature Phosphor Thermometry of Rotating Turbine-Blades*. AIAA Journal, **28**(8): p. 1485-1490, 1990.
30. J.P. Feist, A.L. Heyes, K.L. Choy and J. Mei, *Smart TBC's for gas turbines*, 15th International symposium on air breathing engines, Bangalore India, 2001.
31. W. Koban, J.D. Koch, R.K. Hanson and C. Schulz, *Toluene LIF at elevated temperatures: implications for fuel-air ratio measurements*. Applied Physics B-Lasers and Optics, **80**(2): p. 147-150, 2005.
32. M. Luong, R. Zhang, C. Schulz and V. Sick, *Toluene laser-induced fluorescence for in-cylinder temperature imaging in internal combustion engines*. Applied Physics B-Lasers and Optics, **91**(3-4): p. 669-675, 2008.

33. G. Tea, G. Bruneaux, J.T. Kashdan and C. Schulz, *Unburned gas temperature measurements in a surrogate Diesel jet via two-color toluene-LIF imaging*, In Proceedings of the Combustion Institute **33**, p. 783-790, 2011.
34. M.C. Thurber, F. Grisch and R.K. Hanson, *Temperature imaging with single- and dual-wavelength acetone planar laser-induced fluorescence*. Optics Letters, **22**(4): p. 251-253, 1997.
35. K. Kohse-Höinghaus, *Laser Techniques for the Quantitative Detection of Reactive Intermediates in Combustion Systems*. Progress in Energy and Combustion Science, **20**(3): p. 203-279, 1994.
36. M.P. Lee, B.K. McMillin and R.K. Hanson, *Temperature-Measurements in Gases by Use of Planar Laser-Induced Fluorescence Imaging of NO*. Applied Optics, **32**(27): p. 5379-5396, 1993.
37. C. Copeland, J. Friedman and M. Renksizbulut, *Planar temperature imaging using thermally assisted laser induced fluorescence of OH in a methane-air flame*. Experimental Thermal and Fluid Science, **31**(3): p. 221-236, 2007.
38. U.E. Meier, D. Wolff-Gassmann, J. Heinze, M. Frodermann, I. Magnusson and G. Josefsson, *LIF imaging of species and temperature in technical combustion at elevated pressures*, International Congress on Instrumentation in Aerospace Simulation Facilities (ICIASF'99), Toulouse France, 1999.
39. J. Engström, *Development of a 2D Temperature Measurement Technique for Combustion Diagnostics using 2-Line Atomic Fluorescence* Doctoral Thesis, Lund University, 2001.
40. H. Haraguchi, B. Smith, S. Weeks, D.J. Johnson and J.D. Winefordner, *Measurement of Small Volume Flame Temperatures by 2-Line Atomic Fluorescence Method*. Applied Spectroscopy, **31**(2): p. 156-163, 1977.
41. N. Omenetto, P. Benetti and G. Rossi, *Flame Temperature Measurements by Means of Atomic Fluorescence Spectrometry*. Spectrochimica Acta Part B-Atomic Spectroscopy, **27 B**(10): p. 453-461, 1972.
42. S. Roy, J.R. Gord and A.K. Patnaik, *Recent advances in coherent anti-Stokes Raman scattering spectroscopy: Fundamental developments and applications in reacting flows*. Progress in Energy and Combustion Science, **36**(2): p. 280-306, 2010.
43. K. Kohse-Höinghaus and J.B. Jeffries, *Applied Combustion Diagnostics*, New York, Taylor and Francis, 2002.
44. D. Hofmann and A. Leipertz, *Temperature field measurements in a sooting flame by filtered Rayleigh scattering (FRS)*. 26th International Symposium on Combustion (The Combustion Institute): p. 945-950, 1996.
45. H. Seyfried, M. Richter, K.-H. Nilsson, M. Aldén and H. Schmidt, *Surface thermometry using laser-induced phosphorescence applied in the afterburner of an aircraft turbofan engine*. Collection of Technical Papers - 45th AIAA Aerospace Sciences Meeting, **18**: p. 12794-12802, 2007.
46. H. Seyfried, Särner. G, A. Omrane, M. Richter and M. Aldén, *Optical diagnostics for characterization of a full-size fighter-jet after-burner*. ASME, GT2005-69058, 2005.

47. S.W. Allison, M.R. Cates, D.L. Beshears and G.T. Gillies, *Phosphor thermometry at ORNL*, 8th International Temperature Symposium, Chicago, USA, 2003.
48. J.S. Armfield, R.L. Graves, D.L. Beshears, M.R. Cates, T.V. Smith and S.W. Allison, *Phosphor Thermometry for Internal Combustion Engines*. SAE Technical Paper 971642, 1997.
49. A. Omrane, F. Ossler and M. Aldén, *Temperature measurements of combustible and non-combustible surfaces using laser induced phosphorescence*. Experimental Thermal and Fluid Science, **28**(7): p. 669-676, 2004.
50. T.J. Horvarth, S.A. Berry and N. Merski, *X-38 Experimental Aerodynamics*, 34th AIAA Thermophysics Conference, Denver USA, 2000.
51. A. Omrane, G. Juhlin, F. Ossler and M. Aldén, *Temperature measurements of single droplets by use of laser-induced phosphorescence*. Applied Optics, **43**(17): p. 3523-3529, 2004.
52. A. Omrane, G. Särner and M. Aldén, *2D-temperature imaging of single droplets and sprays using thermographic phosphors*. Applied Physics B-Lasers and Optics, **79**(4): p. 431-434, 2004.
53. A. Omrane, F. Ossler and M. Aldén, *Two-dimensional surface temperature measurements of burning materials*, In Proceedings of the Combustion Institute **29**, p. 2653-2659, 2002.
54. A. Omrane, P. Petersson, M. Aldén and M.A. Linne, *Simultaneous 2D flow velocity and gas temperature measurements using thermographic phosphors*. Applied Physics B-Lasers and Optics, **92**(1): p. 99-102, 2008.
55. J.P.J. van Lipzig, *2D temperature measurements in the EHPC using Laser-Induced Phosphorescence*, Master Thesis, Eindhoven University of Technology, 2012.
56. T. Kissel, E. Baum, A. Dreizler and J. Brübach, *Two-dimensional thermographic phosphor thermometry using a CMOS high speed camera system*. Applied Physics B-Lasers and Optics, **96**(4): p. 731-734, 2009.
57. R.J. Woods, S. Scypinski, L.J.C. Love and H.A. Ashworth, *Transient Digitizer for the Determination of Microsecond Luminescence Lifetimes*. Analytical Chemistry, **56**(8): p. 1395-1400, 1984.
58. J. Brübach, J. Janicka and A. Dreizler, *An algorithm for the characterisation of multi-exponential decay curves*. Optics and Lasers in Engineering, **47**(1): p. 75-79, 2009.
59. L. Armstrong and S. Feneuille, *Theoretical-Analysis of Phase-Shift Measurement of Lifetimes Using Monochromatic Light*. Journal of Physics B-Atomic Molecular and Optical Physics, **8**(4): p. 546-551, 1975.
60. L.P. Goss, A.A. Smith and M.E. Post, *Surface Thermometry by Laser-Induced Fluorescence*. Review of Scientific Instruments, **60**(12): p. 3702-3706, 1989.
61. D.J. Bizzak and M.K. Chyu, *Rare-Earth Phosphor Laser-Induced Fluorescence Thermal Imaging-System*. Review of Scientific Instruments, **65**(1): p. 102-107, 1994.
62. A. Omrane, G. Juhlin, M. Aldén, G. Josefsson, J. Engström and T. Benhamn, *Two-dimensional temperature characterization of valves and piston of a GDI optical engine*. SAE Technical Paper 2004-01-0609, 2004.

63. G. Särner, M. Richter and M. Aldén, *Investigations of blue emitting phosphors for thermometry*. Measurement Science and Technology, **19**(12): p. 125304, 2008.
64. Hamamatsu, *Photomultiplier Tubes Basics and Applications*, 3d ed, Word Technical Writing, Inc., Hamamatsu Photonics K.K., 2007.
65. A.G. Wright, *Amplifiers for use with photomultipliers - who needs them?* Nuclear Instruments & Methods in Physics Research Section a-Accelerators Spectrometers Detectors and Associated Equipment, **504**(1-3): p. 245-249, 2003.
66. J. Brübach, A. Patt and A. Dreizler, *Spray thermometry using thermographic phosphors*. Applied Physics B-Lasers and Optics, **83**(4): p. 499-502, 2006.
67. J.P. Holman, *Heat Transfer*, 8th ed, New York, McGraw-Hill, 1997.
68. W.E. Ranz and W.R. Marshall, *Evaporation from Drops .1.* Chemical Engineering Progress, **48**(3): p. 141-146, 1952.
69. X.Q. Cao, R. Vassen and D. Stoever, *Ceramic materials for thermal barrier coatings*. Journal of the European Ceramic Society, **24**(1): p. 1-10, 2004.
70. R.M. Ranson, C.B. Thomas and M.R. Craven, *A thin film coating for phosphor thermography*. Measurement Science and Technology, **9**(12): p. 1947-1950, 1998.
71. H. Kunz, *Representation of Temperature Scale above 1337.58 K with Photoelectric Direct Current Pyrometers*. Metrologia, **5**(3): p. 88-102, 1969.
72. J. Brübach, J.P. Feist and A. Dreizler, *Characterization of manganese-activated magnesium fluorogermanate with regards to thermographic phosphor thermometry*. Measurement Science and Technology, **19**(2): p. 025602 (11pp), 2008.
73. D.S. Montgomery, R.P. Drake, B.A. Jones and J.D. Wiedwald, *Flat-field response and geometric distortion measurements of optical streak cameras*, In Proceedings of SPIE **832**, p. 283-288, 1987.
74. T.C. Williams and C.R. Shaddix, *Simultaneous correction of flat field and nonlinearity response of intensified charge-coupled devices*. Review of Scientific Instruments, **78**(12): p. 123702(6p), 2007.
75. C.A. Kruschwitz, M. Wu, K. Moy and G. Rochau, *Monte Carlo simulations of high-speed, time-gated microchannel-plate-based x-ray detectors: Saturation effects in dc and pulsed modes and detector dynamic range*. Review of Scientific Instruments, **79**(10): p. 10E911, 2008.
76. J.D. Wiedwald and R.A. Lerche, *Streak camera dynamic range and optimization*. Proceedings of SPIE, **832**: p. 275-282, 1987.
77. G. Bizarri and B. Moine, *On $BaMgAl_{10}O_{17} : Eu^{2+}$ phosphor degradation mechanism: thermal treatment effects*. Journal of Luminescence, **113**(3-4): p. 199-213, 2005.
78. Y.R. Do and J.W. Bae, *Application of photoluminescence phosphors to a phosphor-liquid crystal display*. Journal of Applied Physics, **88**(8): p. 4660-4665, 2000.
79. D. Ravichandran, S.T. Johnson, S. Erdei, R. Roy and W.B. White, *Crystal chemistry and luminescence of the Eu^{2+}-activated alkaline earth aluminate phosphors*. Displays, **19**(4): p. 197-203, 1999.
80. C. Pflitsch, D. Viefhaus and B. Atakan, *CVD of thin ruby films on Si(100) and stainless steel for surface temperature sensor applications*. Chemical Vapor Deposition, **13**(8): p. 420-426, 2007.

81. C. Eckert, C. Pflitsch and B. Atakan, *Sol-gel deposition of multiply doped thermographic phosphor coatings Al_2O_3:(Cr^{3+}, M^{3+}) (M = Dy, Tm) for wide range surface temperature measurement application*. Progress in Organic Coatings, **67**(2): p. 116-119, 2010.
82. C. Pflitsch, R.A. Siddiqui, C. Eckert and B. Atakan, *Sol-gel deposition of chromium doped aluminium oxide films (ruby) for surface temperature sensor application*. Chemistry of Materials, **20**(8): p. 2773-2778, 2008.

Summary of Papers

Paper I. This paper employs the thermographic phosphor YAG:Dy for temperature imaging in a heated-grid reactor. The experiment was a qualitative assessment of the rate of pyrolysis of the biomass being processed, which should be the same everywhere on such a heated grid. The temperature distribution across the grid was measured using thermographic phosphors in the absence of solid material on the grid, and was also compared with values obtained from a thermocouple. The results were in line with the expectations based on models implying the real temperature to be significantly higher than that of the thermocouples.

I performed the part of the experimental dealing with the thermographic phosphors together with M.J. Prins. I carried out the evaluation, preparation and illustration of these experimental results, and participated in preparation of the manuscript.

Paper II. This paper reports on an investigation of the possible heating of phosphor particles employed in gaseous flow measurements. An air flow at room temperature seeded with the thermographic phosphor BAM was illuminated by laser radiation, and the phosphorescence signal was recorded by a spectrometer for a range of different laser fluences. The results indicated no heating effects to occur due to the high laser power.

I conducted the experiments and carried out the evaluation. I prepared the manuscript and conducted the illustrations employed and wrote most of the manuscript.

Paper III. This paper concerns a survey investigation of the impact of the thickness of the phosphor coating on a cylinder wall during crank-angle resolved temperature measurements. The phosphorescence of La_2O_2S:Eu was detected from two directions on the inside surface of a quartz liner extension in a Toyota engine: from the side facing the in-cylinder gas and from the side facing the quartz liner. Two different coating thicknesses were investigated at different engine operating modes. The results showed the temperature

differences between the “gas-side” and the “wall-side” of the phosphor coating to increase with the thickness of the coating and for higher temperature gradients over time. This was seen as indicating a need for caution in performing measurements in environments in which strong temperature gradients, both spatial and temporal, are present.

I participated in the experimental work together with C. Knappe, P. Andersson and M. Algotsson. I contributed to parts of the text and to preparation of the manuscript and of the illustrations employed.

Paper IV. This paper reports on an experiment in which thermographic phosphors were employed for detecting temperature gradients. The experiment aimed at accurately measuring laminar burning velocity using the Heat Flux method. The thermographic phosphor ZnO:Zn was used for detecting small variations in temperature, which were used for determining theoretically the laminar burning velocity of a methane/air flame.

I participated in the preparation of the experiment and contributed to preparation of the manuscript and of the illustrations employed.

Paper V. This paper deals with a novel test procedure used to determine the linear operating region of optical detectors used for phosphorescence decay time measurements. Weak saturation effects that are far from obvious were identified and their relations to optical and to electrical saturation were studied. In addition, means of compensating for non-linear response in the detectors employed were introduced, through use of reference values obtained from a detector response database.

I performed a preparatory experiment and participated in the preparation both of the experiment and of the manuscript.

Paper VI. This paper investigates non-linear features caused be the intensifier in an ICCD camera, the effects these have on the results obtained in performing two-dimensional thermometry using thermographic phosphors, and how such features can be avoided. It is concluded that in performing quantitative measurements there is an upper limit of counts of the camera one should careful to not exceed.

I conducted most of the experiments and carried out most of the evaluations, as well preparation of the manuscript and of the illustration employed.

Paper VII. In this paper, the highest achievable precision in temperature when employing the two-color ratio technique utilizing thermographic phosphors was investigated. The results obtained are valid for the particular setup involved and for the temperature ranges studied. The relation between precision and the spatial resolution was studied, since these two properties involve a trade-off in this case. The results provide guidance concerning the precision to be expected when performing two-dimensional thermometry.

I conducted most of the experiments and carried out most of the data evaluation. I prepared the manuscript and the illustration employed.

Paper VIII. In this paper, four different detectors for phosphorescence decay time measurements were investigated. The linear response regime for the detectors, when used for phosphor thermometry, was studied. The results indicated none of the detectors to be totally linear with respect to detector gain and excitation laser intensity, and that the useful workspace needs to be investigated prior to any measurement in order to ensure reliable quantitative results.

I participated in the preparation of the experiment and of the manuscript.

Paper I

Visualization of Biomass Pyrolysis and Temperature Imaging in a Heated-Grid Reactor

M. J. Prins,*,† J. Lindén,‡ Z. S. Li,‡ R. J. M. Bastiaans,† J. A. van Oijen,† M. Aldén,‡ and L. P. H. de Goey†

Combustion Technology Group, Eindhoven University of Technology, Post Office Box 513, 5600 MB Eindhoven, The Netherlands, and Division of Combustion Physics, Lund University, Post Office Box 118, S-221 00 Lund, Sweden

Received June 2, 2008. Revised Manuscript Received November 28, 2008

The main advantage of a heated-grid reactor for studying pyrolysis kinetics of solid fuel samples is that high heating rates of up to 1000 K/s can be obtained. However, one of the concerns is whether the temperature distribution over the grid material is uniform and whether the presence of a thermocouple welded to the grid causes any measurement errors. Biomass samples were placed on the heated-grid reactor, and the volatiles, emitted in the biomass pyrolysis process as hot gas plumes, were imaged with an infrared camera with a high framing speed. The temporal resolved infrared images indicate that the pyrolysis process does not take place at the same rate everywhere on the grid. Two-dimensional temperature images of a heated grid made of stainless steel were recorded using the method of laser-induced thermometry with thermographic phosphors. As expected from a heat-transfer model, measured temperatures were found to be significantly higher than temperatures indicated by a thermocouple welded to the bottom of the grid. It was also observed that there is a large temperature gradient between the two electrodes on which the grid is connected. It is shown that replacing a wire mesh by a foil as a grid material may lead to more homogeneous temperature distribution. The paper recommends additional research to demonstrate the suitability of the heated-grid reactor for carrying out accurate measurements.

1. Introduction

To study the thermal decomposition of solid fuel materials, such as coal, biomass, and waste, the heated-grid reactor has been used for over 25 years. It generally consists of a wire mesh, which is electrically heated, and connected to a thermocouple for measuring its temperature. This type of reactor facilitates the characterization of solid samples at high heating rates up to 1000 K/s. The main benefit involved here is that the weight loss during heating of the sample (which invariably happens in other methods, such as thermogravimetric analysis) can be minimized. Therefore, the reactivity of the fuel is not altered before it reaches the final temperature, at which decomposition kinetics are studied. Another benefit is that the devolatilization products enter directly into a cold gas phase, so that they are quenched. This minimizes secondary reactions, so that the primary pyrolysis gases can be determined. Initial experiments[1−3] have been carried out under so-called "zero hold time" conditions, where the grid was heated to the final temperature and, immediately, the power was turned off. In most experiments, samples are kept at the final temperature, so that kinetic data can be obtained.[4] For kinetic studies, it may be important (especially when pyrolysis is incomplete) to minimize also the cooling time. The wire mesh will typically be cooled by radiation and natural convection at a rate of several hundred degrees per second, but cooling rates can be increased by forced convection.[5] More recent research describing the use of a heated-grid reactor is available.[6,7]

Despite its advantages, results obtained from a heated-grid reactor should be handled with care. First of all, it must always be verified whether the particle size and, hence, the Biot number, is small enough to ensure that the particles on the grid can follow the large temperature gradient imposed. Typically, a fine powder with a particle size of several hundreds of micrometers up to a few millimeters must be used. As a consequence for the reactor design, the aperture between the wires of the mesh cannot be too large. Second, the thermal load on the grid is restricted. If too much sample material were placed on the wire mesh, the amount of electric energy dissipated into heat will be insufficient for rapid heating. Finally, the question is whether all of the particles of the solid sample are heated at the same rate, i.e., whether heating takes place in a uniform way. This requires that the particles are evenly distributed over the grid, so that the thickness of the sample layer is the same everywhere. Another requirement is that the temperature distribution over

* To whom correspondence should be addressed. E-mail: mark.prins@shell.com.
† Eindhoven University of Technology.
‡ Lund University.

(1) Suuberg, E. M.; Peters, W. A.; Howard, J. B. *Seventeenth International Symposium on Combustion*; The Combustion Institute: Pittsburgh, PA, 1979; pp 117−130.
(2) Desypris, J.; Murdoch, P.; Williams, A. *Fuel* **1982**, *61*, 807–816.
(3) Unger, P. E.; Suuberg, E. M. *Fuel* **1984**, *63*, 606–611.
(4) Niksa, S. J.; Russel, W. B.; Saville, D. A. *Nineteenth International Symposium on Combustion*; The Combustion Institute: Pittsburgh, PA, 1982; pp 1159−1167.
(5) Freihaut, J. D.; Proscia, W. M. *Energy Fuels* **1989**, *3*, 625–635.
(6) Mühlen, H.-J.; Sowa, F. *Fuel* **1995**, *74* (11), 1551–1554.
(7) De Jong, W. Nitrogen compounds in pressurised fluidised bed gasification of biomass and fossil fuels. Ph.D. Thesis, Delft University of Technology, Delft, The Netherlands, 2005.

10.1021/ef800419w CCC: $40.75
Published on Web 02/02/2009

the grid material is uniform. During calibration measurements, in which a sample of solid bismuth was melted, slight non-isothermalities have been observed.[5] The bismuth melted at the edges of the grid before it melted at the center, where the thermocouple was located. The presence of the thermocouple, with a radius of the same magnitude as the wires of the grid, may disturb the thermal field. A model developed by Guo[8] shows that, because of heat loss via the thermocouple, the indicated temperature may be significantly lower than the average grid temperature. Using an optical pyrometer, Guo measured grid temperatures that were 150−200 K higher than the thermocouple temperature in the range of 800−1600 K.

The primary aim of this paper is a qualitative assessment of the pyrolysis rate of biomass, which should be the same everywhere on the heated grid. Some insight can be obtained by measuring the temperature distribution of the heated grid, in the absence of a solid sample on the grid, using methods that are described later. To verify whether the biomass is pyrolyzed in a uniform way, i.e., independent of its horizontal and vertical position on the grid, experiments are also carried out in the presence of biomass. Because infrared active gases, e.g., carbon dioxide, are produced during the biomass decomposition procedure, infrared emission can be used to visualize qualitatively the distribution of hot volatiles. Temporal resolved infrared images of the hot volatile gas plumes were recorded during the rapid gas pyrolysis process.

Another aim of this work is to study the 2D temperature distribution of the heated grid, investigate the relation between the temperature of the wire mesh and temperature indicated by the thermocouple, and verify the model of Guo. The method for measuring temperature involves laser-induced emission from thermographic phosphors, which enable remote temperature diagnostics to be performed with high sensitivity and accuracy. The technique is superior to methods based on thermocouples and pyrometry. An optical pyrometer, focusing the radiation from the hot platinum grid onto a screen, will only work at high temperatures and requires focusing time (during which time the grid may break down because of thermal fatigue). The method applied in this research works quickly and is valid over a wide temperature range. This paper comprises principles of the applied spectroscopic methods, a description of the experimental setup, and discussion of results, including the validity of specific heat-transfer models described below.

2. Heat-Transfer Theory

The systematic measurement error in the temperature of the heated grid, because of the presence of the thermocouple leading to disturbances of the temperature field, is examined in detail in this paper. Other sources of systematic errors,[9] such as intrinsic errors in the circuit, extraneous signals or influences, and errors in signal processing, are not considered. Another important factor to avoid measurement errors is to make sure that the thermocouple wires are firmly welded onto the object, of which the temperature is to be measured.

To obtain an idea of how significant the systematic error can be, Keltner and Beck[10] derived a model that calculates the temperature difference between a thermocouple and a thick wall, against which the thermocouple is pressed. The model is based on the unsteady surface element method.[11] The steady-state solution of the model calculates the temperature measured by the thermocouple wires (T_s) as function of the actual wall temperature (T_{wall})

$$T_s = \frac{T_{wall}\exp(-4\sqrt{Bi})}{1+2K\sqrt{Bi}\left(\frac{1}{B}+\frac{\pi}{4}\right)} \tag{1}$$

with

$$K=\frac{k_{Tc}}{k_{wall}} \quad B=\frac{hr_{Tc}}{k_{wall}} \quad Bi=\frac{h_{Tc}r_{Tc}}{2k_{Tc}}$$

In the equations, k is the heat conduction coefficient of the metals, h is the contact heat-transfer coefficient between the wall and the thermocouple, while h_{Tc} is the heat-transfer coefficient of the thermocouple to the ambient, and r_{Tc} is the radius of the thermocouple.

The grid cannot be compared to a thick wall, because its height is in the order of 100 μm, whereas the diameter of the thermocouple is of the same order. Guo[8] developed a model to predict the temperature error in this situation; the derivation of this model can be found in Appendix A. It is essentially an energy balance for the weld, which is considered to have an isothermal temperature T_s. The energy losses from this volume to the thermocouple, the environment (by convection and radiation), and the rest of the grid have to be compensated by dissipation of electric energy. The model is valid for negligible thermal resistance of the interface (i.e., $B \rightarrow \infty$). It assumes that the temperature of the thermocouple only varies in the z direction and the temperature of the grid only varies in the r direction. The steady-state result is given in eq A38 for the situation where one wire is attached to the grid. For a thermocouple, which consists of two wires welded together onto the grid, the radius of the weld is approximately 1.4 times the radius of a thermocouple wire[12]

$$r_s = \sqrt{2}r_{Tc} \tag{2}$$

with r_{Tc} being the radius of a single thermocouple wire.

Assuming that both wires have the same radius and (more or less) the same heat-transfer properties, eq A38 changes to

$$T_s = \frac{T_a\left(\sqrt{\frac{2h_{Tc}k_{Tc}}{r_{Tc}}}-h_{grid}\right)+T_\infty\left(2h_{grid}+\sqrt{\frac{8h_{grid}\delta k_{grid}}{r_s^2}}\frac{K_1(r'_s)}{K_0(r'_s)}\right)}{\left(h_{grid}+\sqrt{\frac{2h_{Tc}k_{Tc}}{r_{Tc}}}+\sqrt{\frac{8h_{grid}\delta k_{grid}}{r_s^2}}\frac{K_1(r'_s)}{K_0(r'_s)}\right)} \tag{3}$$

with

$$r'_s = \sqrt{r_s^2\frac{2h_{grid}}{\delta k_{grid}}}$$

From these expressions, it is clear that the measured temperature depends upon the thermal conductivity of the grid as well as the thermocouple, their heat-transfer coefficients to the gaseous environment, the thickness of the grid (which equals the diameter of the wires), the grid temperature, and the ambient temperature.

(8) Guo, J. Pyrolysis of wood powder and gasification of wood-derived char. Ph.D. Thesis, Eindhoven University of Technology, Eindhoven, The Netherlands, 2004.
(9) Bentley, R. E. *Handbook of Temperature*; Springer: Singapore, 1998.
(10) Keltner, N. R.; Beck, J. V. *J. Heat Transfer* **1983**, *105*, 312–318.
(11) Keltner, N. R.; Beck, J. V. *J. Heat Transfer* **1981**, *103*, 759–764.
(12) Hill, J. M.; Dewynne, J. N. *Heat Conduction*; Blackwell Scientific Publications: London, U.K., 1987.

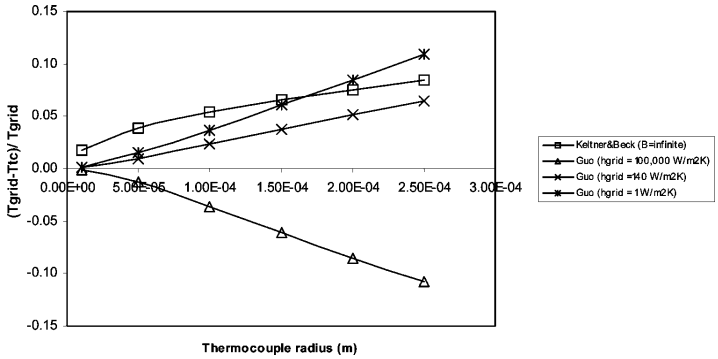

Figure 1. Temperature measurement error predicted by models of Keltner and Beck and Guo. Parameters: $k_{Tc} = 70$ W m^{-1} K^{-1}; $h_{Tc} = 140$ W m^{-2} K^{-1}; $k_{grid} = 70$ W m^{-1} K^{-1}; $\delta = 100$ μm; $T_{grid} = 1000$ K; $T_{ambient} = 300$ K.

Figure 1 compares the relative measurement error of the model of Keltner and Beck (for a thermocouple attached to an infinite plate) and the model of Guo (for a thermocouple attached to an infinite plate but of finite thickness; the plate loses energy to the environment and is heated by electric energy) as a function of the thermocouple radius. In both cases, perfect contact between the thermocouple and object is assumed. If the radius of the thermocouple is increased, the temperature measured by the thermocouple will decrease, because of the heat loss through the thermocouple, leading to higher temperature measurement error.

The errors predicted are rather similar for a typical value of the heat-transfer coefficient from the plate to ambient of 140 W m^{-2} K^{-1}. If this heat-transfer coefficient is much smaller, this also means that much less electric energy is needed to maintain the temperature of the plate. As a consequence, the heat loss via the thermocouple has a much bigger influence and the measurement error increases. On the other hand, if heat transfer from the grid to ambient is extremely high, it may happen that the temperature in the weld becomes higher than the temperature of the rest of the grid. However, this is a rather theoretical situation.

3. Spectroscopic Methods

3.1. Visualization of Volatile Gas Plumes. Real-time visualization of the generated volatile gas flows during the pyrolysis is attractive to understand the reaction kinetics of the process. However, this is not an easy task because the gas components are invisible, with regard to the lack of electronic transitions probed for these molecular species. Carbon dioxide and water are among the major components in the volatiles. Although invisible in the ultraviolet/visible spectral range, they are infrared-active. The infrared radiation from these hot volatile carbon dioxide and water vapor can be used for visualization of fresh volatile plumes from the heat-grid reactor. Because of the relatively high infrared radiation probability of CO_2 at 4.5 μm from its unsymmetric stretching vibration, the major infrared radiation is expected to be located around this wavelength.[13,14]

3.2. Temperature Measurements Using Laser-Induced Phosphorescence. The use of thermographic phosphor materials is a recent technique, which has been developed for remote temperature measurements in various applications.[15] These include static as well as moving surfaces, such as rotor engines[16,17] and turbine engines.[18] Some attempts have been made to apply the method to combustion,[19] e.g., for flame spread scenarios.[20] For thermal decomposition, i.e., pyrolysis, laser-induced phosphorescence was pioneered by Omrane et al.[21] and Svenson et al.,[22] who studied the surface temperature of decomposing materials.

The technique is based on exciting a thermographic phosphor material by an appropriate light source. The phosphor becomes highly fluorescent or phosphorescent, and typically, the emission is in the visible region, with a lifetime in the order of 1 ms. These phosphors used for temperature measurements consist of a ceramic host material and a doping agent from which light is emitted. A large number of different phosphors are known today, covering a wide range from cryogenic temperatures up to 1600 °C or higher. For every application, a specific phosphor can be selected with a typical accuracy of 1% or better, depending upon the conditions.

These temperature measurements can essentially be performed in two ways: (1) Temporally resolved measurements; these are based on the principle that the decay of the phosphorescence signal is temperature-dependent. At higher temperatures, the lifetime becomes shorter. (2) Spectrally resolved measurements; these are based on monitoring the emission versus wavelength. Thermographic phosphors emit phosphorescence signals at different wavelengths; some of these wavelengths are more temperature-sensitive than others. Figure 2 illustrates how the

(13) Clausen, S.; Bak, J. *J. Quant. Spectrosc. Radiat. Transfer* **1999**, *61*, 131–141.
(14) Bak, J.; Clausen, S. *Meas. Sci. Technol.* **2002**, *13*, 150–156.
(15) Allison, S. W.; Gillies, G. T. *Rev. Sci. Instrum.* **1997**, *68* (7), 2615–2650.
(16) Allison, S. W.; Cates, R. M.; Noel, W. B.; Gillies, G. T. *IEEE Trans. Meas.* **1988**, *37* (4), 637–641.
(17) Omrane, A.; Juhlin, G.; Aldén, M.; Josefsson, G.; Engström, J.; Benham, T. The Society of Automotive Engineers World Congress, Session: CI and SI Power Cylinder Systems (Parts 1 and 2), Detroit, MI, 2004; paper 2004-01-0609.
(18) Alaruri, S.; Bonsett, T.; Brewington, A.; McPheeters, E.; Wilson, M. *Opt. Lasers Eng.* **1999**, *31*, 345–351.
(19) van der Wal, R. L.; Householder, P. A.; Wright, T. W. *Appl. Spectrosc.* **1999**, *53* (10), 1251–1258.
(20) Omrane, A.; Ossler, F.; Aldén, M. *Exp. Therm. Fluid Sci.* **2004**, *28*, 669–676.
(21) Omrane, A.; Ossler, F.; Aldén, M.; Svenson, J.; Pettersson, J. B. C. *Fire Mater.* **2005**, *29*, 39–51.
(22) Svenson, J.; Pettersson, J. B. C.; Omrane, A.; Ossler, F.; Aldén, M.; Bellais, M.; Lilliedahl, T.; Sjöström, K. Proceedings of the science in thermal and chemical biomass conversion conference, Victoria, British Columbia, Canada, 2004.

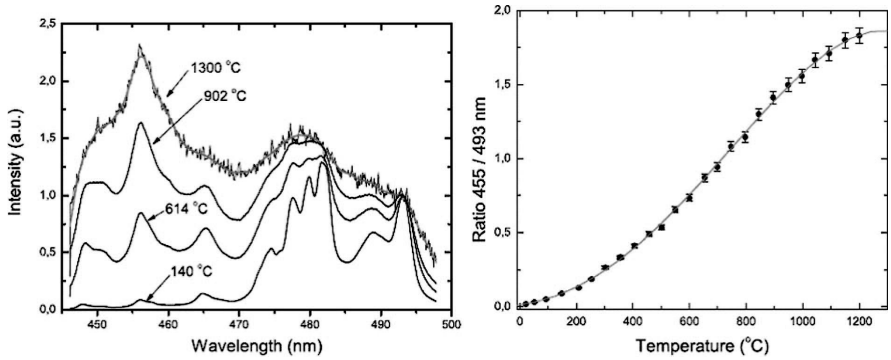

Figure 2. YAG:Dy spectra at different temperatures. When the temperature increases, the ratio from 455 to 493 nm increases. This figure was reproduced with permission from Omrane.[23]

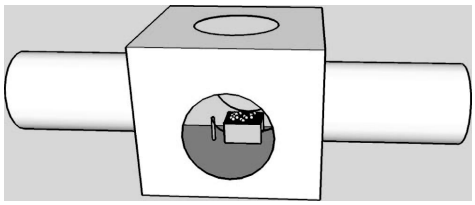

Figure 3. Schematic picture of the heated-grid reactor.

temperature can be derived from taking the ratio of the emission at two different wavelengths, in this case, 455 and 493 nm.

The precision of the first method, i.e., the lifetime technique, is 1−5 K, whereas for the second method, i.e., the ratio technique, it is 5−10 K. Both methods are able to give 2D or even 3D images and avoid interferences from laser scattering and broadband (nanosecond) fluorescence. The second method has the advantage of less interference with blackbody emission and is therefore applied for this research, because its accuracy is sufficiently high. Another benefit of the ratio technique is that it is insensitive to fluctuations in the laser profile over the surface that is studied, because two images are overlaid, so that any fluctuations are always corrected.

4. Experimental Section

4.1. Heated-Grid Reactor. Figure 3 shows a picture of the heated grid reactor. This consists of an optically accessible reactor cell, which contains a heated grid with dimensions of 1.6 × 1 cm. Optical windows made of fused silica are located on the top and both sides of the reactor, so that the process can be investigated with an intensified CCD camera. The grid can be heated quickly by electrodes on both sides of the grid. To power the grid, a control box was designed and built in-house, containing three main components: a Delta power source, a mini PC, and a Keithley data acquisition module. The Delta power source is a type S 6-40, with a voltage range of 0−6 V and a current range of 0−40 A. To read the thermocouple that is fixed to the grid, a Keithley module is used. The KUSB_3108 has cold junction compensation (CJC) and a reading rate of 50 kHz. Finally, a mini-PC is built into the box of the power source. The task of the mini-PC, which uses Labview software, is to control the Delta power source; the control loop needs to be very quick to ensure that the grid reaches the desired temperature quickly enough without excessive overshoot. The electric energy required to maintain a certain grid temperature (below 700 °C) was found to increase linearly with temperature, as shown in Figure 4, which agrees with observations of Freihaut and Proscia.[5] This is as expected when heat loss mechanisms have insufficient time to start their exchange.

The grid consists of AISI 316 L stainless steel. Three different mesh sizes have been used, which are referred to as extra fine, fine, and coarse (see Table 1 for the respective wire diameters and apertures). For some experiments, the grid was coated with a thin layer (3 ± 1 μm) of ceramic AlCrN coating (available from Oerlikon Balzers Benelux NV). The purpose of this coating is to avoid direct contact of the solid sample with the Cr- and Ni-containing metal, so that possible catalytic effects are avoided.

The temperature of the grid is measured by a thermocouple, existing of two un-insulated wires of a different material, welded to the grid. In the temperature range of 400−1000 K, which is of interest for pyrolysis of biomass and coal, a K-type thermocouple is frequently applied. This type has a steady, linear relation between the thermal electromotive forces and the temperature.[22]

4.2. Chemiluminescence Experiments. These experiments were carried out in the presence of biomass on the heated grid. For this purpose, two side windows of the reactor cell were replaced with sapphire plates to enable the transmission of infrared light from hot volatile gases. An infrared camera used in this experiment was a 256 × 256 pixel InSb camera (Santa Barbara Focal Plane, SBF LP134), with a spectral response cover 1.2−5.5 μm. When the biomass was pyrolyzed, the emitted hot volatile gas plumes were recorded horizontally by the infrared camera through the sapphire window at a frame rate of 50 Hz (maximum is 200 Hz). To avoid the interference from the strong blackbody radiation from the hot heating wires, a black screen was used to block the heating wire in the vision of the infrared camera.

All experiments were performed with pinewood in pulverized form and sieved to a particle diameter range of 0.1−0.2 mm. The amount of wood placed on the grid varied from 3 to 6 mg. After carefully weighing the biomass and placing it on the grid (an extra fine grid was used), the reaction chamber was flushed with nitrogen to create an inert atmosphere. This was performed carefully to avoid blowing the biomass from the grid. After each experiment, the grid is replaced, because it is very difficult to remove residual char. In the experiments, the temperatures were varied from 500 to 700 °C, the heating rates were varied from 300 to 600 °C/s, and the holding time was varied from 7 to 20 s.

4.3. Thermometry Experiments. The metal wire mesh (uncoated stainless steel, coarse; coated stainless steel, coarse; and uncoated stainless steel, fine) of 1.6 × 1 cm is impregnated with a thin layer of YAG:Dy phosphore ($Y_3Al_5O_{12}$:Dy; yttrium alumini-

(23) Omrane, A. Thermometry using laser-induced emission from thermographic phosphors: Development and applications in combustion. Ph.D. Thesis, Lund University, Sweden, 2005.

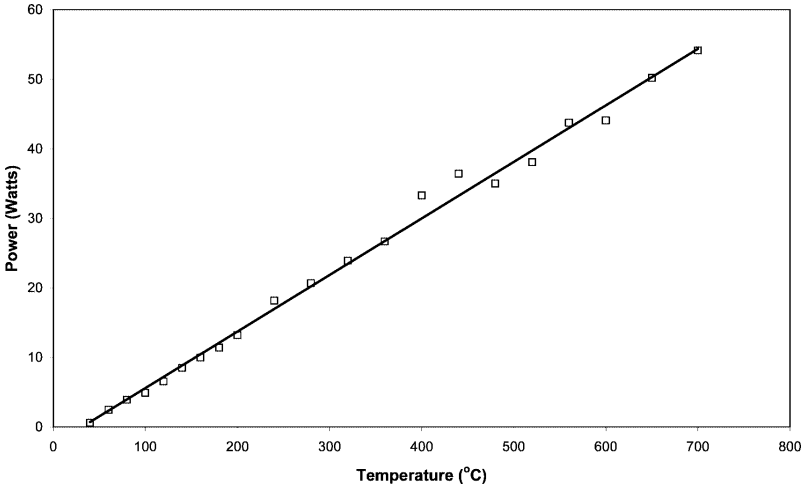

Figure 4. Electricity energy required to maintain the grid temperature; data points calculated from measured current and voltage to maintain the grid temperature.

Table 1. Dimensions of Grids Used in Experiments

	extra fine	fine	coarse
mesh	250	150	60
wire diameter (mm)	0.04	0.065	0.16
aperture (mm)	0.062	0.104	0.263
mesh width (mm)	0.102	0.169	0.423
N (number of wires/m)	9804	5917	2364

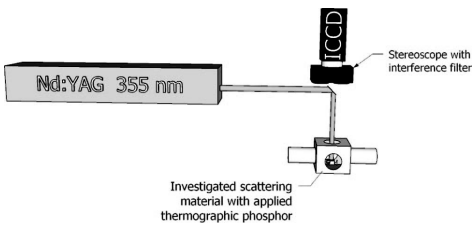

Figure 5. Experimental setup for thermometry measurements.

umoxid dysprosium) and placed between two electrodes. The experimental setup comprising the laser, optical filter, detector, stereroscope, and reactor cell is shown in Figure 5. For thermometry measurements, the top window of the reactor cell is used. Laser light from a NdYAG laser (manufactured by Quantel) is transformed by frequency doubling and tripling to a wavelength of 355 nm. Pulse energy was approximately 10 mJ/pulse. The phosphoresence signal from the thermographic phosphor on the grid was detected with a Princeton Instruments ICCD camera, with a frame rate of 10 frames per second. A gate delay of 120 ns was applied to filter away the laser. The camera was used in connection with a stereoscope and two optical filters at 455 and 493 nm. By overlaying the two pictures obtained and taking the ratio of the signals, a 2D temperature image was determined. The resolution of the ICCD is equivalent to 5 pixels per the smallest (square) element of the finest grid; the other grids had more pixels per element. White image correction was applied to ensure that measured temperatures are not influenced by the spectroscope or other optic distortions.

Prior to any measurements, the method was calibrated by measuring on a surface target, of several square centimeter, placed in an oven at thermal equilibrium. The method may also be verified with measurements of a well-calibrated IR camera.

Subsequently, the set point for the grid temperature, as measured by the thermocouple, was increased in steps of 50 °C up to a final temperature of 800 °C. At each set temperature, the time was allowed to stabilize and, subsequently, thermometry measurements were carried with the aim of determining the temperature distribution of the grid.

An alternative thermometry method was also applied. At the high end of the temperature range, the grid emits radiation in the visible range, which was recorded with a standard photo camera. By calibrating with objects at thermal equilibrium, it was possible to determine a temperature scale for the recorded images. This method was used to study the effect of replacing the wire mesh with a metal foil, to check whether the shape of the grid has any influence on its temperature distribution.

5. Results

5.1. Results of Chemiluminescence Experiments. The infrared natural emission from the volatiles produced in biomass pyrolysis was visualized, for different grid temperatures. Parts a−f of Figure 6 and parts a−f of Figure 7 show the results for a temperature set point of 500 and 800 °C, respectively. The first picture, shown in Figure 6a and, respectively, Figure 7a, was taken immediately after the current through the grid drops (because the desired thermocouple temperature was reached), and subsequent pictures shown were recorded with 0.1 s intervals. These pictures show that the biomass particles on the heated grid are pyrolyzed faster at the higher temperature and that more volatiles are formed at the higher temperature. This is in agreement with literature in this field, e.g., ref 24; devolatilization of biomass is more rapid and more complete at higher temperatures.

Although it is difficult to see properly, the chemiluminescence experiments show that the volatiles are not produced as an evenly distributed thermal plume. It is clear that the first volatiles are formed on the left side, and only later, more volatiles are formed on the right side of the grid. This effect is most

(24) Antal, M. J. Biomass pyrolysis: A review of the literature. Part II−Lignocellulose pyrolysis. In *Advances in Solar Energy*; Boer, K. W., Duffie, J. A., Eds.; American Solar Energy Society: Boulder, CO, 1985; Vol. 2, pp 175−255.

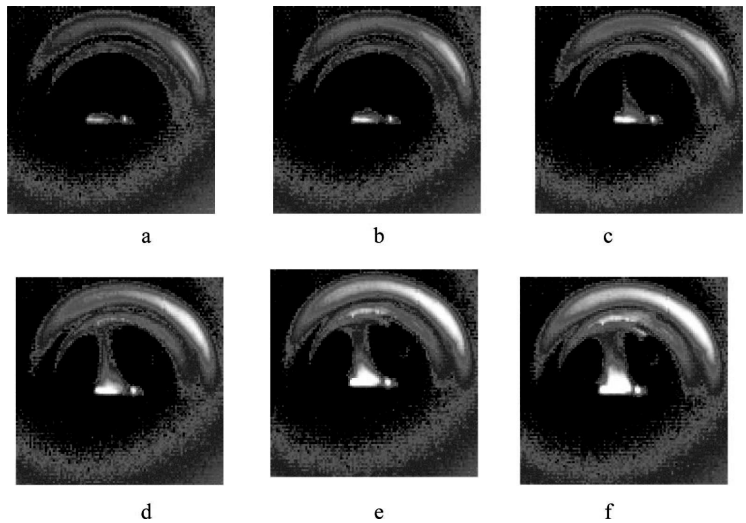

Figure 6. (a−f) Two-dimensional images of natural emission from volatiles produced by pyrolysis of biomass particles on the heated grid. Grid temperature = 500 °C; amount of biomass = 2 mg on a 1 cm^2 grid; pictures are taken with 0.1 s intervals (note: the two half circles on the pictures are reflections from the reactor wall).

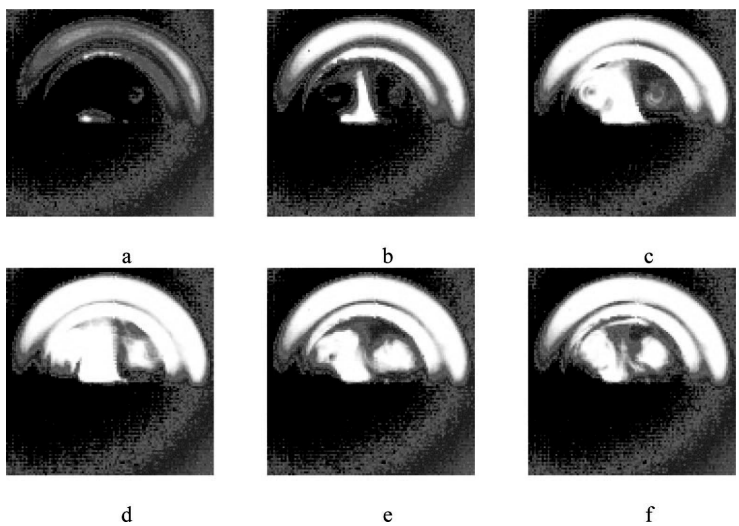

Figure 7. (a−f) Two-dimensional images of natural emission from volatiles produced by pyrolysis of biomass particles on the heated grid. Grid temperature = 800 °C; amount of biomass = 4 mg on a 1 cm^2 grid; pictures are taken with 0.1 s intervals (note: the two half circles on the pictures are reflections from the reactor wall; these are stronger compared to Figure 6 because of the higher temperature used in this measurement).

noticeable at the lower temperature in Figure 6c. At higher grid temperatures, the formation of volatiles as seen by the chemiluminescence in Figure 7 takes place more evenly.

The observed phenomena, which were unexpected, may be explained by the presence of temperature gradients on the grid. This would mean that that the temperature on the left side is higher than on the right side of the picture, especially when the grid temperature is relatively low. To confirm whether this is indeed the case, thermometry measurements were carried out, which are described in the next section.

5.2. Results of Thermometry Experiments. For all of the grids used in experiments (coarse grid, coarse grid with AlCrN coating, and fine grid), the actual temperatures as determined by laser-induced thermometry with thermographic phosphors were higher than the temperatures indicated by the thermocouple. As explained in the section on heat-transfer theory, this

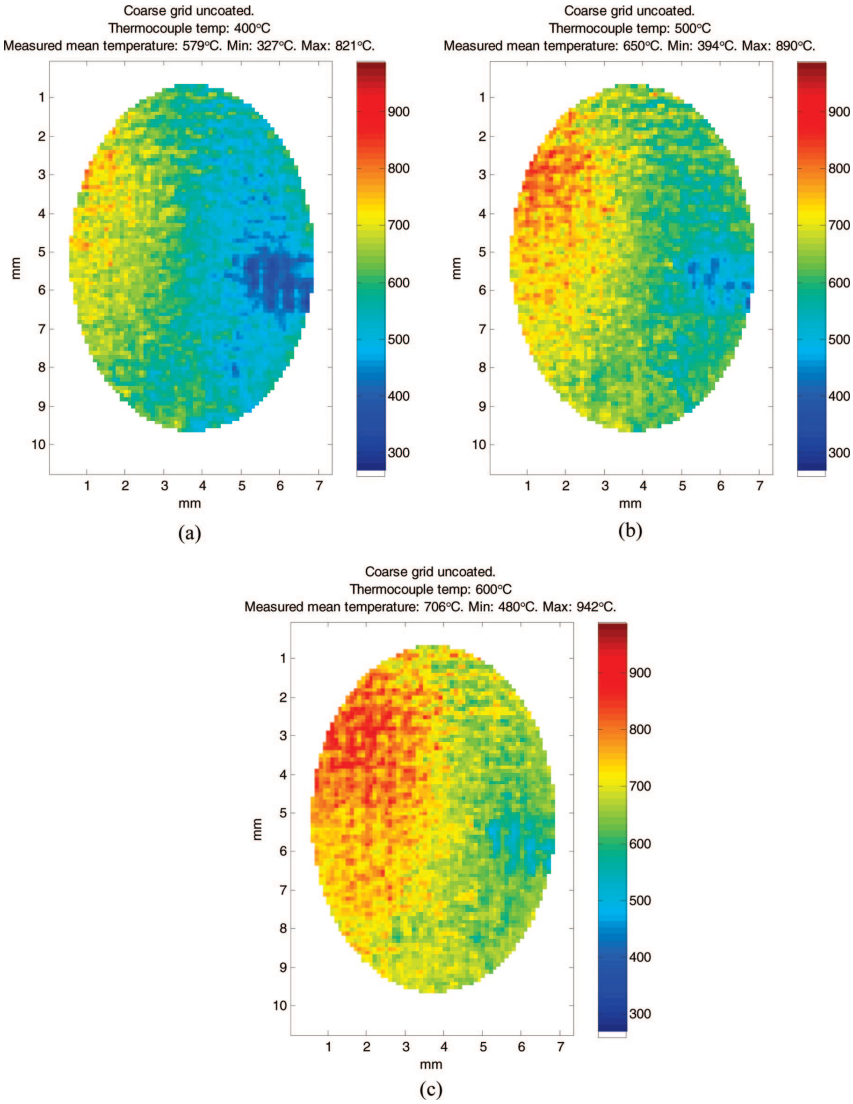

Figure 8. (a−c) Two-dimensional image of the measured temperature on the grid for thermocouple temperatures of (a) 400 °C, (b) 500 °C, and (c) 600 °C (note: the shape is oval because the edges of the grid have been omitted).

result was expected. Furthermore, parts a−c of Figure 8 confirm that the temperature on the grid has a gradient from one electrode to the other electrode. Again, this was observed for all of the different grids. The temperature distribution seemed to become more equal at higher temperatures. Nevertheless, the temperature on one side of the grid (the left-hand side in parts a−c of Figure 8) remained higher than on the other side.

The average grid temperature measured was determined, as well as the average error based on a 95% interval. This average error is caused by measurement uncertainty (which is only 1−5 K) and temperature variation on the heated grid (which gives a much larger contribution). Parts a−c of Figure 9 compare these measured temperatures with temperatures predicted by the model of Guo for two wires, i.e., eq 3. For the latter case, which is the most realistic, Table 2 shows that the relative measurement error predicted may range from 10−15% at 300 °C to 16−25% at 800 °C (the lower numbers are for the coarse grid, and the higher numbers are for the fine grid). For all grids, there is a very large measurement error at low temperatures, which happens because the thermocouple (in the middle of the oval pictures in Figure 5) is still far away from the hot zone in the left of the picture. At higher temperatures, the measurement error becomes smaller

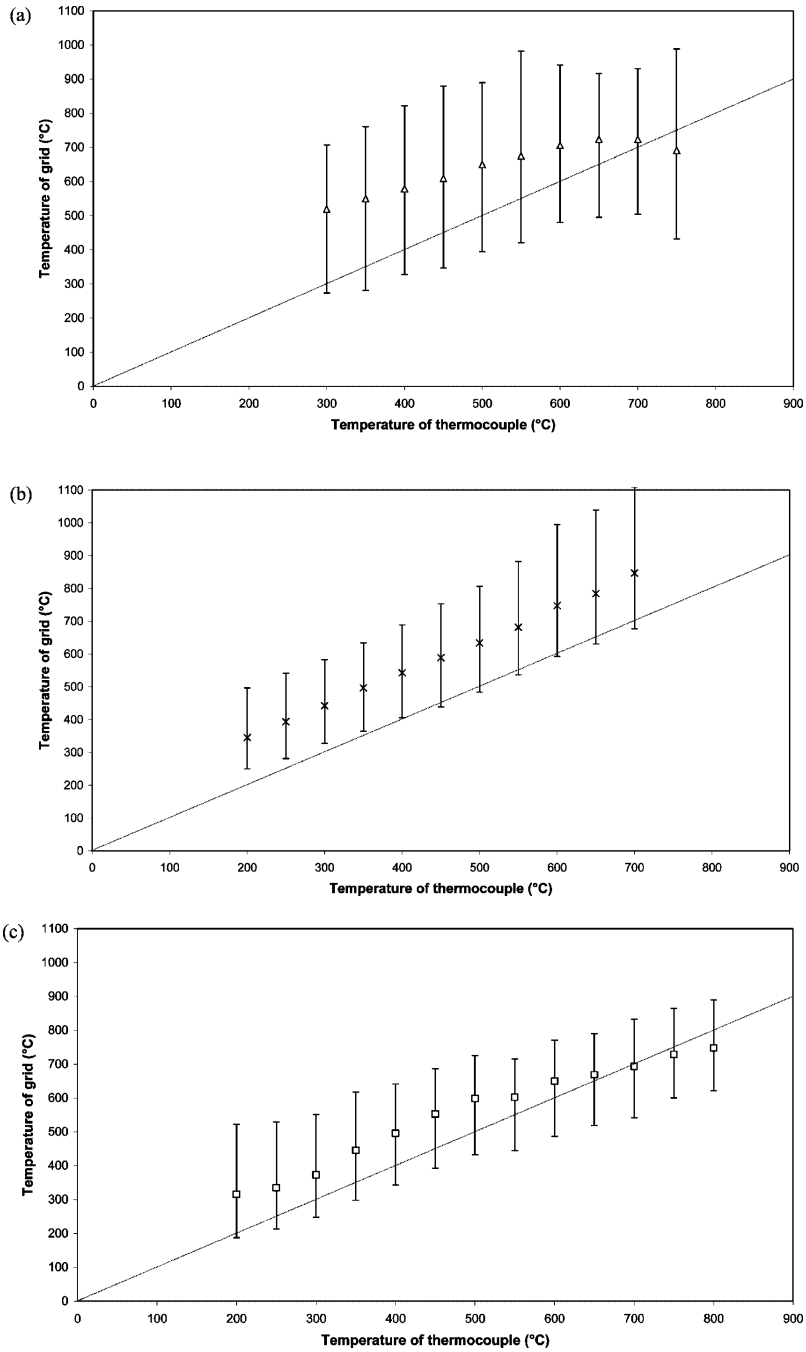

Figure 9. Continued.

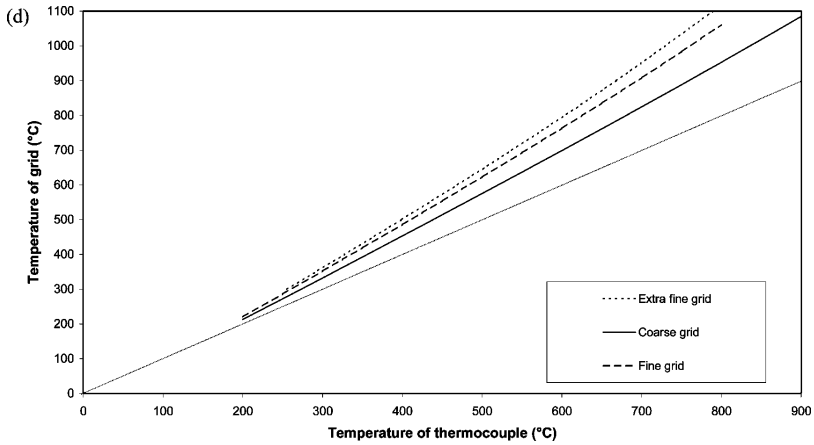

Figure 9. (a−d) Comparison of grid temperatures, experimentally measured by laser-induced thermometry and predicted by eq 3, as a function of the measured thermocouple temperature, for (a) uncoated grid, coarse; (b) coated grid, coarse; (c) uncoated grid, fine; and (d) model predictions.

Table 2. Relative Temperature Measurement Error Predicted from the Model by Guo for the Heated Grid of AISI 316L Stainless Steel

	for one wire	for two wires
Coarse Grid		
thermocouple temperature = 300 °C	0.06	0.10
thermocouple temperature = 800 °C	0.10	0.16
Fine Grid		
thermocouple temperature = 300 °C	0.10	0.15
thermocouple temperature = 800 °C	0.17	0.25

because of a more homogeneous temperature distribution; for the uncoated grids in parts a and c of Figure 9, it becomes even less than the error predicted by the model. For the coated grid in Figure 9b, the measurement error at higher temperatures appears to be more consistent with the model. However, it must be realized that the model assumes isothermal conditions, except for the area to which the thermocouple wires are welded. The situation is very different in reality, which invalidates the model.

These results could be explained in several different ways: (1) The hypothesis was formulated that not only heat but also a current may leak away through the thermocouple. This hypothesis was tested by performing a few experiments without thermocouple wires welded to the grid. However, this had little effect on the temperature distribution, which invalidated the hypothesis. (2) Second, it is possible that the emissivity coefficient of the grid rises substantially at elevated temperatures, so that radiation becomes much stronger. The benefit of increased radiation is that more electric energy is dissipated in the grid, so that the heat lost via the thermocouple plays a relatively smaller role. However, this explanation is not very likely, because most of the heat lost from the grid is a convective heat loss, even if the grid were a blackbody. Our calculations, in line with those of Guo, show that the radiative heat-transfer coefficient is at least 5 times smaller than the convective heat-transfer coefficient at temperatures around 1000 °C. Furthermore, it must be remembered that there is a layer of white thermographic phosphor present on the grid, which actually suppresses radiation (although radiative heat transfer between the wires of the grid can take place). (3) Probably, the temperature differences stem from the relatively poor thermal conductivity of the stainless-steel grid; with increasing temperatures, the temperature distribution becomes more homogeneous as the grid conducts heat better. This may explain the difference between the uncoated grid (parts a and c of Figure 9) and coated grid (Figure 9b); changes in thermal conductivity, when a ceramic coating is applied, could give rise to a change in temperature homogeneity of the grid. For the stainless-steel grids, the thermal conductivity may increase with temperature, but this effect was not taken into account in the model. For the grids that are coated with the AlCrN layer, the thermal conductivity does not seem to improve with temperature.

In fact, thermal conductivity is one of the most important parameters in the model. A better heat-conducting grid should make the grid more homogeneous in temperature and also decrease the measurement error. For platinum grids, which have a much higher conductivity (around 58 W m^{-1} K^{-1}) than stainless steel, the measurement errors predicted by the model are only 2.0−2.2% compared to 6−17% (for the dimensions of the coarse grid; error increases with temperature). Alternatively, stainless steel could be used as a foil rather than as a wired mesh; the disadvantage of a mesh is that, even when thicker wires are used, because of construction reasons also, bigger apertures must be applied. Therefore, an experiment was carried out using a nickel/chromium (Ni80/Cr20) foil with a thickness of 0.1 mm as grid material. It was carried out at a thermocouple temperature of 725 °C; the 2D temperature distribution was measured and shown in Figure 10. Note that, because the temperature measurement is based on radiation, temperatures shown below 600 °C have no physical meaning. In Figure 10a, it can be observed that a more homogeneous temperature profile can indeed be obtained. Furthermore, because of the higher thermal mass when compared to a wired mesh, the effect of a thermal leak via the thermocouple does not appear to have an effect. Heat losses from the sides of the foil do have an influence, because the temperature is highest in the middle. Finally, Figure 10b shows what happens when the foil is not fixed very tightly to the electrodes. In this case, the bottom right of the foil is loose (because a screw was not tightly fixed) and it stays relatively cold. In the future, more research is recommended using a foil, also at lower temperatures using

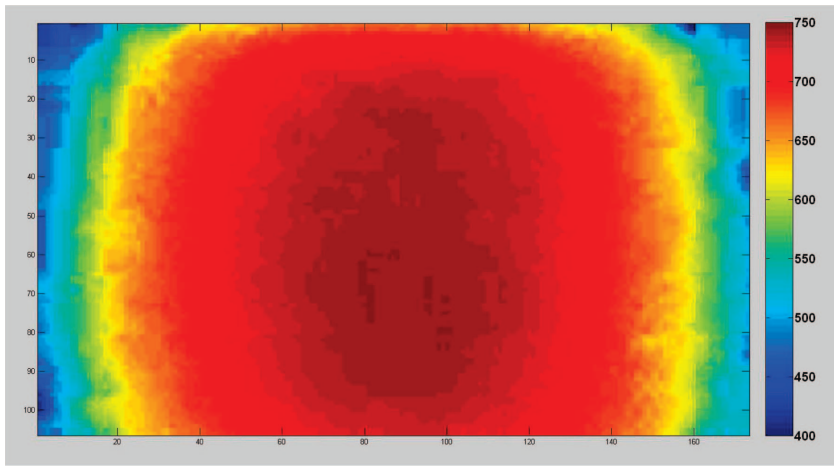

(a)

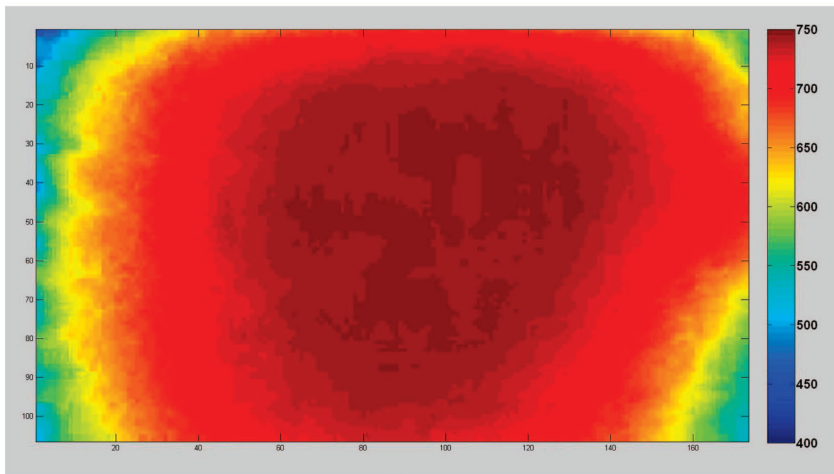

(b)

Figure 10. (a and b) Comparison of grid temperatures, experimentally measured by capturing visible emission with a standard camera, at a thermocouple temperature of 725 °C: (a) good contact between the grid and clamp holders/electrodes and (b) insufficient contact between the grid and clamp holders/electrodes.

thermographic phosphors or IR camera, with the final aim to demonstrate homogeneous devolatilization of solid fuel on the grid.

6. Conclusions and Recommendations

The natural emission from volatiles produced in biomass pyrolysis in a heated-grid reactor was visualized; this process does not take place at the same rate everywhere on the grid. It was also observed that there is a significant temperature gradient between the two electrodes on which the grid is connected.

Two-dimensional temperature images of the temperature on a heated grid were successfully recorded using the method of laser-induced thermometry with thermographic phosphors. It was found that the measured temperatures were significantly higher than temperatures indicated by a thermocouple welded to the bottom of the grid. This was in line with expectations from heat-transfer models that take the systematic measurement error, because of the presence of the thermocouple leading to disturbances of the temperature field, into account.

To improve both the measurement error and the uniformity of the temperature, it was suggested to use a material with high heat conductivity and/or in the form of a foil rather than a wire mesh. Indeed, a more homogeneous temperature profile was observed from an experiment using a Ni/Cr foil as grid material.

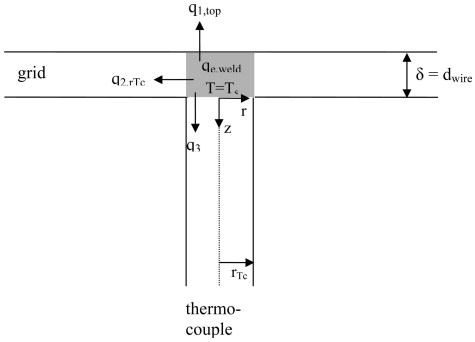

Figure A1. Geometry for a thermocouple attached on the surface of the grid.

Additional research, both in the absence and presence of biomass on the heated grid, is recommended to confirm the suitability of the heated-grid reactor for pyrolysis experiments.

Acknowledgment. Bo Li is thanked for his kind assistance with the experiments, and Dr. Alexei Sepman is thanked for providing Figure 10. We are also grateful for the financial support of CECOST (Centre for Combustion Science and Technology) and the European Union in the framework of the large-scale facility.

Appendix A: Model for Temperature Measurement Accuracy of Heated Wire Mesh

A1. Heat Balance for Thermocouple Wire Attached to a Horizontal Surface. Figure A1 shows a horizontal surface to which a vertical thermocouple wire of radius r_{Tc} is welded. An initially uniform temperature distribution, in the absence of a thermocouple, is disturbed by the application of the thermocouple to the grid acting as a heat sink. To derive the magnitude of the heat flow through this heat sink, the spot where the thermocouple wire is welded to the grid is examined separately. This welded spot is assumed to be an isothermal disk with temperature T_s and radius r_{Tc} and has the same height and material as the grid. The horizontal surface is assumed to be infinite, so that it extends along the r coordinate from r_{Tc} to infinity; likewise the thermocouple has infinite length in the z direction. The essence of the model developed by Guo[8] is a heat balance for the weld, the shaded area shown in Figure A1

$$q_{1,top} + q_3 = q_{e,weld} - q_{2,r_{Tc}} \tag{A1}$$

where $q_{1,top}$ is the heat loss from the top of the weld to the gaseous environment, $q_{2,r_{Tc}}$ is the heat conducted from the weld to the rest of the heated surface (which will usually have a negative sign because the temperature in the weld is expected to be lower than the temperature in the rest of the heated surface), q_3 is the heat conduction from the weld to the thermocouple, and $q_{e,weld}$ is the electric energy dissipation in the weld. The individual terms of this equation will now be derived.

Heat Loss from the Weld to the Gaseous Environment. This term can be expressed by

$$q_{1,top} = \pi {r_{Tc}}^2 h_{grid}(T_s - T_a) \tag{A2}$$

where h_{grid} is the combined radiative and convective heat-transfer coefficient from the grid to the gaseous environment, T_s is the uniform temperature of the weld, thus, the temperature actually measured by the thermocouple, and T_a is the temperature of the ambient gas.

Heat Loss from the Weld to the Rest of the Heated Surface. This term may be derived by setting up a heat balance, similar to eq A1, for a shell of the horizontal surface, between r and $r + dr$

$$q_{1,top} + q_{1,bottom} = q_e + q_{2,r} - q_{2,r+dr} \tag{A3}$$

where $q_{1,bottom}$ is the heat loss from the bottom of the heated wire to the gaseous environment. On both the top and the bottom of the grid, the heat flow to the environment is supposed to be equal to each other, assuming the ambient gas has the same conditions on both sides of the grid. This leads to

$$q_{1,top} = q_{1,bottom} = 2\pi r dr h_{grid}(T - T_a) \tag{A4}$$

The heat produced by dissipation of electric energy in the shell of the surface can be expressed as

$$q_e = 2\pi r dr \delta S_e \tag{A5}$$

The term S_e is the electrical heat input per unit of volume.

The net heat flow is described by

$$\begin{aligned} q_{2,r} - q_{2,r+dr} &= -2\pi r \delta k_{grid}\left(\frac{dT_r}{dr} - \frac{dT_{r+dr}}{dr}\right) \\ &= 2\pi r \delta k_{grid}\left(\frac{d^2T}{dr^2}dr + \frac{1}{r}\frac{dT}{dr}dr\right) \end{aligned} \tag{A6}$$

where k_{grid} is the effective thermal conductivity of the grid material, which is assumed to be constant, and a Taylor series expansion was applied as in Hill and Dewynne.[12]

Filling the terms of eqs A4−A6 into eq A3 leads to

$$4\pi r dr h_{grid}(T - T_a) = 2\pi r dr \delta S_e + 2\pi r \delta k_{grid}\left(\frac{d^2T}{dr^2}dr + \frac{1}{r}\frac{dT}{dr}dr\right) \tag{A7}$$

which can be rewritten to

$$r^2\frac{d^2T}{dr^2} + r\frac{dT}{dr} - r^2\frac{2h_{grid}}{\delta k_{grid}}(T - T_a) + r^2\frac{S_e}{k_{grid}} = 0 \tag{A8}$$

This differential equation describes the temperature distribution within the horizontal surface. The following boundary conditions apply

$$T = T_s \quad \text{at} \quad r = r_{Tc} \tag{A9}$$

$$T \to T_\infty \quad \text{at} \quad r \to \infty \tag{A10}$$

To solve eq A8, two new variables are introduced

$$T' = T - T_a \tag{A11}$$

$$r'^2 = r^2\frac{2h_{grid}}{\delta k_{grid}} \tag{A12}$$

which leads to

$$r'^2\frac{d^2T'}{dr'^2} + r'\frac{dT'}{dr'} - r'^2T' = -r'^2\frac{S_e\delta}{2h_{grid}} \tag{A13}$$

with the boundary conditions

$$T' = T_s - T_a \quad \text{at} \quad r' = r'_{Tc} = \sqrt{{r_{Tc}}^2\frac{2h_{grid}}{\delta k_{grid}}} \tag{A14}$$

$$T' \to T_\infty - T_a \quad \text{at} \quad r' \to \infty \tag{A15}$$

The equation can be recognized as a form of Bessel's zero-order equation.[25] The general solution of this function, related to this problem, can be written as

$$T'(r') = C_1 I_0(r') + C_2 K_0(r') + \frac{S_e \delta}{2h_{grid}} \quad \text{(A16)}$$

I_0 and K_0, are the modified Bessel functions of the first and second kind, respectively. I_0 increases to infinity with an increasing r', while K_0 is gradually decreasing to zero. Therefore, I_0 has to be discarded, and C_1 becomes zero.

Subsequently, filling in the boundary condition of eq A15 leads to

$$T'(\infty) = C_2 K_0(\infty) + \frac{S_e \delta}{2h_{grid}} = \frac{S_e \delta}{2h_{grid}} \quad \text{(A17)}$$

The boundary condition of eq A14 gives

$$T'(r'_{Tc}) = C_2 K_0(r'_{Tc}) + \frac{S_e \delta}{2h_{grid}} \quad \text{(A18)}$$

Combining the above equations gives the constant C_2

$$C_2 = \frac{1}{K_0(r'_{Tc})}\left(T'(r'_{Tc}) - \frac{S_e \delta}{2h_{grid}}\right) = \frac{1}{K_0(r'_{Tc})}(T'(r'_{Tc}) - T'(\infty)) \quad \text{(A19)}$$

so that eq A16 becomes

$$T'(r') = \frac{K_0(r')}{K_0(r'_{Tc})}(T'(r'_{Tc}) - T'(\infty)) + T'(\infty) \quad \text{(A20)}$$

Now that the temperature distribution of the heated surface is known, $q_{2,r_{Tc}}$, i.e., the heat conducted from the weld to the rest of the heated surface, may finally be calculated

$$q_{2,r_{Tc}} = -2\pi r_{Tc} \delta k_{grid} \frac{dT}{dr}\bigg| r = r_{Tc} \quad \text{(A21)}$$

$$q_{2,r_{Tc}} = -2\pi r_{Tc} \delta k_{grid} \left(\sqrt{\frac{2h_{grid}}{\delta k_{grid}}}\right) \frac{dT'}{dr'}\bigg| r = r_{Tc} \quad \text{(A22)}$$

To evaluate this expression, the recurrence relation $K_0'(x) = -K_1(x)$ is used

$$q_{2,r_{Tc}} = 2\pi r_{Tc} \delta k_{grid} \left(\sqrt{\frac{2h_{grid}}{\delta k_{grid}}}\right) \frac{K_1(r'_{Tc})}{K_0(r'_{Tc})}(T'(r'_{Tc}) - T'(\infty)) \quad \text{(A23)}$$

$$q_{2,r_{Tc}} = 2\pi r_{Tc} \delta k_{grid} \left(\sqrt{\frac{2h_{grid}}{\delta k_{grid}}}\right) \frac{K_1(r'_{Tc})}{K_0(r'_{Tc})}(T_s - T_\infty) \quad \text{(A24)}$$

Heat Loss from the Weld to the Thermocouple. This heat conduction term may be derived from a cooling fin analysis. Let z represent the length coordinate of the thermocouple wire. The heat flow rate is described by

$$q_3 = -\pi r_{Tc}^2 k_{Tc} \left(\frac{dT_{Tc}}{dz}\right)\bigg| z = 0 \quad \text{(A25)}$$

In this equation, k_{Tc} is the thermal conductivity of the thermocouple wire.

An expression needs to be derived for the distribution of T_{Tc}, the temperature of the thermocouple, in the z direction. If the distance z is increased, the temperature drops because of the heat loss from the thermocouple wire to the environment. The rate of heat loss is a function of the surface area of the thermocouple, depending upon the radius and the length, and the heat-transfer coefficient between the thermocouple and the environment (h_{Tc})

$$\frac{dq_3}{dz} = -2\pi r_{Tc} h_{Tc}(T_{Tc} - T_a) \quad \text{(A26)}$$

in which T_a is the temperature of the ambient gas. Introducing the Fourier law into the above equation gives the following differential equation:

$$-\pi r_{Tc}^2 k_{Tc}\left(\frac{d^2 T_{Tc}}{dz^2}\right) = -2\pi r_{Tc} h_{Tc}(T_{Tc} - T_a) \quad \text{(A27)}$$

Introducing a relative temperature (T'_{Tc}) simplifies the differential equation to

$$\left(\frac{d^2 T'_{Tc}}{dz^2}\right) - m^2 T'_{Tc} = 0 \quad \text{(A28)}$$

where

$$T'_{Tc}(z) = T_{Tc}(z) - T_a \quad \text{and} \quad m^2 = \frac{2h_{Tc}}{k_{Tc} r_{Tc}}$$

The following boundary conditions apply: at z equals zero, the temperature is equal to the temperature of the weld (T_s), and if the thermocouple wire is infinitely long, the temperature at the end of the wire will be equal to the temperature of the ambient gas

$$T'_{Tc} = T'_s = T_s - T_a \quad \text{at} \quad z = 0 \quad \text{(A29)}$$

$$T'_{Tc} \to 0 \quad \text{at} \quad z \to \infty \quad \text{(A30)}$$

The most general solution can be derived as

$$T'_{Tc}(z) = C_1 \exp(-mz) + C_2 \exp(mz) \quad \text{(A31)}$$

According to the second boundary condition, the relative temperature tends to go to zero if z is increased; thus, this cancels out the second term, leaving only the first term. When the first boundary condition is also applied, the solution becomes

$$T'_{Tc}(z) = T'_s \exp(-mz) \quad \text{(A32)}$$

If this solution is inserted into eq A25, the heat flow rate (q_3) can finally be derived

$$q_3 = -\pi r_{Tc}^2 k_{Tc}\left(\frac{dT_{Tc}}{dz}\right) = \pi r_{Tc}^2 k_{Tc} \sqrt{\frac{2h_{Tc}}{k_{Tc} r_{Tc}}}$$

$$T'_s = \pi r_{Tc}^2 k_{Tc} \sqrt{\frac{2h_{Tc}}{k_{Tc} r_{Tc}}}(T_s - T_a) \quad \text{(A33)}$$

Dissipation of Electric Energy to Heat in the Weld. The electrical heat production in the volume of the weld is calculated as follows:

$$q_{e,weld} = A_s \delta S_e \quad \text{(A34)}$$

Because the temperature of the heated surface for $r \to \infty$ equals

$$T_\infty - T_a = \frac{S_e \delta}{2h_{grid}}$$

It is becomes possible to express S_e and substitute it into eq A34

$$q_{e,weld} = A_s \delta S_e = \pi r_{Tc}^2 2h_{grid}(T_\infty - T_a) \quad \text{(A35)}$$

Now, having all of the terms of the heat balance of this problem derived, these terms can be combined in the heat balance (eq A1)

(25) Michalski, L.; Eckersdorf, K.; Kucharski, J. *Temperature Measurement*, 2nd ed.; Wiley: New York, 2000.

(26) See http://www.lenntech.com/Stainless-steel-316L.htm (accessed on Oct 30, 2007).

(27) Ho, C. Y.; Powell, R. W.; Liley, P. E. *J. Phys. Chem. Ref. Data* **1972**, *1* (2), 279–422. [see http://www.nist.gov/srd/reprints.htm (accessed on Oct 30, 2007)].

$$\pi r_{Tc}{}^2 h_{grid}(T_s - T_a) + \pi r_{Tc}{}^2 k_{Tc}\sqrt{\frac{2h_{Tc}}{k_{Tc}r_{Tc}}}(T_s - T_a) = \pi r_{Tc}{}^2 2h_{grid}(T_\infty - T_a) - 2\pi r_{Tc}\delta k_{grid}\left(\sqrt{\frac{2h_{grid}}{\delta k_{grid}}}\right)\frac{K_1(r'_{Tc})}{K_0(r'_{Tc})}(T_s - T_\infty) \quad \text{(A36)}$$

This equation has been written by Guo as

$$\frac{(T_s - T_a)}{(T_s - T_\infty)} = \frac{-\sqrt{\frac{8h_{grid}\delta k_{grid}}{r_{Tc}{}^2}}\frac{K_1\pi(r'_{Tc})}{K_0(r'_{Tc})} - 2h_{grid}\frac{(T_a - T_\infty)}{(T_s - T_\infty)}}{h_{grid} + \sqrt{\frac{2h_{Tc}k_{Tc}}{r_{Tc}}}} \quad \text{(A37)}$$

It is also possible to derive an explicit expression for the temperature in the weld, i.e., the temperature measured by the thermocouple

$$T_s\left(h_{grid} + \sqrt{\frac{2h_{Tc}k_{Tc}}{r_{Tc}}} + \sqrt{\frac{8h_{grid}\delta k_{grid}}{r_{Tc}{}^2}}\frac{K_1(r'_{Tc})}{K_0(r'_{Tc})}\right) = T_a\left(\sqrt{\frac{2h_{Tc}k_{Tc}}{r_{Tc}}} - h_{grid}\right) + T_\infty\left(2h_{grid} + \sqrt{\frac{8h_{grid}\delta k_{grid}}{r_{Tc}{}^2}}\frac{K_1(r'_{Tc})}{K_0(r'_{Tc})}\right) \quad \text{(A38)}$$

In the theoretical situation that h_{grid} goes to zero, the equation above shows that the temperature in the weld T_s will equal the temperature of the surrounding gas T_a. If there were no heat loss from the horizontal surface, there would be no dissipation of electric energy and the entire surface would be isothermal. On the other hand, if h_{grid} is very large, it might be that the temperature in the weld actually becomes higher than in the rest of the grid. This happens because the heat, which may be removed by conduction via the cross-sectional area onto which the thermocouple is welded, is less than what may be removed by radiation and convection from the same area. However, for realistic values of h_{grid}, this is not the case and the thermocouple will act as heat sink. The value of h_{grid} will be discussed further in the next section.

A2. Thermal Properties of the Grid. In the derivation of eq A37, it was assumed that there is a horizontal surface, which has a heat-transfer coefficient h_{grid} (comprising convection as well as radiation) between said surface and the gaseous environment. However, the real situation is different; the surface is a heated wire mesh, also known as a heated grid. To evaluate the thermal properties of the grid, it must be realized that it is not a homogeneous body (i.e., a plate) but consists of individual wires, which are woven together, as shown in Figure A2. This difference affects the heat conduction coefficient, the heat-transfer coefficients, and the effective surface area, so that it must be corrected.

Heat Conduction through the Grid. Because the conduction coefficient is directly linked to the cross-section surface, the model can be corrected by multiplying the conduction coefficient with a correction factor A_{eff}

$$k_{grid} = A_{eff}k_{wire} \quad \text{(A39)}$$

In this equation, k_{wire} is the thermal conductivity of the wire material. The correction is achieved by summing up the cross-section areas of all of the wires of the grid and dividing it by the cross-section area of the plate

$$A_{eff} = \frac{N_{grid}L\frac{\pi}{4}d_{wire}{}^2}{Ld_{wire}} = N_{grid}\frac{\pi}{4}d_{wire} \quad \text{(A40)}$$

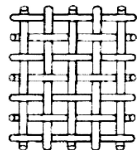

Figure A2. Geometry of a grid consisting of woven wires.

where L represents the length of the plate and d_{wire} represents the diameter of the individual grid wires (which equals the thickness δ of the plate). N_{grid} is the number of wires per meter, with a value of

$$N_{grid} = \frac{1}{d_{wire} + d_{ap}} \quad \text{(A41)}$$

where d_{ap} is the aperture width. The sum of the aperture width and the wire diameter equals the mesh width.

The thermal conductivity of the grid material AISI 316 L is reported as 16.2 W m^{-1} K^{-1} at 100 °C and 21.4 W m^{-1} K^{-1} at 500 °C.[26] However, it may not rise further with temperature, because the bulk consists of iron, for which the thermal conductivity actually decreases with temperature.[27] Therefore, the thermal conductivity was taken to be constant at 20 W m^{-1} K^{-1}.

Convective Heat Transfer. The convective heat transfer from the grid to the ambient is

$$Q_{grid,c} = S_{eff}h_{wire,c}(T_{grid} - T_a) \quad \text{(A42)}$$

In which S_{eff} is the effective surface, which is given for a grid with length L, width W, and thickness of d_{wire} by

$$S_{eff} = \pi d_{wire}LWN_{grid} + \pi d_{wire}WLN_{grid} - LWN_{grid}{}^2 d_{wire}{}^2 \quad \text{(A43)}$$

The last term in this equation represents the overlap between the wires and may be neglected if the wires are far apart from each other.

The derivation of the surface averaged convective heat-transfer coefficient, $h_{wire,c}$, can be performed using the average Nusselt number, which represents the ratio of the actual heat transferred from the surface of the cylinder to the ambient gas and the occurrence of heat conduction through the ambient gas. The average Nusselt number can be defined by

$$\overline{Nu}_D = \frac{h_{wire,c}d_{wire}}{k_a} \quad \text{(A44)}$$

where k_a is the heat conduction coefficient of the ambient gas. If the Nusselt number is known and the temperature, pressure, and composition of the ambient gas are given, the heat-transfer coefficient can be calculated. In the current experiment, the ambient gas is nitrogen, kept at a pressure of about 1 atm, and the temperature is assumed to be around 300 K. The Nusselt number, applied to a horizontal cylinder, can be calculated using this information of the ambient gas for natural convection. For this case, an empirical formula is used,[25] requiring the Rayleigh and Prandtl numbers

$$\overline{Nu}_D = \left\{0.60 + \frac{0.387Ra_D{}^{1/6}}{\left[1 + \left(\frac{0.559}{Pr}\right)^{9/16}\right]^{8/27}}\right\}^2 \quad \text{(A45)}$$

Both the Rayleigh and Prandtl numbers depend upon the properties of the surrounding gas. The Rayleigh number is a combination of the Prandtl and Grashof numbers and can be written as

$$\mathrm{Ra_D} = \mathrm{PrGr_D} = \mathrm{Pr}\frac{g\beta(t - t_a)D^3}{\nu^2} \quad \text{(A46)}$$

where β is the coefficient of linear expansion, which is estimated to be $1/t_a$,[28] ν is the kinematic viscosity, and g is the gravitational acceleration. The calculation of the averaged Nusselt number is valid for values of $\mathrm{Ra_D}$ between 10^{-5} and 10^{12}.

The Rayleigh number is also used for calculating the heat-transfer coefficients of the thermocouple wires to the environment. The averaged Nusselt number applied to vertical cylinders[28] can be calculated from

$$\overline{\mathrm{Nu}}_\mathrm{D} = 0.93\left(\mathrm{Ra_D}\frac{D}{L}\right)^{0.05} \quad \text{(A47)}$$

which is valid for $\mathrm{Ra_D}(D/L) \leq 0.05$, a condition which is easily satisfied for a typical thermocouple diameter D of 0.1−0.2 mm and length L of around 30 mm.

Radiative Heat Transfer. The radiant heat transferred from the grid to the ambient is given by[29]

$$Q_{\mathrm{grid,c}} = S_{\mathrm{eff}} h_{\mathrm{wire,r}} (T_{\mathrm{grid}}{}^4 - T_\infty{}^4) \quad \text{(A48)}$$

If we wish to write this equation in the same form as eq A43, the radiation heat-transfer coefficient can be expressed in the following way:[27]

$$h_{\mathrm{wire,r}} = \frac{\varepsilon\sigma(T_{\mathrm{grid}}{}^4 - T_a{}^4)}{(T_{\mathrm{grid}} - T_a)} \quad \text{(A49)}$$

where ε is the emissivity coefficient of the materials of the wires, representing a fraction of the blackbody radiation and σ is the Stefan−Boltzmann constant (=5.6704 × 10^{-8} W m^{-2} K^{-4}). The emissivity coefficient of the grid material (AISI316 L stainless steel) may vary but was estimated at 0.2.

A3. Thermal Properties of the Thermocouple. For a K-type thermocouple, the wires are made of nickel−chrome or nickel−aluminum, also called chromel and alumel. To obtain a less complicated calculation, only the heat conductivity of chromel is considered

$$k_{\mathrm{Tc}} = 0.0191T + 53.22 \quad \text{(A50)}$$

The same approach is followed for the radiant heat transferred from the thermocouple to ambient. The emissivity of a chromel thermocouple wire can be described by[30]

$$\varepsilon_{\mathrm{Tc}} = 0.0001T + 0.0595 \quad \text{(A51)}$$

EF800419W

(28) Janna, W. S. *Engineering Heat Transfer*, 2nd ed.; Van Nostrand Reinhold: London, U.K., 2000.

(29) Eckert, E.; Goldstein, R. *Measurements in Heat Transfer*, 2nd ed.; Hemisphere Publishing: New York, 1976.

(30) Sasaki, S.; Masuda, H.; Higano, M.; Hishinuma, N. *Int. J. Thermophys.* **1994**, *15* (3), 547–565.

Paper II

Appl Phys B (2009) 96: 237–240
DOI 10.1007/s00340-009-3608-7

Applied Physics B
Lasers and Optics

RAPID COMMUNICATION

Investigation of potential laser-induced heating effects when using thermographic phosphors for gas-phase thermometry

J. Lindén · N. Takada · B. Johansson · M. Richter · M. Aldén

Received: 16 March 2009 / Revised version: 25 May 2009 / Published online: 18 June 2009

Abstract The spectral emission from thermographic phosphors in free flow and its dependence of laser energy per cross section area (laser fluence [J/cm^2]) has been investigated. Temperature measurements in gaseous flows using thermographic phosphors require higher laser energy than measurements performed on surfaces, due to lower particle density. A troublesome systematic error associated with high fluences would be introduced if the excitation laser heats the particles. In the presented work, three different types of the thermographic phosphor $BaMg_2Al_{10}O_{17}$:Eu (BAM) are investigated. Spectra of the phosphorescence are achieved for a range of laser fluences. The results show no indications of the laser heating the particles, making further development of phosphor thermography in free-flow applications feasible.

PACS 79.20.Ds · 32.50.+d · 07.20.Dt

J. Lindén (✉) · M. Richter · M. Aldén
Division of Combustion Physics, Lund Institute of Technology,
P.O. Box 118, 221 00 Lund, Sweden
e-mail: johannes.linden@forbrf.lth.se
Fax: +46-46-222-45-42

M. Richter
e-mail: mattias.richter@forbrf.lth.se
Fax: +46-46-222-45-42

M. Aldén
e-mail: marcus.alden@forbrf.lth.se
Fax: +46-46-222-45-42

N. Takada
Advanced Power Train Engineering Div.1, R&D Group 2,
Toyota Motor Corporation, 1200 Misyuku, Susono,
Shizuoka 410-1193, Japan
e-mail: noriyuki@takada.tec.toyota.co.jp
Fax: +81-55-997-7877

B. Johansson
Division of Combustion Engines, Lund Institute of Technology,
P.O. Box 118, 221 00 Lund, Sweden
e-mail: Bengt.Johansson@energy.lth.se
Fax: +46-46-222-47-17

1 Introduction

Thermographic phosphors (TP) are ceramic crystal substances, often in the form of a fine powder. Usually they are doped with some kind of rear earth metal, which gives them specific phosphorescence properties. These phosphorescence properties are sometimes temperature dependent, which makes TP useable in temperature measurement applications. The use of TP is well established for measuring temperature on surfaces [1–5]. By applying laser-induced phosphorescence (LIP), temperature can be monitored by registering the change in phosphorescence lifetime or the change in spectral profile. Both point- and two-dimensional measurements are possible. The point measurement approach usually utilizes the temperature dependence of the phosphorescence signal lifetime to retrieve temperature information [6]. By using a high-speed framing camera it is also possible to do 2D measurements using this property [7]. Exploration of the temperature dependence of the spectral profile makes it possible, with the use of suitable optical filters, to do 2D temperature measurements on a surface either through the use of two separate detectors or a single detector equipped with an image doubling device (stereoscope) [8]. With a suitable choice of phosphor material, measurements can be carried out at temperatures from cryogenic to 2000 K. Due to interference with background Planck radiation at higher temperature, phosphors with emission in the blue

spectral region are preferable in order to increase the signal-to-noise ratio. In addition, short lifetime of the phosphorescence gains the possibility to time gate for background discrimination [9].

Lately, attempts have been made to seed TP in gaseous flows in order to investigate the feasibility of temperature measurements in gas volumes [10]. Having access to such a technique with its 2D capability is highly desirable, e.g., in combustion engine research. In gas-phase LIP measurements a laser beam is preferably formed into a laser sheet in order to establish spatial resolution in the depth dimension. A higher laser fluence compared to what is applied for surface thermometry is necessary in order to achieve a sufficient signal from the relatively diluted particle flow. In a typical engine application, a laser sheet could be about 20-mm high and 0.5-mm thick. This limits the laser pulse energy to a maximum in the region of 100 mJ due to the risk of damaging optical components. These numbers result in an upper limit for the fluence of 1.3 J/cm^2 in such practical applications. When reaching high laser fluences, an obvious, but still highly relevant, question is whether the laser itself is heating the particles or not. For example, laser-induced incandescence, LII, a standard technique for soot diagnostics, is based on laser heating of particles. If such heating should occur also for the phosphor particles, this would make measurements in gaseous media virtually impossible. To investigate this, an air flow at room temperature seeded with the thermographic phosphor BAM is illuminated with laser radiation, and the phosphorescence signal is recorded with a spectrometer at a range of different laser fluences.

$BaMg_2Al_{10}O_{17}$:Eu, or BAM, emits very strong phosphorescence in the blue spectral region when illuminated with laser radiation of 355 nm. This emission originates from the $4f^6 5d \rightarrow 4f^7$ transition of Eu^{2+} [11] and has its peak at about 450 nm, which broadens towards shorter wavelengths with increasing temperature, see Fig. 1 [12]. The ratio of the phosphorescence intensities, collected through a 40-nm wide (fwhm) interference filter centered at 400 nm and a 10-nm wide (fwhm) interference filter centered at 456 nm, will show a temperature dependence as shown in Fig. 2. Using these two filters, BAM is very suitable for achieving 2D temperature images of a coated surface. Because of its high signal intensity, BAM is also beneficial in free-flow applications. It is also favorable to use BAM in this kind of investigation, since it is sensitive at room temperature. The short lifetime of the phosphorescence, about 2 µs at room temperature and about 10 ns at 1100 K, also make BAM suitable for measurements with high temporal resolution, whether the measurements are done on surfaces, in free flow, or in sprays [10, 13]. With such a short lifetime it is possible to resolve sub-millimeter structures at velocities up to 300 m/s.

A criterion for LIP temperature measurements using TP is optical access, both for the exciting laser radiation and for the detection of the phosphorescence signal. However, using TP as a fine powder seeded in gaseous flow, in such an environment optical access might become troublesome due to particles sticking onto surfaces. One way to reduce this issue is to use coated phosphor particles. From the manufacturer (Phosphor Technology) it was possible to order two types of "anti-stick" coating for BAM, SiO_2 coating, and Al_2O_3 coating. Experiments where these different types of BAM were applied on surfaces show that the phosphorescence spectrum is not affected by the coating. From experience BAM coated with SiO_2 seems to stick the least. In

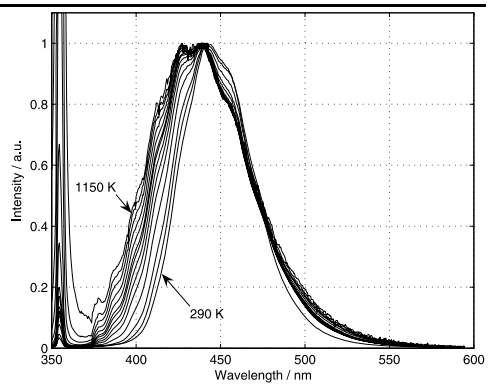

Fig. 1 BAM emission spectrum at different temperatures when excited with 355-nm laser radiation. The exposure time of the ICCD camera connected to the spectrometer was 8 µs

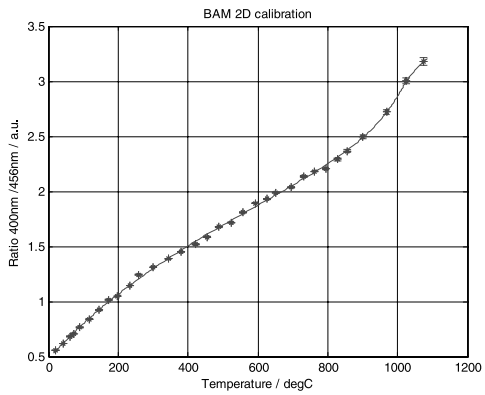

Fig. 2 Calibration of BAM for 2D measurements. The ratio of the intensities collected through the 400 ± 20-nm interference filters to that collected through the 456 ± 5 nm interference filters shows a significant temperature dependence. The filters were placed on a stereoscope connected to an ICCD camera with the exposure time of 8 µs

the free-flow experiments, all three types are investigated for possible laser-induced heating.

The mean size of the particles used in the experiments is 4.2 μm and, the density about 3.7 kg/dm^3 according to the supplier. The small size allows the particles to follow possibly turbulent flow well when the Stokes number is much smaller than 1.0, which is the case in most engine applications and under the present experiment conditions. The coating with SiO_2 and Al_2O_3 is of nanometer-scale thickness and has a negligible effect on the particle size.

Another criterion for using seeded particles in a gaseous flow to measure its temperature is that the particles establish local thermal equilibrium with the surrounding gas on a time scale comparable to the temporal temperature variations. Assuming the internal temperature distribution in the phosphor particle to be homogeneous, this relaxation time is estimated by solving the heat convection equation [14]

$$hA(T_\infty - T) = c_p \rho_p V \frac{\mathrm{d}T}{\mathrm{d}t},$$

where h is the convection heat transfer coefficient, A is the surface area of the particle, T_∞ is the gaseous temperature, T is the particle temperature, c_p is the specific heat of the particle material, ρ_p is the density of the particle, and V is the particle volume. With the initial condition that T_0 is the initial particle temperature at $t = 0$, the solution is described by

$$\frac{(T - T_0)}{(T_\infty - T_0)} = 1 - e^{-\frac{t}{\tau}},$$

where τ is the so-called time constant,

$$\tau = \frac{\rho_p c_p V}{hA}.$$

The time by which the phosphor particles establish local thermal equilibrium in gaseous flows with rapidly varying temperatures depends very much on the current conditions, such as temperature of the surrounding gas, particle size, particle substance, turbulence, and, in particular, air properties such as density, heat capacity, viscosity, and thermal conductivity, which all are temperature dependent. The heat transfer coefficient h can be calculated using the following relation [15]:

$$\mathrm{Nu} = \frac{hd}{k} = 2 + 0,6 \cdot \mathrm{Pr}^{1/3} \cdot \mathrm{Re}^{1/2},$$

where Nu is the Nusselt number, d the particle diameter, k the thermal conductivity of the gas, Pr the Prandtl number, and Re the Reynolds number.

For a particle initially at room temperature, this would result in a relaxation time of 170 μs for the particle to reach 90% of a surrounding air temperature of 700 K. However, the model is based on spherical particles, which have the smallest possible surface area to volume relation, thus the relaxation time is thought to be shorter for real phosphor particles. Also the assumption that the particles have an even internal temperature distribution is simplified. Initially there most probable is a temperature gradient over the particle. The collected signal is biased towards phosphorescence originating from the particle surface, where the temperature more closely corresponds to the gas temperature.

The argumentation above should be considered as a rough estimation. Future work calls for both theoretical and experimental investigations regarding phosphor particles establishing thermal equilibrium and the timescales involved.

2 Experimental

In the experiments a 10 Hz pulsed Nd:YAG laser operating at its third harmonic producing 355-nm radiation was used as excitation source. The exiting beam profile was circular (Gaussian) with a diameter of about 8 mm. A single cylindrical lens ($f = 1000$ mm) was used to focus the beam in the vertical plane. 500 mm after the lens, the narrowed beam crossed an air flow that was kept at room temperature and seeded with phosphor particles. Thus, at this position, the laser beam had the shape of an ellipsoid with the size of 8 mm in the vertical direction and 4 mm in the horizontal direction. With the laser pulse energy set at 400 mJ, a corresponding fluence of 1.5 J/cm^2 was produced. The phosphorescence signal, collected by a lens system into a spectrometer, was detected with an ICCD camera. Spectra were recorded for a range of fluences from 0.1 to 1.5 J/cm^2.

3 Results and discussion

Figure 3 shows emission spectra of uncoated BAM at three different laser fluences. As can be seen, the spectra are completely overlapping, showing no indication of temperature change. The emission spectra of BAM with SiO_2 coating and with Al_2O_3 coating, showed the exact same behavior as that of uncoated BAM at different fluences and are therefore not included in the paper.

In a real measurement situation, the spectrum is not recorded, but the area of interest is being photographed through two adequate filters. In order to simulate what the ratio of the intensities through the two filters would be, the recorded spectra were multiplied by normalized transmission spectra for the two filters mentioned above. The resulting ratios as functions of laser fluence are shown in Fig. 4. As can be seen, there is no tendency of the ratio changing with laser fluence and therefore neither any induced temperature change.

Using excessively high laser fluence (above 10 J/cm^2), a completely different spectrum is detected, as compared to

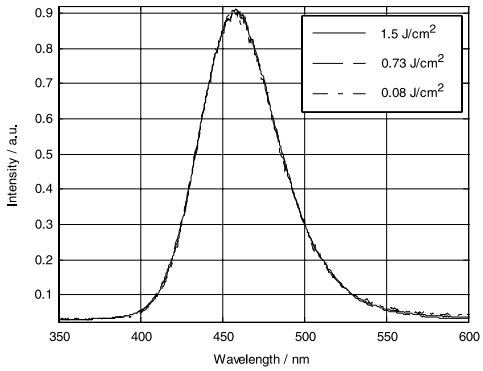

Fig. 3 BAM emission spectrum at three different laser fluences

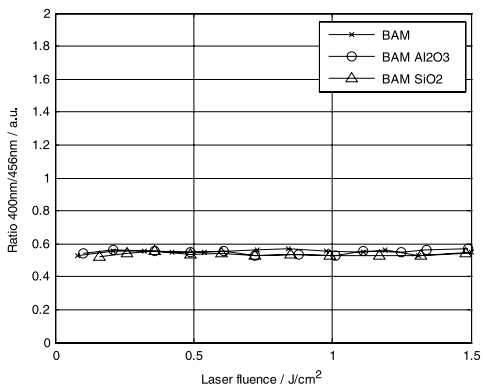

Fig. 4 Evaluated ratio with respect to the transmission of the 400 ± 20-nm and 456 ± 5-nm interference filters, as a function of laser fluence for all three types of BAM

the phosphorescence spectrum, with discrete peaks more resembling a laser-induced breakdown spectrum, LIBS. The spectra from the three different BAM types differ slightly. The SiO_2-coated BAM seems to be a bit more resistant to higher laser fluence, since the intensities from the distinct peaks are relatively lower than the ordinary phosphorescence signal, compared to the other BAM types. BAM coated with SiO_2 is thus preferable, not only because of its better "anti-stick" properties, but also because it is more resistant to higher fluences.

4 Conclusion

The experimental results show that high laser fluence, up to 1.5 J/cm^2, does not tend to heat phosphor particles when used in gaseous flow measurements. In this kind of measurements higher laser energy (compared to surface thermometry), and thus higher laser fluence, is needed to achieve a sufficient signal level due to the low particle density. Therefore heating the particles with the excitation laser is the biggest concern. In the range of typical laser fluences used in LIP applications there are no indications of the laser heating the particles of the thermographic phosphor BAM, when seeded in a gaseous flow of room temperature. This makes further development of free-flow measurement techniques promising.

Acknowledgements This research was supported by the Center for Combustions Science and Technology, CECOST, and the Center of Competence Combustion Processes, KCFP. The authors would also like to thank Gustaf Särner for the permission of using his data.

References

1. S.W. Allison, G.T. Gillies, Rev. Sci. Instrum. **68**, 2615 (1997)
2. A. Khalid, K. Kontis, Sensors **8**, 5673 (2008)
3. H. Seyfried, M. Richter, K.-H. Nilsson, M. Aldén, H. Schmidt, Collection of Technical Papers—45th AIAA Aerospace Sciences Meeting, vol. 18 (2007), p. 12794
4. T. Husberg, S. Girja, I. Denbratt, A. Omrane, M. Aldén, J. Engström, SAE 2005-01-1646 (2005)
5. J. Brubach, J.P. Feist, A. Dreizler, Meas. Sci. Technol. **19**(2), 025602 (2008)
6. L.J. Dowell, G.T. Gillies, Rev. Sci. Instrum. **62**, 242 (1991)
7. A. Omrane, F. Ossler, M. Aldén, Proc. Combus. Inst. **29**, 2653 (2003)
8. H. Seyfried, G. Särner, A. Omrane, M. Richter, M. Aldén, ASME, GT2005-69058 (2005)
9. S. Gustaf, R. Mattias, A. Marcus, Meas. Sci. Technol. **19**, 125304 (2008)
10. A. Omrane, P. Petersson, M. Alden, M.A. Linne, Appl. Phys. B—Lasers Opt. **92**, 99 (2008)
11. S. Shionoya, H. Yamamoto, W.M. Yen, *Phosphor Handbook*, 2nd edn. (CRC Press/Taylor and Francis, Boca Raton, 2007)
12. G. Särner, Doctoral Thesis, Lund University (2008)
13. J. Brubach, A. Patt, A. Dreizler, Appl. Phys. B—Lasers Opt. **83**, 499 (2006)
14. J.P. Holman, *Heat Transfer*, 8th edn. (McGraw-Hill, New York, 1997)
15. W.E. Ranz, W.R. Marshall, Chem. Eng. Prog. **48**, 141 (1952)

Paper III

SAE International®

Laser-Induced Phosphorescence and the Impact of Phosphor Coating Thickness on Crank-Angle Resolved Cylinder Wall Temperatures

2011-01-1292
Published
04/12/2011

Christoph Knappe
Div. of Combustion Physics, Lund Institute of Technology

Peter Andersson and Martin Algotsson
Div. of Combustion Engines, Lund Institute of Technology

Mattias Richter, Johannes Linden and Marcus Alden
Div. of Combustion Physics, Lund Institute of Technology

Martin Tuner and Bengt Johansson
Div. of Combustion Engines, Lund Institute of Technology

doi:10.4271/2011-01-1292

ABSTRACT

In order to further improve the energy conversion efficiency in reciprocating engines, detailed knowledge about the involved processes is required. One major loss source in internal combustion engines is heat loss through the cylinder walls. In order to increase the understanding of heat transfer processes and to validate and generate new heat transfer correlation models it is desirable, or even necessary, to have crank-angle resolved data on in-cylinder wall temperature.

Laser-Induced Phosphorescence has proved to be a useful tool for surface thermometry also in such harsh environments as running engines. However, the ceramic structure of most phosphor coatings might introduce an error, due to its thermal insulation properties, when being exposed to rapidly changing temperatures. In this article the measurement technique is evaluated concerning the impact from the thickness of the phosphorescent layer on the measured temperature. Experiments with different layer thicknesses are performed both during motored and fired operation of a HCCI engine. The results reveal a need for caution when applying the technique for in-cylinder measurements.

INTRODUCTION

Increasing fuel prices and more stringent legislation on emissions of greenhouse gases, such as CO_2, have driven the requirement for engines with higher efficiency. The upper limit has been pushed forward and is now approaching 60% indicated thermal efficiency (ITE) [1, 2]. In order to reach 60% ITE and beyond, all losses in combustion engines need to be considered. Heat loss through the cylinder walls is one major source of losses in internal combustion engines [3]. To gain knowledge about the heat transfer processes it is crucial to have information about the boundary conditions, including the wall temperature. In-cylinder wall temperature studies have previously been performed by e.g. Woschni et al [4] and Chang et al [5].

Homogeneous Charge Compression Ignition (HCCI) is a combustion process that can be described as a hybrid between the Spark Ignition (SI) and Compression Ignition (CI) engines. During the last decade the HCCI concept has been more intensively studied due to its higher efficiency at lower loads, compared to SI engines, and having lower emission of nitrogen oxides and soot than the CI engines [6, 7]. There are, however, drawbacks such as difficulty of controlling the combustion phasing and the heat release rate which is

globally high and thus resulting in high pressure rise rates. The pressure rise rate can, to some extent, be reduced by for example using diluted mixtures of air or recirculated exhaust gas.

Besides giving structural stresses and high noise, the high pressure rise rates also have an effect on the heat transfer to cylinder walls [8]. Similar observations have also been made for partially premixed combustion engines where high pressure rise rates lead to strong pressure oscillations and increased heat losses [9]. The thermal boundary layer (TBL) is a layer of fluids that to some extent insulates the cylinder walls from the high temperature of the burned gas during combustion, figure below. With high pressure rise rates and the resulting severe pressure oscillations, the TBL can be reduced or even broken exposing the relatively cooler cylinder walls to the hot gas and thus the heat transfer increases.

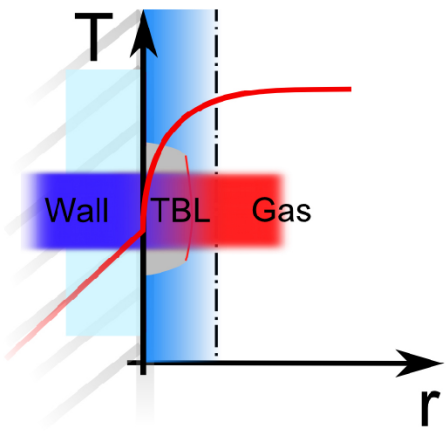

Figure 1. Schematic temperature gradient in a combustion engine showing the TBL near the chamber surface as well as a phosphor dot on top of the surface.

Understanding of the behavior of the TBL will aid the development of all combustion systems with high pressure rise rates. For understanding which variables and to what extent they will affect the TBL, the temperature within and near the TBL is of high interest. In recent experiments Laser-Induced Phosphorescence combined with other optical techniques, such as Filtered Rayleigh Scattering or Coherent Anti-Stokes Raman Spectroscopy proved its potential to measure temperature transients near and on surfaces [10, 11].

During the past years the technique of using LIP for thermometry has been proven to be an alternative to thermocouples and infrared pyrometry for surface temperature probing. The phosphor technique is believed to be non-intrusive and capable of remote probing while still offering high spatial and temporal resolution with good accuracy [12, 13, 14].

Cylinder wall temperature measurements have previous been studied at Lund University, for instance by Särner et al [15] and Wilhelmsson et al [16]. In both cases the aim was to measure the temperature on the valves and the cylinder head. Särner and Wilhelmsson showed that the phosphor technique was capable of providing crank-angle resolved temperature data.

The aim of this paper is to evaluate the LIP technique with respect to different phosphor layer thicknesses. When applying LIP for surface thermometry it is common practice to apply what is considered a “thin” layer of phosphor material to the surface of interest. Ideally, the measured temperature should reflect the temperature of the coated surface. However, one should keep in mind that the active elements are often embedded in a ceramic host material. As familiar, ceramics are used as thermal barrier coatings (TBC) in for example gas turbines [17, 18]. Although the TBC coatings are significantly thicker compared to what is found in LIP thermometry, it is relevant to ask if the thermal insulating properties of the ceramic host material influence the measured temperatures. This is especially important in extreme environments such as in a reciprocating engine where the temperature gradients across the surfaces/in-cylinder gas interface are severe and subject to rapid oscillations during operation.

EXPERIMENTAL SETUP

ENGINE

The engine used in this experiment was a 2 liter port injected in-line 4 cylinder Toyota engine that was running in single cylinder operation and in HCCI mode. The combustion chamber was in the shape of a disc, i.e. no bowl in the piston.

Figure 2 shows a picture of the engine used in the experiments, whereas table 1 presents some vital engine parameters.

The engine was equipped with a piston extension (Bowditch) and a metal piston. The location of the phosphor dot was chosen to be on the inside of a quartz liner right below the combustion chamber ceiling, covering the full squish height of 3 mm (see fig. 3). This position enabled optical access throughout the whole cycle without being restricted to a certain range of Crank-Angle Degrees (CADs). The width of the phosphor dot was chosen wide enough (ca. 7 mm) to account for vibrations during engine operation and to assure laser illumination at all times.

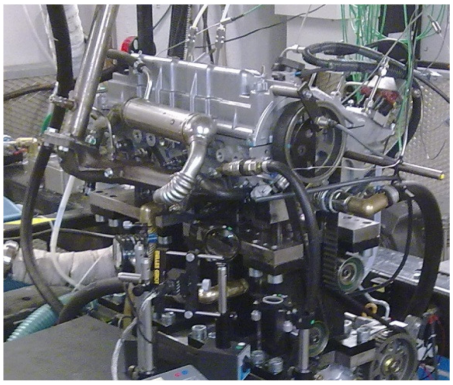

Figure 2. The Toyota engine with piston extension and a quartz liner.

Table 1. Geometric properties of the Toyota engine.

Displacement volume	499 cc
Stroke	94 mm
Bore	82.2 mm
Compression ratio	11.2:1
Number of Valves	4

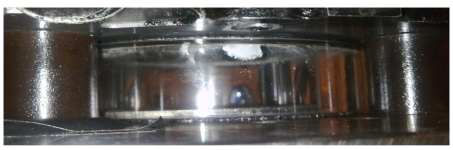

Figure 3. Outside view of the phosphor dot below the cylinder ceiling, sprayed onto the quartz ring's inner side surface.

The fuel used in this work was PRF 50, i.e. Primary Reference Fuel consisting of 50% iso-octane and 50% n-heptane. The engine was controlled by a LabView computer program, developed in-house. The engine control software also triggered the laser in order to timely adjust laser pulses to desired CADs. During combustion the inlet air was heated to around 120-125 °C with a manually controlled Leister heater to ensure HCCI combustion. The gas temperatures are calculated from recorded pressure traces by taking an average over 100 cycles and then use the ideal gas law to calculate the gas temperature for a given CAD.

$$\frac{p \cdot V}{T} = \text{const.} \;\Rightarrow\; T_{\text{CAD}} = T_{\text{ivc}} \cdot \frac{p_{\text{CAD}} \cdot V_{\text{CAD}}}{p_{\text{ivc}} \cdot V_{\text{ivc}}} \tag{1}$$

In equation (1) (p_{ivc}, V_{ivc}, T_{ivc}) are variables for pressure, volume and temperature after inlet valve closing whereas (P_{CAD}, V_{CAD}, T_{CAD}) are corresponding variables at any given CAD during the cycle. Equation (2) was used to estimate the uncertainty for T_{CAD} from the errors of all input parameters in (1):

$$\Delta T_{\text{CAD}} = T_{\text{CAD}} \cdot \left(\frac{\Delta p_{\text{CAD}}}{p_{\text{CAD}}} + \frac{\Delta p_{\text{ivc}}}{p_{\text{ivc}}} + \frac{\Delta V_{\text{CAD}}}{V_{\text{CAD}}} + \frac{\Delta V_{\text{ivc}}}{V_{\text{ivc}}} \right) \tag{2}$$

ΔT_{CAD} was therewith estimated to be below 5 °C before TDC, then reaches up to 60 °C around TDC and decreases to 10 °C after TDC.

However, the ideal gas law approximation estimates the mean gas temperature and does not take the spatial temperature profile seen, in figure 1, into account. It also implies a number of limitations: It considers changes of states to happen instantaneously and thus energy transfer with the environment can only be taken into account as a subsequent process. Particle interactions are neglected such that it applies best for small molecules with a long mean free path (high temperature, low pressure). Moreover it does not hold for thermodynamically open systems, which means that it applies only when the inlet and outlet valves are closed, i.e. from -149 CAD ATDC to 129 CAD ATDC (ATDC = After Top Dead Center).

LASER-INDUCED PHOSPHORESCENCE

By utilizing the well known phosphorescence from thermographic phosphors, temperatures can be measured remotely and non-intrusively with high accuracy in the range between cryogenic temperatures up to 1700 °C [19,20]. An appropriate phosphor is applied on the surface area of investigation using an appropriate non-fluorescent binder, e.g. HPC [14]. The surface is then irradiated with pulsed UV laser radiation for excitation of the phosphor material. The resulting emission intensity will decay exponentially according to

$$I = I_0 \cdot e^{-\frac{t}{\tau}} \tag{3}$$

where I_0 is the initial emission intensity, t is time and τ is the lifetime of the phosphorescence, i.e. the time after which the intensity has decreased to $1/e$ of the initial emission I_0 [12]. The phosphorescence time-decay depends on the temperature of the thermographic phosphor. Temperature can thus be

calibrated and determined by calculating the phosphorescence lifetime from the measured intensity decay. This is normally done by fitting the intensity decay to the theoretical model (eq. 3), using a non-linear fitting procedure. The error in such a measurement can ideally be less than 1% [18].

In the present measurement series the phosphor La_2O_2S:Eu was used. The light emitting substance is the Eu^{3+} ion doped into the host La_2O_2S. The Eu^{3+} ion has a broad absorption spectrum in the UV-region and mainly emits from its ^5D state to its F ground state. The host, La_2O_2S, interacts with the Eu^{3+} ion via its Charge Transfer State, making the emission temperature dependent according to the Boltzmann distribution [21].

Several of the spectral emission peaks originating from the ^5D - F transitions have a temperature dependent lifetime [22]. For these measurements the $^5D_2$ - F relaxation producing emission at 538 nm was used as it is very sensitive in the range 100 - 300 °C. Interference filters centered at 540 nm with a full width half maximum of 10 nm were used to suppress emission wavelengths other than the phosphorescence peak of interest.

The calibration of the thermographic phosphor was made in a controlled environment, in this case an ENTECH oven, where the temperature was constantly logged by a type S thermocouple (specified error: ΔT=±1 °C). The lifetime was measured for a number of temperatures in the expected temperature range, i.e. 100 - 300 °C. Lifetime versus temperature from the calibration is plotted in figure 4.

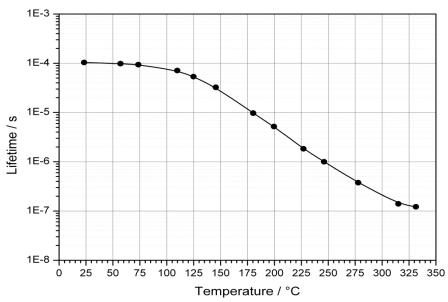

Figure 4. Phosphorescence lifetime as a function of temperature for the La2O2S:Eu 538 nm emission line.

As shown in figure 3 a phosphor dot was sprayed onto the inner side of the quartz liner right below the cylinder ceiling. Since point measurements of the temperature were intended, the size of the phosphor dot was kept reasonably small (3 mm × 7 mm) to prevent the phosphor from insulating a larger surface area. Also the laser beam cross section was reduced to 1 mm and centered onto the phosphor dot. By doing so, the collected temperatures originate from a limited area and thus surface temperature gradients over the probed area are reasonably small and less likely to modify the collected decay curves. HPC was used as a binding agent. The piston extension mentioned earlier greatly facilitated the phosphor applying procedure as it enabled convenient access to the combustion chamber without needing to dismantle the cylinder head every time a new phosphor was about to be applied.

The phosphor was excited by UV-light laser radiation at 355 nm produced by a pulsed Nd:YAG-laser working at its third harmonic. The laser operated at 10 Hz with pulse duration of 5 ns per pulse. The pulse energy was kept as low as 70 µJ throughout all experiments and illuminated a circular phosphor dot size of 8 mm in diameter. Thus errors from heating the wall locally by laser absorption can be neglected whereas the signal-to-noise level for phosphorescence decays maintains reasonably high. The phosphor dot was excited by the laser from two opposing directions, i.e. the phosphor's wall-side and the gas-side were illuminated simultaneously. To achieve this, a polarizing beam splitter was used in combination with a λ/2-plate as shown in figure 5. It creates two beam paths whose intensities can be tuned relatively to each other.

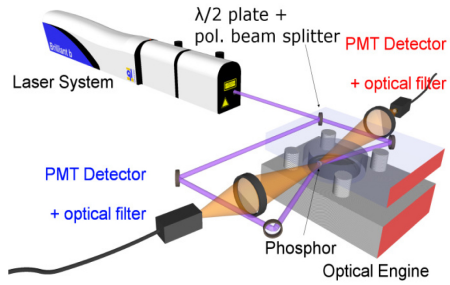

Figure 5. Experimental setup for two-face phosphor temperature determination in an optical engine.

Due to very short absorption lengths of UV light in ceramic materials (such as the phosphor's host material), two separate temperature readings can be obtained from the phosphor, i.e. one from each side of the substrate. In principle, although the excitation light is heavily absorbed, the generated red-shifted phosphorescence could to some extent leak trough the substrate. To quantify this effect, the beam path has been blocked either way before each experiment. The amount of signal that leaked through the phosphor into the opposite detector was at the order of 20% or less. Clearly distinct temperature results shown later indicate that the overhearing

was of none or at least only marginal effect. The induced phosphorescence was collected with quartz glass lenses (f_1 = +100 mm, f_2 = +200 mm, $d_{1,2}$ = 50 mm) and focused on two Photo Multiplier Tubes (PMTs). Interference filters, centered at 538 nm, were placed in front of the PMTs for spectral filtering. The PMT signal passed through a current-to-voltage amplifier and then was sampled and saved by a Lecroy 3 GHz oscilloscope.

Ten measurements were sampled and saved every second to obtain cycle-to-cycle resolution at 1200 rpm, corresponding to 10 Hz.

ENGINE OPERATION PROCEDURE

The measurement procedure contains three measurement cycles. Before the first cycle, the engine was warmed up by motoring the engine. After a warm-up time of 13 minutes a stable temperature of 87±1 °C was obtained for the outer surface of the quartz liner. Also the temperature of the phosphor was continuously monitored during the whole warm-up process using an integrated fast evaluation routine. Measurements were not started before the phosphor temperatures appeared to be stable in time. CAD-resolved temperatures were measured consecutively in steps of 30 CADs from −180 to +180 CAD ATDC. This measurements cycle took about 12 minutes. After this, the engine was heated up and run in HCCI mode. Once the combustion was stable the second measurement cycle was started. A list of operating temperatures during stable HCCI combustion is summarized in table 2.

Table 2. Typical operating temperatures during steady-state HCCI combustion.

Oil temperature	87±2 ˚C
Coolant temperature before engine	76±1 ˚C
Coolant temperature after engine	79±1 ˚C
outer quartz liner temperature (outside - thin phosphor layer)	111±2 ˚C
quartz liner temperature (outside - thick phosphor layer)	115±2 ˚C

As combustion was expected to cause significantly bigger and faster temperature changes than observed during motoring the CAD-resolution was increased down to steps of 5 CADs around TDC. The third and final measurement cycle was started directly after the fuel injection had been terminated and thus measured the cool-down of the engine during motoring for two different CADs, −180 and +5 CAD ATDC. This entire procedure has been repeated for the comparison of two different layer thicknesses of the La_2O_2S:Eu phosphor, one at 32±3µm and another one at 59±2µm. The error numbers indicate the uncertainty of the average thickness at a 95% confidence level. Local thickness variations in the order of ±10 µm have been observed for each phosphor.

RESULTS & DISCUSSION

Crank-angle resolved wall temperature measurements in an HCCI engine have been performed using Laser Induced Phosphorescence. Temperature was measured on a quartz liner slightly below the combustion chamber ceiling, giving simultaneous access to two opposing sides of the phosphor. To illustrate the impact of the phosphor coating thickness on the temperature reading, experiments have been performed comparing a layer of 32µm with a 59µm thick phosphor layer. A Crank-angle range between −180 CAD and 180 CAD ATDC has been investigated for fired and motored engine operation. This makes it possible to compare how different gas/wall temperature gradients have an effect on the phosphor's two-face response.

In figure 6 the CAD-resolved phosphor surface temperatures is shown for the two different thicknesses during HCCI combustion (second measurement cycle). It is obvious that there is a strong influence from the layer thickness. The thicker phosphor (59 µm) clearly indicates an insulating effect when compared to the thinner coating (32 µm). The difference in measured temperature between the two sides is significantly greater for the thicker coating. Furthermore, the side towards the wall shows a smaller temperature increase during combustion for the thicker coating. This implies that there is a stronger shielding effect for the thicker phosphor.

The corresponding measurements for the motored case are presented in Fig. 7. The gas temperature is here reaching 450 °C at TDC, hence, the gas temperature oscillations are significantly reduced compared to the fired operation. With the thin layer of phosphor, the temperature on both sides of the phosphor material increases by 20 °C during the motored compression stroke. With the thicker layer of phosphor, the temperature on the gas side of the phosphor increases by 20 °C during the motored combustion stroke but only by 10 °C on the glass side of the phosphor. For the thinner coating the temperature difference between wall-side and gas-side reaches a maximum of 5 °C for this case, in spite of the gas temperature oscillating with an amplitude ~400 °C. These results are consistent with the findings from the fired operation presented above. There is definitely an insulating effect, especially for the thicker coating, but it is significantly less pronounced during motored operation.

Figure 8 shows an excerpt of the raw data from the 59 µm phosphor that is presented in figure 6. Single-shot temperatures for 100 successively recorded cycles are displayed. For the figures 6, 7 and 10, series like these have been averaged and are displayed together with their standard deviation as error bars. The dataset for figure 8 was chosen to provide a closer look on how the single-shot temperatures are

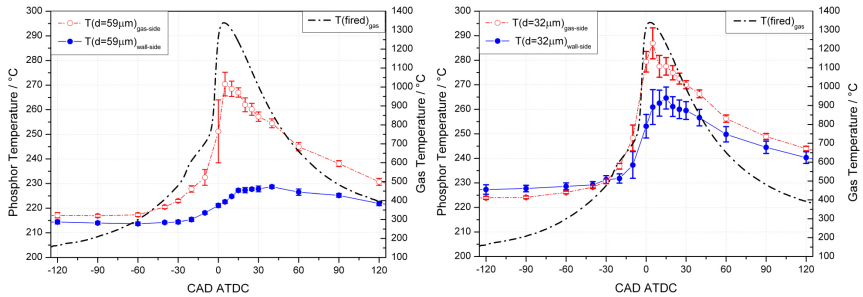

Figure 6. CAD-resolved phosphor surface temperatures during HCCI combustion set into relation to the in-cylinder gas temperature. The thicker phosphor coating (left hand side) can be compared to the thinner phosphor coating (right hand side).

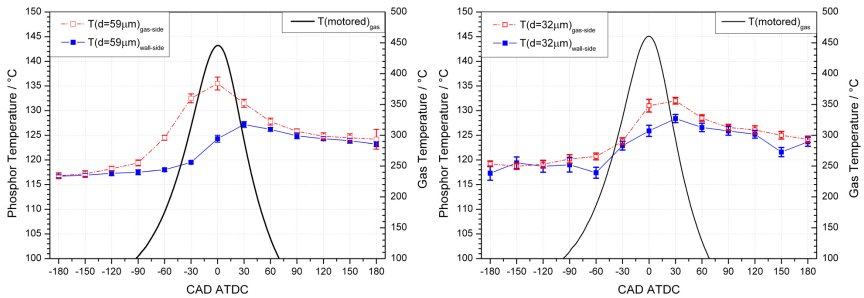

Figure 7. CAD-resolved phosphor surface temperatures during motored operation set into relation to the in-cylinder gas temperature. The thicker phosphor coating (left hand side) can be compared to the thinner phosphor coating (right hand side).

distributed at TDC during combustion - as this was the point with the highest temperature spread for the gas-side temperatures in figure 6. Cycle-to-cycle variation in combustion timing clearly show an effect on the phosphors gas-side temperature ($T_{gas\text{-}side}$=(251±13)°C) as expected. The standard deviation in CA50, i.e. 50 % of heat released, is 0.5 CAD for each series of 100 cycles. From looking at the phosphor's wall-side it is clear that not only the temperature is significantly lower here, but also the standard deviation ($T_{wall.side}$=(221.1±0.8)°C). This indicates the walls to be much more resistant to cycle-to-cycle variations in combustion phasing, i.e. the gas-side of the coating is much more affected by the varying gas temperature. It should also be mentioned that the insulating effect of this thicker phosphor helps dampening the temperature response measured on the wall-side.

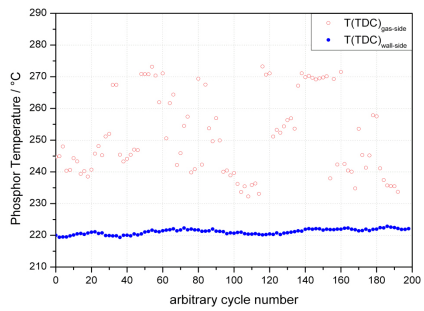

Figure 8. Single-shot phosphor temperatures at TDC during HCCI combustion, obtained for 100 consecutive cycles with the 59 µm phosphor coating.

In order to check whether there is a visible connection between the phosphor's two surface temperatures, they have been overlapped in figure 9 by using a double y-axis plot with different temperature scalings. Additionally, a sliding average filter over 20 neighboring values has been performed to reveal the overall time trend in temperature.

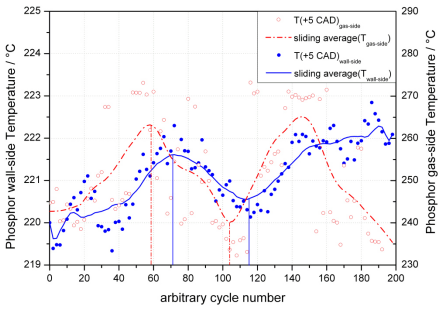

Figure 9. Rescaled single-shot temperatures that have been previously displayed in figure 7. Sliding averages over 20 neighboring points are displayed as lines for both temperatures.

The filtered curves in figure 8 show the wall-side to lag roughly 12 cycles behind the gas-side temperature. This conclusion was drawn by comparing and matching the turning points in the averaged temperature trends (see vertical lines in figure 9). The time delay between the curves has been measured twice, yielding $\Delta t = 0.67$ s for the first maximum, and $\Delta t = 0.53$ s for the first minimum.

In figure 10 the crank-angle resolved phosphor temperatures are set into relation to the gas temperature for the two running conditions. Here the combustion case can, more easily, be compared to the results obtained during motored operation.

As a result of the steeper gas temperature gradients during combustion, the heat transfer through the 59 µm phosphor layer does not keep up with the pace of the engine cycle speed (1200 rpm). This is expressed by the greater temperature differences between the two phosphor surfaces, which are significantly higher during HCCI combustion.

The absolute temperature differences between each side of the phosphor coatings (extracted from figures 6 and 7) are plotted in figure 11 as a function of CAD.

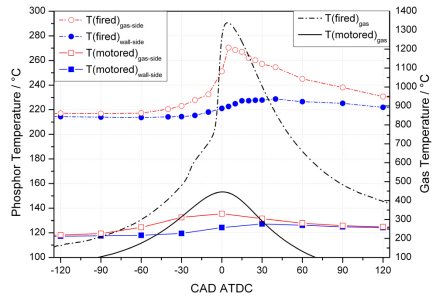

Figure 10. Gas- and phosphor temperature comparison between fired- and motored operation using the example of the 59 µm phosphor coating experiment.

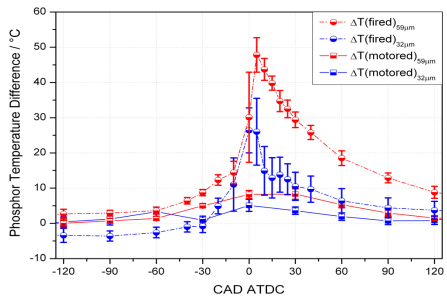

Figure 11. Temperature difference between the phosphor's gas- and wall-side as a function of CAD during fired- and motored engine operation Results for both coating thicknesses are displayed.

Clearly, one can determine differences between the motoring case and the combustion case. For the 59 µm layer during HCCI operation, the maximum temperature difference is almost as high as 50 °C whereas for the 32 µm layer the difference between the gas side and the wall side is only 25 °C. When comparing these results to the motoring case with a much lower average temperature and where the changes in gas temperature are both smaller and slower one can observe that the difference between both sides of the phosphor remain below 10 °C for the thick-, and about 5 °C for the thin phosphor, which is again roughly half of the difference that has been observed for the thicker phosphor coating. The highest temperature difference was observed around 0 CAD regardless of the phosphor coating thickness and mode of engine operation. The lowest temperature differences can be found around the edges of both plots in figure 11. Obviously this is where gas and wall temperatures change the slowest (see figures 6, 7). For the combustion case, the temperature

differences show an asymmetric behavior yielding higher differences at positive crank-angle degrees. This can be explained by the higher temperatures of the burnt gases after combustion that introduce a steeper gradient to the TBL in contrast to their corresponding negative CADs. Error bars plotted in figure 11 correspond to the superposition of the single temperature errors according to the laws of error propagation.

In figure 12 the cool-down behavior of the phosphor coatings is illustrated for −180 CAD and +5 CAD as a function of time after terminating the fuel injection, going from fired operation to external motoring. Displayed are single shot temperatures of two subsequent measurement series as only one CAD position could be monitored at a time. The two time axes have been overlapped such that the fuel termination takes place after 12 s, meaning that there are up to 120 single shot temperatures for each measurement to verify that walls were warmed up sufficiently such that the phosphor temperatures did not drift in time.

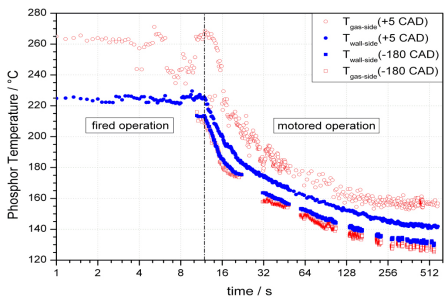

Figure 12. Phosphor temperature (thick coating) at −180 CAD and +5 CAD as a function time, passing from stable combustion on to motored operation.

Figure 12 shows that during a monitored time frame of 10 minutes, each temperatures converged towards a constant temperature T_{const}, reaching T_{const} + 10 % after 95 s (for +5 CAD) and 108 s (−180 CAD). The time difference of 13 s between the two measurements is relatively small and thus indicates that the subsequent measurements had been performed under quite similar conditions. Also comparing the temperatures prior to fuel extinction for +5 CAD ($T_{gas-side}$=265 °C; $T_{wall-side}$=225 °C) with the measurement taken earlier in figure 6 ($T_{gas-side}$=270 °C; $T_{wall-side}$=222 °C), shows that the temperatures could be reproduced quite accurately.

The cycle-to-cycle variations during combustion at +5 CAD had a clear effect on the spread of the gas side phosphor temperature, which had a standard deviation of about ±4.0 % before combustion was terminated and a value of only ±0.7 % after 10 minutes cooling time while motoring the engine externally. As the wall temperature decreases during the cooling, the difference between the two faces of the phosphor coating becomes less pronounced. In accordance to previous observations in figure 6, figure 12 shows the phosphor's temperature to be colder for −180 CAD compared to the +5 CAD case, regardless the engine's mode of operation.

A final conclusion that can be drawn in figure 12 is again the wall-side of the phosphor clearly to be less affected by the CAD-dependent, fast changing gas temperatures. This conclusion is based on the observation that for +5 CAD (where the gas temperature is close to its maximum) the phosphor's gas-side is hotter than its corresponding wall-side, whereas it is the other way round for −180 CAD, where the gas temperature is rather low. The wall-side phosphorescence thus reflects the inert/tardy characteristics of the cylinder wall as a heat reservoir much more accurate than the gas-side does.

SUMMARY & CONCLUSIONS

Crank-Angle resolved wall temperatures have been measured on the quartz liner close to the cylinder ceiling in an optical Toyota engine during motored and fired operation. According to our knowledge all previous experiments using LIP to determine surface temperatures rely on the assumption that the phosphor coating is non-intrusive to the surface, and sufficiently thin to attain the same temperature as the wall it is attached to without altering it.

For the first time, surface temperatures from phosphors were collected from two sides simultaneously, revealing differences that show a clear dependency on the thickness of the phosphor coating. This difference can be related to the steep temperature gradient that the phosphor coating experiences through the TBL close to the walls. Therefore the temperature difference can be observed to increase for thicker phosphors and with higher temperature gradients in time. The wall-side is believed to reflect the actual wall temperature more accurately than the gas-side of the phosphor coating. This observation is strengthened by the fact that it is much less sensitive to thickness variation of the phosphor compared the gas-side. In fact, the cylinder wall seems by far less sensitive to cycle-dependent gas temperature variations than assumed from previous experiments. It acts tardy and oscillates with lesser amplitude around the time-weighed average of the gas temperatures.

However the amount of heat transfer from the gas through the phosphor towards the wall-side is yet unknown and also the disturbance of the TBL that is introduced by the phosphor dot. This could have an impact on the wall-side temperature reading as the phosphor layer might shield the wall locally and the disturbance of the TBL could introduce some

inhomogenity to the surface temperature distribution (=intrusiveness of the phosphor technique).

In most applications access to the phosphor is solely possible from the gas-side as engine walls are usually non-transparent to laser radiation. This implies that the presented results reveal a need for caution when applying the technique for in-cylinder measurement. For engine experiments in similar temperature regimes as the results presented here, the phosphor coating thickness should be kept as thin as possible and well below 30um if it is of importance that systematic errors in the order of up to +30 °C are to be avoided.

For thinner phosphor coatings the temperature readings from the gas-side and from the wall-side should converge. However, the layer cannot be made infinitely thin since that would compromise the signal-to-noise ratio and also the durability of the coating. Unlike sprayed phosphor coatings, very thin phosphor coatings in the range of 0.1 µm to 5 µm can be produced using methods such as RF magnetron sputtering or Electrostatic Assisted Combustion Chemical Vapor Deposition [18, 23]. Ranson et al. showed, that the thickness of such a layer can be made as thin as 1 µm without compromising phosphorescence intensity [23]. It should be noted that the corresponding limit is probably higher for phosphors that have been applied using the spray technique, where phosphor particles are embedded in a transparent binding agent.

Nevertheless are sprayed phosphor coatings widely used in combustion engine research, where the access to internal surface areas is limited. Future work includes more detailed experiments in order to define how and under which restrictions the phosphor technique is applicable for accurate temperature measurements in engine environments.

REFERENCES

1. Splitter, D., Reitz, R., and Hanson, R., "High Efficiency, Low Emissions RCCI Combustion by Use of a Fuel Additive," *SAE Int. J. Fuels Lubr.* **3**(2):742-756, 2010, doi: 10.4271/2010-01-2167.

2. Manente, V., Zander, C., Johansson, B., Tunestal, P. et al., "An Advanced Internal Combustion Engine Concept for Low Emissions and High Efficiency from Idle to Max Load Using Gasoline Partially Premixed Combustion," SAE Technical Paper 2010-01-2198, 2010, doi:10.4271/2010-01-2198.

3. Heywood, J. B., "Internal Combustion Engine Fundamentals", McGraw-Hill, New York, ISBN 0-07-100499-8, 1988.

4. Woschni, G. and Fieger, J., "Determination of Local Heat Transfer Coefficients at the Piston of a High Speed Diesel Engine by Evaluation of Measured Temperature Distribution," SAE Technical Paper 790834, 1979, doi: 10.4271/790834.

5. Chang, J., Güralp, O., Filipi, Z., Assanis, D. et al., "New Heat Transfer Correlation for an HCCI Engine Derived from Measurements of Instantaneous Surface Heat Flux," SAE Technical Paper 2004-01-2996, 2004, doi: 10.4271/2004-01-2996.

6. Vressner, A., "Studies on the Load Range of an HCCI Engine using In-Cylinder Pressure, Ion Current and Optical Diagnostic," Ph.D. thesis, Lund Institute of Technology, Lund, 2007.

7. Christensen, M., "HCCI Combustion - Engine Operation and Emission Characteristics," Ph.D. thesis, Lund Institute of Technology, Lund, 2002.

8. Tsurushima, T., Kunishima, E., Asaumi, Y., Aoyagi, Y. et al., "The Effect of Knock on Heat Loss in Homogeneous Charge Compression Ignition Engines," SAE Technical Paper 2002-01-0108, 2002, doi:10.4271/2002-01-0108.

9. Manente, V., Johansson, B., Tunestål, P., "Half Load Partially Premixed Combustion, PPC, with High Octane Number Fuels. Gasoline and Ethanol Compared with Diesel," *SIAT 2009* **295**, 2009.

10. Brübach, J., Zetterberg, J., Omrane, A., Li, Z.S., Aldén, M., Dreizler, A., "Determination of surface normal temperature gradients using thermographic phosphors and filtered Rayleigh scattering," *Appl. Phys. B* **84**, 2006.

11. Brübach, J., Hage, M., Janicka, J., Dreizler, A., "Simultaneous phosphor and CARS thermometry at the wall-gas interface within a combustor," *Proc. Combust. Inst.* **32**, 2009.

12. Eckbreth, A.C., "Laser Diagnostics for Combustion Temperature and Species, 2nd edition," Gordon and Breach, ISBN 9056995324, 1996.

13. Allison, S.W., Gilles, G.T., "Remote thermometry with thermographic phosphors: Instrumentation and applications," *Rev. Sci. Instrum.*, **68**(7): 2616, 1997.

14. Allison, S.W., Beshears, D.L., Bencie, T., Hollerman, W.A., Boudreaux, P., "Development of temperature sensitive paints for high temperature aeropropulsion applications," *AIAA-2001-3528*, 2001.

15. Särner, G., Richter, M., Aldén, M., Vressner, A. et al., "Cycle Resolved Wall Temperature Measurements Using Laser-Induced Phosphorescence in an HCCI Engine," SAE Technical Paper 2005-01-3870, 2005, doi: 10.4271/2005-01-3870.

16. Wilhelmsson, C., Vressner, A., Tunestål, P., Johansson, B. et al., "Combustion Chamber Wall Temperature Measurement and Modeling During Transient HCCI Operation," SAE Technical Paper 2005-01-3731, 2005, doi: 10.4271/2005-01-3731.

17. Cao, X.Q., Vassen, R., Stoever, D., "Ceramic materials for thermal barrier coatings," *J. Eur. Ceram. Soc.* **24**:1-10, 2004.

18. Feist, J.P., Heyes, A.L., Choy, K.L., Su, B., "Phosphor thermometry for high temperature gas turbine applications," *IEEE-0-7803-5715-9*, 1999.

19. Krauss, R.H., Hellier, R.G., McDaniel, J.C., "Surface temperature imaging below 300 K using," *Appl. Opt.* **33**:3901, 1994.

20. Cates, M.R., Allison, S.W., Jaiswal, S.L., Beshears, D.L., "YAG:Dy and YAG:Tm fluorescence to 1700°C," *The 49th International Instrumentation Symposium - The Instrumentation, Systems, and Automation Society*. Orlando, Florida. May 2003.

21. Shionoya, S., Yen, W.M., "Phosphor handbook", CRC Press, 1999.

22. Husberg, T., Gjirja, S., Denbratt, I., Omrane, A. et al., "Piston Temperature Measurement by Use of Thermographic Phosphors and Thermocouples in a Heavy-Duty Diesel Engine Run Under Partly Premixed Conditions," SAE Technical Paper 2005-01-1646, 2005, doi: 10.4271/2005-01-1646.

23. Ranson, R.M., Thomas, C.B., Craven, M.R., "A thin film coating for phosphor thermometry," *Meas. Sci. Technol.* **9**, 1998

CONTACT INFORMATION

Christoph Knappe, Dipl.-Phys.
christoph.knappe@forbrf.lth.se
Telephone: +46 46 22 23733
Fax: +46 46 22 24542
Department of Physics
Division of Combustion Physics
Lund University
P.O. Box 118, SE-221 00, Lund, Sweden

ACKNOWLEDGEMENTS

This work has been performed within the "D60 - The 60% efficient diesel engine" -project, an integrated part of the Centre of Competence for Combustion Processes (KCFP) at Lund Institute of Technology, Sweden. The authors kindly acknowledge the funding from the Swedish Energy Agency.

DEFINITIONS/ABBREVIATIONS

(A)TDC
(After) Top Dead Center

CAD
Crank-Angle Degrees

CI
Compression Ignition

HCCI
Homogenous Charge Compression Ignition

ITE
Indicated Thermal Efficiency

LIP
Laser-Induced Phosphorescence

PMT
Photo Multiplier Tube

SI
Spark Ignition

TBL
Thermal Barrier Layer

TBC
Thermal Boundary Coating

Paper IV

Available online at www.sciencedirect.com
ScienceDirect
Proceedings of the Combustion Institute 33 (2011) 939–946
Proceedings of the Combustion Institute
www.elsevier.com/locate/proci

Accurate measurements of laminar burning velocity using the Heat Flux method and thermographic phosphor technique

B. Li [a], J. Lindén [a], Z.S. Li [a,*], A.A. Konnov [a], M. Aldén [a], L.P.H. de Goey [b]

[a] Division of Combustion Physics, Lund University, P.O. Box 118, S-221 00 Lund, Sweden
[b] Eindhoven University of Technology, P.O. Box 513, 5600 MB Eindhoven, The Netherlands

Available online 16 September 2010

Abstract

The Heat Flux method was further developed to significantly reduce its experimental uncertainty and used to determine burning velocities under conditions when the net heat loss from the flame to the burner is zero. Non-stretched flames were stabilized on a perforated plate burner at 1 atm. Measurements of the adiabatic burning velocity of methane/air flames at initial mixture temperatures of 318 K are presented. Previously, tiny thermocouples in the thin burner plate were used to evaluate when the heat flux of the flame to the burner is zero. Related errors limit the accuracy of the method so far. A new experimental procedure based on thermographic phosphors is described which avoids these errors. The new experimental procedure is described. An UV thermographic phosphor ZnO:Zn was selected and used to sensitively control the temperature uniformity on the burner plate to within 60 mK. Uncertainties of the measurements were analyzed and assessed experimentally. A more accurate evaluation of the gas velocities, using mass weighting, was introduced to increase the accuracy further. The uncertainty of the measured adiabatic burning velocities due to the temperature scattering can be reduced from typically ± 1.5 cm/s at $\Phi = 0.7$ methane/air flame to ± 0.25 cm/s. The overall accuracy of the burning velocities including the uncertainty from the employed mass flow controllers was evaluated to be better than ± 0.35 cm/s. Possibilities to further improve the measurement accuracy are discussed with practical considerations.

Keywords: Burning velocity; Heat Flux method; Thermographic phosphor

1. Introduction

The adiabatic laminar burning velocity is a fundamental parameter of each combustible mixture, which depends on the stoichiometric ratio, pressure and temperature. The laminar burning velocity at standard conditions, i.e. atmospheric pressure and initial temperature of 298 K is invaluable for the characterization of combustion properties of the given fuel, for understanding of the underlying chemistry, validation of models, etc.

Comparison of kinetic mechanisms often serves to prove that one or another model is the best in predicting new experimental data. Comparison and validation of the models is usually based on visual perception; this qualitative

* Corresponding author. Fax: +46 46 222 4542.
E-mail address: Zhongshan.li@forbrf.lth.se (Z.S. Li).

1540-7489/$ - see front matter © 2010 The Combustion Institute. Published by Elsevier Inc. All rights reserved.
doi:10.1016/j.proci.2010.06.111

judgment could be acceptable only when the disparity between measurements and predictions of different mechanisms is obvious and exceeds experimental uncertainties. Model development and improvement, however, requires a quantitative measure of the discrepancy and evaluation of the sensitivity of the model predictions to variation of reaction rates or thermo-chemistry. An example of such a quantitative analysis was given by Brown et al. [1], who demonstrated that variation of each rate constant within its evaluated uncertainty results in the uncertainty in the computed burning velocity of about 8–10% for hydrogen flames and 12–13% for methane flames. This means that the accuracy of the measured laminar burning velocities should be below these values to be useful for the model development.

Burning velocities of many different fuels as a function of temperature, pressure, and stoichiometric ratio have been measured by many investigators; however, the data were incompatible for a long time. Wu and Law [2] demonstrated experimentally that the flame stretch due to flame front curvature and/or flow divergence must be taken into account in the data processing. The methodology of the determination of laminar burning velocities with the counter-flow twin-flame technique by extrapolation to zero stretch rate has been further improved by Vagelopoulos et al. [3]. The uncertainty of the counter-flow twin-flame technique is limited by the accuracy of the LDV (laser Doppler velocimetry) technique, which was estimated to be 1–2 cm/s for burning velocities less than 60 cm/s and up to 10 cm/s for those above 170 cm/s [4].

In constant-volume bombs, the un-stretched burning velocities were determined in many research groups using essentially the same approach. The experimental uncertainty of the laminar burning velocities derived from expanding spherical flames was estimated [5,6] to be about 10%. Recent work aimed at improving methodology [7] demonstrates a maximum random error of 1.45% for the observed flame speed; the uncertainty of the derived laminar burning velocity, however, may reach up to 2 cm/s in rich mixtures.

The Heat Flux method for the stabilization of adiabatic premixed laminar flames on a flat flame burner has been proposed by de Goey et al. [8] and further developed by van Maaren et al. [9,10]. This method was extensively used for measuring laminar burning velocities of gaseous fuels, e.g. [9–12]. Detailed analysis of the uncertainties of this method was performed [11,13] and showed that the overall accuracy of the burning velocity measurements is better than ± 1 cm/s (double standard deviation with 95% confidence level). The relative accuracy of the equivalence ratio was found to be below 1.5%.

One can conclude that contemporary experimental methods for measuring laminar burning velocities have accuracy of the order of 1–2 cm/s and for the purpose of model validation and development the accuracy should be improved. This is particularly important in slowly burning lean and rich flames; burning velocities of hydrocarbons mixed with air are of the order of 10–20 cm/s at these conditions, and thus the uncertainty is here up to 10%, which is relatively too high. The present work therefore aimed at significant reduction of the experimental uncertainty of the Heat Flux method. Two major sources of experimental uncertainties pertinent to the Heat Flux method were identified [11,13] as follows: irregular thermocouple placement in the burner plate and inaccuracy in the mass flow control. The series of thermocouples attached to the burner plate are essential in the measurements of the temperature distribution as will be described below. In the present work an alternative technique to measure the surface temperature using thermographic phosphors was successfully employed.

Thermographic phosphors (TP) are ceramic crystal substances often in the form of a fine powder. Usually they are doped with some kind of rare earth metal, which gives them specific phosphorescence properties. These phosphorescence properties are sometimes temperature dependent, which makes TP a sensor in temperature measurements applications. The use of TP is well established for measuring temperature on surfaces [14–18]. By applying laser-induced phosphorescence (LIP), temperature can be monitored by registering the change in either phosphorescence lifetime or the change in spectral profile. Both point- and two-dimensional measurements are possible. The point measurement approach usually utilizes the temperature dependence of the phosphorescence signal lifetime to retrieve temperature information [19]. Exploration of the temperature dependence of the spectral profile makes it possible, with the use of suitable optical filters, to do 2D temperature measurements on a surface, either through the use of two separate detectors or a single detector equipped with an image-doubling device (stereoscope) [20,21]. With suitable choice of phosphor material, measurements can be carried out at temperatures from cryogenic values to 2000 K. Due to interference with background Planck radiation at higher temperature, phosphors with emission in the blue spectral region are preferable in order to increase the signal-to-noise ratio. In addition short lifetime of the phosphorescence gains the possibility to time gate for background discrimination [22].

In the following the principles of the Heat Flux method are outlined. Then the choice of the suitable thermographic phosphor and optical arrangement are described. Finally, typical measurements are presented and compared with those using the classical configuration of the Heat Flux method. Uncertainties of the measurements were analyzed and assessed experimentally.

2. Experimental details

2.1. Heat flux burner facility

A detailed description of the Heat Flux method and associated experimental uncertainties are given elsewhere [11,13]. Important features of the method are, therefore, only shortly outlined in the following. This paper reports new developments to significantly reduce its experimental uncertainty. The key part of the experimental setup for the adiabatic flame stabilization using the Heat Flux method is the burner shown in Fig. 1. A 2 mm thick burner plate perforated with small holes (0.5 mm in diameter) is attached to the burner outlet. The burner head has a heating jacket supplied with thermostatic water to keep the temperature of the burner plate constant. During the experiments this temperature was fixed at 358 K. The plenum chamber has a separate cooling system supplied with water at a temperature of 298 K (standard conditions), or could be increased up to 358 K. This fixes the initial temperature of the fresh gas mixture. The heating jacket keeps the burner plate edges at a certain temperature higher than the initial gas temperature, thus warming up the (unburned) gases flowing through. Conductive heat transfer of the flame to the burner plate cools the gas flow on its turn. If the flame is stabilized under sub-adiabatic conditions, the gas velocity is lower than the adiabatic flame burning velocity and the sum of the heat loss and heat gain is higher than zero. Then, the centre of the burner plate is hotter than the heating jacket. If the unburned gas velocity is higher than the adiabatic burning velocity (super-adiabatic conditions), the net heat flux is lower than zero and the centre of the burner plate is cooler than the heating jacket. By changing the flow rate of the gas mixture an appropriate value of the gas velocity can be found to nullify the net heat flux. In this case the radial temperature distribution in the burner plate is uniform and equal to the temperature of the heating jacket.

In the classical configuration of the Heat Flux method, a series of thermocouples attached to the burner plate as shown in Fig. 1 allows the temperature distribution measurements in it. The flow rate at which the net heat flux is zero is shown to be the adiabatic flame burning velocity [8,9].

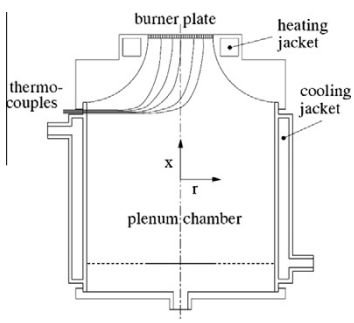

Fig. 1. The schematic of the heat flux burner.

A mixing panel was assembled for the gas supply from gas cylinders to the inlet of the plenum chamber of the burner. It consists of three ducts for the fuel, oxidizer and diluent gases. Each duct connected to its own gas cylinder has a buffer vessel and a Bronkhorst Hi-Tech mass flow controller (MFC). The 2 l buffer vessels are dimensioned according to the recommendation of the MFC manufacture. In the present work the MFCs were calibrated just before the experiments by measuring the mass change.

2.2. Thermographic phosphor

The temperature of the heat flux burner plate used in this work is around 358 K, so we need to choose an appropriate TP accordingly. There are several TP available in this range, among which zinc oxides are probably the best candidates, since they feature a very high temperature sensitivity in this temperature range. Zinc oxides have since long been utilized for a variety of applications such as UV-sun-blocking and LEDs [23]. The substance used in the experiment is ZnO:Zn with a particle size of 5 μm delivered by Phosphor Technology, UK.

ZnO:Zn has been investigated in detail by Särner et al. [24]. It is a blue emitting phosphor which, when excited with 355 nm laser, emits radiation with a peak at 388 nm. This UV/blue emission has a lifetime shorter than 1 ns, and is strongly red shifted with temperature. This phosphor also has a broad emission peak around 510 nm with a much longer lifetime of about 1 μs. With short camera exposure time, however, interference from this emission is avoided during spectral ratio temperature measurements.

The UV emission line of ZnO:Zn is according to Zhang et al. [25] originating from near-band-edge emission due to excitation states. The unusually large spectral line shift of ZnO:Zn enables temperature measurements with a very high precision from room temperature to 900 K, using the spectral ratio method. The filters used in this work are an interference filter at 390 ± 5 nm and a GG420 long pass filter. The ratio of the intensities through the two filters shows high temperature sensitivity.

2.3. Optical setup

The optical arrangement of the experimental setup is shown in Fig. 2. A thin layer of the ZnO:Zn was coated on top of the cap of each thermocouple, which can be seen in Fig. 3 as white dots labeled from one to eight. A Brilliant B laser system with a 3rd harmonic package was adopted to generate the 355 nm laser as light source. The laser was

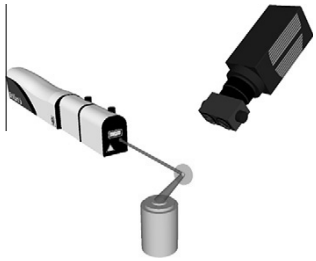

Fig. 2. The schematic of the experimental setup for the laser-induced phosphorescence measurements.

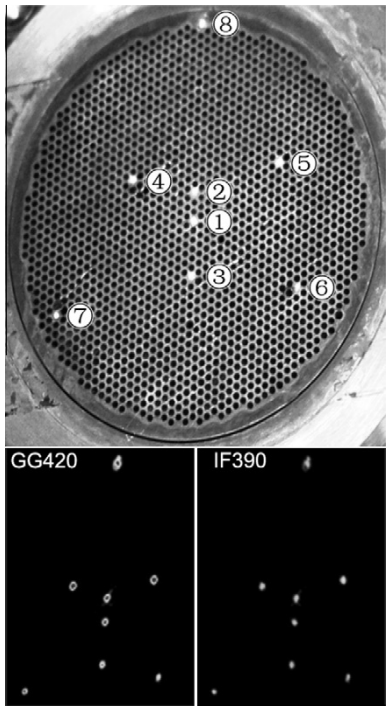

Fig. 3. Photograph of the perforated burner disc coated with eight thermographic phosphor dots on top of the installed thermocouples installed. Showing beneath are a typical twin laser-induced phosphorescence images collected through two different filters as marked in the corresponding images.

reflected and expanded to the burner disc by a concave mirror, which covered all the phosphor dots. The phosphorescence from the dots was then collected by a camera system, which includes a stereoscope, an objective (Nikon, 105 mm, f/2.5), and an ICCD camera (Princeton PI-MAX, 1024 × 1024 pixels). The stereoscope is an image-doubling device attached to the objective of the camera for

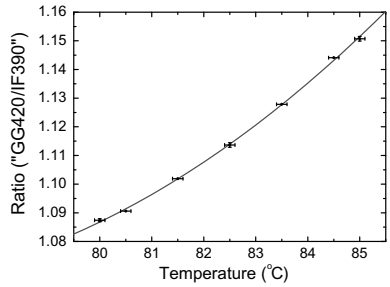

Fig. 4. Temperature sensitivity calibration curve of ZnO:Zn using the ratio between phosphorescence intensities collected with an interference filter (390 ± 5 nm) and a long pass filter (GG420).

simultaneous recordings of two optically identical images on a single CCD-chip [21]. An interference filter (390 ± 5 nm) and a long pass filter (GG420) were used in the stereoscope to obtain the two images on the CCD-chip. The ICCD camera was synchronized with the laser, and the gate width was set to be 30 ns. The typical twin phosphor images are shown in Fig. 3 as well. By calculating the ratio for the intensities between the two corresponding phosphor dots in the twin images, we can get the temperature distribution on the burner plate.

3. Results and discussion

3.1. Typical measurement

The sensitivity of the TP method has been tested on the burner plate by varying the temperature of the heating jacket water. The results are shown in Fig. 4, in which the error bars in horizontal direction represent temperature uncertainty of the water heating system (provided by the manufacture) and error bars in vertical direction represent the standard deviation of three independent measurements of the intensity ratio, which have been performed for temperatures at 80, 82.5 and 85 °C. For such an error bar, the corresponding uncertainty of the temperature is about 60 mK, which is in good agreement with the results of Särner et al. [24]. Hence the ratio from the twin images (see Fig. 3) can be converted into temperature and the temperature of eight dots can be obtained at each flame condition.

According to Bosschaart and de Goey [13], the temperature distribution along the radius of the burner disc can be written as:

$$T(r) = T_c + ar^2, \tag{1}$$

where T_c is the temperature in the burner disc centre, and a is the parabolic coefficient varied with the gas flow speed as described above. T_c and a

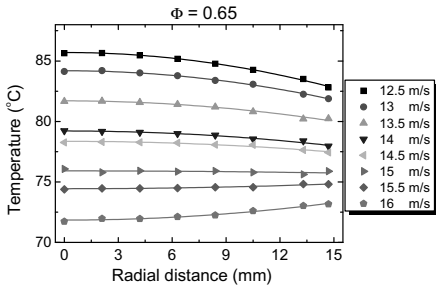

Fig. 5. Temperatures measured with thermographic phosphors at different radial distance on top of the burner disc (symbol) at different gas supply speeds and fitting curves (solid lines) for methane/air ($\Phi = 0.65$) flame speed evaluation.

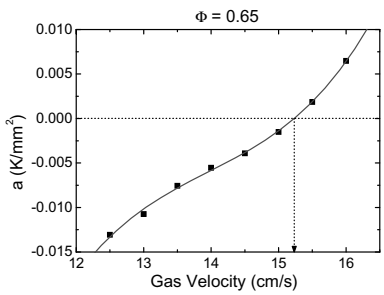

Fig. 6. The gas supply velocity dependence of the parabolic coefficient a, fitted with a third order polynomial function.

can be obtained by fitting the temperatures of the distributed eight dots with a parabolic curve. Interpolation of the relation curve between a and gas supply speed gives the adiabatic flame speed S_L with the Heat Flux method.

Figure 5 is an example of the temperatures measured on the eight TP coated dots (shown in Fig. 3) on top of the burner plate when burning a $\Phi = 0.65$ methane/air flame. The measured temperatures of the eight dots are represented by symbols and the parabolic fittings are represented by solid lines. Each fitted curve will give a parabolic coefficient as expressed in Eq. (1). Figure 6 is the relation curve between the parabolic coefficients a and the gas flow speeds fitted by the third order polynomial function. The flame speed can be determined as ~15.2 cm/s when the coefficient a approaches zero.

The described TP method was applied to the adiabatic laminar burning speed measurement of methane/air flames of a wide range of stoichiometric ratios (0.65–1.45) at initial gas mixture temperature of 318 K. The results are illustrated in Fig. 7 together with the results obtained with conventional thermocouple (TC) method for comparison. The two series show good agreement with a difference less than 0.5 cm/s, except for the very lean cases ($\Phi = 0.65$ and 0.7) where the difference is around 1 cm/s but still within the uncertainty of the TC method of about 2 cm/s [13].

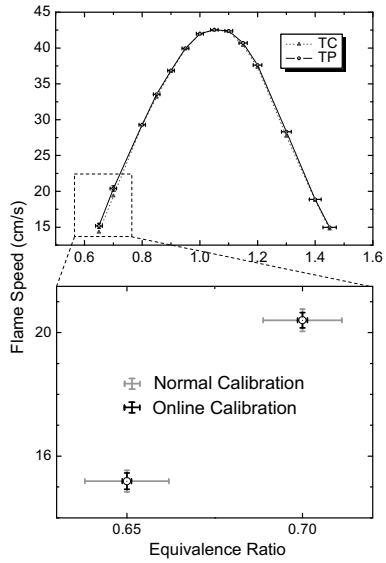

Fig. 7. Above, comparison of results of flame speed measurements obtained with thermocouple (TC) method and thermographic phosphor (TP) method. Below, error bars for the flame burning speeds measured with TP method for methane/air flames of $\Phi = 0.65$ and 0.7, black bars represent the possible values employing the online calibration method.

3.2. Error evaluation

The uncertainty of the adiabatic flame speed measured with the Heat Flux method originates mostly from two sources: the scattering of the measured temperatures from the parabolic fitting and the uncertainty of the employed MFCs.

3.2.1. Error from the temperature scatterings

In the measurement with the phosphor technique demonstrated in Fig. 5, the averaged temperature scattering is 50 mK and the maximum scattering is 160 mK, which is much better than thermocouple (typically 500 mK). The resulting error bar in the measured burning velocity can be estimated by the following equation [13]:

$$\sigma_{S_L} = \frac{1}{s}\frac{2\sigma_{tp}}{r_b^2}, \tag{2}$$

where s is a sensitivity parameter defined as:

$$s = \left.\frac{da}{dS_L}\right|_{a=0} \tag{3}$$

and can be extracted from Fig. 6; and r_b is the radial distance of the outermost TP dot which is 14.7 mm in this case; and σ_{tp} is the maximum temperature scatting 0.16 K in this measurement. The error bar of the measured flame speed σ_{S_L} was calculated to be 0.25 cm/s.

This measurement was performed for two lean flames with $\Phi = 0.65$ and 0.7, where the thermocouple method gives the largest error bars. Compared with the flame speed measurement uncertainties summarized in Ref. [11], the present measurement provides much higher precisions.

3.2.2. Error from the MFC

Due to the dramatic suppression of errors introduced by temperature scattering, the uncertainty aroused from MFC become dominant. Hence a proper calibration of the applied MFCs is crucial. In our laboratory, a convenient and highly precise MFC calibration system was built based on the precise measurement weight change. In the system, a bottle of sample gas connecting to the MFC with soft gas lines is placed on a platform scales. When the gas flow through the MFC is stable, the time on a stopwatch together with the value of the scales can be recorded simultaneously by taking an image of both displays. After a certain amount of gas flowing out, the time and the bottle weight are recorded again in the same way. Then the weight change per unit time will give the real mass flow rate of the MFC at the chosen opening percentage. This calibration method is superior to the commonly applied method in monitoring the volume change, which might be influenced by the ambient temperature and pressures.

During this calibration procedure; after several set-points (e.g. from 10% to 100%) being calibrated a fitting to a third order polynomial function is used to correct for non-linear effects. In this way, following the instructions given by the MFC manufacturer, the uncertainty (ΔF, ln/min) of the MFC (in the range of 10–100%) can be written as

$$\Delta F = 0.5\% \cdot \mathrm{Rd} + 0.1\% \cdot \mathrm{FS}, \tag{4}$$

where Rd is the reading of the MFC, and FS is the full scale of the MFC. Since the full scale of the MFC is involved in the error, over-dimension of the MFCs has to be avoided.

The uncertainty of the MFC will contribute to the errors for both burning velocity and stoichiometric ratio, which can be estimated by partial derivatives:

$$\frac{\Delta\Phi}{\Phi} = \frac{\Delta F_{\mathrm{CH_4}}}{F_{\mathrm{CH_4}}} + \frac{\Delta F_{air}}{F_{air}}, \tag{5}$$

$$\Delta S_L = \frac{\Delta F_{\mathrm{CH_4}} + \Delta F_{air}}{600 \cdot A}. \tag{6}$$

The uncertainties in stoichiometric ratio estimated by Eq. (5) are shown in Fig. 7 (horizontal error bar). It is ~0.01 when $\Phi < 1$, and it becomes ~0.02 when $\Phi = 1.45$. According to Eq. (6), where A is area of the burner plate in m^2 and ΔS_L in cm/s, the uncertainties from MFCs will add ~0.1 cm/s error to S_L when $\Phi = 0.65$ (and $\Phi = 1.45$), and it will add ~0.2 cm/s when $\Phi = 1$. In this work, the overall errors for two lean cases ($\Phi = 0.65$ and 0.7) were calculated and displayed in Fig. 7, marked as normal calibration. In this work, the error from the MFCs is of the same order as the error from temperature fitting scatters, which is not negligible anymore. Moreover, it introduces significant errors to the stoichiometric ratios. Further efforts are needed to decrease the errors from MFCs.

Here we propose an online calibration method (calibration during experiments), instead of the normal one (calibration before experiments). The weight changes of fuel and air bottles can be measured along with the experiments. Then the error from the MFCs will be determined only by the uncertainty of the scales (ΔS) and weight change (ΔM):

$$\Delta F = \frac{\Delta S}{\Delta M} \cdot \mathrm{Rd}. \tag{7}$$

Assuming that we have scales with precision $\Delta S = 0.01$ g, and for each online calibration $\Delta M \geqslant 10$ g, then Eq. (7) will become

$$\Delta F = 0.1\% \cdot \mathrm{Rd}. \tag{8}$$

According to Eqs. (5), (6) and (8), errors for both stoichiometric ratios and burning velocities based on online calibration were calculated. It has a value of less than 0.003 for all the stoichiometric ratios and adds less than 0.004 cm/s to the uncertainty of S_L for all the stoichiometric ratios. The overall error from normal calibration and online calibration are compared in Fig. 7, and the advantage of the online calibration is obvious.

3.2.3. Other resources of errors

One should remember that significant suppression of the errors caused by irregular thermocouple placement in the burner plate and the inaccuracy in the mass flow control probably brings the importance of other non-idealities of the Heat Flux method into view. A number of assumptions behind this method of the adiabatic flame stabilization have been validated numerically and experimentally employing Laser Doppler Velocimetry, Laser-Induced Fluorescence and Coherent Anti-Stokes Raman Scattering. The velocity profiles of the cold flow issuing from the burner mouth were found uniform with small distortions next to the burner edges [26,27]. The velocity profiles of the burnt gas above the flame were found to be symmetric and uniform in a core region of the flame. The measured maximum velocity variations in flames close to the adiabatic value were within 1–2% at radii smaller than about 80% of the burner radius [26,27]. This flow non-uniformity is compa-

rable to the uncertainty of the method achieved in the present work. Burners with a larger diameter might be required to suppress the impact of the edge-effects.

The small-scale structure of the flat flames stabilized on the perforated plate was analyzed by de Goey et al. [28] to reveal the range of flame velocities where the flame front is one-dimensional. It was concluded that with the drilling pattern of the burner plate employed here, the small flamelets converge completely forming a perfect 1-D flame at flow velocities below about 0.5 m/s. The criteria used for this evaluation are also comparable to the uncertainty of the method achieved. Further improvement may be gained in smaller diameter the holes and a reduction of the plate thickness.

It is believed that radicals do not touch the burner because of the presence of methane, which consumes the radicals very rapidly [29]. This chemical aspect of the method is difficult to evaluate experimentally as compared to the physical parameters which are under control. Although no indication of the influence of surface reactions was found by many investigations using this method, further experimental prove is required, which is the objective of the authors.

Radiative effects have a negligible effect ($<$0.2 cm/s) on the relevant heat fluxes in the system. Absorption of gas radiation by the burner and radiative heat losses by the burner itself has an error of the order of 2% on the relevant heat fluxes. This has been validated experimentally by changing the plate temperature, see [30].

4. Conclusions

Accurate measurements of laminar burning velocity have been demonstrated with Heat Flux method, which determine burning velocities of non-stretched flames stabilized on a perforated plate burner at 1 atm under conditions when the net heat loss from the flame to the burner is zero. Previously, tiny thermocouples mounted on several places in the thin burner plate served to evaluate the heat flux of the flame to the burner. Systematic errors of the order of 1 K in the measurements account for the bottleneck in the accuracy of the method so far. A new experimental procedure is described which avoids these errors. A UV thermographic phosphor ZnO:Zn was selected and used to monitor the temperature uniformity on the burner plate, which was proved to provide a sensitivity better than 60 mK for in situ measurements. Measurements of the adiabatic burning velocity of methane/air flames at initial mixture temperatures of 318 K are presented with the new experimental procedure and the measurements uncertainties were analyzed and assessed experimentally. The uncertainty of the measured adiabatic burning velocities due to the temperature scattering was reduced from typically $\pm$1.5 cm/s at $\Phi = 0.7$ methane/air flame to $\pm$0.25 cm/s. The overall accuracy of the burning velocities including the uncertainty from the employed mass flow controllers (MFCs) was evaluated to be better than $\pm$0.35 cm/s. A novel method for on line MFC calibrations was proposed, which in principle can be used not only to remove the uncertainties introduced by the MFCs but also to reduce substantially the error bars in the equivalent ratio values. Possible error bars from other resource was also discussed.

Acknowledgements

This work has been financed by SSF (Swedish Foundation for Strategic Research) and the Swedish Energy Agency through CECOST (Centre for Combustion Science and Technology) and VR (Swedish Research Council).

References

[1] M.J. Brown, D.B. Smith, S.C. Taylor, *Combust. Flame* 117 (1999) 652–656.
[2] C.K. Wu, C.K. Law, *Proc. Combust. Inst.* 20 (1984) 1941–1949.
[3] C.M. Vagelopoulos, F.N. Egolfopoulos, C.K. Law, *Proc. Combust. Inst.* 25 (1994) 1341–1347.
[4] F.N. Egolfopoulos, C.K. Law, *Proc. Combust. Inst.* 23 (1990) 333–340.
[5] K.T. Aung, M.I. Hassan, G.M. Faeth, *Combust. Flame* 109 (1997) 1–24.
[6] O.C. Kwon, G.M. Faeth, *Combust. Flame* 124 (2001) 590–610.
[7] T. Tahtouh, F. Halter, C. Mounaim-Rousselle, Combust. Flame 156 (9) (2009) 1735–1743.
[8] L.P.H. de Goey, A. van Maaren, R.M. Quax, *Combust. Sci. Technol.* 92 (1993) 201–207.
[9] A. van Maaren, D.S. Thung, L.P.H. de Goey, *Combust. Sci. Technol.* 96 (1994) 327–344.
[10] A. van Maaren, L.P.H. de Goey, *Combust. Sci. Technol.* 102 (1994) 309–314.
[11] I.V. Dyakov, A.A. Konnov, J. de Ruyck, K.J. Bosschaart, E.C.M. Brock, L.P.H. de Goey, *Combust. Sci. Technol.* 172 (2001) 81–96.
[12] K.J. Bosschaart, L.P.H. de Goey, *Combust. Flame* 136 (2004) 261–269.
[13] K.J. Bosschaart, L.P.H. de Goey, *Combust. Flame* 132 (2003) 170–180.
[14] S.W. Allison, G.T. Gillies, *Rev. Sci. Instrum.* 68 (1997) 2615.
[15] A. Khalid, K. Kontis, *Sensors* 8 (2008) 5673.
[16] H. Seyfried, M. Richter, K.-H. Nilsson, M. Aldén, H. Schmidt, *Collection of Technical Papers – 45th AIAA Aerospace Sciences Meeting*, vol. 18, 2007, p. 12794.
[17] T. Husberg, S. Girja, I. Denbratt, A. Omrane, M. Aldén, J. Engström, SAE 2005-01-1646, 2005.
[18] J. Brubach, J.P. Feist, A. Dreizler, *Measur. Sci. Technol.* 19 (2008).
[19] L.J. Dowell, G.T. Gillies, *Rev. Sci. Instrum.* 62 (1991) 242.
[20] A. Omrane, F. Ossler, M. Aldén, *Proc. Combust. Inst.* 29 (2003) 2653.

[21] H. Seyfried, G. Särner, A. Omrane, M. Richter, M. Aldén, ASME, GT2005-69058, 2005.
[22] G. Särner, M. Richter, M. Aldén, *Measur. Sci. Technol.* 19 (12) (2008) 125304.
[23] A.L. Fischer, *Photonics Spectra* 40 (2006) 95.
[24] G. Särner, M. Richter, M. Aldén, *Opt. Lett.* 33 (2008) 1327.
[25] Y. Zhang, B.X. Lin, X.K. Sun, Z.X. Fu, *Appl. Phys. Lett.* 86 (2005).
[26] A. van Maaren, L.P.H. de Goey, *Combust. Sci. Technol.* 99 (1994) 105.
[27] A. van Maaren, L.P.H. de Goey, R. van de Velde, *Temperature measurements in flat laminar premixed gas/air flames by Laser Doppler Velocimetry*, in: K.K. Kuo (Ed.), *Non-intrusive Combustion Diagnostics*, Begell House, 1994, pp. 544–551.
[28] L.P.H. de Goey, L.M.T. Somers, W.M.M.L. Bosch, R.M.M. Mallens, *Combust. Sci. Technol.* 104 (1995) 387.
[29] A. van Maaren, D.S. Thung, L.P.H. de Goey, *Combust. Sci. Technol.* 96 (1994) 327.
[30] R.T.E. Hermanns, Ph.D. Thesis, Eindhoven University of Technology, 2007.

Paper V

Investigation and compensation of the nonlinear response in photomultiplier tubes for quantitative single-shot measurements

C. Knappe, J. Lindén, F. Abou Nada, M. Richter, and M. Aldén
Division of Combustion Physics, Lund University, Box 118, SE-221 00 Lund, Sweden

(Received 6 December 2011; accepted 23 February 2012; published online 15 March 2012)

A concept for time-sensitive optical detectors is described that shows how to confirm whether the detection device is operating in the linear response regime. By evaluating the recorded time decay of a thermographic phosphor, even weak saturation effects far from obvious situations can be identified and further related to either optical or electrical saturation. The concept has been validated by running a PMT detector close to saturation and exposing it to the optical signal decay of two different thermographic phosphors, La_2O_2S:Eu and $CdWO_4$. It was confirmed that short but intense light exposures at the beginning of an individual time decay influence the detector response for the rest of the decaying signal including temporal areas, where the anode current has dropped well below the manufacturer specified current limit. Such situations are common when applying, e.g., phosphor thermometry where it is necessary to retrieve the full decay curve from a single-shot event, i.e., standard techniques based on single-photon counting are omitted. Finally, means of compensation are introduced in order to facilitate the retrieval of useful information from the measurement data when operation in the non-linear response regime is inevitable. © *2012 American Institute of Physics*. [http://dx.doi.org/10.1063/1.3693618]

I. INTRODUCTION

The purpose of an optical detector is to convert incoming light into a measurable signal, principally electronic, which is proportional to the light intensity. While there are many different types of detectors, all are applied in one of two ways: to reproduce light intensity in a temporally resolved manner, e.g., photodiodes or photomultiplier tubes (PMTs); to integrate the light intensity over time, e.g., CCD detectors. Both applications can be used for quantitative measurements, providing that the signal response is linear (linear response region), or that corrections can be made when the input-to-output signal is nonlinear. The linear response region for detectors is often defined relative to the noise threshold and a maximum value such as anode current or digitizer limit; however, in practice, saturation effects can be seen at values much lower than these perceived extrema.

When measuring phosphorescence decay times with a PMT, for investigation of phosphor thermometry, it was found that the photomultiplier settings for gain and exposure level were linked to variations in the measured decay time, though levels were below the proscribed limits. This behavior was consistent with saturation phenomena. The purpose of this paper is to present a simple method to determine the true linear response region for any temporally resolved optical detector, as well as presenting a method to correct measurements outside the linear response region. For consideration of similar effects in integrating optical detectors see Ref. 1, where an image intensified CCD is investigated.

Photomultiplier tubes are perhaps the most widely used electronic tool in spectroscopy, having been applied in every manner of optical measurement.[2–4] The PMT provides opto-electrical conversion combined with internal electrical amplification, see Figure 1, making it suitable for low light level measurements. They are temporally resolved detectors; depending on circuitry they can resolve, in real time, the impingement of single photons on the detector, or measure continuous streams of photons. It is the ability of a PMT to operate continuously that is used in phosphor thermometry to measure the temperature dependent phosphorescence decay. For a more in-depth description of the working principles of a PMT, see Hakamata *et al.*[5] For a detailed model of photomultiplier gain, see Moatti.[6]

Significant efforts have been made to characterize nonlinearity in PMTs thus far. Sauerbrey,[7] for example, published a substantial experimental study of PMT nonlinearity in which five essentially independent sources of photomultiplier nonlinearity were measured. According to Ref. 7 some sources of PMT nonlinearity can be easily avoided as they are introduced by external circuitry connected to the PMT. Complementary to Sauerbrey's work, Aspnes and Studna[8] designed a circuit for improving photomultiplier linearity. More recent work dealt with the calibration of non-linear photomultiplier response. In 2003, Vićić *et al.*[9] used an ultraviolet pulsed-light source and determined the response of a photomultiplier within a range of light intensities from single photoelectrons up to well beyond the linear response region. Whilst

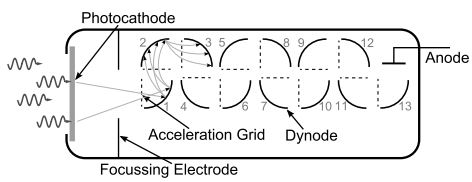

FIG. 1. Schematic construction of a PMT with 13 dynodes.

maintaining an "excellent agreement" between their measured data and the fitted model, Vićić admitted that the procedure described in Ref. 9 was "extremely computer-intensive."

It is not in the scope of this paper to present yet another in-depth discussion of PMT physics; rather, a rapid and easily accessible tool is constructed to properly evaluate the operating region of the PMT. To this end, a simple view of PMT behavior was adopted for temporally resolved, non-photon-counting instances. Ideally, the PMT response is a linear relationship between photon flux and output current. The linear response is susceptible to two independent processes that drive the PMT into the nonlinear response region when approaching saturation.[10]

The first process, photocathode bleaching, occurs when the photocathode is struck by a sufficient number of photons per time interval to deplete the valence band in the photocathode. A radial voltage drop at the photocathode is caused by large current densities and a certain time is needed for the photocathode to recover and re-enter the linear response region.

The accumulation of local electric fields inside the PMT accounts for the second process. At high gains, a space charge builds at the anode and last few dynode stages. This space charge electrically shields and decelerates advancing electrons. Hence, increasing electrical gain above a certain threshold drives the dynode chain into the saturated region. This is often considered as the major source of saturation in PMTs.[11]

The total detector response, can be understood as the product of the optical- (photocathode) and the electrical (dynode chain) response functions. These processes are not discrete, as the number of electrons arriving at the anode, and thus gain saturation, depends on the photocathode sensitivity and the amount of incoming light. Alternatively, reducing incoming light intensities will suppress the development of a space charge (as does lowering gain or applying a higher voltage across the last few dynodes). As a result, uncorrected quantitative measurements can only be performed if the PMT is operated in the linear region for both of these two responses.

Most PMTs are specified to run at a maximum DC output current of 100 μA,[5,12] which equals approximately 6×10^5 electrons/ns released at the last dynode. This current value can be understood as the absolute limit for linear dynode operation, though the photocathode may already be saturated due to the incoming light flux. According to Becker and Hickl,[13] this maximum output current can be increased almost by a factor of 1000 to around 100 mA when operating in the PMT in "pulsed" mode, mostly because the PMT can recover, to some extent, from bleaching and space charge accumulation in between two adjacent pulses.

A motivation for extending the output current beyond 100 μA is to increase the output signal: most PMTs come with a load resistance of 50 Ω, meaning that the readout instrument's input resistance has to match in order to avoid back and forth reflection ("ringing") of the signal in the cable. By Ohm's law, a current of 100 μA over 50 Ω generates a maximum voltage of 5 mV, close to the lower resolution limit of common digital oscilloscopes. This often results in unacceptably low signal/noise ratios when digitizing the analog current, without time averaging or special amplification electronics. When approaching pulse lengths of as much as a few milliseconds, as in some cases of phosphorescence, it is dubious that these enhanced limits still apply, and caution should be exercised when extending the PMT workspace by exceeding the anode's current limit.

II. DATA ACQUISITION AND EVALUATION

Temporally, resolved intensity decay curves were acquired for two different phosphors (La_2O_2S:Eu with 2 at. % Eu and $CdWO_4$) in order to generate different optical intensity time-distributions that the detector has to reproduce. The major difference between these two phosphors is an intense, short-lived, fluorescence peak, that is present for the La_2O_2S:Eu, but is missing in the $CdWO_4$ time decay (see Figure 2).

Each phosphor was excited by a 10 Hz pulsed, Q-switched and frequency tripled (355 nm, La_2O_2S:Eu) or frequency quadrupled (266 nm, $CdWO_4$) Nd:YAG laser (Quantel Brilliant B). Low laser pulse energies between 70 and 140 μJ were used in order to avoid saturating the phosphor. The resulting phosphorescence was imaged onto a photomultiplier module (Hamamatsu H6780-04) after passing an interference filter, centered at 540 nm (FWHM = 10 nm) for the La_2O_2S:Eu phosphor and 450 nm for $CdWO_4$ (FWHM = 40 nm). The filters were placed in front of the detector to eliminate spurious laser radiation and to spectrally isolate the phosphorescence emission.

In the PMT, a nominal electrical gain can be chosen within the range of 10^2 to 10^6 (Ref. 12), depending on the amount of optical signal that is available for collection. The gain number is defined by the ratio of output electrons divided by photocathode electrons. The photomultiplier output current was read out by a 350 MHz digital oscilloscope (Lecroy WaveRunner WA6030) at an input resistance of 50 Ω, allowing sampling of decay times as short as a few ns at a dynamic range of 8 bit.

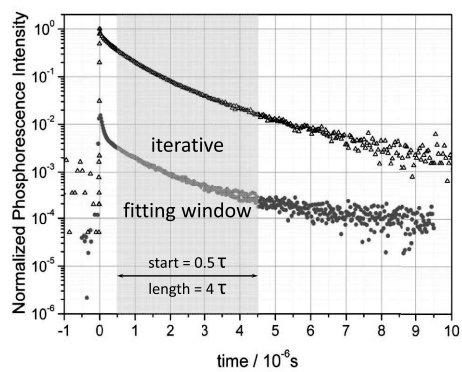

FIG. 2. A comparison of similar phosphorescence decays for La_2O_2S:Eu (at 540 nm, T = 518 K blue dots) and $CdWO_4$ (at 450 nm, T = 387 K, black triangles). The gray area indicates the time window in which the decay time is determined.

Both phosphors offer emission peaks that decay exponentially after laser excitation. The time decay can be approximated by

$$I = I_0 \cdot \exp\left(-\frac{t}{\tau}\right), \tag{1}$$

where I_0 is the initial emission intensity, t is time and τ is the decay time of the phosphorescence, i.e., the time after which the intensity has decreased to $1/e$ of the initial emission I_0.

To extract the time constant τ from the measured decay curves, a Levenberg-Marquard fitting algorithm (MATLAB) has been applied, that varies I_0 and τ and iteratively adapts the $(n+1)$th fitting window region according to the nth evaluated decay time τ_n until stability is achieved. As indicated in Figure 2 (grayed out), the fitting window was chosen to range from $0.5\tau_n$ to $4.5\tau_n$. Further details on the iterative decay time algorithm can be found in Ref. 14.

For obvious reasons, the recorded phosphorescence decay time τ is a measure of the time-distribution of the detector output signal $S_{out}(t)$. Therefore, τ is also a suitable target for analyzing the linearity of a detector's input-to-output signal conversion. In other words, the detector operates in the linear region when the evaluated decay time is purely dependent on the light source and thus insusceptible to minor changes regarding detector gain and light exposure. Consequently, the detector linearity can be analyzed either by changing the electrical amplification (gain) or by attenuating the light before it hits the detector. In case of linear operation the evaluated decay time will be constant, regardless these changes that were made on the detector side.

In a simplified approach that emphasizes how detector saturation distorts the output signal, detector response functions were simulated according to

$$S_{out}(I_{in}) = S_{max} \cdot \left[1 - \exp\left(-\frac{I_{in}}{S_{max}}\right)\right] \tag{2}$$

where I_{in} is the incoming signal intensity and S_{max} is the maximum signal output intensity. Such response curves were plotted in Figure 3(a) together with the response curve of an ideal detector indicated by the black solid line. By inserting a phosphorescence intensity distribution as I_{in} into equation (2), a distorted detector output signal can be obtained, which is shown in part (b) of Figure 3 for each corresponding response curve from Fig. 3(a). A least squares exponential fit according to equation (1) was performed within the indicated time window illustrated in grey. The graph in Figure 3(c) displays the associated decay times, which clearly depend on the saturation level, that was defined by how much the initial output (see Fig. 3(b), black curve) signal was reduced due to detector saturation in percentage.

As displayed in Figure 4, the time decays of $CdWO_4$ and La_2O_2S:Eu exhibit a strong temperature dependence between 300 K and 600 K, which makes them a sensitive remote temperature sensor, for example in engine applications.[4,15,16]

Both phosphors combined have a common range of decay times from 10 μs down to 100 ns. This broad overlap region is beneficial as it allows achieving similar decay times by keeping the two phosphors at different temperatures. This

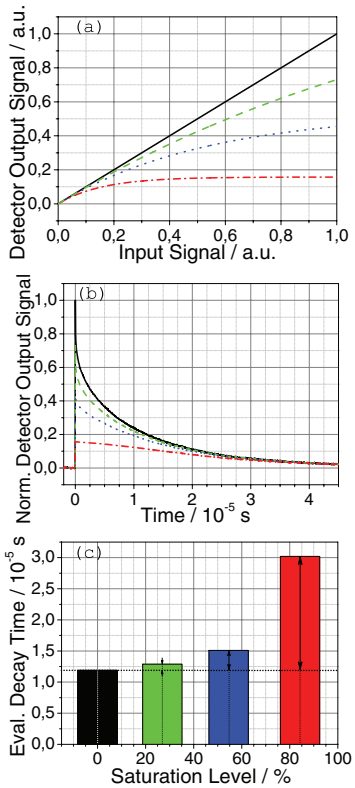

FIG. 3. Example on how different saturation states in the detector (a) change the shape of the output time-signal (b) and the evaluated decay time (c). The time decay in black corresponds to an average of 100 measured decay curves from La_2O_2S:Eu at room temperature.

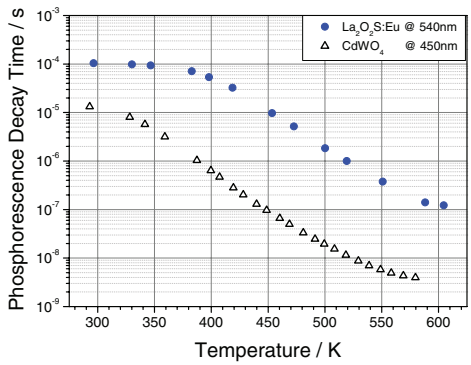

FIG. 4. Phosphorescence decay time as function of temperature for La_2O_2S:Eu and $CdWO_4$.

in turn enables the impact of an intense initial peak (present for La_2O_2S:Eu, absent for $CdWO_4$) on the detector response to be studied by comparison under otherwise similar operating conditions.

III. RESULTS

A. Saturation analysis using phosphorescence time decay

For 100 consecutive laser shots at room temperature, the La_2O_2S:Eu phosphorescence decay time τ is displayed in Figure 5(a). At a PMT gain of 4700 and mean laser pulse energy of 70 μJ, the spread in phosphorescence decay time ranges from 103.5 μs to 104.2 μs. According to the measurement data displayed in Figure 4, the spread corresponds to a temperature interval from 294 K to 299 K. What initially looks like a statistical distribution due to noise in the signal or temperature variation (see Figure 5(a)) becomes a linear trend when the measurement points are re-arranged according to the output signal voltage $S_{\text{out}}(t = 0.5\tau)$, see Figure 5(b). $S_{\text{out}}(t = 0.5\tau)$ is equal to the very first readout voltage within the fitting window, see Figure 2 for an example. Its average value is 4.75 mV, which corresponds to 95 μA in PMT output current at 50 Ω oscilloscope input resistance. The spread in voltage is about 3 % and corresponds to laser energy shot-to-shot variations that induced proportionally shifting phosphorescence yields. According to Ref. 12, an output current of 95 μA is still below the 100 μA specified limit of the cw PMT operation. However only half a decay time earlier (see Figure 2), where the phosphorescence signal coincides with spurious laser reflexes, i.e., 52 μs prior to the fitting window start position, the PMT was struck by far more photons, corresponding to 20 mA PMT output current (not shown in Figure 5) which is 200 times higher than the specified cw limit, but still only about 1/5 of what would be the limit for pulsed operation according to Ref. 13.

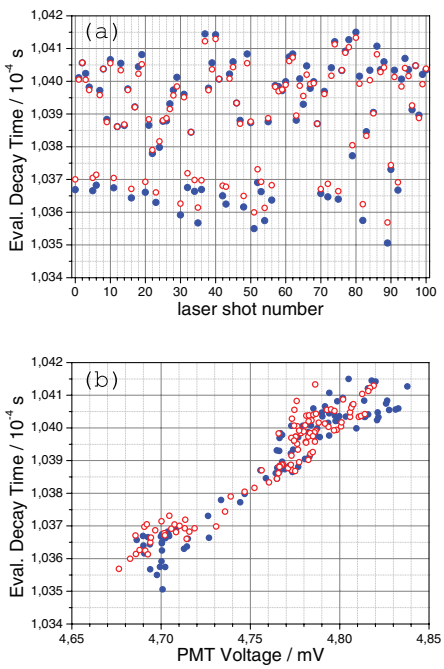

FIG. 5. La_2O_2S:Eu phosphorescence decay time at 296 K using gain 4700 and 100 consecutive laser shots at ~70 μJ (a). In graph (b), the same data has been re-arranged according to the first output voltage within the fitting window $S_{\text{out}}(t = 0.5\tau)$. Blue dots represent decay times obtained by using an iteratively changing time window (see Ref. 14) whereas the red circles illustrate the same data evaluated in a fixed time window.

The results from Figure 5 are obtained taking two different approaches: An iteratively changing fitting window that adapts its size and position according to the length of each individual decay curve (red circles) and a fixed time window for all curves, which was determined by the average iterative fitting window (blue dots). As can be seen in Figure 5, the method of data reduction has an influence on its own upon the obtained results. Similarly, it can be shown that even low level spurious background radiation can have an effect on measurement accuracy. However, being able to reproduce the intensity dependence of τ with a fixed time window is an evidence for a physical change in decay time, showing that these effects are not simply induced by evaluating different time windows. Even though the results in Figure 5(b) overlap quite nicely, the slope for the iterative time window (blue dots) is a little higher accounting for the slight differences in the window positions: Due to the slight multi-exponential time decay that characterizes phosphorescence emitted by La_2O_2S:Eu (see Figure 2), a decay time evaluated in an earlier part of the curve results in a smaller value compared to a decay time evaluated slightly later in the same curve. In summary, the trends shown in Figure 5 can clearly be interpreted as a distortion of the temporal signal shape that correlates with the amount of light hitting the PMT. The different intensities were induced by laser shot-to-shot variations and cannot be avoided, which makes this dependence a concern for any quantitative, time dependent optical measurement involving lasers. The positive slope is in agreement with what would be expected from a saturation effect (see Figure 3). However, it remains yet unclear, whether the saturation was caused by photocathode bleaching and/or by applying too high electrical amplification.

For investigating the source of saturation further, Figure 6 displays two measurement series of time decays, taken at 382 K, this time using two different gains (4700 and 7400) at constant mean laser energy of 70 μJ.

The two point clusters shown in Figure 6 correspond to the lower gain value (left) and the higher gain (right), and incorporate a series of 100 laser shots each, represented by the spread in x-direction. For a linear responding detector, the two point clusters in Figure 6 were expected to collapse in y-direction into one single decay time. Hence, PMT saturation shows its effect by linearly distributing the decay times as a function of PMT output

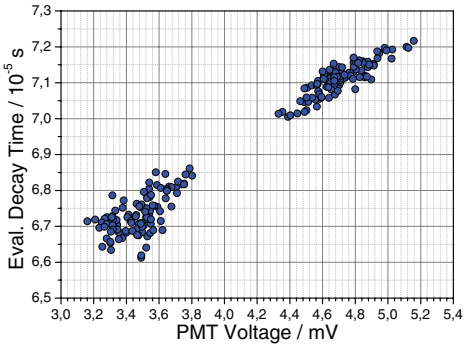

FIG. 6. La_2O_2S:Eu phosphorescence decay times at 382 K using two gains, 4700 (left group) and 7400 (right group) with 100 consecutive laser shots at ~70 μJ each. The data has been plotted as a function of the PMT Voltage $S_{out}(t = 0.5\tau)$.

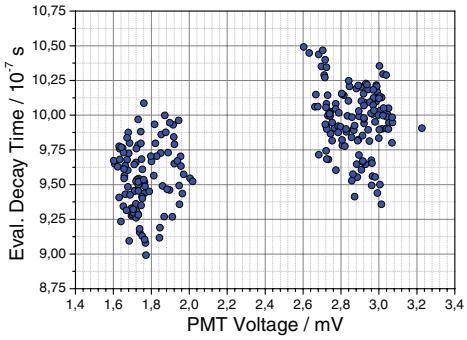

FIG. 7. La_2O_2S:Eu phosphorescence decay times at 519 K using two gains, 4700 (left) and 8400 (right), with 100 consecutive laser shots at ~ 70 μJ each.

voltage. An interesting observation is that both clusters are positioned to each other such that the individual slope from each gain measurement matches the other data cluster. In other words, the slope caused by variation from the photocathode's amount of primary electrons (shot-to-shot based) is identical to the cluster offset slope that is caused by elevating the gain. From these observations it is possible to conclude the following:

1. Since both point clusters show a non-constant decay time distribution – both gain measurement are subject to a nonlinear detector response.
2. The gain-driven cluster offset indicates electrical saturation: If the slope within each cluster was only due to photocathode saturation – the second point cluster would result in similar decay times obtained at higher output voltages, i.e., a cluster offset parallel to the x-direction.
3. The saturation seen in Figure 6 is purely gain-driven with no significant contributions of photocathode saturation, meaning that if the number of primary photoelectrons would be increased, the decay curve shape would change the same way as if the gain is increased. If also the photocathode was subject to saturation, the individual point cluster slopes would not match the gain-based cluster offset slope.

Figure 7 shows data that is similar to those that was presented in Figure 6, only this time at an elevated temperature of 519 K. The laser energy was kept low again to 70 μJ and two gain values are compared to each other (4700 and 8400).

From a comparison with Figure 6 the cluster offset slope is a factor of 84 smaller in Figure 7. Also, the relative decay time spread in each measurement increased as shorter decay times become more difficult to evaluate. Since the phosphorescence intensity decreases towards higher temperatures, the PMT voltage at gain 4700 for 382 K (see Figure 6) is almost twice as high as for 519 K (see Figure 7) for the same mean laser pulse energy. Additionally, the decay time at 519 K was 71 times shorter than for 382 K in Figure 6, reducing the mean light exposure time. Therefore less load was put on the dynode chain, which could explain the reduced cluster offset slope, seen in Figure 7.

B. Compensation approach

Operating outside the linear workspace of a detector is often required due to the higher signal intensity availed. However, the distortions in the response signal due to saturation are a source of systematic error. Nevertheless, a compensation that accounts and corrects for these effects is possible, providing systematic changes in the response are mapped into a library and thus can be sufficiently predicted. In practice, a biased result originating from a slightly saturated signal can be transformed into an unbiased result by extrapolating it towards lower signal levels into the linear operating region, using a slope proposed by the detector library. For probe techniques that rely on calibration rather than an absolute physical quantity, such as thermographic phosphorescence, the compensation is simplified because the reference is not restricted to the linear detector operating region: Any signal output can become a reference for extrapolation. For further considerations, the reference was chosen as the PMT-readout voltage $S_r(t = 0.5\tau)$ recorded over 50 Ω.

The upper part (a) of Figure 8 shows the PMT decay response slope $d\tau/dS$ for La_2O_2S:Eu decays as a function phosphorescence decay time (red circles). In graph (b) on the bottom of Figure 8, $d\tau/dS$ is presented in red as a function of temperature together with corresponding decay time values (blue dots) that were taken from the calibration curve in Figure 4. The spline interpolation (red dashed line) can be used to correct decay times obtained in the nonlinear detector regime. It refers to an output reference voltage of $S_r(t = 0.5\tau) = 4.8$ mV at the start of the decay window, for which the calibration was performed.

As the comparison between Figure 6 and 7 suggested, the slope declines for shorter time decays, probably due to the competition between saturation and space charge recovery that was briefly discussed above. The spline interpolation

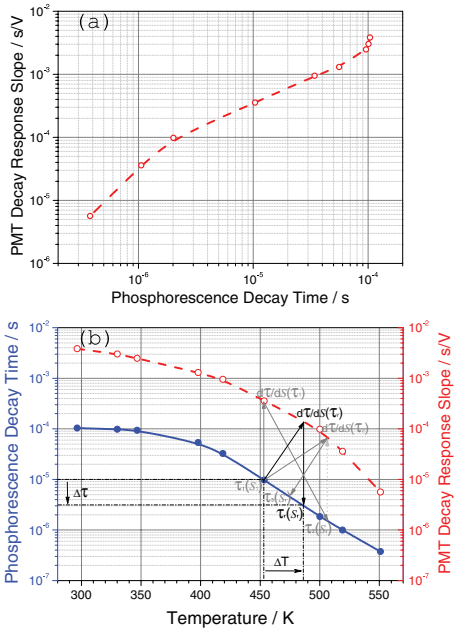

FIG. 8. PMT decay response slope for La_2O_2S:Eu (red circles) as a function of phosphorescence decay time (a) and as a function of temperature (b). The black arrows in graph (b) indicate how a measured decay time $\tau_1(S_1)$ can be iteratively corrected towards τ_r at reference signal output S_r ($< S_1$) for which the phosphor was calibrated (blue dots).

indicated in red, can further be used for compensating any obtained decay time towards the reference output voltage of $S_r(t = 0.5\tau) = 4.8$ mV, which refers to the first output voltage within the decay evaluation window. Knowing how detector distorted decay times evolve, the correction of τ_1 recorded at a output voltage of $S_1(t = 0.5\tau)$ can be performed to the reference value τ_r at reference voltage S_n according to equation (3),

$$\tau_r = \tau_1 - \left.\frac{d\tau}{dS}\right|_{\tau_r} \cdot (S_1 - S_r). \quad (3)$$

Although $d\tau/dS(\tau_r)$ is initially unknown because it requires knowledge over τ_r, it can be approached iteratively by starting with $d\tau/dS(\tau_1)$. For $d\tau/dS > 0$ and $S_1 > S_r$ it follows that $\tau_1 > \tau_r$ and $d\tau/dS(\tau_1) > d\tau/dS(\tau_r)$ as seen in Figure 8(b), meaning that the first iteration $\tau_2(S_r)$ will underestimate τ_r when correcting from S_1 against S_r. In a second iteration step, the slope $d\tau/dS(\tau_2) < d\tau/dS(\tau_r)$ can be used to correct $\tau_1(S_1)$ towards $\tau_3(S_r) < \tau_1(S_1)$, which in term is an overestimation of τ_r. Since τ_3 already is a closer estimate of τ_r compared to τ_1, the iterative solution converges oscillating towards τ_r, granted that $d\tau/dS$ is monotonic. Considering $d\tau/dS > 0$ and signal intensities smaller than the reference, i.e., $S_1 < S_r$, a similar

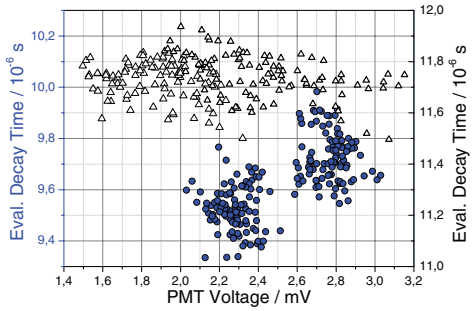

FIG. 9. Comparison of response slopes for two different phosphors (blue dots: La_2O_2S:Eu at 473 K; black triangles: $CdWO_4$ at 308 K) at similar decay times, using equal PMT gains (4700 and 6300) and laser energies that yield the same decay signal voltages.

argumentation results in τ_i converging towards $\tau_r > \tau_1$, however this time without oscillations. In summary, if measurements of a certain decay time are taken at output voltages S_1 different from the reference signal S_r for which the calibration $d\tau/dS$ (see Figure 8) was performed, the decay time has first to be corrected towards that reference signal intensity before the decay time can be converted into a temperature.

It is, however, important that the PMT is corrected for the same type of signal/phosphor, as indicated by the earlier assumption that the detector might be affected by pre-existing saturation states. To test this hypothesis, the PMT was now used to detect similar time decays from La_2O_2S:Eu and $CdWO_4$ at laser energies adjusted to generate the same output current for both signals within the investigated time window. Since the gain was identical in both cases, the laser energy was adapted to compensate for the two different phosphorescence yields and to account for the spectral photocathode sensitivity within the corresponding emission wavelengths such that the same amount of primary electrons were released from the photocathode. The experiment is set up in a way that an ideal time gated PMT, switched on only during the evaluated time window, should have no means to distinguish the two different phosphorescence emissions. However the PMT used here also recorded a peak voltage prior to the evaluation window, that was about 54 times higher for the La_2O_2S:Eu phosphor than for $CdWO_4$. In Figure 9, the results for the two cases are displayed, showing a horizontal response distribution for $CdWO_4$ in contrast to the results obtained with La_2O_2S:Eu. The bigger spread in PMT voltage for $CdWO_4$ is due the higher signal yield for $CdWO_4$ that required less, and thus more unstable, laser excitation energy.

According to Figure 9, the decay time slope has drastically changed by the presence of the peak prior to the fitting window in which the decay time was evaluated. It can thus be concluded that strong and saturating peaks in the beginning have an impact on the time progression of the detected signal. As long as these peaks cannot be avoided by some sort of time-gating, detector compensation should also take into account the time dependent photon emission curve of the light source that is to be investigated.

IV. CONCLUSIONS

In this paper, a novel test procedure is described that can be used to determine the linear operating region of any optical detector, capable of performing time-resolved measurements. Additionally, information is provided on how such a detector can be operated outside the linear regime as is often required when signal decay time information must be retrieved from single-shot measurements. The procedure was applied to the extended afterglow of thermographic phosphors and compares evaluated signal decay times as a function of electrical gain and incident intensity by creating a detector response database. By evaluating and comparing the recorded time decay within the response database even weak saturation effects (far from obvious situations) can be identified and further related to either photocathode or dynode saturation.

These saturation events introduce a systematic error on quantitative measurements results. Such errors can be corrected towards a reference value from the detector's response database. The reference value needs to be part of the linear response regime in most cases. However, if the reference value is used only to calibrate another quantity – as it is for phosphor thermometry – any value from the detector response database can be chosen as a reference.

Furthermore, a comparison of the decay signals from $CdWO_4$ and La_2O_2S:Eu has shown that an accurate correction for PMT non-linearity should also consider the history of the signal, e.g., the photo-current at the start of the decay. It is thus important from a compensation point of view to use the same sort of signal for both, the actual measurement and the generation of the response database.

ACKNOWLEDGMENTS

This work was financially supported by the HELIOS research project within the 7th EU framework program for Research and Technical Development/Transportation and the research project D60, financed by the Swedish Energy Agency. The authors gratefully acknowledge A. W. Sloman for helpful discussions.

[1]J. Lindén, C. Knappe, M. Richter, and M. Aldén, Meas. Sci. Technol. **23**, 035201 (2012).
[2]M. P. Bristow, Appl. Opt. **37**, 6468 (1997).
[3]H. Bladh, J. Johnsson, and P. E. Bengtsson, Appl. Phys. B **96**, 645 (2009).
[4]C. Knappe, P. Andersson, M. Algotsson, M. Richter, J. Lindén, M. Tunér, B. Johansson, and M. Aldén, SAE Int. J. Engines **4**, 1689 (2011).
[5]T. Hakamata, H. Kume, K. Okano, K. Tomiyama, A. Kamiya, Y. Yoshizawa, H. Matsui, I. Otsu, T. Taguchi, Y. Kawai, H. Yamaguchi, K. Suzuki, S. Suzuki, T. Morita, and D. Uchizono, *Photomultiplier Tubes – Basics and Applications* (Hamamatsu Photonics K.K., Iwata City, 2007).
[6]P. Moatti, L'Onde Electrique **43**, 787 (1963).
[7]G. Sauerbrey, Appl. Opt. **11**, 2576 (1972).
[8]D. E. Aspnes and A. A. Studna, Rev. Sci. Instrum. **49**, 291 (1978).
[9]M. Vićić, L. G. Sobotka, J. F. Williamson, R. J. Charity, and J. M. Elson, Nucl. Instrum. Methods A **507**, 636 (2003).
[10]D. H. Hartman, Rev. Sc. Instrum. **49**, 1130 (1978).
[11]H. Kunz, Metrologia **5**, 88 (1969).
[12]H6780-04 PMT Datasheet, http://sales.hamamatsu.com/assets/pdf/parts_H/H6780-04.pdf.
[13]W. Becker and H. Hickl, *How (and why not) to Amplify PMT Signals* (Becker & Hickl GmbH, Berlin, 2000), http://www.becker-hickl.de/pdf/ampmt.pdf.
[14]J. Brübach, J. Janicka, and A. Dreizler, Opt. Las. Eng. **47**, 75 (2009).
[15]G. Särner, M. Richter, and M. Aldén, Meas. Sci. Technol. **19**(12), (2008).
[16]A. Omrane, G. Särner, and M. Aldén, Appl. Phys. B **79**, 431 (2004).

Paper VI

IOP PUBLISHING MEASUREMENT SCIENCE AND TECHNOLOGY
Meas. Sci. Technol. **23** (2012) 035201 (8pp) doi:10.1088/0957-0233/23/3/035201

Limitations of ICCD detectors and optimized 2D phosphor thermometry

J Lindén, C Knappe, M Richter and M Aldén

Division of Combustion Physics, Lund University, Box 118, S-22100 Lund, Sweden

E-mail: johannes.linden@forbrf.lth.se

Received 7 July 2011, in final form 25 October 2011
Published 25 January 2012
Online at stacks.iop.org/MST/23/035201

Abstract
This paper presents investigations on the limitations of intensified CCD (ICCD) cameras when performing quantitative 2D temperature measurements using thermographic phosphors. The temperature is evaluated using a two-color ratio technique, which demands high signal linearity of the detector. However, this work shows that the ICCD cameras used suffer from nonlinearity at levels of irradiance that do not necessarily produce particularly high count levels, i.e. well below the saturation limit of the A/D converter. For the phosphor thermometry, this results in false absolute temperature readings and decreased measurement precision. The results show that there is a useful workspace in the irradiance/camera gain combination where the detector should preferably be used. A response function for the ICCD camera used is constructed. Furthermore, in order to perform quantitative measurements, there is an upper limit of counts that should not be exceeded. This limit must be investigated for each experimental configuration since it depends on the characteristics of the specific light source and also varies between different cameras.

Keywords: laser-induced phosphorescence, thermographic phosphors, thermometry, image intensifier, ICCD detectors, saturation

(Some figures may appear in colour only in the online journal)

1. Introduction

The use of intensified CCD (ICCD) cameras is widely spread in many research disciplines. For 2D detectors such as CCD cameras, the most common intensifiers consist of three functional units: a photocathode, a microchannel plate (MCP) and a phosphor screen, see figure 1. The photocathode converts the incident photons to photoelectrons, which are accelerated by an electrical field toward the MCP. This in turn multiplies these electrons which are converted back into photons by the phosphor screen. Lastly these photons are directed to a CCD chip by either an optical fiber bundle or a lens system, and read out as a digital image. The addition of an image intensifier brings certain benefits. Primarily the MCP serves to intensify the signal several orders of magnitude, enabling detection of very weak signals. In addition, by pulsing the control voltage to either the photocathode or the MCP, the image intensifier can serve as a very fast electronic shutter, enabling time gating for short-lived signals which would otherwise have been lost in the interfering background. Furthermore, the photocathode can be made sensitive to UV radiation. Effectively, the image intensifier can frequency shift an incoming UV signal, to which the CCD itself is not sensitive, into the visible range where the CCD has a high sensitivity. Together these features make ICCD cameras very useful in pulsed laser applications, where short laser pulses, of the order of 10 ns duration, are used for visualization of various substances, either by detecting the scattered laser light itself, e.g. Rayleigh scattering, or a signal emitted from the substance induced by the laser light, e.g. laser-induced fluorescence, laser-induced phosphorescence or laser-induced incandescence.

However, it has been shown that ICCD cameras suffer from spatially non-uniform image gain factors and nonlinear response functions [1, 2]. The nonlinearity is mainly due to the onset of saturation within the MCP, when the camera is subjected to high light intensities in combination with excessive gain settings. This falloff in response, or gain saturation, has to do with the MCP recovery process and is caused by the MCP's inability to produce enough secondary electrons from the original photoelectron [3, 4]. In addition,

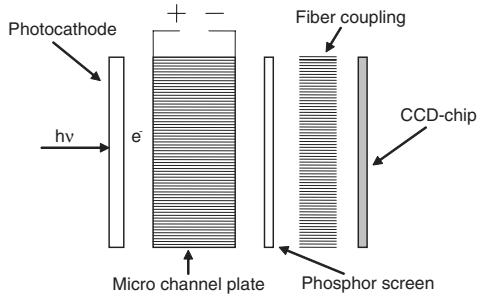

Figure 1. Principles of an image-intensified CCD camera with fiber coupling.

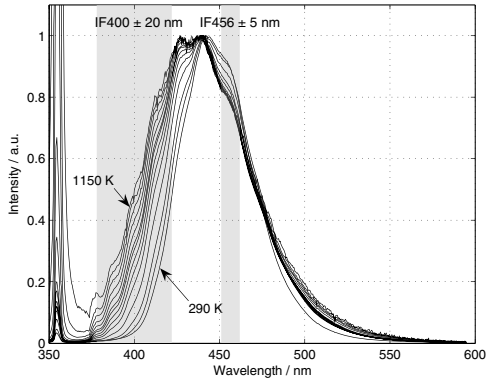

Figure 2. BAM emission spectra at different temperatures when excited with 355 nm laser radiation. The exposure time of the ICCD camera connected to the spectrometer was 8 μs. The transmission regions of the interference filters used are marked out.

bleaching of the photocathode, especially when collecting intense long-lived radiation, can also contribute to saturation. The phosphor screen can also be subject to saturation, causing a nonlinear output due to response falloff at higher intensities. Other saturations can occur after the intensifying process, i.e. in the CCD chip (filled charge wells causing blooming) and in the A/D converter, where the analog charge from the CCD is converted into digital signals. These types of saturations are usually easily avoided, since it is rather obvious when they occur.

Saturation within the intensifier is usually not a concern when performing qualitative measurements; however, quantitative measurements, and in particular the two-color ratio measurement technique, are easily affected by small nonlinearities. The presented work describes how systematic errors caused by nonlinearity due to saturation of the MCP can be avoided by operating the detectors within the proper workspace. In this context, it should be mentioned that in most practical situations it is not obvious when the MCP begins to become subject to gain saturation.

Thermographic phosphors (TPs) have been utilized in temperature measurement applications for several decades. Used for both point and two-dimensional surface measurements, TPs offer a combined temperature-sensitive range that stretches from cryogenic up to 2000 K, depending on the choice of phosphor [5–10].

The TP used in this experiment is $BaMg_2Al_{16}O_{27}$:Eu (BAM) [11]. When excited by a UV-laser pulse at 355 nm it emits broadband phosphorescence peaking at around 440 nm, with a lifetime τ of about 2 μs at room temperature. This peak broadens toward shorter wavelengths as the phosphor is heated; see figure 2. Thus, the phosphorescence intensity of the shorter wavelength side of the peak relative to the longer wavelength side of the peak will increase with temperature. Using two interference filters, one with 10 nm spectral width (FWHM) centered at 456 nm and one with 40 nm (FWHM) centered at 400 nm, a temperature sensitive intensity ratio of the phosphorescence can be determined. A pair of filtered images can be recorded by the use of either two cameras or an image-doubling device (stereoscope) [12]. Dividing the intensities in these images by each other, pixel-by-pixel, will result in a temperature-dependent ratio image. The ratios are then converted into temperatures using a predefined calibration curve derived from measurements performed in a controlled environment. Note that the procedure of utilizing signal ratios rather than absolute intensities brings an inherent advantage with this approach. The resulting ratio becomes independent of the overall phosphorescence intensity and laser excitation intensity. Hence, the technique does not require absolute homogeneous exciting laser profile, phosphor coating nor a linear relation between laser excitation and phosphorescence intensity. Despite the appearance of the spectra in figure 2, it is not recommended to use BAM for temperature measurements higher than 800 K due to degradation mechanisms [13].

The accuracy of these experiments, ideally, depends only on the accuracy of the reference thermocouples used during calibration. The precision on the other hand depends on several factors, such as the S/N ratio, flat field camera correction and the perfection of the image superposition of the two images that are to be divided. As this paper will show, both the accuracy and the precision depend on properties of the camera, which from the beginning are not obvious, but the focus will be kept on the precision.

In order to make quantitative two-color ratio measurements, it is important that the detector response is linear. The presented work shows that when performing quantitative two-color temperature measurements with TPs using a Princeton Instruments PI-MAX2 ICCD camera, it is necessary to stay below a certain count level in order to avoid nonlinear effects which would otherwise cause false absolute values and reduced precision. For the experiments performed, the trade-off between useable irradiance and gain corresponds to a number of counts less than half the numerical range of the A/D converter.

The results presented herein are valid at room temperature for the particular phosphor and individual camera used; tests must be performed with any new system in order to secure correct readouts. However, since the phosphorescence

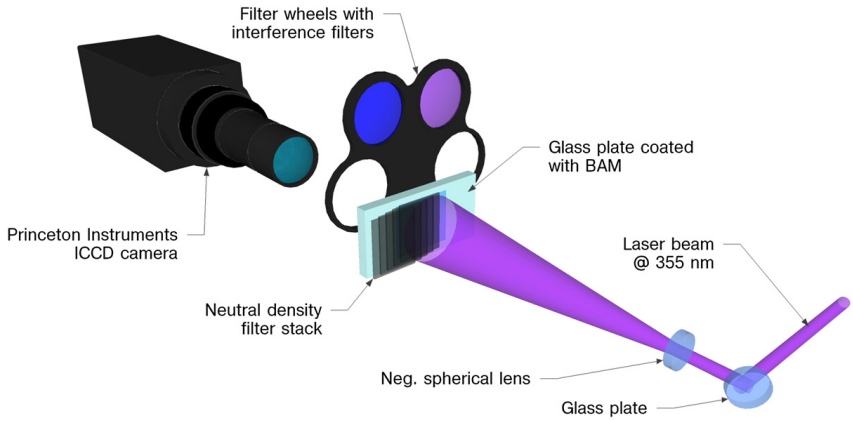

Figure 3. Experimental setup.

generally decreases with higher temperature, it is assumed that nonlinear effects due to too high irradiance will not occur once detector saturation is avoided at room temperature.

2. Experimental work

Figure 3 shows the experimental setup. The laser used is a 10 Hz pulsed Nd:YAG operating at its third harmonic, producing a wavelength of 355 nm with an energy of ∼0.5 mJ/pulse. The laser beam is directed and expanded to illuminate a glass plate surface coated with BAM. The phosphor is applied using an airbrush pen (Rich AB 300) containing a solution of the phosphor, binder (HPC) and ethanol. The thickness of the layer is approximately 10–20 μm. On the camera side of the plate, a filter wheel with appropriate filters is placed. The phosphorescence, seen through the filters, is recorded by a PI-MAX2 ICCD camera. All the measurements are performed at room temperature; thus, it is assumed that the temperature distribution across the coated phosphor surface is homogeneous.

Since this experiment focuses on the measurement error introduced by the ICCD camera rather than evaluating the overall thermometry, it is advisable to suppress extraneous error contributions. Two such errors would be incorrect image superposition and flat field correction, which would be necessary in the case of using two cameras or a stereoscope. In order to eliminate these, only one camera is used for this experiment. By switching the interference filters in front of the camera, the two images would be identical with exception to the wavelength detected and also the pixel-to-pixel variations on the CCD chip would cancel out by the image division. While this approach eliminates the source of errors caused by image superposition and flat field correction, it assumes stability in time. To reduce the influence of shot-to-shot variations in the laser profile, accumulations of ten images were made for each measurement.

As described in the setup, the filter wheel is positioned as close to the phosphor-coated surface as possible, rather than in front of the camera lens, as might be expected. The reason for this is an image distortion introduced by the design of the filters which caused displacement of the focal plane and translation of the image. Since the distortion differs between the two filters, this effect would obstruct straightforward superposition of the two images. This distortion effect would probably be eliminated by the use of higher image quality filters, which were unavailable at the time of the experiment. With the filters positioned close to the coated surface, it is impossible to illuminate the phosphor from the side facing the camera. Hence, the surface is illuminated from the backside, which requires a transparent phosphor substrate (the glass plate). The phosphor is coated on the surface facing the laser; as a result, the glass plate acts as a filter, rejecting spurious UV laser contribution to the recorded images while being transparent for the phosphorescence emission. This arrangement is limited in a realistic application due to both setup issues regarding the interference filters and restriction to measurements with more temporally stable temperatures, since the measurements cannot be performed in a single shot.

In order to investigate the linearity of the camera, different areas of the BAM-coated surface are illuminated with different laser fluences. This is achieved by using a filter stack, consisting of five identical neutral-density filters, successively partwise overlapping each other. By this approach, six different areas of the BAM-coated surface are illuminated, each with different laser fluence: one without any laser attenuation, and five with gradually increasing optical densities. The transmission of the five gradually increasing optical densities was measured to be 9%, 14%, 22%, 39% and 67%.

Figure 4 shows an example of two phosphorescence images (*a* and *b*) and the resulting ratio image (*c*) for one particular gain setting on the image intensifier (150 of 255). At this gain setting the different areas, despite illumination with different laser fluence, result in the same ratio, as can be seen in figure 4(*c*), and thus would read the same temperature as expected. For each area, the mean value and the standard deviation of the ratio is investigated. This is done for 26 different gain settings, spanning 0–250 (max value 255) in

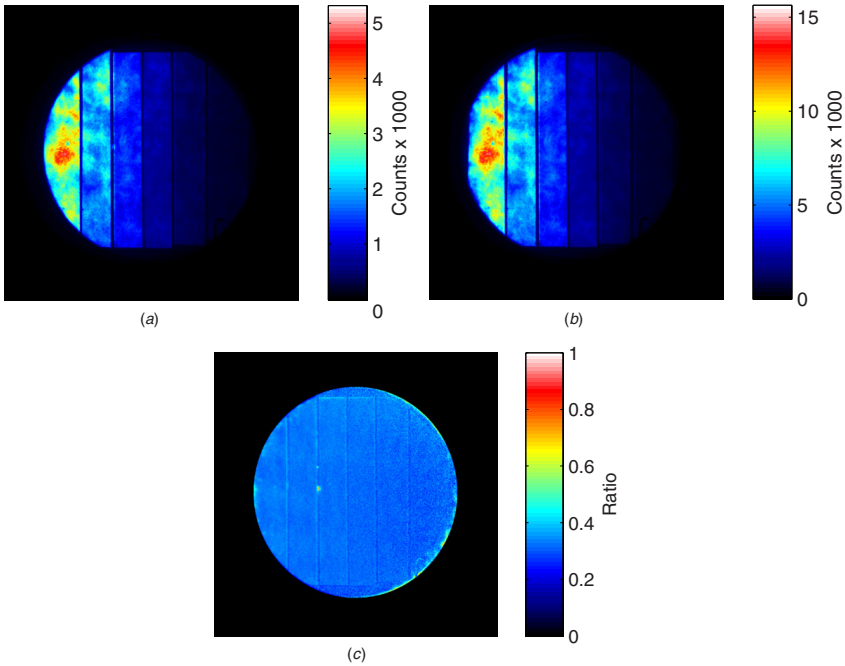

Figure 4. Example of two phosphorescence images achieved through two different interference filters ((*a*) 400 ± 20 nm, (*b*) 456 ± 5 nm) which when divided generate a ratio image (*c*).

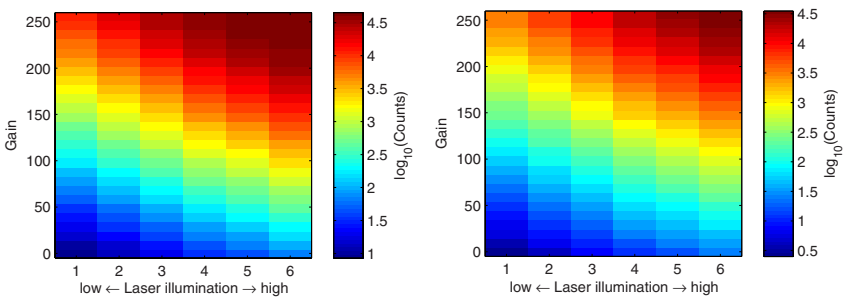

Figure 5. Mean signal in counts for the signals achieved through the IF456 filter (left) and the IF400 filter (right). Note that the count intensity scale is logarithmic.

increments of 10. With six areas of different illumination intensities, this results in 156 different gain and laser fluence combinations investigated. Prior to the experiment, the laser energy is adjusted so that, in the measurement with a gain of 250, the maximum number of counts in the area with highest intensity is just below the saturation level of the 16 bit A/D converter, i.e. 65 535 counts.

3. Results and discussion

Figure 5 displays the measured mean value, in counts, for all 156 different gain and laser fluence combinations for each filter applied (left: the 456 nm interference filter, henceforth IF456, and right: the 400 nm interference filter, henceforth IF400). Because of the exponential behavior of the camera gain, the signal intensity is displayed using a logarithmic scale. The maximum mean value from the area illuminated with highest laser fluence and amplified with the highest gain, illustrated by the upper-right corner in the IF456 chart, is 45 000 counts or $\sim 10^{4.6}$.

Figure 6 illustrates the camera's ability to reproduce the different intensities induced by the filter stack. The bars represent the measured transmission (67%, 39%, 22%, 14%

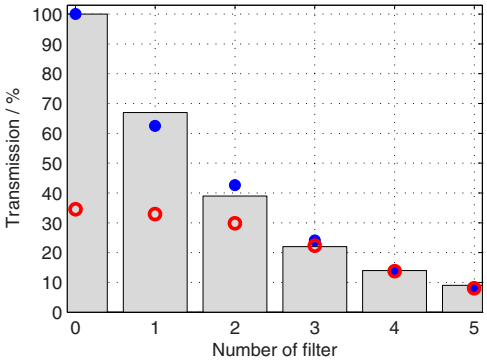

Figure 6. Measured filter stack transmission and scaled camera counts through IF456. The bars indicate the measured filter stack transmission, with values of 67%, 39%, 22%, 14% and 9%. The circles represent the normalized camera counts for gain 80 (blue, filled) and gain 250 (red unfilled).

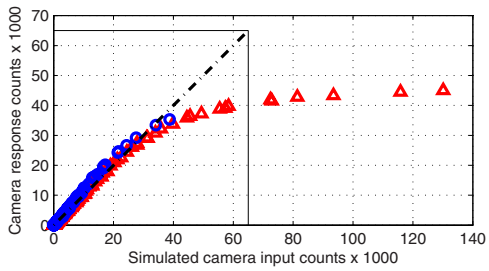

Figure 7. Camera response function for the two different filter wavelengths (IF400 blue circles; IF456 red triangles). The straight dashed line indicates the ideal linear response curve, limited to 65 000 counts by the A/D converter's bit depth.

and 9%) through the five different parts of the filter stack, in relation to 100% transmission, indicated by the first bar. The blue filled circles show the normalized average signal counts through the IF456 at gain 80, obtained from figure 5 (left). They show good agreement with the average filter transmission, indicating that the overall camera response (including the MCP) operates in its linear regime.

The red circles, on the other hand, show the normalized average signal counts at the highest gain value of 250. Here, the signal counts measured for 0, 1 and 2 filters do not reach the expected values such that the 'camera's response' is lowered to 35% only, reflecting that the ICCD camera has left its linear operating workspace. Since only the gain has changed between the two cases displayed in figure 6, while the photon flux remained constant, the saturation can be attributed to the MCP. The red circles start to differ from the expected values when less than three filters are present, where the signal level exceeded 29 000 counts or $10^{4.464}$ (corresponds to the left chart in figure 5, third column, top row). At that point, the initial amount of phosphorescence light hitting the photocathode was reduced to 22% by the filter stack.

Figure 7 utilizes all data information displayed in both charts in figure 5 to extract the camera's response function for the two investigated wavelengths: 400 and 456 nm. This is done by simulating the expected count behavior for the two charts, starting with the first column for each chart (representing five filters' transmission), assuming that each decrease in transmission through the steps of the filter stack increases the counts with respect to the measured transmission. Since the highest count level, reached behind five filters (at a gain of 250), corresponds to approximately 10 000 counts, the whole first column in both charts in figure 5 represents data accumulated in the linear response regime.

The data displayed in figure 7 represent the overall camera response for a photocathode that operates in the linear regime. The counts through IF400 (blue circles) show a slightly steeper slope compared to those through IF456 (red triangles). This could be explained by the wavelength-dependent photocathode sensitivity which possibly emits slightly more primary electrons at 400 nm. For both wavelengths, the initial linear behavior tends to tip between 20 000 and 30 000 counts, indicating the beginning of MCP saturation. Another interesting aspect from figure 7 is that assuming a linear detector response, a measured output signal of 45 000 counts corresponds to a simulated signal level of 130 000 counts. It is remarkable that this is more than twice the numerical range of the A/D converter.

Each of the 156 count values from the IF400 image set is divided by the value from the corresponding gain and laser illumination from the IF456 image set. The result is a ratio chart illustrated by figure 8 (left), which basically could be thought of as the right chart divided by the left chart in figure 5 (if the charts in figure 5 showed the true count values and not the logarithm). The right chart in figure 8 is the same as the left, only with the ratio values translated into temperatures, using a ratio to temperature relation resulting from reference measurements done at temperatures ranging from room temperature to 500 K.

As can be seen in figure 8, the mean ratio value and hence the mean corresponding evaluated temperature are rather constant within the major part of the chart, with the exception of the upper-right corner. Despite the measurements done at constant room temperature, it is clearly seen that the evaluated temperature gives a false result and too high values are acquired for the high laser illumination and high intensifier gain. As can be seen on the right chart in figure 8, this results in a false readout of the absolute temperature, with a deviation of almost 200 K from the true value.

In terms of precision, figure 9 shows the most interesting results. It shows the spatial standard deviation, i.e. the pixel-to-pixel standard deviation, within each gain and laser illumination combination area, translated into corresponding temperature standard deviation. For BAM, the relation between temperature and ratio is rather linear within the considered temperature range, with a dT/dR relation equal to 0.0026 K^{-1}, where T is the temperature and R the ratio. To illustrate, a standard deviation in the ratio of 0.009 corresponds to a standard deviation in temperature of $0.009/0.0026 = 3.5$ K.

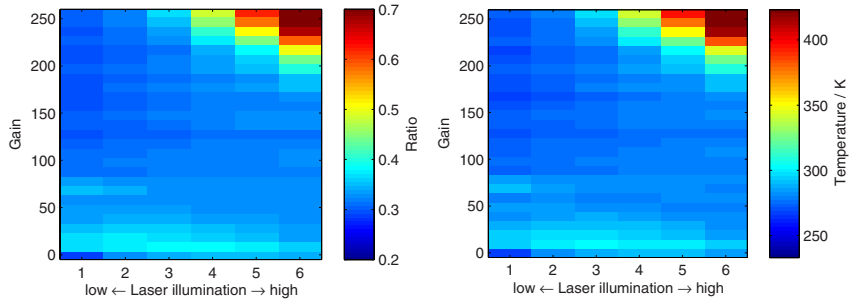

Figure 8. Evaluated ratio for all the different gains and laser illuminations (left), and corresponding values translated into temperatures (right).

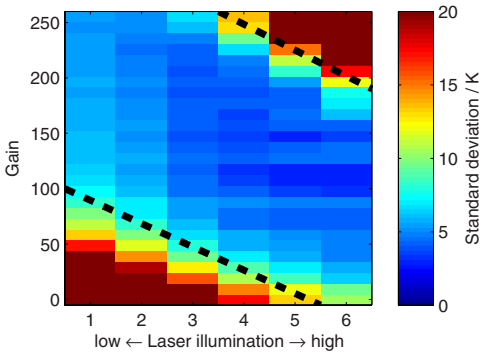

Figure 9. Evaluated spatial standard deviation within the selected areas of different gains and laser illumination, translated into standard deviation in temperature.

As can be seen in figure 9, a diagonal-shaped area, marked in between the two dashed lines, could be identified as a proper working space for higher precision measurements. Within this area, the camera exhibits a linear response independent of MCP gain or laser illumination. Below the lower line, the standard deviation becomes high simply because the S/N level is too low. The signal is still high enough to give reasonable values for the absolute temperature, as can be seen in figure 8, but the noise contribution is too high for the pixel-to-pixel precision to be sufficiently high. The number of counts at which this occurs is very low, about 30 counts per pixel.

The increase in standard deviation above the upper-dashed line indicates a more critical limitation of the camera. The value of counts where this limit is reached can be determined from figure 10, showing the spatial standard deviation of counts in each area for every gain and laser illumination combination through IF456 and IF400, respectively. In the measurements corresponding to a gain setting of 190 in the column for the highest level of laser illumination in figure 9, it can be seen that the standard deviation of the measured temperature, in other words precision, has degraded with a factor of 2 compared with the highest value achieved. Considering the left chart in figure 5, it can be determined that this condition corresponds to a count value of 26 000 through the IF456 ($10^{4.42}$). It can be clearly seen in figure 10 (left) that signal suppression is occurring under these conditions, i.e. the nonlinear regime has been entered. The standard deviation is reaching a maximum value at gain 190 and is then decreasing with higher gain, indicating that an upper limit for counts has been reached and that gain saturation will occur for higher gains and illuminations. It is notable that this saturation already occurs at count levels as low as 26 000 counts, less than half of the maximum counts of 65 535. The same effect is seen for the signals detected through the IF400 filter. In figure 10 (right), it can be seen that the value of the standard deviation reaches a maximum in the column for the highest laser illumination at a gain of 230. Considering the right chart in figure 5, it can be determined that this corresponds to a count level of about 29 000 counts ($10^{4.47}$).

Figure 9 illustrates a region identified as a useful workspace for this camera and phosphor. The upper-dashed line indicates the limit for the gain/illumination trade-off. In the left chart in figure 5, the position of the upper-dashed line in figure 9 would correspond to a count value range of 25 000–30 000 counts ($10^{4.4}$–$10^{4.5}$). Higher counts should be avoided. The fact that there is a range of gain in which the absolute evaluated temperature and precision are rather constant, regardless of laser illumination (between gain 100 and 190, see figure 9), shows that the saturation occurs after the photocathode. Hence, the strength of the light source, in itself, or the photocathode are not responsible for the saturation. However, it cannot be excluded that the saturation detected, or a portion of it, could be caused by the phosphor screen in the image intensifier. It should be mentioned that the experiments are performed using one ICCD camera and one TP only, and that the saturation limit of 25 000–30 000 counts is only valid under these conditions. However, as a precaution, an additional test was performed using a nominally identical ICCD camera and the results were very similar.

Within the useful workspace, the precision in temperature measurement spans from ± 1 to ± 10 K. This number depends on temperature and on the choice of the spatial resolution of the detection system. This relationship will be addressed in an upcoming work by the authors.

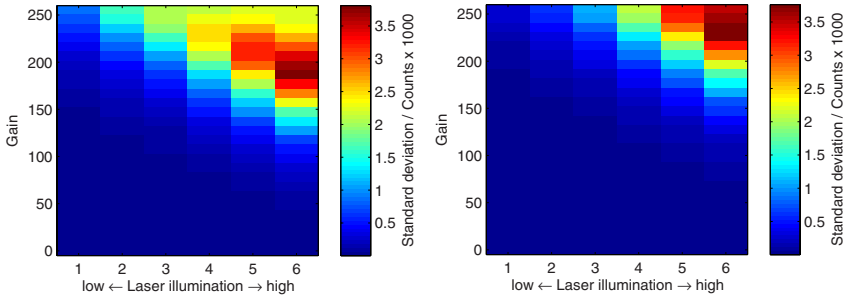

Figure 10. The spatial pixel-to-pixel standard deviation in counts for the signals achieved through the IF456 filter (left) and the IF400 filter (right) for all the different gains and laser illuminations.

This work has not only focused on the precision of measurements but has also mentioned accuracy-related issues. The authors would like to see reproducibility investigations on how the accuracy could be affected by long- and short-term drifts of cameras. Also similar investigations to the one described here, but with different types of ICCD cameras, and with different types of TPs (with different emission wavelengths and lifetimes) and at different temperatures, would be a suitable target for further investigations.

4. Conclusion

In this work, a useful workspace within the gain/illumination combination of an ICCD camera (Princeton Instruments PI-MAX2) has been identified. It has been shown that the camera used suffers from nonlinear effects due to gain saturation in the MCP, when exceeding a certain level of counts. The results show that there is a possibility of saturating the camera, and in so doing introducing nonlinearity, even though other components of the camera are not saturated. The level at which this occurs corresponds to as low as half the maximum counts allowed by the CCD chip, making the occurrence of saturation far from obvious. It is conspicuous that the count value read as 45 000 in fact represents an intensity that should actually correspond to a count value of 130 000. Another interesting conclusion drawn from figure 7, is that the nonlinearity of response has a slight dependence on the observed wavelength. In this study, two nominally identical ICCD cameras were used and showed similar results. However, each detector should be treated individually, and the behavior likely depends on the type of light source as well. This means that an investigation such as the one presented here should be done prior to any experiment involving quantitative measurements using a two-color ratio method.

To conclude, there is an upper limit of counts below which the ICCD cameras should be used in order to give reliable results. This limit is shown to be in the 25 000–30 000 count range out of a nominal 65 000 counts allowed by the 16-bit A/D converter. This level was shown to be valid for any gain.

It is inferred from our analysis that system nonlinearity is also dependent on the type of light source being investigated. In this study, the phosphorescence of BAM is detected at room temperature and at a certain distance between camera and phosphor. If cameras are to detect light at other wavelengths and with a different duration, the limitations of the ICCD cameras are likely to be different.

Acknowledgments

This work was supported by the Centre of Competence Combustion Processes and the HELIOS project within the seventh EU framework program.

References

[1] Williams T C and Shaddix C R 2007 Simultaneous correction of flat field and nonlinearity response of intensified charge-coupled devices *Rev. Sci. Instrum.* **78** 123702

[2] Montgomery D S, Drake R P, Jones B A and Wiedwald J D 1987 Flat-field response and geometric distortion measurements of optical streak cameras *Proc. SPIE* **832** 283–8

[3] Kruschwitz C A, Wu M, Moy K and Rochau G 2008 Monte Carlo simulations of high-speed, time-gated microchannel-plate-based x-ray detectors: saturation effects in dc and pulsed modes and detector dynamic range *Rev. Sci. Instrum.* **79** 10E911

[4] Wiedwald J D and Lerche R A 1987 Streak camera dynamic range and optimization *Proc. SPIE* **832** 275–82

[5] Allison S W and Gillies G T 1997 Remote thermometry with thermographic phosphors: instrumentation and applications *Rev. Sci. Instrum.* **68** 2615–50

[6] Husberg T, Girja S, Denbratt I, Omrane A, Aldén M and Engström J 2005 Piston temperature measurements by use of thermographic phosphors and thermocouples in a heavy-duty Diesel engine run under partly premixed conditions *SAE 2005-01-1646*

[7] Khalid A and Kontis K 2008 Thermographic phosphors for high temperature measurements: principles, current state of the art and recent applications *Sensors* **8** 5673–744

[8] Knappe C, Andersson P, Algotsson M, Richter M, Linden J, Alden M, Tuner M and Johansson B 2011 Laser-induced phosphorescence and the impact of phosphor coating thickness on crank-angle resolved cylinder wall temperatures *SAE Technical Paper*

[9] Seyfried H, Richter M, Nilsson K-H, Aldén M and Schmidt H 2007 Surface thermometry using laser-induced phosphorescence applied in the afterburner of an aircraft turbofan engine *Collection of Technical Papers 45th AIAA Aerospace Sciences Meeting* vol 18 pp 12794–802

[10] Aldén M, Omrane A, Richter M and Särner G 2010 Thermographic phosphors for thermometry: a survey of combustion applications *Prog. Energy Combust. Sci.* **37** 422–61

[11] Särner G, Richter M and Alden M 2008 Investigations of blue emitting phosphors for thermometry *Meas. Sci. Technol.* **19** 125304

[12] Seyfried H, Särner G, Omrane A, Richter M and Aldén M 2005 Optical diagnostics for characterization of a full-size fighter-jet after-burner *ASME GT2005-69058*

[13] Bizarri G and Moine B 2005 On BaMgAl10O17: Eu^{2+} phosphor degradation mechanism: thermal treatment effects *J. Lumin.* **113** 199–213

Paper VII

IOP Publishing Measurement Science and Technology
Meas. Sci. Technol. **23** (2012) 085205 (9pp) doi:10.1088/0957-0233/23/8/085205

Precision in 2D temperature measurements using the thermographic phosphor BAM

J Lindén, C Knappe, M Richter and M Aldén

Division of Combustion Physics, Lund University, Box 118, S-22100, Lund, Sweden

E-mail: johannes.linden@forbrf.lth.se

Received 23 March 2012, in final form 22 May 2012
Published 28 June 2012
Online at stacks.iop.org/MST/23/085205

Abstract
Investigation of optimized spatial precision for surface temperature measurements is performed. The temperature is measured by means of two-color ratio imaging with ICCD cameras, using the thermographic phosphor BAM. The precision in temperature is put in relation to the spatial resolution, two quantities which involve a trade-off in this case: the more spatial smoothing the better precision, but also the worse spatial resolution. Two different setups are used in order to investigate the influence of laser shot-to-shot variations, the flat-field correction and image registration process on the precision. In order to achieve high precision it is crucial to operate the ICCD cameras with a gain setting that does not introduce nonlinearity effects at the present level of irradiance. The results provide guidance on the precision to be expected from surface temperature measurements using the two-color ratio technique in combination with thermographic phosphors and also confirm the importance of highly stable and linear ICCD detectors. At room temperature and low spatial resolution the precision is evaluated to 0.4%.

Keywords: laser-induced phosphorescence, thermographic phosphors, thermometry, ICCD detectors

(Some figures may appear in colour only in the online journal)

1. Introduction

Thermographic phosphors have been a subject for development of thermometry techniques for several decades and are used in many applications, e.g., combustion research on reciprocating engines and gas turbines [1–6]. By utilizing the phosphorescence temperature sensitivity, measurements can be done over a wide range of temperatures, depending on the choice of phosphor. The phosphorescence from thermographic phosphors shows temperature dependence in two ways: both the spectral profile and/or the lifetime of the phosphorescence may change with temperature. The former property is often used for two-dimensional (2D) surface measurements using ICCD (intensified charge coupled device) cameras and the latter for point measurements using photomultiplier tubes for detection. This paper will consider the former technique.

When performing 2D surface temperature measurements using thermographic phosphors, either two cameras or one camera equipped with a stereoscope is used, in order to capture two images of the probed area [7]. The two images are obtained through different optical filters, which are chosen with respect to the spectral properties of the phosphor used. As the temperature changes, the intensity through the different filters will change, relative to each other. The relation between the different wavelength intensities is dependent on temperature, and thus, by dividing one image by the other, pixel by pixel, a ratio map of the surface is achieved. This ratio is translated into temperature by the use of a pre-defined ratio-to-temperature relation constructed from calibration measurements at controlled reference temperatures.

The precision achieved when performing 2D temperature measurements using thermographic phosphors is often estimated on the basis of the signal-to-noise ratio (S/N), the

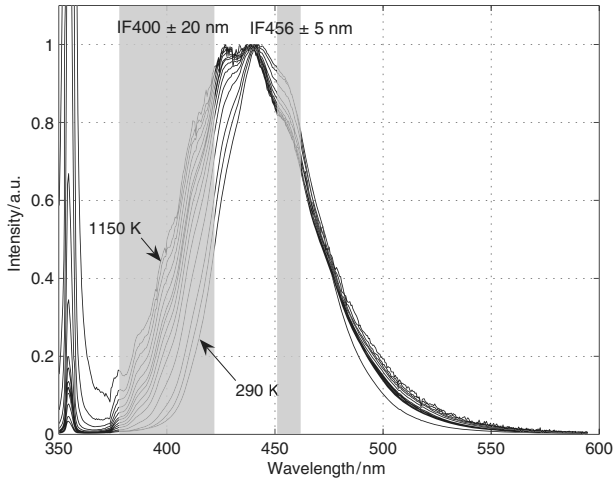

Figure 1. BAM emission spectrum at different temperatures when excited with 355 nm laser radiation. The exposure time of the ICCD camera connected to the spectrometer is 8 μs. The spectral properties of the interference filters used are marked out.

temperature sensitivity of the phosphor or the temporal and spatial repeatability. The amount of statistics varies, and the precision is seldom put in relation to the spatial resolution. The precision of the measured temperature depends on several factors. The most decisive one is of course how sensitive to temperature variations the phosphor is in the investigated temperature range, i.e. the change in spectral ratio as a function of temperature change.

Other factors that influence the precision are background and flat-field corrections, i.e. compensating for dc light contributions and pixel-to-pixel sensitivity variations on the CCD chip, respectively. In this work, it is experienced that the exposure time affected the flat field and by extension both accuracy and precision. Therefore, care needs to be taken when recording the flat-field image regarding the gain and exposure time settings. Other properties of the detection systems can also affect the precision, such as drift in sensitivity over time or nonlinear effects of ICCD cameras, which is especially crucial in two-color ratio techniques [8–11]. A final factor that affects precision is the quality of the image registration process, where geometric image correction such as warping and alignment is needed to ensure that corresponding pixels in the two images contain data from the same point in the image plane. This is done in order to superimpose the two images and generate an intensity ratio image. Here, software smoothing of the phosphorescence images before division would enhance the precision in temperature, since the precision of the overlap becomes less critical.

This paper describes the variations of the pixel-to-pixel precision (spatial precision) of the temperature at various spatial resolutions using the thermographic phosphor $BaMg_2Al_{16}O_{27}$:Eu (BAM), a blue emitting phosphor when illuminated with UV light, and Princeton PIMAX-II ICCD cameras.

BAM emits a spectrally broad phosphorescence peak around 440 nm, which broadens toward shorter wavelengths with increasing temperature, see figure 1. The phosphorescence has a constant lifetime of about 2 μs at room temperature up to about 700 K and decreases to about 10 ns at 1150 K. With two interference filters, one 10 nm wide (FWHM) centered at 456 nm and one 40 nm wide (FWHM) centered at 400 nm, a temperature-dependent intensity relation can be observed, when the phosphorescence intensity at 400 nm increases with temperature relative to the phosphorescence emission at 456 nm. The selection of wavelength and the spectral width of the interference filters were optimized using a simulation based on the measured emission spectra [12]. Dividing the intensity in these images by each other, pixel by pixel, will result in a temperature-dependent ratio image. These ratios are then translated into temperature using a pre-defined calibration curve achieved from measurements performed in controlled environments. The resulting ratio, and thus the resulting temperature, then becomes independent of the overall phosphorescence intensity and laser excitation intensity. BAM exhibits temperature sensitivity from room temperature up to 1150 K [12]. However, degradation at elevated temperatures may restrict its use for thermometry to below 800 K [13]. BAM is commercially used as the blue emitting component in fluorescent lamps and plasma display panels [14].

2. Experimental work

Performing 2D temperature measurements using the approach described above includes several sources of error. Such error can be caused by using a stereoscope, as it may introduce artifacts due to internal reflections and, as mentioned above,

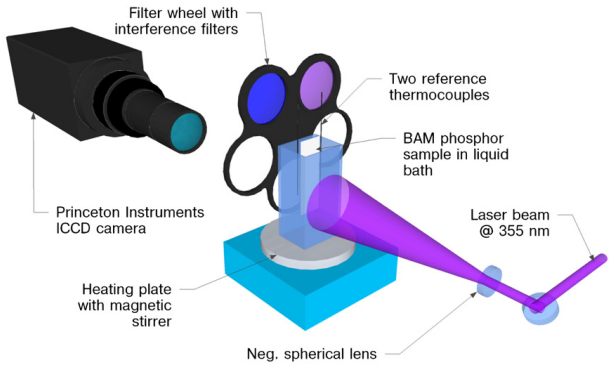

Figure 2. Experimental setup for the single-camera experiment.

by image processing such as image registration and flat-field corrections.

The experiment presented here is performed in two setups, neither of which uses a stereoscope. The first uses only one camera, in front of which the filters are switched. There is thus no need for either image registration or flat-field correction in this case. However, with this setup, measurements cannot be performed in a single shot, making it more sensitive to shot-to-shot laser energy fluctuations and temperature variations. In the second setup, two cameras and a cubic beam splitter mirror are used, and measurements can be performed in a single shot. These two different setups are used in order to investigate the impact of image registration, flat-field corrections and shot-to-shot variations on the calculated temperature field.

For both setups a 10 Hz pulsed Nd:YAG laser, working at its third harmonic and producing laser emission at 355 nm, is used to excite the phosphor. Because of the high quantum efficiency of BAM (80%–95%) [13, 15, 16], the laser power required is very low, <1 mJ. Considering the expansion of the laser beam, enhanced using a negative lens, the fluence illuminating the measured surface is calculated to be about 5 μJ cm^{-2}.

Since the aim of this study is to investigate the measurement precision of the 2D phosphor thermometry technique, it is crucial to establish a reference surface with an even temperature distribution. For this purpose, the phosphorescent material is coated onto a thin glass plate (1 mm) that is joined together with another glass plate to form a hermetically sealed cell with the phosphor between the two glass plates. This cell is then submerged in a liquid bath. The liquid, with high heat capacity, will disperse heat and buffer against rapid temperature variations. At lower temperatures, i.e. between 273 and 373 K, water is used as the dispersing fluid. To extend the temperature range complementary measurements are performed with glycerol, which has a boiling point of 563 K. The liquid bath is placed on an electrical heating plate equipped with a magnetic stirrer. Due to the limited capacity of the heater the maximum temperature achieved is 470 K. The temperature in the bath is measured with two K-type thermocouples, providing an accuracy of ± 1.5 K within the observed temperature range. The calibrated thermocouples will act as a reference in this study; hence, the accuracy of the temperatures retrieved from the phosphor measurements will never be better than the accuracy of the thermocouples. However, as this study focuses on the precision, the absolute temperature is only of secondary importance. In order to verify any potential offset for the thermocouple readings an initial measurement is performed in an ice-bath (273 K). During a measurement the temperature from the two thermocouples was logged and thanks to the magnetic stirrer the standard deviation of the temperature stayed below 0.2 K during all measurements.

Figure 2 shows the first experimental setup, using only one camera. The laser beam is guided and expanded via a mirror and lens system to illuminate the thermographic phosphor inside the cell. A filter wheel loaded with the mentioned filters is located on the camera side of the liquid bath. The reason for the position of the filter wheel, close up to the liquid bath and not immediately in front of the camera lens, is an image distortion caused by the internal design of the filters. With the filters directly in front of the camera, both focus and image positions on the camera chip change with different filters. By placing the filters close to the surface to be measured, these effects are minimized. With this filter position the phosphor sample needs to be illuminated from the backside, the reason for the phosphor being coated onto a glass plate.The phosphorescence seen through the filters is captured by a PIMAX II ICCD camera (Princeton Instruments).

Figure 3 shows the experimental setup for the dual-camera setup, involving two nominally identical PIMAX II ICCD cameras. A cubic beam splitter allows the cameras to observe the target from virtually identical positions. The cubic beam splitter was preferable to a semi-transparent optical flat mirror, because of the risk of artifacts caused by internal reflections in the mirror. In contrast to the single-camera setup, the phosphor cell is illuminated from the front, with a slight angle. This is possible in this setup since the interference filters are now placed at the very front of the cameras.

For both setups, the cameras are trigged by the laser and the exposure time is set to 5 μs. Phosphorescence images of

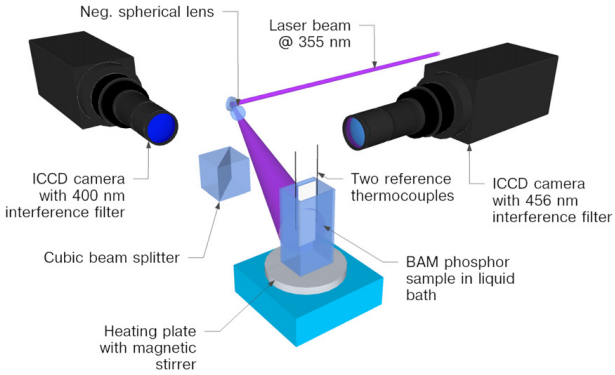

Figure 3. Experimental setup for the dual-camera experiment.

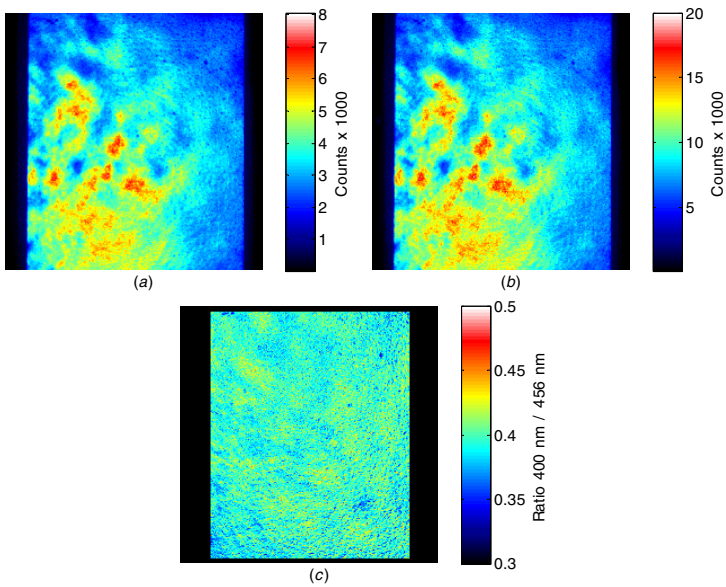

Figure 4. Examples of measurement images at 334 K done with the single-camera setup. Phosphorescence at 400 nm (*a*), at 456 nm (*b*) and the resulting ratio image (*c*). The phosphorescence images are ten averaged images.

the coated surface are recorded at different temperatures in the range from 279 to 470 K.

After stabilization at the desired liquid temperature, ten images through each filter and ten background images are recorded. The ten images are software averaged before being processed. The read-out noise is considered not to be a problem, since the phosphorescence signal is very high. For the dual-camera setup the images taken using the different filters are recorded simultaneously, while for the single-camera setup they are recorded in sequence, by rotating the filter wheel.

3. Data post processing

After background subtraction (and for the dual-camera setup, flat-field correction and image transformation registration) the images taken using the different filters are treated as described above, generating a ratio image, R. The procedure is illustrated in equation (1) for the single-camera setup and equation (2) for the dual-camera setup:

$$R = \frac{I_{400} - \mathrm{BG}_{400}}{I_{456} - \mathrm{BG}_{456}}, \tag{1}$$

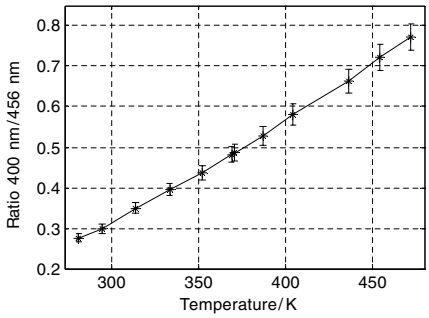

Figure 5. Relation between temperature and the phosphorescence ratio achieved using the single-camera setup. The error bars indicate the spatial standard deviation of the ratio.

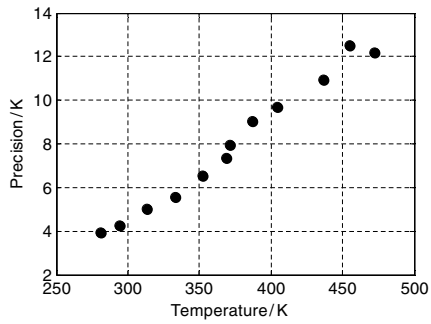

Figure 6. Evaluated precision versus temperature of data achieved using the single-camera setup.

$$R = \frac{I_{400} - \mathrm{BG}_{400}}{\mathrm{FF}_{400}} \Big/ \frac{I_{456} - \mathrm{BG}_{456}}{\mathrm{FF}_{456}}, \tag{2}$$

where I is the phosphorescence image, BG is the background image and FF is the flat-field image. The subscript indicates the phosphorescence wavelength observed, and hence which camera is being used. For the dual-camera setup, the denominator is subject to an image registration transformation.

The mean value and spatial standard deviation of the ratio are evaluated within an area of about 1000 × 850 pixels, corresponding to an object area of about 2.8 × 2.4 cm^2.

Prior to division, the individual images from each camera are smoothed through software Gaussian filtering using MATLAB. This makes the precision of the overlapping of the two images less critical, and hence the precision of the ratio is increased, but at the expense of decreased spatial resolution.

In addition to the measurements, an image of a resolution test target is recorded, in order to measure the spatial resolution. By repeating the software filtering on the image of the resolution test target, a measure of the spatial resolution for the smoothed spectral ratio images is achieved. This procedure is repeated with different strengths of the software Gaussian filtering, resulting in a relation between precision and spatial resolution.

For the dual-camera setup, a reference grid image and a reference flat-field image are recorded for each camera. The grid image is used to construct an image transform in MATLAB in order to accomplish a proper pixel-by-pixel overlap, prior to image division. In this study, a transparent film with reference points and symbols is attached to the phosphor-coated glass plate while submerged in the liquid bath. In order to achieve as good image registration as possible, it is important to use a grid reference image with clearly distinct patterns of small structures with high contrast. By experience it is recommended to use grid patterns of small points rather than i.e. check patterns.

The flat-field reference image is used to compensate for pixel-to-pixel sensitivity variations of the CCD caused by all camera components, such as optics, image intensifier and detector chip. Because of varying pixel sensitivity for different wavelengths, the flat-field image, as the grid image, needs to be obtained with the filters in place. An ideal flat-field image is a completely uniform surface light source, best achieved by using an integrating sphere, with its aperture placed at the image plane of the camera. In this case, the flat field is generated by a tungsten halogen lamp at 3300 K mounted to a 250 mm integrating sphere with a 65 mm diameter output aperture. When achieving the flat-field image, the gain settings are kept the same as when recording the measurement images and the gate width of the cameras is adjusted so that the number of counts is similar to those in the measurement images. Before using the flat-field images they are normalized by dividing by their maximum value, according to

$$\mathrm{FF} = \frac{\mathrm{FF}_{\mathrm{raw}} - \mathrm{BG}_{\mathrm{raw}}}{\mu}, \tag{3}$$

where μ is the maximum value within $\mathrm{FF}_{\mathrm{raw}}$–$\mathrm{BG}_{\mathrm{raw}}$.

4. Results and discussion

Figure 4 shows an example of the results of a measurement in water at 334 K using the single-camera setup. Figures 4(*a*) and (*b*) show the phosphorescence observed through the 400 nm interference filter (henceforth IF400) and through the 456 nm interference filter (henceforth IF456), respectively. After background subtraction, figure 4(*a*) is divided by 4(*b*) and the ratio image 4(*c*) is achieved. Pixels outside the selected area are masked out. As can be seen, despite the inhomogeneity of the phosphorescence intensity, seen in figure 4(*a*) and 4(*b*), the ratio image becomes very homogenous. This illustrates the inherent advantage of the two-color ratio approach, as the technique does not require an absolutely homogeneous excitation laser profile, phosphor coating or a linear relation between laser excitation and phosphorescence intensity.

Ratio images similar to that in figure 4(*c*) are generated at 12 different temperatures spanning from 281 to 473 K. For each ratio image, the mean value and spatial standard deviation of the ratio within the selected area (about 850 000 pixels) are evaluated. Figure 5 shows the resulting relation between the temperature and the ratio with the error bars indicating the spatial standard deviation of the ratio.

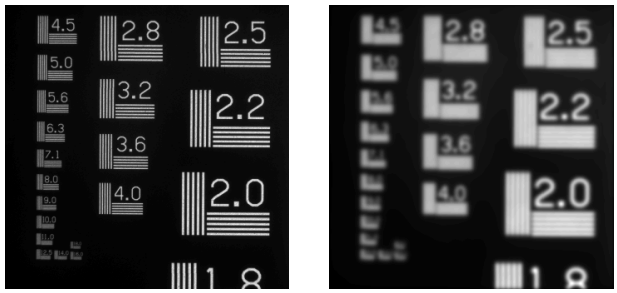

Figure 7. An image of a resolution test target before software filtering (left) resulting in a spatial resolution of 11 lines mm^{-1}, and after software filtering (right) where the target has been subjected to a spatial smoothing applying a software Gaussian filter of pixel size 50 × 50 and a sigma value of 7, resulting in a spatial resolution of 2.2 lines mm^{-1}.

As can be seen, the relation is close to linear. The slope of a fitted line gives the temperature sensitivity of the phosphor. The values in figure 5 give that the slope, and hence the sensitivity of BAM, is 0.0026 K^{-1}. The spatial standard deviation of the ratio within the selected area at room temperature is ± 0.011, giving a precision of ± 4.2 K, or 1.4 %.

As can be seen in figure 5, the error bars increase with temperature. Figure 6 illustrates this increase in spatial standard deviation, or degradation in precision, as the temperature increases from 281 to 473 K.

The precision at the lowest temperature of 281 K is ± 3.9 K, or 1.4%, while at the highest temperature of 473 K it is ± 12 K, or 2.6%.

The precisions in figure 6 will be increased if the original phosphorescence images are subjected to spatial smoothing, using software Gaussian filtering, since this will decrease the standard deviation caused by the shot noise. A spatial smoothing, as such, simulates in a way a lower spatial resolution, but also how pixel binning would increase the S/N ratio. An image of a resolution test target, see figure 7, is subject to the same treatment in order to quantify this reduction of resolution.

Before division, the phosphorescence images are processed with a software Gaussian filter of different strengths, smoothing out the resulting ratio image. With increasing strength the spatial resolution decreases, while the precision increases. This is illustrated by figure 8, showing the relation between the gain in precision and the loss in resolution at three different temperatures.

As can be seen, the precision at low temperature (281 K), at the highest resolution (11 lines mm^{-1}), is ± 3.9 K, or 1.4%. As the phosphorescence images are subjected to smoothing filtering, the resolution decreases gradually to 2 lines mm^{-1}, and the precision is increased to ± 1.7 K, or 0.6%. Similarly, for measurements done at high temperature, 455 K, the precision spans from ± 12.5 K, or 2.8 %, at highest resolution, to ± 6.5 K, or 1.4 %, at lowest resolution. Accordingly, in the case of the single-camera setup, the precision varies from 0.6% to 2.8%, depending on absolute temperature and resolution.

Concerning the dual-camera setup an example of a measurement done in water with the temperature of 331 K

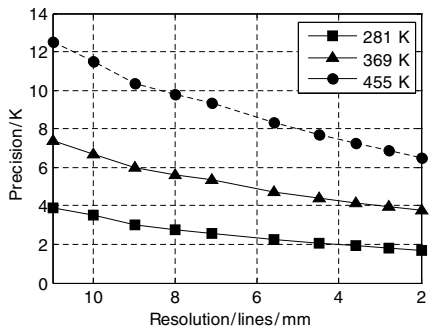

Figure 8. Relation between precision and resolution at three different temperatures.

is shown in figure 9. In contrast to the single-camera setup, the phosphorescence images here need to be flat-field corrected. Furthermore, one of the images, in this case IF456, is subjected to an image registration transform, in order to optimize image superimposition. Figure 9(*c*) shows the resulting ratio image of IF400 divided by IF456.

As in the case of the single-camera setup, the ratio image is very homogeneous, despite the inhomogeneity of the phosphorescence images. For each temperature, the mean value and spatial standard deviation of the ratio are evaluated.

Figure 10 shows the relation between the ratio and temperature for BAM, also this is close to linear. However, the slope is different, 0.005 K^{-1}, from that in the single-camera setup. This is due to the different conditions for which the two phosphorescence images are achieved, compared to the case where only one camera is used. The two cameras might have different sensitivities, the cubic beam splitter might separate the light not precisely 50/50 at the present wavelengths, etc. However, because of this, the evaluated spatial standard deviation is also somewhat different. At room temperature it is ± 0.015, giving a precision of ± 3 K, or 1%, slightly better than for the single-camera setup.

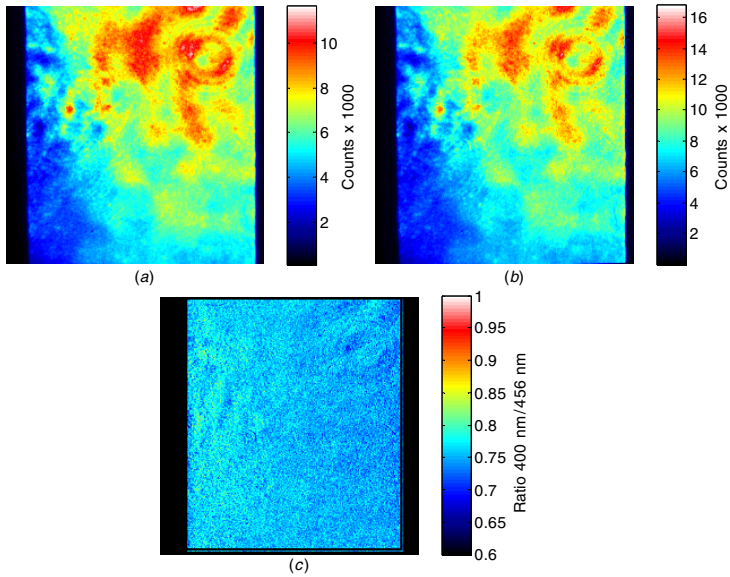

Figure 9. Examples of measurement images at 331 K done with the dual-camera setup. Phosphorescence at 400 nm (*a*), at 456 nm (*b*) and the resulting ratio image (*c*). The phosphorescence images are ten averaged images.

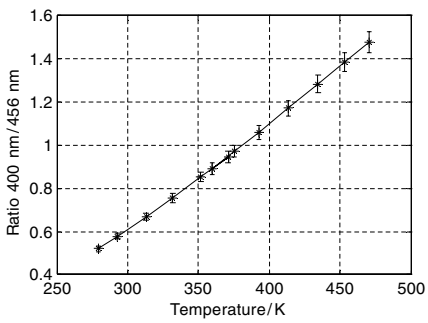

Figure 10. Relation between the phosphorescence ratio and temperature for the dual-camera setup.

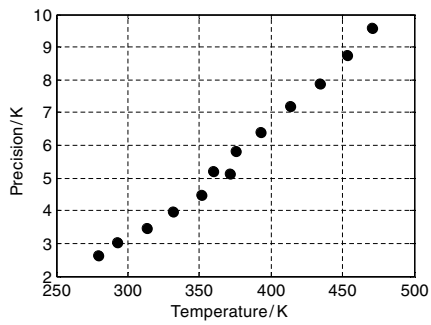

Figure 11. Evaluated precision versus temperature of data achieved using the dual-camera setup.

Figure 11 shows the increasing spatial standard deviation, or degradation in precision, with temperature from 280 to 471 K.

As can be seen, there is a discontinuity between the measurements at 360 and 370 K. This is the overlap of the measurements performed in water (280–370 K) and in glycerol (360–470 K). The reason for the discontinuity is a drift over time in one of the ICCD cameras. It is aggravated between 360 and 370 K due to a 3 h delay between continuous water and glycerol measurement sequences. During this break the local sensitivity of one of the cameras drifted, causing a gradient offset across the chip, causing this degradation in precision. This instability in the cameras is hardly notable in other applications, and indicates how easily affected this two-color ratio method is by small variations in, e.g., linearity or detector drift.

It is the authors' belief that the detector drift is, at least generally, associated with the loss in precision. This long term detector drift is a possible explanation of the increasing slope in figure 11, and without the drift, the trend would have been more linear and the slope less steep, i.e. the precision at higher temperatures would have been better than that seen in figure 11. Since Särner *et al* have shown that the phosphorescence lifetime of BAM does not decrease

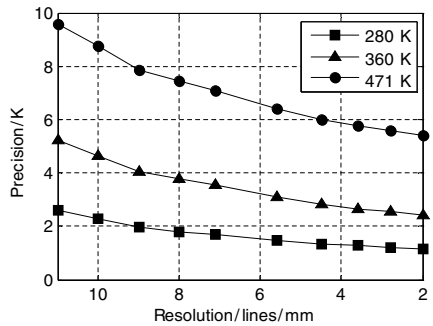

Figure 12. The increase in precision with decreasing resolution for three different temperature measurements with the dual-camera setup, i.e. with two cameras.

appreciably before 700 K, it follows that loss in accumulated signal intensity is not believed to be the reason for the decrease in precision [12].

From figure 11, it can be seen that the precision at the lowest temperature (280 K) is ± 2.6 K, or 0.9%, and at the highest temperature (471 K) is ± 9.6 K, or 2%. Figure 12 illustrates how this precision is improved when the phosphorescence images are subjected to spatial smoothing using Gaussian filter routines.

For the lowest temperature, the precision is increased to ± 1.2 K, or 0.4%, as the resolution is decreased to 2 lines mm^{-1}. For the highest temperature, the precision is increased to ± 5.4 K, or 1.2 %. Accordingly, in the case of the dual-camera setup, the precision varies from 0.4% to 2%, depending on absolute temperature and resolution. This is an improvement over the single-camera experiment results, with precision spanning from 0.6% to 2.8 %, despite both flat-field and image registrations being needed for the dual-camera experiment. The explanation for this is that, in the single-camera experiment, the phosphorescence images were recorded by different laser shots, introducing errors caused by laser shot-to-shot variations, even though these variations were determined to be very small during the experiments. It is these shot-to-shot variations that cause the deviation of especially the second last point in figure 6.

Additionally, the evaluation of the results from the dual-camera experiment is compared with those without flat-field correction. This results in a precision span from 2.3% to 5.1%, that is, a degradation of about 2–3 percentage points, indicating the importance of flat-field corrections in this particular case.

5. Conclusions

In this work, the precision in 2D temperature measurements using the thermographic phosphor BAM in the range from about 280 to 470 K has been investigated. The purpose of this work was to evaluate the technique of 2D phosphor thermometry on surfaces concerning precision, something that to the knowledge of the authors is lacking in the field today. The main contribution of the work is to provide guidance on the precision to be expected from 2D surface temperature measurements, using the two-color ratio technique with thermographic phosphors. The precision was put in relation to the spatial resolution, since better precision is possible at the expense of resolution. Depending on temperature and resolution, the precision ranges from 0.4% at the lowest temperature with the lowest investigated resolution, corresponding to 2 lines mm^{-1}, to 2.8% at the highest temperature with highest resolution of 11 lines mm^{-1}. This emphasizes the potential of precision in the 2D phosphor thermometry, since the temperature sensitivity of BAM is by no means remarkable, with the ratio spanning over a factor of 3 in the investigated temperature range. For example, Särner *et al* have demonstrated that the ratio of ZnO:Zn spans over one order of magnitude in the same temperature interval [12]. The sensitivity of ZnO:Zn, i.e. the slope in a corresponding chart such as figure 5 or 10, would be 2×10^{-8} K^{-1}, compared to 0.0025 K^{-1} for BAM. The resulting precision depends of course on the value of the standard deviation of the ratio in a measurement as such, but this high sensitivity indicates the potential of ZnO:Zn as a sensor for 2D temperature measurements.

The measurements have been performed in two different setups: one using only one ICCD camera and one using two. The results were similar for both setups, but precision slightly improved when two cameras were used. The conditions that differ for the two setups were the use of flat-field correction and image registration transformation in the dual-camera setup. The uncertainties that are introduced by the laser shot-to-shot variations are thus found to be greater than the uncertainties introduced by the proper use of an image registration procedure; hence, in terms of precision it is thus preferable to achieve the data single shot.

The impact of excluding flat-field correction on the precision was a degradation of about 2–3 percentage points in this particular case.

One final conclusion from the work carried out is the importance of stable detectors. Even small drifts and instabilities may affect the results significantly.

Acknowledgments

This work was supported by the D60 project within the Swedish Energy Agency, Centre of Competence Combustion Processes and the HELIOS project within the seventh EU framework program.

References

[1] Allison S W and Gillies G T 1997 Remote thermometry with thermographic phosphors: instrumentation and applications *Rev. Sci. Instrum.* **68** 2615–50

[2] Brübach J, Feist J P and Dreizler A 2008 Characterization of manganese-activated magnesium fluorogermanate with regards to thermographic phosphor thermometry *Meas. Sci. Technol.* **19** 025602

[3] Husberg T, Girja S, Denbratt I, Omrane A, Aldén M and Engström J 2005 Piston temperature measurements by

use of thermographic phosphors and thermocouples in a heavy-duty diesel engine run under partly premixed conditions *SAE* 2005-01-1646

[4] Khalid A and Kontis K 2008 Thermographic phosphors for high temperature measurements: principles, current state of the art and recent applications *Sensors* **8** 5673–744

[5] Aldén M, Omrane A, Richter M and Särner G 2010 Thermographic phosphors for thermometry: a survey of combustion applications *Prog. Energy Combust. Sci.* **37** 422–61

[6] Seyfried H, Richter M, Nilsson K-H, Aldén M and Schmidt H 2007 Surface thermometry using laser-induced phosphorescence applied in the afterburner of an aircraft turbofan engine *Collection of Technical Papers—45th AIAA Aerospace Sciences Meeting* vol 18 pp 12794–802

[7] Seyfried H, Särner G, Omrane A, Richter M and Aldén M 2005 Optical diagnostics for characterization of a full-size fighter-jet after-burner *ASME Conf. Proc.* pp 813–9

[8] Kruschwitz C A, Wu M, Moy K and Rochau G 2008 Monte Carlo simulations of high-speed, time-gated microchannel-plate-based x-ray detectors: saturation effects in dc and pulsed modes and detector dynamic range *Rev. Sci. Instrum.* **79** 10E911

[9] Lindén J, Knappe C, Mattias R and Marcus A 2012 Limitations of ICCD detectors and optimized 2D phosphor thermometry *Meas. Sci. Technol.* **23** 035201

[10] Wiedwald J D and Lerche R A 1987 Streak camera dynamic range and optimization *Proc. SPIE* **832** 275–82

[11] Williams T C and Shaddix C R 2007 Simultaneous correction of flat field and nonlinearity response of intensified charge-coupled devices *Rev. Sci. Instrum.* **78** 123702

[12] Särner G, Richter M and Alden M 2008 Investigations of blue emitting phosphors for thermometry *Meas. Sci. Technol.* **19** 125304

[13] Bizarri G and Moine B 2005 On $BaMgAl_{10}O_{17}:Eu^{2+}$ phosphor degradation mechanism: thermal treatment effects *J. Lumin.* **113** 199–213

[14] Shionoya S, Yamamoto H and Yen W M 2007 *Phosphor Handbook* (Boca Raton, FL: CRC Press)

[15] Do Y R and Bae J W 2000 Application of photoluminescence phosphors to a phosphor-liquid crystal display *J. Appl. Phys.* **88** 4660–5

[16] Ravichandran D, Johnson S T, Erdei S, Roy R and White W B 1999 Crystal chemistry and luminescence of the Eu^{2+}-activated alkaline earth aluminate phosphors *Displays* **19** 197–203

Paper VIII

Accepted to 9th International Temperature Symposium, ITS9, 2012

Response Regime Studies on Standard Detectors for Decay Time Determination in Phosphor Thermometry

C. Knappe, F. Abou Nada, J. Lindén, M. Richter and M. Aldén

Division of Combustion Physics, Lund University, Sweden
E-mail (corresponding author): christoph.knappe@forbrf.lth.se

Abstract. This work compares the extent of linear response regimes from standard time-resolving optical detectors for phosphor thermometry. Different types of Photomultipliers (ordinary and time-gated) as well as an Avalanche Photodiode are tested and compared using the phosphorescent time decay of $CdWO_4$ that ranges from 10 µs down to a few ns within a temperature span of 290 to 580 K. Effects originating from incipient detector saturation, far from obvious to the operator's eye, are revealed as a change in evaluated phosphorescence decay time. Since the decay time of thermographic phosphors itself is used for temperature determination – systematic temperature errors up to several tens of Kelvins may be introduced by such detector saturation. A detector mapping procedure is suggested in order to identify linear response regions where the decay-to-temperature evaluation can be performed unbiased. Generation of such a library is highly recommended prior to any quantitative measurement attempt. Using this detector library, even signals collected in the partly saturated regime can be corrected to their unbiased value extending the usable detector operating range significantly. Further, the use of an external current-to-voltage amplifier proved useful for most applications in time-based phosphor thermometry helping to limit saturation effects whilst maintaining a reasonable bandwidth and signal outputs.

Keywords: thermographic phosphor, laser-induced phosphorescence, lifetime, decay time, time-resolved, saturation

INTRODUCTION

Phosphors are ceramic materials that exhibit an extended afterglow after being optically excited. A phosphor is thermographic when the phosphorescent light emission varies as a function of temperature. Both the changes in phosphorescence decay as well as the intensity ratio of different regions in the emission spectra can be exploited for thermometry [1].

As the decay-time of a phosphor can change several orders of magnitude for a given temperature range, point measurements exploiting the time decay are often preferred over intensity-ratio based methods when high temperature accuracy is demanded. Consequently, recent attempts pushed the decay-time retrieval towards 2D application by either using a stack of sequentially gated CCD cameras [2] or fast framing CMOS devices [3].

Measurement precision in phosphor thermometry highly depends on the phosphor itself, its sensitivity to temperature and whether phosphorescence is affected by other interfering factors such as pressure [4], ambient gas composition [5] or in some cases the post growth process of annealing [6,7,8]. In some application the layer thickness of the phosphor may contribute as a substantial source of error [9], also multi-exponential decays can introduce ambiguities to the retrieval of a distinct temperature [10].

Apart from phosphor characteristics, there are other factors to consider that restrict the accuracy of phosphor thermometry. For obvious reasons, the reliability of the temperature calibration is a key feature, i.e. how well is the temperature known during calibration, how many calibration points are sufficient for a given temperature interval and whether the same decay time can be reproduced for a set of different signal intensities. The latter question is a matter of light detection and is aimed to be addressed in this paper. Previous studies have shown that detector saturation might introduce substantial systematic errors to the signal evaluation process in phosphor thermometry [11,12]. This work seeks to compare the performance of four different standard detectors under identical test conditions. Each detector was exposed to the phosphorescence of cadmium tungstate ($CdWO_4$) at five different temperatures under varying light intensities and detector gains.

EXPERIMENTAL

Selection of Detectors

Four time-resolving point detectors have been chosen for comparison within this study. The selection consists of two different photomultiplier tubes (PMTs), a multi-channel plate photomultiplier tube (MCP-PMT) and a fiber-coupled avalanche photodiode (APD). One of the two PMTs can optionally be run in time-gated mode and also offers a more sensitive photocathode within the investigated wavelength range around 450 nm. The MCP-PMT could only be used in time-gated mode. However, by triggering the PMT-gate to open 10ns before / after the first phosphorescence photons hit the detector allowed to study the impact of an initial peak on the signal shape. Signal outputs from detection devices were either directly coupled to a 350 MHz digital oscilloscope using an input resistance of 50 Ω, or optionally connected to an in-house made external current-to-voltage amplifier (5 MHz bandwidth). In total, seven different detector configurations were tested as listed in table 1.

TABLE 1. Detectors and tested operating modes.

Detector Type	Mode of Operation	Gain Range
PMT1	continuous	480-43000
PMT1	cont. + amplified	42-80
PMT2	continuous	950-7700
PMT2	time-gated: +10ns	950-7700
MCP-PMT	time-gated: -10ns	36-3000
MCP-PMT	time-gated: +10ns	36-3000
APD	continuous	62-470

The gain column above represents the electrical amplification range that was investigated for each detector. It has been defined according to oscilloscope peak voltages ranging for each temperature from less than 100 mV up to a few Volts depending on detector specific threshold signal output levels. In addition, figure 1 shows control voltages necessary for each detector to reach an electronic gain corresponding to the gain intervals, given in table 1.

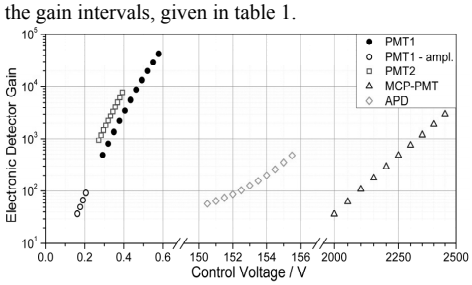

FIGURE 1. Electronic gain as a function of control voltage for each detector given by the manufacturer's data sheets.

Experimental Setup

Figure 2 displays the experimental setup, which was used to compare all detectors in their individual modes of operation (see table 1). A 10 Hz pulsed Nd:YAG laser, operating at 266 nm was used as an excitation source for $CdWO_4$, that was placed in a tube furnace. $CdWO_4$ was chosen in particular as it emits strong and almost single-exponential phosphorescence light, without suffering from irreversible emission changes when exposed to elevated temperatures below 600 K. Its broadband emission centered around 470 nm is temperature sensitive from room temperature up to around 580 K, offering a vast range of decay times that span from 10 µs down to less than 10 ns. For every detector configuration that was listed in table 1, the tube furnace was heated to five constant temperatures at 294, 373, 454, 519 and 561 K, which were monitored by a K-type thermocouple. Temperatures were carefully chosen in order to maintain a reasonable step size for the decay-time in between two proximate temperatures.

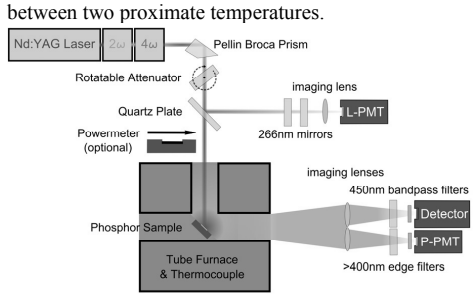

FIGURE 2. Experimental setup for testing the temporal performance of a detector as a function of light intensity, gain and temperature. L- and P-PMT are two identical PMTs referencing the amount of impinging photons per time interval after being calibrated against the power meter.

The phosphorescence was imaged onto the detector by a 300 mm quartz lens at a 90° angle to the laser path axis. A combination of a > 400 nm transmission edge filter and a 450 nm bandpass filter (FWHM = 40 nm) was placed in front of the detector to eliminate spurious laser radiation and to spectrally isolate the phosphorescence emission.

In addition, two identical PMTs are placed in the setup, see figure 2, to monitor the phosphor's response to laser intensity changes. This type of phosphor surveillance is important as any process that shows a change in decay-time as a function of laser intensity might superimpose on the detector-specific results [8]. The L-PMT also monitors the laser pulse-to-pulse fluctuations and once calibrated against a powermeter,

it serves as a reference for the laser pulse energy. The P-PMT, however, sits behind identical optics as the detector and served as a reference for the amount of phosphorescence light that hits the detector, assuming that phosphorescence scattered isotropic within one half-space. Finally, both L- and P-PMT were put to the same gain at 6300 and additional transmission losses were introduced in front the L-PMT to maintain comparable peak output voltages in between these two reference detectors.

By assuming a Gaussian laser pulse shape in time and taking into account all transmission losses in between the power meter and the laser reference, it is possible to estimate the amount of photons hitting the L-PMT per time interval and calibrating its maximum output voltage against the maximum photon exposure within 1 ns centered around the peak of the laser pulse. In another step, by taking into account how the spectral sensitivity of the photocathode compares for the two different wavelengths (266 nm vs. 450 nm), this calibration can be wavelength-corrected and used as an estimate for the amount of photons arriving at the P-PMT or the detector.

As the laser energy is scanned from 15 µJ to 5 mJ using a rotatable attenuator, the phosphorescence intensity changes proportionally allowing to investigate each detector responding to various intensities at several gain settings (see table 1). Figure 3 supports this approach as it shows a largely linear relation between the laser energy (~ L-PMT signal) and phosphorescence signal (P-PMT). However, some minor deviations from linearity can be observed at low laser energies.

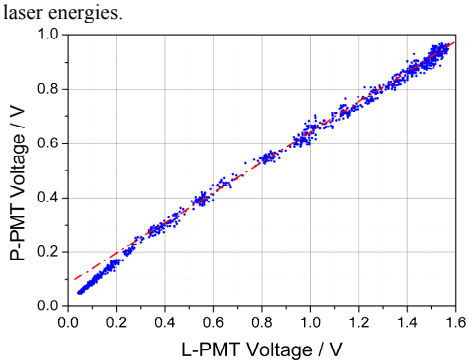

FIGURE 3. Reference PMT peak signal voltages at gain 6300 corresponding to a full laser excitation energy scan from 15 µJ to 5 mJ.

RESULTS AND DISCUSSION

The phosphorescence decay time was evaluated based on a least squares fit (Levenberg-Marquardt) to a single-exponential function. To avoid contributions from changing fitting window positions to the evaluated results, a fixed evaluation time window was chosen for at a given temperature. However, the window size was adapted according to the temperature in order to capture large parts of the decay, see table 2.

TABLE 2. Fitting time window positions after the initial signal peak as a function of Temperature.

Temperature, K	start, s	stop, s
294	10^{-8}	$5x10^{-5}$
373	10^{-8}	$1x10^{-5}$
454	10^{-8}	$8x10^{-7}$
519	10^{-8}	$1.5x10^{-7}$
561	10^{-8}	$8x10^{-8}$

One exception to table 2 has been made for the case of external current-to-voltage amplification: Due to the limited bandwidth of the amplifier the start of the decay was set to 60 ns.

For obvious reasons, the recorded phosphorescence lifetime is a measure for the time-distribution of the detector output signal: An ideal optical detector having a linear response should reproduce signal shapes of constant decay time, regardless the amount of light intensity it is exposed to or the extent of internal signal amplification.

Figure 4 shows the detector response surface for PMT1 at 373 K. The evaluated decay time is displayed in color as a function of gain and photon impingement within 1 ns at maximum signal levels. Every matrix element contains contributions of approximately 100 single decays on average, each evaluated individually and then averaged. In the upper right corner at high gains and photon numbers, the evaluated decay is longer. As this behavior changes with gain, the area can be identified as a detector artifact, caused by saturation. The lower right area in figure 4 has a rather constant decay time distribution, which is desirable for phosphorescence measurements. For low light exposures, there is a lifetime gradient visible that is gain-independent.

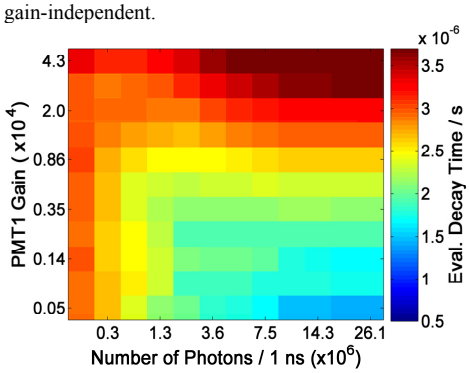

FIGURE 4. Response surface of PMT1 at 373 K.

Figure 5 shows the same detector line-up at 561 K. Lower phosphorescence quantum yields at elevated temperatures caused the last photon number column to be empty. The two elements that made an exception contain just a single decay each, caused by random laser fluctuation. Also the area of saturation in the upper right corner retreated to some extent, which is likely to be caused by shorter decays limiting the build-up time for space charge at the dynodes. The lifetime gradient for low light intensities (present in figure 4) has vanished and some elements at low gains and intensities remained empty as it gets increasingly challenging to evaluate shorter decays.

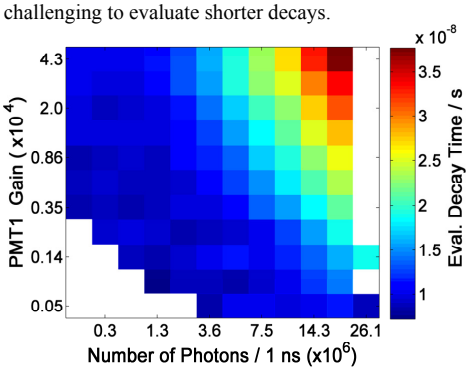

FIGURE 5. Response surface of PMT1 at 561 K.

In figure 6 another PMT (PMT2) was exposed to phosphorescence radiation at 373 K. The gain range was chosen smaller this time to limit output currents since PMT2 had a significantly higher sensitivity around 450 nm: The upper gain region ended at 7700, which is where PMT1 in figure 4 still was not influenced by the saturated region of high gain and intensity. In accordance to these results, figure 6 does not show any saturation limits for the high signal regions, which makes it a preferable device for phosphor thermometry in comparison to PMT1.

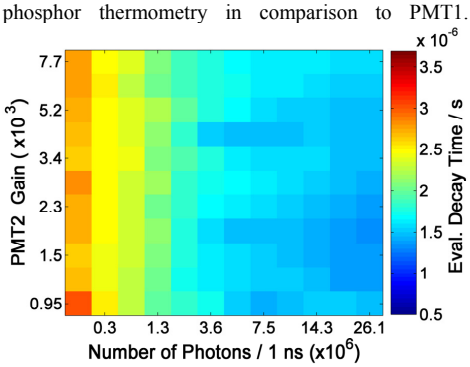

FIGURE 6. Response surface of PMT2 at 373 K.

PMT2 has another advantage, which is being capable of operating in time-gated mode. This can allow cutting off strong fluorescence peaks accompanied with phosphorescence and thus increasing the signal-to-noise ratio without saturating the detector [12]. Since the saturated region was not reached during experiments with PMT2, time-gated results showed very little variation to the presented plots and are thus omitted.

However, the lifetime gradient for the low light level region is still present and stretches across the same range of intensities as observed with PMT1, i.e. for excitation energies lower than 30 µJ (peak phosphorescence < $2x10^6$ photons / ns). It has been confirmed in pre-studies that laser energies at this point are still too low to induce a significant heating effect to the surface. Also simulations have been performed to verify, that this gradient was not caused by the evaluation routine as a result of decreasing signal-to-noise ratios at low excitation energies. Hence, this behavior might be phosphor-intrinsic, which is backed up by the deviation from a linear relation at low laser energies between the two reference PMTs in figure 3. Moreover, similar findings have been reported by [8] showing the phosphorescence decay time of another phosphor, Mg_4FGeO_6:Mn, decreasing for increasing laser excitation energies.

Using PMT1 together with the external current-to-voltage amplifier resulted in reasonable signal levels at much lower gain settings, but came at the cost of reduced time-resolution. This helps avoiding detector saturation as seen in figure 7, but also bandwidth-limits the retrieval of shorter decays, i.e. the highest temperatures that $CdWO_4$ responds to.

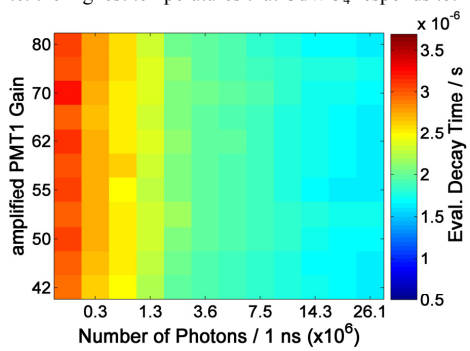

FIGURE 7. Response surface of PMT1 (amplified) recorded at 373 K.

Figure 8 presents the detector response surface of the MCP-PMT at 373 K, with the gate opening 10ns prior to the phosphorescence onset. Even though

output currents have been four times higher for the MCP-PMT compared to PMT1 (figure 4), this device seems not to be affected by high signal saturation. Therefore, cutting off the first intense part of the phosphorescence by triggering the gate to open 10 ns after the initial peak did not show a significant difference.

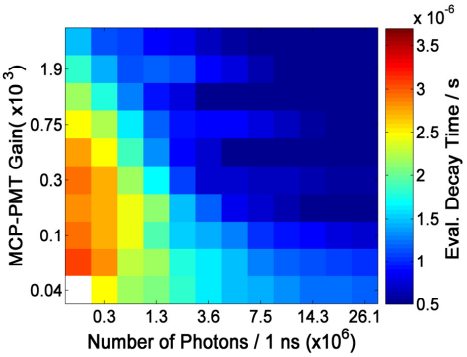

FIGURE 8. Response surface of MCP-PMT at 373 K, triggered 10 ns before the signal arrived.

Finally, figure 9 displays decay-time results, accumulated by using the APD at 373 K. A significant amount of data for the low light intensities has been rejected by the S/N-criteria during evaluation. This is mainly owed to the comparatively high transmission losses in the optical fiber coupling. In addition, the moderate gain range accessible for the APD contributed to recorded signal intensities being less than ½ compared to the other detectors. Other than that, the evaluated decay time seems to be stable for the majority of the displayed workspace, except for the row where the gain was highest. This feature at maximum gain appears for all other temperatures that the APD has experienced and indicates that the APD has approached its global gain limit.

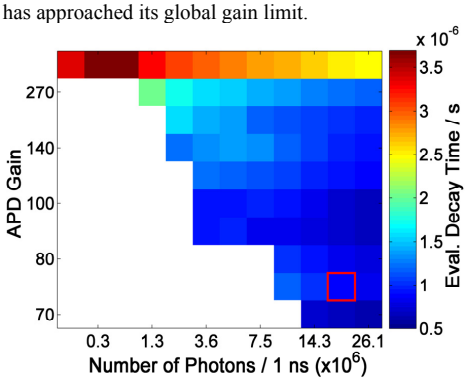

FIGURE 9. Response surface of APD at 373 K.

In figure 10 temperature calibration curves for $CdWO_4$ are plotted, showing the results from all four detectors for the five temperatures under investigation. Since the decay time distribution within one response surface can vary to a substantial extent, the points displayed in figure 10 only describe data from a single fixed matrix element. In order to represent a fairly linear part of the workspace as well as having data available for most of the detectors the chosen element corresponds to the second lowest gain at second highest light exposure, i.e. originates from the lower right corner of each surface plot (see red square in figure 9).

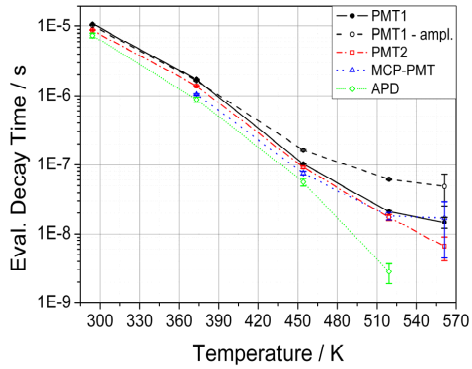

FIGURE 10. Temperature calibration points for all detectors from a fixed response matrix element. Error bars indicate one standard deviation from the mean value.

The external amplification of the PMT1 signal shows a systematic effect on the evaluated lifetime. The loss in bandwidth forced the evaluation window to start later in the decay curve at 60 ns compared to the other detectors and operation modes. This, accompanied with the slight multi-exponential phosphorescence behavior of $CdWO_4$, accounts for the prolonged decay times that were evaluated here. The result is decreased temperature sensitivity and the inability to measure accurate decays shorter than the broadening that is caused by the limited amplifier bandwidth.

For the MCP-PMT the lowest temperature is missing. This is owed to the fact that the maximum gate length was restricted to 10 µs, corresponding to only 1/5 of the sampling time used for the other detectors (see table 2).

The APD proved to exhibit the highest lifetime sensitivity within all investigated detectors. However the low signal output appeared to be one major restriction leaving no useful data for the highest temperature case.

For clarity, the two operational modes where the first 10 ns of the phosphorescence tail were cut off by time-gating were omitted. They carried no further relevant information, but were slightly shifted towards longer decays. The change in decay time can be attributed to the slight multi-exponential shape of $CdWO_4$ phosphorescence accompanied with a fitting window that shifted 10 ns towards a later part of the decay curve.

CONCLUSIONS

The outcome of evaluated exponential decays is strongly biased by light intensity, electrical gain and detector type. Within the investigated operating conditions, the evaluated decay time most commonly varies by a factor of two across an individual response matrix. In some cases the maximum decay time can be as much as six times longer than its minimum counterpart for a given temperature (see figure 8). Clearly, variations of this magnitude add decisive distortions to temperature readings in phosphor thermometry, making detector linearity a key priority for applications with varying signal intensities. Especially, deviations of signal intensities in between calibration and experiment may inflict major systematic temperature errors if detectors are operated outside their linear workspace.

All detectors that were involved in the test showed a declining decay-time gradient, visible within the first four intensity columns. This behavior will be subject for further investigation as it might be phosphor related, suggested by its gain- and detector independence.

PMT2 achieved the best performance amongst all tested devices, providing a large linear workspace without being compromised by additional bandwidth limitations of an external amplifier. Its capability to operate time-gated has not proved its full potential in combination with $CdWO_4$, but is believed to improve linearity for phosphors that exhibit strong fluorescence peaks along with the phosphorescent decay [12]. The MCP-PMT could only run in time gated mode and the maximum gate length was limited to 10 µs, which can be a drawback for phosphors with longer decay times. Performing external signal amplification proved to be useful, helping to limit signal saturation in PMT1 whilst maintaining reasonable signal outputs. Its limited bandwidth however affected the detection sensitivity for decays, shorter than 200 ns (see figure 10). The APD's capability to reproduce short decays is superior to any other detector within this test, as seen in figure 10. Nevertheless, signals acquired with the avalanche photodiode exhibited the lowest signal intensities and originated from a very limited gain range. Yet, the former drawback might be of individual nature as the design of the APD's external housing demanded fiber-optical signal collection, accompanied by relatively high coupling losses.

In summary, this study presents a concept of mapping individual detector responses to gain- and light level variations. It can be used for creating a library of decay response curves allowing to correct evaluated decays from measurements performed outside the linear workspace.

ACKNOWLEDGEMENTS

This work was financially supported by the HELIOS research project within the EU´s 7th Framework program for Research and Technical Development/Transportation (contract number: 030696) and the D60-project financed by the Swedish Energy Agency.

REFERENCES

1. Allison, S. W., and Gillies G. T., *Rev. Sci. Instrum*. **68** 2615–2650 (1997)
2. Omrane, A., Ossler, F. and Aldén, M., *Proc. Comb. Inst.* **29** 2653–2659 (2002)
3. Kissel, T., Baum, E., Dreizler, A. and Brübach, J., *Appl. Phys. B* **96** 731–734 (2009)
4. Chen, Y. R. and Bray, K. L., *Phys. Rev. B* **56** 10882-10891 (1997)
5. Brübach, J., Dreizler, A. and Janicka, J., *Meas. Sci. Technol.* **18** 764-770 (2007)
6. Allison, S. W., Beshears, D. L., Bencic, T., Hollerman, W. A. and Boudreaux, P., "Development of Temperature-Sensitive. Paints for High Temperature. Aeropropulsion Applications" 37th AIAA/ASME/SAE/ ASEE Joint Propulsion Conference Proceedings, AIAA-2001-3528
7. Ranson, R. M., Thomas, C. B. and Craven, M. R., *Meas. Sci. Technol.* **9** 1947-1950 (1998)
8. Brübach, J., Feist, J. P. and Dreizler, A., *Meas. Sci. Technol.* **19** 025602 (2008)
9. Knappe, C., Andersson, P., Algotsson, M., Richter, M., Lindén, J., Aldén M., Tunér, M. and Johansson B., *SAE Int. J. Eng.* **4** 1689-1698 (2011)
10. Lakowicz, J. R., "Time-Domain Lifetime Measurements," in *Principles of Fluorescence Spectroscopy*, Springer Science + Business Media, 2006, pp. 141.
11. Lindén, J., Knappe, C., Richter, M. and Aldén, M., *Meas. Sci. Technol.* **12** (8pp) (2012)
12. Knappe, C., Abou Nada, F., Lindén, J., Richter, M. and Aldén, M., *Rev. Sci. Instrum.* (submitted: December 2011)